Master's thesis

NTNU
Norwegian University of Science and Technology
Faculty of Engineering
Department of Structural Engineering

Håvard Blekastad
Philip A. E. Schell

Seaquake Response of a Floating Wind Turbine

Master's thesis in Civil and Environmental Engineering
Supervisor: Amir M. Kaynia
June 2020

NTNU
Norwegian University of
Science and Technology

Håvard Blekastad
Philip A. E. Schell

Seaquake Response of a Floating Wind Turbine

Master's thesis in Civil and Environmental Engineering
Supervisor: Amir M. Kaynia
June 2020

Norwegian University of Science and Technology
Faculty of Engineering
Department of Structural Engineering

NTNU
Norwegian University of
Science and Technology

Department of Structural Engineering
Faculty of Engineering
NTNU – Norwegian University of Science and Technology

ACCESSIBILITY

Open

MASTER THESIS 2020

SUBJECT AREA:	DATE:	NO. OF PAGES:
Earthquake Engineering	09.06.2020	152+34

TITLE:

Seaquake Response of a Floating Wind Turbine

Sjøskjelv Respons av en Flytende Vindturbin

BY:

Håvard Blekastad

Philip A. E. Schell

SUMMARY:
In this thesis, the effects on a floating wind turbine (FWT) and its mooring system, due to seismic activity in the seabed, are studied. Moreover, the response of an innovative new anchor design for FWT's during earthquake excitation in the seabed is studied. The vertical earthquake excitation of the seabed generates vertically propagating pressure waves in the water, called a seaquake. The resulting pressure is determined using acoustic finite element (FE) models in Abaqus. A two-dimensional acoustic FE model is developed, where the platform of the FWT is represented by a rigid body. Vertical accelerations are applied at the bottom of the models and the resulting pressure under the platform is extracted. The pressure is then applied on a SIMA model of the FWT. The response due to environmental loads, such as wind, current and waves, is also studied and used as a reference for the seaquake response. Considerable vertical accelerations can occur in the nacelle due to amplification of the platform accelerations through the tower. Moderate stresses occur in the tower during seaquake. The mooring tensile forces during seaquake do not exceed the design tension obtained by considering harsh environmental conditions. However, the mooring lines experience zero tension during seaquake, which could cause snap-tension. The anchor design is studied w.r.t. soil-structure interaction (SSI) effects during an earthquake. Plate thicknesses are determined based on analyses considering geostatic stresses from a Plaxis model comprising the structure and a general soil profile, in addition to a design mooring tension. An SSI model of the anchor and the soil profile is established using Abaqus. Several modelling options for the soil and the anchor are investigated and validated against theoretical solutions. Horizontal and vertical accelerations are applied at the bottom of the soil profile in the SSI model. The resulting stresses which occur in the anchor and the displacements of the surrounding soil are studied. The additional stresses due to earthquake accelerations results in exceedance of the capacity of certain components of the anchor. The soil displacements and -strains indicate that the anchor could be pulled out of the seabed during earthquake excitation. These results suggest that the effects of earthquakes should be considered for the design of the anchor.

RESPONSIBLE TEACHER: Prof. Amir M. Kaynia

SUPERVISOR(S): Prof. Amir M. Kaynia

CARRIED OUT AT: Department of Structural Engineering, NTNU

Preface

This thesis is the product of 20 weeks of work and marks the end of our Master's degree at the Norwegian University of Science and Technology (NTNU), within the field of structural engineering. The main focus of the thesis is to study the effects of vertical ground motion during an earthquake on a floating wind turbine (FWT). A floating platform design for FWT's from Dr. techn. Olav Olsen (OO) is investigated. Another focus of the work is to consider the effects of horizontal earthquake ground motion on an anchor design, developed by OO, w.r.t. soil-structure interaction (SSI). The creation of pressure waves in water due to ground motion at the seabed is referred to as a seaquake. Previously, the effect of earthquakes on an FWT have been considered for a turbine mounted on a tension leg platform (TLP). However, the effects of seaquakes on stresses and accelerations of a catenary moored FWT have, to our knowledge, not yet been investigated. This lack of previous studies sparked our interest to dive into the field of hydrodynamics and analysis of marine structures, despite our limited knowledge on the subjects.

The numerical modelling of the seaquake was done using the FE program Abaqus. The work related to developement and validation of numerical models was inspired by a Master's thesis written by two previous students at NTNU. We would like to thank Matias L. Røsvik at Dr. techn. Olav Olsen for sharing his previous experiences related to the development of an acoustic model in Abaqus. His contribution helped us save valuable time during the development of the acoustic models presented in this thesis.

We would like to express an immense gratitude and appreciation towards our supervisor prof. Amir M. Kaynia for his continuous support, engagement and guidance during these last 20 weeks. He led us into the field of FWT's through inspiring discussions. His previous work and experience, related to studies on the effects of earthquakes on bottom fixed turbines, convinced us that floating wind turbines would be a very interesting topic for our Master's thesis. During the semester he always showed great interest in the topic and provided valuable feedback. His contributions were essential for all parts of the thesis and his assistance is gratefully acknowledged.

The study of seaquake effects on an FWT was done using SIMA, a program for analysis and simulation of floating structures and marine operations. We would like to thank Petter A. Berthelsen, at SINTEF Ocean, for providing us with the SIMA model of the FWT. Much gratitude is directed to Erik L. Walter at Dr. techn Olav Olsen, who continuously assisted us and gave us feedback related to technical aspects of the software. Much time was spent to get familiar with SIMA and his efforts helped us acquire the necessary knowledge in order to obtain the desired results in this thesis.

Finally, we would also like to express our gratitude towards prof. Erin Bachynski. She also assisted us with technical aspects related to SIMA. In addition, she provided insight into the field of hydrodynamics, and gave us valuable feedback related to the modelling of a seaquake on an FWT.

Trondheim, 09.06.2020

Håvard Blekastad

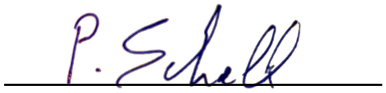

Philip André Eidsvik Schell

Abstract

In order to further exploit available offshore wind for energy production, floating wind turbines (FWT) are being developed to surpass the challenges w.r.t. water depth for bottom fixed turbines. Through the Horizon 2020 funded LIFES50+ research program, a platform concept for wind turbines, called the "OO-Star Wind Floater", was chosen as a candidate for further development and full-scale testing. The platform concept is developed by Dr. techn. Olav Olsen (OO). In this thesis, the effects on an FWT and its mooring system, due to seismic activity in the seabed, are studied. Moreover, the response of an innovative new anchor design for FWT's during earthquake excitation in the seabed is studied. The design is called the "OO-Anchor" and is also developed by OO. The vertical earthquake excitation of the seabed generates pressure waves in the water, propagating towards the water surface. The propagation of pressure waves in water resulting from an earthquake is referred to as a seaquake. Specific values regarding ocean depth, oceanography and meteorological conditions used for the modelling purposes are collected from a LIFES50+ report, describing conditions at the Gulf of Maine on the east coast of the United States.

The pressure during a seaquake is determined using acoustic finite element (FE) models in Abaqus. Accelerations measured during the Loma Prieta earthquake on October 18th, 1989 in California are considered for all of the studies in the thesis. Several one-dimensional acoustic models are developed and validated against corresponding analytical solutions. A two-dimensional acoustic FE model is then developed, where the platform of the FWT is represented by a rigid body. No coupling between the motion of the platform and the pressure under the structure is accounted for in the acoustic models. Vertical accelerations are applied at the bottom of the acoustic models and the resulting pressure under the platform is extracted. The seaquake loading is determined by integrating the pressure over the area of the bottom of the platform. This seaquake loading is then applied as concentrated forces in a SIMA model of the FWT, where coupling between the motion of the platform and forces from the surrounding water is included.

The seaquake loading in the SIMA model is scaled, to investigate for which peak vertical accelerations (PVA) at the seabed the effects due to seaquake become important for the capacity of the components of the FWT. The response due to environmental loads, such as wind, current and waves, is also studied and used as a reference for the seaquake response. Considerable vertical accelerations can occur in the nacelle due to amplification of the platform accelerations through the tower. The nacelle accelerations exceed a commonly used operational limit range of 0.2-0.3g for all of the considered PVA's of the seabed. This should be taken into account for the design of FWT's in regions prone to seismic activity. Moderate stresses occur in the tower during a seaquake. The mooring tensile forces, due to motion of the platform during a seaquake, do not exceed the design tension obtained by considering harsh environmental conditions. However, the mooring lines experience zero tension during seaquake, which could cause snap-tension.

The anchor design is studied w.r.t. soil-structure interaction (SSI) effects during an earthquake. An initial geometry of the anchor is proposed by OO. Plate thicknesses are determined based on analyses considering geostatic stresses from a Plaxis model comprising the structure and a general soil profile, in addition to a design mooring tension recommended by OO. An SSI model of the anchor and the soil profile is established using Abaqus. Several modelling options for the soil and the anchor are investigated and validated against theoretical solutions. Horizontal and vertical accelerations are applied at the bottom of the soil profile in the SSI model. The resulting stresses which occur in the anchor, and the displacements of the surrounding soil are studied. The additional stresses due to earthquake accelerations results in exceedance of the capacity of certain components of the anchor. The soil displacements and -strains indicate that the anchor could be pulled out of the seabed during earthquake excitation. These results suggest that the effects of earthquakes should be taken into account for the design of the anchor.

Sammendrag

For å kunne utnytte tilgjengelige energiressurser tilknyttet havvind, utvikles flytende vindturbiner for å overkomme utfordringene relatert til vanndybde for bunnfaste turbiner. Gjennom det Horizon 2020 støttede LIFES50+ forskningsprogrammet, ble et plattform-konsept kalt "OO-Star Wind Floater" valgt ut som en kandidat for videre utvikling og full-skala testing. Plattform-konseptet er utviklet av Dr. techn. Olav Olsen (OO). I denne oppgaven er effektene på grunn av seismisk aktivitet i sjøbunnen på en flytende vindturbin og dets forankringssystem studert. I tillegg er responsen av et nytt og innovativt ankerdesign for flytende vindturbiner, på grunn av jordskjelv-eksitasjon i sjøbunnen, studert. Navnet på ankerdesignet er "OO-Anchor" og er også utviklet av OO. Vertikal jordskjelv-eksitasjon i sjøbunnen genererer trykkbølger i vann, som propagerer mot vannoverflaten. Propageringen av trykkbølger i vann i forbindelse med jordskjelv kalles et sjøskjelv. Spesifikke verdier for vanndybde, oseanografi og meteorologiske forhold brukt for modelleringen er hentet fra en LIFES50+ rapport, som beskriver forhold ved Gulf of Maine på østkysten av USA.

Trykket som oppstår under et sjøskjelv blir bestemt ved hjelp av akustiske finite element (FE) modeller i Abaqus. Akselerasjoner målt under jordskjelvet Loma Prieta 18. Oktober 1989 i California blir brukt for alle studiene i oppgaven. Flere én-dimensjonale akustiske modeller utvikles og valideres mot tilsvarende analytiske løsninger. En to-dimensjonal akustisk FE modell utvikles, hvor plattformen til den flytende vindturbinen representeres av et fastholdt stivt legeme. Ingen kobling mellom bevegelsen til plattformen og trykket under bunnen av strukturen er tatt hensyn til i de akustiske modellene. Vertikale akselerasjoner er påført bunnen av de akustiske modellene, og trykket under plattformen blir hentet ut. Sjøskjelvlasten blir bestemt ved å integrere trykket over bunnen av plattformen. Lastene påføres deretter som konsentrerte krefter i en SIMA modell av vindturbinen, hvor kobling mellom plattform-bevegelsen og det omkringliggende vannet er inkludert.

Sjøskjelvlasten i SIMA-modellen blir skalert, for å undersøke hvilke vertikale akselerasjons-amplituder ved sjøbunnen som gjør at effektene av sjøskjelvbelastningen på plattformen blir viktig for ulike komponenter av vindturbinen. Responsen på grunn av miljølaster som vind, strøm, og bølger blir også undersøkt og brukes som referanse for responsen under sjøskjelv. Betraktelige vertikale akselerasjoner kan oppstå i nacellen på grunn av amplifikasjon av plattform-akselerasjonene gjennom tårnet. Nacelle-akselerasjonene overskrider en vanlig operasjonell grense på 0.2-0.3g for alle betraktede skaleringer av vertikal akselerasjon ved sjøbunnen. Dette burde tas med i betraktning under dimensjonering av flytende vindturbiner i områder med høy seismisk aktivitet. Moderate spenninger oppstår i tårnet på grunn av sjøskjelv. Strekk i ankerliner, på grunn av plattformbevegelse under sjøskjelv, overskrider ikke dimensjonerende strekk basert på respons på grunn av store miljølaster. Ankerlinene opplever dog null strekk under sjøskjelv, som muligens kan føre til smell i enkelte kjetting-lekker.

Ankerdesignet er studert med tanke på interaksjon mellom jord og struktur under et jordskjelv. Et utgangspunkt for geometrien til ankeret er foreslått av OO. Platetykkelser er bestemt basert på analyser som betrakter geostatiske spenninger, gitt av en Plaxis modell som inneholder strukturen og et generelt jordprofil, i tillegg til en dimensjonerende ankerlast anbefalt av OO. En modell for jord-struktur-interaksjon, som inneholder ankeret og jordprofilet, er etablert i Abaqus. Forskjellige alternativer for modellering av jorden og ankeret er undersøkt og validert mot teoretiske løsninger. Horisontale og vertikale akselerasjoner introduseres i bunnen av jordprofilet i modellen. De resulterende spenningene i ankeret og forskyvningene av jorden rundt strukturen er betraktet. Tilleggsspenningene på grunn av jordskjelv fører til overskridelse av kapasiteten til enkelte komponenter av ankeret. Forskyvningene og tøyningene i jorden viser at det er mulig at ankeret kan bli dratt ut av sjøbunnen i løpet av et jordskjelv. Disse resultatene tilsier at effekter på grunn av jordskjelv burde tas i betraktning for ankerets utforming.

Table of contents

List of symbols

Lowercase Latin letters

a	Side length
a_1, a_2	Gumbel distribution parameters
c	Damping coefficient
c	Material cohesion
c_d	Speed of sound in medium
d	Diameter
d_0	Pin hole diameter
d_xi, d_zi and $d_{\theta\mathrm{i}}$	Local displacements in tower beam model
d_0	Half of the water depth at the Gulf of Maine
f	Force
f_max	Maximum frequency
f_s	Sampling frequency
f_yd	Design yield limit
g	Acceleration of gravity
k	Stiffness
k	Wave number
k^*	Complex wave number
m	Mass
m_ij	Added mass coefficient
m_M	Mean value of maximum samples
n_min	Minimum number of internodal intervals per acoustic wavelength
p	Pressure
q	Evenly distributed load
r	Exponent of velocity
s_u	Undrained shear strength
t	Time
t	Thickness
u, $\dot{u}$ and $\ddot{u}$	Displacement, Velocity and Acceleration
$\dot{u}$, $\dot{v}$ and $\dot{w}$	Fluid velocity in x-, y- and z-direction
$u_{10}(z)$	Wind speed with an averaging period of 10 minutes as a function of elevation
$v_\mathrm{c,tide}$	Tide induced current speed at the surface
$v_\mathrm{c,wind}$	Wind induced current speed at the surface
v_p	Pressure wave velocity
v_p^*	Complex pressure wave velocity
v_s	Shear wave velocity
x, y, z	Spacial coordinates

Uppercase Latin letters

A	Area
A_{33}	Added mass in heave
A_γ	Normalizing factor
A_{cs}	Cross sectional area
B_{33}	Viscous damping
$C_a(\mathrm{u})$	Axial damping coefficient
C_{P}	Power coefficient
D	Water depth
D_0	Half of the reference water depth
D_{33}	Potential damping
D_{Xi}, D_{Zi} and $D_{\theta\mathrm{i}}$	Global displacements in tower beam model
E	Young's modulus
F	Force
F_{a}	Axial force
F_{as}	Axial stiffness force
F_{D}	Damping force
$F_{\mathrm{D}}^{\mathrm{drag}}$	Drag force
F_{z}	Concentrated force due to seaquake pressure
G	Shear modulus
H	Depth
H_{s}	Significant wave height
H_w	Wave height
$H(\omega)$	Transfer function
I	Second moment of area
K_{s}	Bulk modulus
K_{s}^*	Complex bulk modulus
K_{33}	Hydrostatic stiffness in heave
L	Length
L_c	Characteristic length
L_e	Characteristic element length
$L_{\mathrm{e,max}}$	Maximum characteristic element length
L_{max}	Maximum internodal interval for an element
M	Mass
M	Moment
N	Axial force
P	Generated power
$P(t)$	External load
R	Reflection coefficient
R_{anchor}	Horizontal component of mooring line length
R_{out}	Outer radius
Re	Reynolds number

S_{J}	JONSWAP spectrum
S_{PM}	Pierson-Moskowitz spectrum
T	Mooring line tension
$T_{\mathrm{c,dyn}}$	Characteristic dynamic tension
$T_{\mathrm{c,mean}}$	Characteristic mean tension
T_{d}	Design tension in mooring line
T_{D}	Damped natural period
T_{n}	Natural period
T_{p}	Wave peak period
T_{s}	Sampling period
T_{S}	Characteristic site period
U	Flow speed
V	Volume and velocity
V_{rel}	Relative velocity
X_i	Random variable
$X_{\mathrm{n,max}}$	Maximum of a finite range of random variables
Z	Acoustic impedance

Greek letters

α	Mass related Rayleigh damping coefficient
β	Stiffness related Rayleigh damping coefficient
δ	Logarithmic decrement
Δt	Time step
Δt_{cr}	Critical time step
ε	Strain
ξ	Damping ratio
ω	Load frequency/Angular frequency
ω_{n}	Natural frequency
ω_{D}	Damped natural frequency
ω_{p}	Angular spectral peak frequency
η_i	Degree of freedom for a floating vessel
ρ	Mass density
σ	Stress and Normal stress
σ	Spectral width parameter
σ_M	Standard deviation of maximum samples
τ	Shear stress
ϕ	Material friction angle
ϕ_n	Mode shape for mode number "n"
γ	Volumetric drag
γ	Peak-shape parameter
γ_{mean} and γ_{dyn}	Load factors
ν	Poisson's ratio
ν	Kinematic viscosity
μ	Absolute viscosity
λ	Wavelength

Bold symbols

$\boldsymbol{B}$	Strain-displacement matrix
$\boldsymbol{C}$	Damping matrix
$\boldsymbol{d}$	Nodal displacement
$\boldsymbol{D}$	Global displacement
$\boldsymbol{F}$	Body forces
$\boldsymbol{K}$	Stiffness matrix
$\boldsymbol{M}$	Mass matrix
$\boldsymbol{N}$	Shape function
$\boldsymbol{P}(t)$	Load vector
$\boldsymbol{R}^{\text{ext}}$	External load vector
$\boldsymbol{R}^{\text{int}}$	Internal load vector
$\boldsymbol{u}$	Displacement vector
$\dot{\boldsymbol{u}}$	Fluid velocity vector
$\ddot{\boldsymbol{u}}$	Fluid acceleration vector
$\boldsymbol{\Gamma}$	Influence vector
$\boldsymbol{\phi}_{\text{n}}$	Mode shape vector
$\boldsymbol{\Phi}$	Surface tractions
$\boldsymbol{\delta u}$	Virtural displacement
$\boldsymbol{\delta \varepsilon}$	Virtual strain

List of abbreviatons

CDF	Cummulative distribution function
DOF	Degree of freedom
DNV GL	Det Norske Veritas Germanischer Lloyd
DTU	Technical University of Denmark
EOM	Equation of motion
FE	Finite element
FEA	Finite element analysis
FFT	Fast Fourier transforn
FWT	Floating wind turbine
L.P.	Loma Prieta earthquake
MDOF	Multi degree of freedom
ML	Mooring line
MPM	Most probable max
NGI	Norges Geotekniske Institutt
NTNU	Norwegian University of Science and Technology
OO	Dr. techn. Olav Olsen
PDF	Probability density function
PGA	Peak ground acceleration
PM	Pierson-Moskiwitz
PVA	Peak vertical acceleration
RNA	Rotor-Nacelle Assembly
SDOF	Single degree of freedom
SSI	Soil-structure interaction
SWL	Still water level
TLP	Tension Leg Platform
ULS	Ultimate Limit State

Chapter 1

Introduction

1.1 State of the art, floating wind

All over the world renewable energy sources are considered in order to reduce the dependence on fossil fuels and the emission of CO_2. In countries where there are no fossil fuel resources, the development of alternative renewable energy sources is especially important. Europe, USA and Japan are all leaning towards solutions within renewable energy. In Europe, the European Union decided in 2009 that 20 % of the energy consumption of the continent should be provided by renewable sources by the year 2020 (Castro-Santos & Diaz-Casas, 2016). Wind energy will represent an important part of the production of renewable energy in the years to come. As the available locations onshore are constantly reduced due to more densely populated regions and the need for agricultural production, inland wind energy sources become harder and harder to utilize. Other important factors to consider for renewable wind energy on land are the environmental constraints this presents. The installation of onshore wind farms can for instance affect the habitat of wildlife and the rotating blades can pose as a threat for endangered birds. It is also considered by some that wind farms can have a negative visual impact on a landscape. Moving the wind related energy production offshore would be beneficial for the wildlife. This is one of the reasons why marine renewable energy sources are likely to increase in Europe and in other regions of the world (Castro-Santos & Diaz-Casas, 2016). Offshore wind will be an important source of energy in order to meet the previously stated energy goals of the EU. The energy produced with offshore wind is expected to increase rapidly between 2020 and 2030. One example of an early offshore wind farm is Vindeby in Denmark, built in 1991, which was the first offshore wind farm (Power technology, 2017). A more recent example is Hywind Scotland, which is the world's first commercial wind farm with floating wind turbines (FWT's) (Equinor, 2017b).

Most of the development within offshore wind farms is concentrated on offshore turbines with a fixed foundation on the seabed. For the fixed offshore turbines, the main components are similar or identical to the ones found in onshore wind turbines. The main difference lies in the foundation. The main challenges w.r.t. construction of bottom fixed offshore structures are the distance to shore and the depth. Designs with fixed foundations at the seabed are restricted to operate at depths smaller than 50-60m due to cost efficiency (Castro-Santos & Diaz-Casas, 2016). Much of the available energy from offshore wind lies in areas with larger water depths. FWT's are developed in order to produce energy in regions with larger depths. For many countries, using bottom fixed offshore wind parks is not an available option due to the topography of the seabed. In northern Europe, sudden and steep drops of the continental shelf make it challenging to use fixed structures (Castro-Santos & Diaz-Casas, 2016). Projects with FWT's have already been developed in Norway. One example is Equinor's Hywind Demonstrator project which involved the installation of an FWT for testing outside of Karmøy in Norway in 2009 (Equinor, 2017a).

Dr. techn. Olav Olsen (OO), a Norwegian engineering company within structural engineering of offshore and onshore structures, have developed a concept of a platform for FWT's called the OO-Star Wind Floater. In April 2020, the EU research and innovation program Horizon 2020 chose this concept for further development. The OO-Star Wind Floater will be built and installed at a test centre outside of Karmøy in Norway (Dr. techn. Olav Olsen, 2020b). This FWT will be considered in this thesis. More specifically, how the FWT responds to pressure waves originating from an earthquake will be studied. An anchor solution for the FWT will also be studied.

1.2 Floating wind turbines

The terminology used for the components and motions of wind turbines is presented in fig. 1.1. It should be noted that some of the components (the pile and transition piece) only apply for bottom fixed turbines. The power generated from a wind turbine can, based on Rankine-Froude theory, be written as

(Karimirad, 2014)

$$P = \frac{1}{2}\rho_{\text{air}} C_P A_S V_{\text{Rel}}^3 \tag{1.1}$$

where: ρ_{air} = air density
C_P = power coefficient
A_S = swept area of the wind turbine blades
V_{Rel} = relative wind velocity (wind speed relative to the motion of the turbine)

This equation shows the importance of the swept area and the relative wind velocity. *The generated power is in fact proportional to the rotor diameter squared, and the relative wind velocity cubed.* This is one of the reasons why the interest in building wind farms offshore, where winds are stronger and more stable, has increased considerably over the last decades.

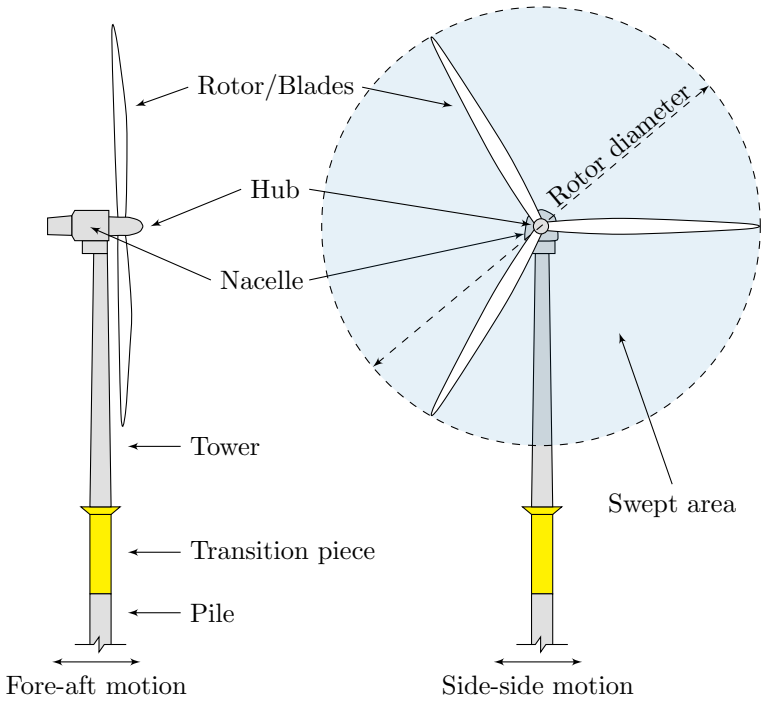

Figure 1.1. Wind turbine nomenclature.

There exist several types of floating platforms to support wind turbines at sea. The three main configurations are semi-submersible, spar, and tension leg platform (TLP) (Castro-Santos & Diaz-Casas, 2016, p.6-7). These are presented in fig. 1.2. A short summary of the three platform alternatives is presented below.

- Semi-submersible platform: The platform is partially submerged, with underwater pontoons supporting the outer columns. The platform is usually anchored to the seabed with catenary or semi-taut mooring lines. A semi-submersible platform is usually a large and heavy structure in order to maintain stability. Stability is also achieved with a large cross-sectional area at still water level (SWL).

- Spar: A vertically oriented floating platform comprising a hollow cylindrical hull. Stability is achieved by having a deep draft with a centre of gravity deeper in the water than the centre of buoyancy. In practice, this is done using ballast weights in the lower part. The relatively small diameter, compared to its draft, makes the spar vertically stable in sea waves. Station keeping is provided by a traditional mooring system e.g. a catenary system.

- Tension leg platform (TLP): The platform is anchored to the seabed by vertical bars in tension, which make the platform very stable in the vertical direction. The tension has to be large enough to avoid slack in the bars, even for the lowest troughs. This induces large vertical forces on the anchors,

which have to be designed accordingly. A TLP platform is possibly a cost effective alternative at large water depths according to some sources (Chandrasekaran, 2018).

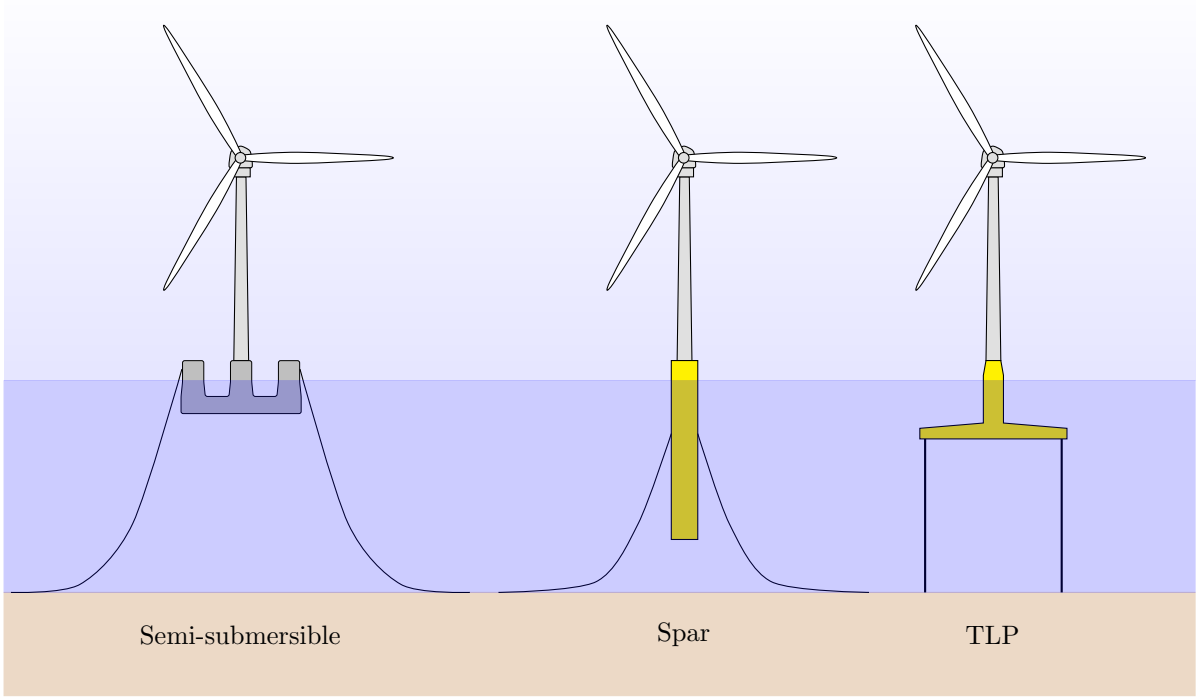

Figure 1.2. Common floater types for wind turbines.

1.3 Seaquakes

The term seaquake is used to denote hydrodynamic pressure waves travelling through the water following an earthquake. Shear waves cannot travel through water due to its low viscosity. Therefore, only compression waves can propagate through water. Vertical motion at the seabed during an earthquake creates pressure waves travelling towards the surface. Thus, seaquakes can affect floating structures such as FWT's. Other floating structures which can be affected by a seaquake are ships. There are multiple examples where ships have experienced the pressure waves produced by an earthquake. One severe incident is a previous Norwegian ship called "MT Ida Knudsen". In 1969, the ship suffered critical damage during an earthquake off the west coast of Gibraltar. The seaquake resulted in severe damages in the hull and disabled some of the machinery on board. After inspections, it was concluded that the ship needed important repair works (Ambraseys, 1985). Another example is the Kobe earthquake in 1995. It was reported that four boats in the Osaka Bay experienced two shock waves during the earthquake (Uenishi & Sakurai, 2014). The shock wave loading from seaquakes could present a threat for floating wind turbines. The acceleration which occurs from the pressure waves could affect components in the turbines, especially the nacelle.

1.4 The effects of seaquakes on floating wind turbines

Studies have already been carried out to assess the effect of seaquake loads on offshore wind turbines. K. Fujioka, Y. Nihei and K. Iijima used a Boundary Element Method and Potential flow theory in order to study the effects of a seaquake on an FWT with a TLP sub-structure (Fukioka et al., 2016). As a seaquake consists of high frequency pressure waves in sea water, it is expected that a seaquake can have an important effect on a TLP-design. In order to avoid resonance with ocean waves, the stiffness of the tension legs is large which gives a high natural frequency and subsequently a low natural period. It was estimated that the dominant frequency of the earthquake excitation which causes a seaquake usually has a dominant frequency content above 2.0 Hz. A consequence of seaquakes can be tension fluctuation of

tensioned tethers, which can be crucial for the capacity of a TLP structure (Fukioka et al., 2016, p.8). It was concluded that seaquakes should be considered for TLP offshore floating wind turbines. The OO-Star Wind Floater has been designed as a structure with a catenary mooring system. Therefore, the natural frequency of the system will be much lower than for a corresponding TLP system. The dominant seaquake frequency is expected to be much larger than the natural frequency of the FWT. Therefore, it is uncertain if a seaquake could lead to any substantial damage on the FWT.

As of today, not many studies on the accelerations which occur in an FWT during a seaquake, have been carried out. The axial acceleration along the turbine tower is of special interest. Especially, the axial acceleration in the top of the tower around the nacelle is important to consider, as the nacelle contains sensitive components. A common industrial practice for the design of floating wind turbines is to set an operational limit in the range 0.2-0.3 g, for the accelerations in the top of the turbine tower (Nejad et al., 2017). This limit is related to the safety of the turbine components in the nacelle. Vertical accelerations from an earthquake have previously been studied for onshore wind turbines with a fixed foundation. It was discovered that the vertical accelerations at the ground surface were amplified by a factor of 2 at the location of the nacelle (Kjølhaug & Kaynia, 2015). Vertical accelerations are generally overlooked during the design of wind turbines. As vertical accelerations can be an important issue for bottom fixed wind turbines, and seaquakes have led to severe damage on ships, the effect of seaquakes on an FWT should be studied.

1.5 Modelling approach

The pressure from a seaquake is determined using acoustic models in the finite element (FE) program Abaqus (ABAQUS Inc. and Dassault Systèmes, 2017). A basic model is investigated to ensure that the model behaves reasonably. Several models are then developed based on this initial basic model, where some are compared with corresponding theoretical solutions.

The effect of a seaquake on the FWT is investigated using a software called SIMA (SINTEF Ocean, 2019b). The program is an analysis and simulation tool for floating structures. The results from the acoustic models in Abaqus are introduced to the model representing the OO-Star Wind Floater in SIMA.

In order to evaluate an anchor design, developed by OO, an FE model is established in Abaqus. More specifically, the anchor along with a chosen soil domain is modelled. The soil and anchor models are validated w.r.t. theoretical results. The objective is to assess the effects of horizontal and vertical earthquake accelerations on the anchor w.r.t. soil-structure interaction (SSI).

1.6 Structure of the thesis

The structure of the thesis is presented below.

- *Chapter 2 Theory*: Relevant theory for structural dynamics, earthquake engineering, hydrodynamics and acoustic modelling is presented.

- *Chapter 3 Case study of an FWT*: The FWT platform is presented along with the considered soil profile. The earthquake accelerations used in the thesis are also presented. Finally, the design of the OO-Anchor is presented.

- *Chapter 4 Acoustic modelling in Abaqus*: The validation of basic acoustic models and the development of more specific models are presented.

- *Chapter 5 Response of an FWT subjected to initial conditions and environmental loads*: Studies of the SIMA modelled FWT behaviour during environmental loading and due to initial conditions are conducted and presented. Alterations made to the original model are described.

- *Chapter 6 Seaquake response of an FWT*: The response of the mooring lines, platform, turbine tower and nacelle due to seaquake is studied.

- *Chapter 7 Numerical model of soil and anchor*: The chosen models for the soil and anchor are presented and validated.

- *Chapter 8 SSI analysis of the anchor*: The full SSI model including the soil domain and the anchor, along with the response of the anchor, are presented.

- *Chapter 9 Discussion*: A discussion of model simplifications and results is presented.

- *Chapter 10 Conclusions and further work*: The conclusions obtained from the results throughout the thesis are presented. Some suggestions for further work are also proposed.

Additional theory, information and results along with Matlab (MathWorks, 2019) scripts are provided in the Appendix.

Chapter 2

Theory

2.1 Structural dynamics

All of the theory related to structural dynamics presented in this section, can be found in Chopra's *Dynamics of structures* (Chopra, 2012).

2.1.1 SDOF and MDOF systems

The equation of motion (EOM) of a single degree of freedom (SDOF) system can be derived by considering equilibrium of the forces and/or moments acting on the system. An example of a SDOF system including the dynamic forces acting on the system is shown in fig. 2.1. A general expression for the SDOF EOM of an arbitrary system is given in eq. (2.1).

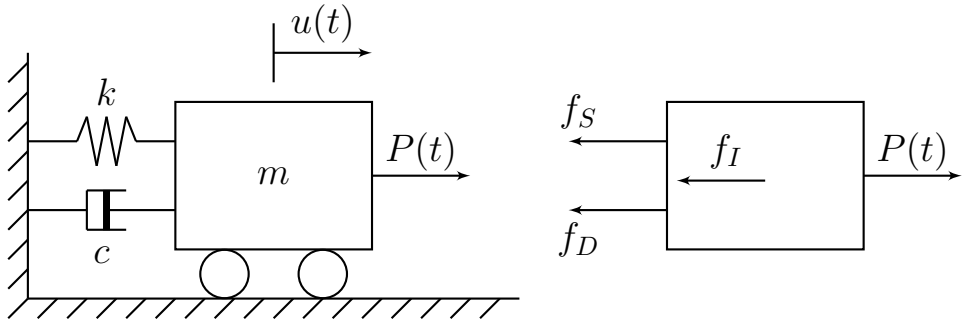

Figure 2.1. SDOF system.

$$f_I + f_D + f_S = P(t) \tag{2.1}$$

where: f_I = Inertia force
f_D = Damping force
f_S = Stiffness force
$P(t)$ = External loading

If the stiffness is assumed to not depend on the displacement of the system, and viscous damping is assumed, the EOM can be expressed as

$$m\ddot{u} + c\dot{u} + ku = P(t) \tag{2.2}$$

where $\ddot{u}$, $\dot{u}$ and u represent the system acceleration, velocity and displacement, respectively. m is the system mass, c is the damping coefficient of the system and k is the system stiffness. Introducing the relations $\omega_n = \sqrt{\frac{k}{m}}$ and $c = 2m\xi\omega_n$ yields a slightly modified EOM.

$$\ddot{u} + 2\xi\omega_n\dot{u} + \omega_n^2 u = \frac{P(t)}{m} \tag{2.3}$$

where ω_n and ξ are the natural frequency and the damping ratio of the system, respectively.
The steady-state response due to a dynamic loading will be the product of a static response term and a transfer function.

$$u_p(t) = H(\omega)\frac{P(t)}{k} \tag{2.4}$$

where $H(\omega)$ is a frequency dependent transfer function, which can also be referred to as a frequency response function. The transfer function will achieve its maximum value when the loading frequency

equals the natural frequency of the system. The steady state response is dependent on $H(\omega)$, which means that it will reach its maximum value when $\omega = \omega_n$. This phenomenon is known as resonance.

Real structures can rarely be represented by a SDOF system, even if many simplifications of the structure are introduced. In order to accurately predict the response of a system, it is modelled as a multi degree of freedom (MDOF) system. An EOM will be associated to each degree of freedom (DOF) and the total

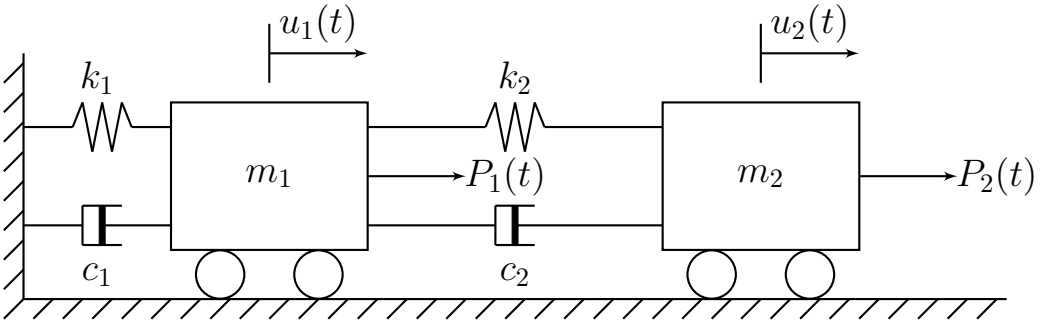

Figure 2.2. MDOF system.

motion of the system is given by "n" coupled equations if there are n DOFs. All of the equations can be written on a compact matrix form.

$$[\boldsymbol{M}]\{\ddot{\boldsymbol{u}}\} + [\boldsymbol{C}]\{\dot{\boldsymbol{u}}\} + [\boldsymbol{K}]\{\boldsymbol{u}\} = \{\boldsymbol{P}(t)\} \tag{2.5}$$

where $[\boldsymbol{M}]$, $[\boldsymbol{C}]$ and $[\boldsymbol{K}]$ designate the mass, damping and stiffness matrices, respectively. $\{\boldsymbol{u}\}$, $\{\dot{\boldsymbol{u}}\}$ and $\{\ddot{\boldsymbol{u}}\}$ represent the displacement and its respective derivatives.

The natural frequencies and the corresponding shape of the vibration modes, also known as mode shapes, can be determined by solving the eigenvalue problem related to the EOM.

$$([\boldsymbol{K}] - \omega_n^2[\boldsymbol{M}])\boldsymbol{\phi}_n = \boldsymbol{0} \implies \det\big([\boldsymbol{K}] - \omega_n^2[\boldsymbol{M}]\big) = 0 \tag{2.6}$$

where $\boldsymbol{\phi}_n$ is the eigenvector and mode shape of the n-th vibration mode. The mode shapes contain information about the displacements relative to each other, they do not show physical values for the displacement.

The response of one DOF depends on the other DOFs. This is known as a coupled system of equations. There are several solution methods for obtaining the response of a system. Direct integration is one of these.

2.1.2 Damping

Damping refers to the process where the amplitude of structural vibrations diminishes due to dissipation of energy. It can occur from several mechanisms. Generally, more than one damping mechanism is present in a structure at the same time. Mechanisms causing energy dissipation are for instance friction in steel connections or opening and closing of microcracks in concrete. Describing each mechanism exactly is challenging and not practical. Instead, damping in structures is usually idealized as one or several linear viscous dampers with damping ratios equivalent to the energy dissipated from the mechanisms. This is denoted classical damping. For nonlinear systems, where nonlinear damping may occur due to inelastic material behaviour, the damping matrix must be defined completely. This is generally the case when modal decomposition, also known as classical modal analysis, cannot be utilized.

For structural systems where similar damping mechanisms are present throughout the structure, such as as a building with multiple storeys which is regular in plan and height (same structural layout and materials), classical damping can be employed to approximate the damping in the system. On the other hand, for systems where different parts have significant different levels of damping, such as a soil-structure system, non-classical damping should be applied. For such systems, the total damping matrix is established by assembling the damping matrices from the different parts, such as the soil and the structure.

A classical damping matrix can be established through the use of Rayleigh damping. The damping matrix is determined using a linear combination of the mass and stiffness matrices, which utilizes the orthogonality properties of these two system matrices. The corresponding modal damping matrix becomes diagonal.

$$[\boldsymbol{C}] = \alpha[\boldsymbol{M}] + \beta[\boldsymbol{K}] \tag{2.7}$$

The damping ratio for mode number n is then given by:

$$\xi_n = \frac{\alpha}{2}\frac{1}{\omega_n} + \frac{\beta}{2}\omega_n \tag{2.8}$$

The damping ratio for mode n will depend significantly on the natural frequency of the mode. Based on experimental data, different modes can have approximately the same damping ratios.
The coefficients α and β can be calculated from two known damping ratios ξ_i and ξ_j for modes i and j.

$$\frac{1}{2}\begin{bmatrix} 1/\omega_i & \omega_i \\ 1/\omega_j & \omega_j \end{bmatrix}\begin{bmatrix} \alpha \\ \beta \end{bmatrix} = \begin{bmatrix} \xi_i \\ \xi_j \end{bmatrix} \tag{2.9}$$

If it is assumed that the damping ratios of modes i and j are the same, then

$$\alpha = \xi\frac{2\omega_i\omega_j}{\omega_i + \omega_j} \qquad \beta = \xi\frac{2}{\omega_i + \omega_j} \tag{2.10}$$

A graphical representation of the damping ratios obtained using Rayleigh damping is shown in fig. 2.3

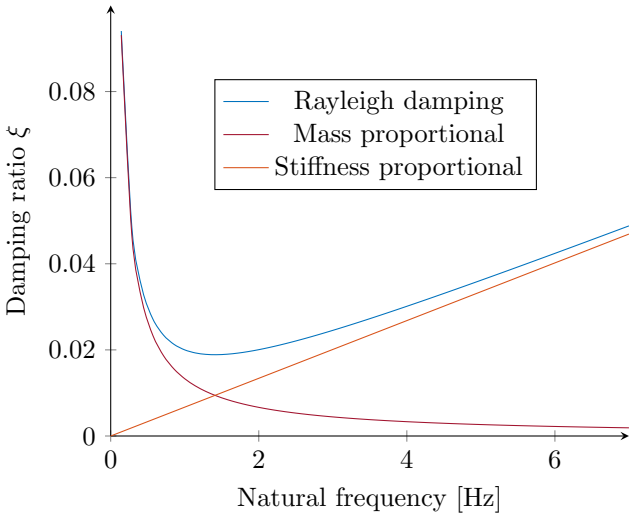

Figure 2.3. Variation of modal damping ratios as a function of natural frequency.

2.1.3 Experimental determination of damping

Because the damping ratio ξ is impossible to determine analytically for real structures, damping has to be assessed in a different way. One method is to perform a free vibration experiment, where the ratio of successive peaks of displacement is measured. The solution of eq. (2.3) subjected to $P(t) = 0$, initial conditions $u(0)$ and $\dot{u}(0)$, is expressed as (Chopra, 2012, p.52-56)

$$u(t) = e^{-\xi\omega_n t}\left[u(0)\cos\omega_{\mathrm{D}}t + \frac{\dot{u}(0) + \xi\omega_n u(0)}{\omega_{\mathrm{D}}}\sin\omega_{\mathrm{D}}t\right] \tag{2.11}$$

The motion described by eq. (2.11) is illustrated in fig. 2.4. The ratio between displacement $u(t)$ and $u\left(t + T_{\mathrm{D}}\right)$ can be derived from eq. (2.11). Utilizing that $T_{\mathrm{D}} = \frac{T_n}{\sqrt{1-\xi^2}}$ and $\omega_n = \frac{2\pi}{T_n}$, the ratio is expressed as

$$\frac{u(t)}{u(t+T_{\mathrm{D}})} = \frac{e^{-\xi\omega_n t}}{e^{-\xi\omega_n(t+T_{\mathrm{D}})}} = e^{\xi\omega_n T_{\mathrm{D}}} = e^{\left(\frac{2\pi\xi}{\sqrt{1-\xi^2}}\right)} \tag{2.12}$$

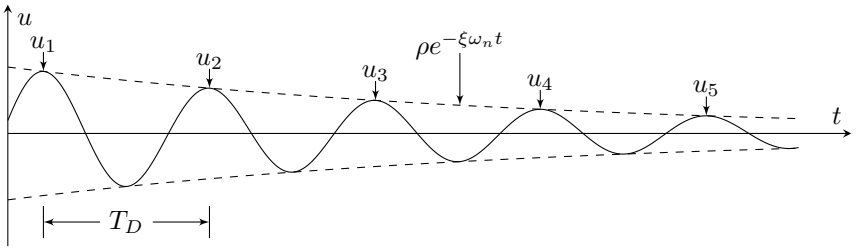

Figure 2.4. Damped free vibration with peaks of displacement indicated by $u_1, u_2, \ldots, u_5$.

The natural logarithm of eq. (2.12) is referred to as the *logarithmic decrement*

$$\delta = \ln \frac{u_i}{u_{\mathrm{i+1}}} = \frac{2\pi\xi}{\sqrt{1-\xi^2}} \tag{2.13}$$

For systems with low damping the denominator $\sqrt{1-\xi^2}$ is approximately equal to one, and eq. (2.13) simplifies to

$$\delta \approx 2\pi\xi \tag{2.14}$$

The ratio between u_1 and a displacement peak several cycles later u_{j+1} can be preferred for assessing the damping present in a slowly decaying motion

$$\frac{u_1}{u_{\mathrm{j+1}}} = \frac{u_1}{u_2}\frac{u_2}{u_3}\cdots\frac{u_j}{u_{\mathrm{j+1}}} = e^{j\delta} \tag{2.15}$$

Taking the natural log of eq. (2.15) and multiplying by $\frac{1}{j}$ yields

$$\delta = \frac{1}{j}\ln\frac{u_1}{u_{j+1}} \approx 2\pi\xi \tag{2.16a}$$

$$\implies \xi = \frac{1}{2\pi j}\ln\frac{u_i}{u_{\mathrm{i+j}}} \tag{2.16b}$$

2.1.4 FE equations of motion

The equation of motion may be derived requiring that the work done by external forces must be equal to the work done by internal forces over any imagined small displacement $\delta\boldsymbol{u}$ satisfying compatibility and boundary conditions (Cook et al., 2001). This work balance is expressed mathematically by the following equation

$$\int \{\delta\boldsymbol{u}\}^T\{\boldsymbol{F}\}\,dV + \int \{\delta\boldsymbol{u}\}^T\{\boldsymbol{\Phi}\}\,dS + \sum_{i=1}^{n}\{\delta\boldsymbol{u}\}_i^T\{\boldsymbol{p}\}_i = \int \left(\{\delta\boldsymbol{u}\}^T\rho\{\ddot{\boldsymbol{u}}\} + \{\delta\boldsymbol{u}\}^T c\{\dot{\boldsymbol{u}}\} + \{\delta\boldsymbol{\epsilon}\}^T\{\boldsymbol{\sigma}\}\right) dV \tag{2.17}$$

where:
- ρ = mass density
- c = damping parameter
- $\{\boldsymbol{F}\}$ and $\{\boldsymbol{\Phi}\}$ = body forces and surface tractions, respectively
- $\{\boldsymbol{p}_i\}$ and $\{\delta\boldsymbol{u}\}_i$ = concentrated load and virtual displacement respectively, at point i
- $\{\delta\boldsymbol{u}\}$ and $\{\delta\boldsymbol{\epsilon}\}$ = Virtual displacements and corresponding virtual strains

The displacements and corresponding strains are discretized by assuming

$$\{\boldsymbol{u}\} = [\mathbf{N}]\{\boldsymbol{d}\} \qquad \{\dot{\boldsymbol{u}}\} = [\mathbf{N}]\{\dot{\boldsymbol{d}}\} \qquad \{\ddot{\boldsymbol{u}}\} = [\mathbf{N}]\{\ddot{\boldsymbol{d}}\} \qquad \{\boldsymbol{\epsilon}\} = [\mathbf{B}]\{\boldsymbol{d}\} \tag{2.18}$$

where:
- $[\mathbf{N}] = [\mathbf{N}(x,y,z)]$ = shape functions
- $[\mathbf{B}] = [\boldsymbol{\partial}]\,[\mathbf{N}]$ = strain-displacement matrix
- $\{\boldsymbol{d}\} = \{\boldsymbol{d}(t)\}$ = nodal displacements
- $\{\dot{\boldsymbol{d}}\} = \{\dot{\boldsymbol{d}}(t)\}$ = nodal velocities
- $\{\ddot{\boldsymbol{d}}\} = \{\ddot{\boldsymbol{d}}(t)\}$ = nodal accelerations

Assuming that the concentrated loads $\{\boldsymbol{p}\}_i$ are located at nodes, and introducing the FE-discretization of eq. (2.18) into eq. (2.17) yields

$$\{\delta \boldsymbol{d}\}^T \Bigg[\overbrace{\int \rho [\mathbf{N}]^T [\mathbf{N}] \, dV}^{[\boldsymbol{m}]} \{\ddot{\boldsymbol{d}}\} + \overbrace{\int c [\mathbf{N}]^T [\mathbf{N}] \, dV}^{[\boldsymbol{c}]} \{\dot{\boldsymbol{d}}\} + \overbrace{\int [\mathbf{B}]^T \{\boldsymbol{\sigma}\} \, dV}^{\{\boldsymbol{r}^{\text{int}}\}} \underbrace{- \int [\mathbf{N}]^T \{\boldsymbol{F}\} \, dV - \int [\mathbf{N}]^T \{\boldsymbol{\Phi}\} \, dS - \sum_{i=1}^{n} \{\boldsymbol{p}\}_i}_{-\{\boldsymbol{r}^{\text{ext}}\}} \Bigg] = 0 \quad (2.19)$$

Since $\{\delta \boldsymbol{d}\}$ may be chosen arbitrarily, the expression inside the brackets of eq. (2.19) has to equal zero, and the equation of motion for a single finite element is obtained.

$$[\boldsymbol{m}]\{\ddot{\boldsymbol{d}}\} + [\boldsymbol{c}]\{\dot{\boldsymbol{d}}\} + \{\boldsymbol{r}^{\text{int}}\} = \{\boldsymbol{r}^{\text{ext}}\} \quad (2.20)$$

For linear elastic materials, the internal force vector $\{\boldsymbol{r}^{\text{int}}\}$ may be expressed by the stiffness matrix and the nodal displacements of the element.

$$[\boldsymbol{m}]\{\ddot{\boldsymbol{d}}\} + [\boldsymbol{c}]\{\dot{\boldsymbol{d}}\} + [\boldsymbol{k}]\{\boldsymbol{d}\} = \{\boldsymbol{r}^{\text{ext}}\} \quad (2.21)$$

On a global level, the element nodal displacements $\{\boldsymbol{d}\}$ are replaced by global displacements $\{\boldsymbol{D}\}$, and the contribution from element matrices $[\boldsymbol{m}]$ and $[\boldsymbol{c}]$ are collected in the global matrices $[\boldsymbol{M}]$ and $[\boldsymbol{C}]$. $\{\boldsymbol{R}^{\text{int}}\}$ for nonlinear material models is constructed by assembling $\{\boldsymbol{r}^{\text{int}}\} = \int [\mathbf{B}]^T \{\boldsymbol{\sigma}\} \, dV$ from each element. If the material model is linear, a global stiffness matrix $[\boldsymbol{K}]$ may be constructed by assembly of $[\boldsymbol{k}]$ from each element. This yields the governing equations of motion for structural dynamics.

$$[\boldsymbol{M}]\{\ddot{\boldsymbol{D}}\} + [\boldsymbol{C}]\{\dot{\boldsymbol{D}}\} + \{\boldsymbol{R}^{\text{int}}\} = \{\boldsymbol{R}^{\text{ext}}\} \quad (2.22)$$

Alternatively for structures with a linear material model

$$[\boldsymbol{M}]\{\ddot{\boldsymbol{D}}\} + [\boldsymbol{C}]\{\dot{\boldsymbol{D}}\} + [\boldsymbol{K}]\{\boldsymbol{D}\} = \{\boldsymbol{R}^{\text{ext}}\} \quad (2.23)$$

These equations represent a semi-discretization. The response is spatially discretized by a finite number of nodes, but the nodal motions are continuous functions of time. When solving eq. (2.22) and eq. (2.23) by direct integration, the equations are also discretized in time, by obtaining solutions at a finite number of time steps.

2.1.5 Direct integration of equations of motion

For a system subjected to arbitrary non-periodic time-varying loading, the transient part of the response may dominate, and direct integration of the equations of motion is required. Usually, the considered time interval is divided into N equal time increments Δt from $t = 0$ to $t = T$, where T is the length of the time interval and $\Delta t = T/N$. An approximate solution of the response $\{\boldsymbol{D}(t)\}$ at time steps $t = \Delta t, 2\Delta t, 3\Delta t, \ldots, N\Delta t$ is then established by the integration scheme at hand. The equations of motion at the n-th time step t_n are

$$[\boldsymbol{M}]\{\ddot{\boldsymbol{D}}\}_n + [\boldsymbol{C}]\{\dot{\boldsymbol{D}}\}_n + \{\boldsymbol{R}^{\text{int}}\}_n = \{\boldsymbol{R}^{\text{ext}}\}_n \quad (2.24)$$

$$[\boldsymbol{M}]\{\ddot{\boldsymbol{D}}\}_n + [\boldsymbol{C}]\{\dot{\boldsymbol{D}}\}_n + [\boldsymbol{K}]\{\boldsymbol{D}\}_n = \{\boldsymbol{R}^{\text{ext}}\}_n \quad (2.25)$$

Different methods of direct integration are classified as either *explicit*- or *implicit* integration. These methods can be used to solve both linear and nonlinear systems, and systems with classical or nonclassical damping. Explicit methods utilize information from equilibrium conditions from previous time steps where the solution is already known, and establishes $\{\boldsymbol{D}\}_{n+1}$ at time step t_{n+1} directly. During implicit integration, $\{\boldsymbol{D}\}_{n+1}$ is obtained indirectly at t_{n+1}, by equilibrium considerations (Mathisen, 2019). Because of these equilibrium considerations, implicit integration is more computationally demanding, compared to explicit integration, during each time step. However, the overall computational expense may be lower. This is because explicit integration requires that the time increment Δt is smaller than a critical value Δt_{cr} to maintain a numerically stable solution, while common implicit integration methods are unconditionally stable. The Newmark method is one example for an implicit time-stepping method (see A.2). This solution method may introduce numerical damping of the response.

2.2 Earthquakes

The majority of the theory on analysis of the effects of earthquakes on soil and structures presented in this section, can be found in Kramer's *Geotechnical Earthquake Engineering* (Kramer, 1996).

2.2.1 Background

An earthquake is a natural hazard that has been occurring on the earth for several million years. Earthquakes give rise to vertical- and horizontal ground motion, and they usually last between 15 and 30 seconds (Chandrasekaran, 2018). Earthquakes occur as a result of sliding of tectonic plates which is a result of accumulations of stresses in the earth's crust (Kramer, 1996). The goal of earthquake engineering is to limit the destructive consequences resulting from such a hazard.

During an earthquake, different types of waves are produced. These are categorized into two main groups: body waves and surface waves. Body waves travel through the interior of the earth and are divided into two wave types: p-waves and s-waves. P-waves are also denoted primary waves, and these are compressional and longitudinal. These can be compared to sound waves and can travel through both solids and liquids, such as water. While P-waves cause deformation parallel to their direction of propagation, S-waves cause deformation perpendicularly to their direction of propagation. For the case of fluids, such as water, the lack of shear stiffness means that S-waves cannot propagate through these. The propagation velocity for body waves depends on the stiffness of the materials these travel through. Geological material are stiffer in compression, which means that P-waves travel faster than S-waves. Surface waves travel along the surface of the earth. These waves are a result of interactions between body waves and the surface. The most important surface waves are Rayleigh and Love waves (Kramer, 1996, p. 2.2.1). An illustration of the previously mentioned wave types is shown in fig. 2.5.

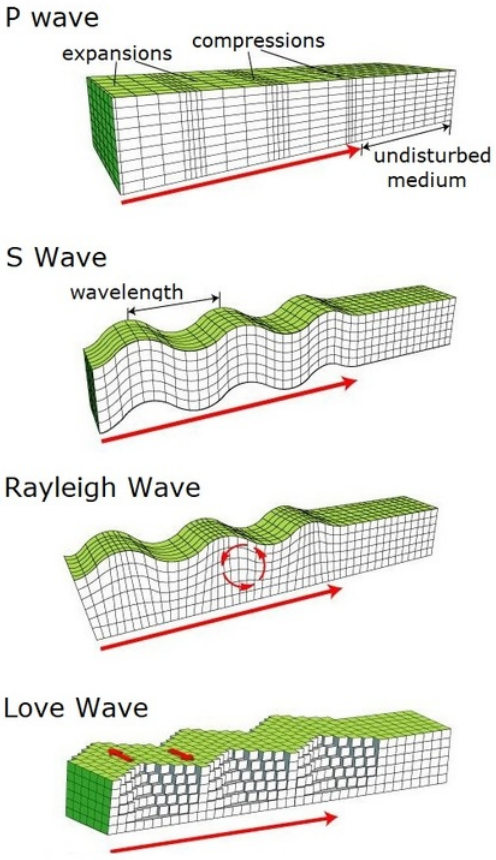

Figure 2.5. An illustration of the most important wave types related to earthquakes (Science Learning Hub Pokapu Akoranga Putaiao, 2007).

2.2.2 Systems subjected to seismic loading

The total displacement u_t is the sum of the displacement of the ground u_g and the relative displacement of the structure u.

$$u_t = u_g + u \tag{2.26}$$

The same applies for the acceleration.

$$\ddot{u}_t = \ddot{u}_g + \ddot{u} \tag{2.27}$$

When assessing the dynamic response of a system subjected to an earthquake, the relative displacement and total acceleration are considered. Considering equilibrium of the forces acting on the system in fig. 2.6, yields the following

$$m\ddot{u}_t + c\dot{u} + ku = 0 \quad \rightarrow \quad m\ddot{u} + c\dot{u} + ku = -m\ddot{u}_g \tag{2.28}$$

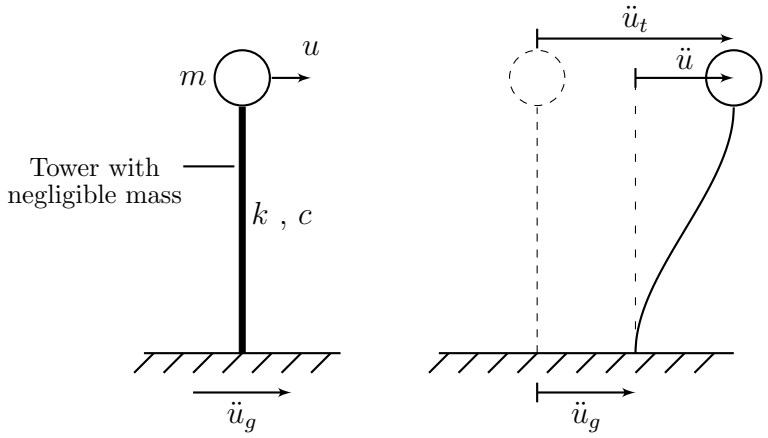

Figure 2.6. A SDOF system subjected to an earthquake.

The inertia force which occurs due to the ground acceleration is the driving force during an earthquake, there is no external force. For a MDOF system, a similar result may be obtained:

$$\boldsymbol{M}\ddot{\boldsymbol{u}} + \boldsymbol{C}\dot{\boldsymbol{u}} + \boldsymbol{K}\boldsymbol{u} = -\boldsymbol{M}\boldsymbol{\Gamma}\ddot{u}_g \tag{2.29}$$

where $\boldsymbol{\Gamma}$ is an influence vector, with as many entries as the number of DOFs, which represents the displacement of the masses within from application of a unit ground displacement.

2.2.3 Propagation of pressure waves in water

Undamped case with a rigid reflector at one end

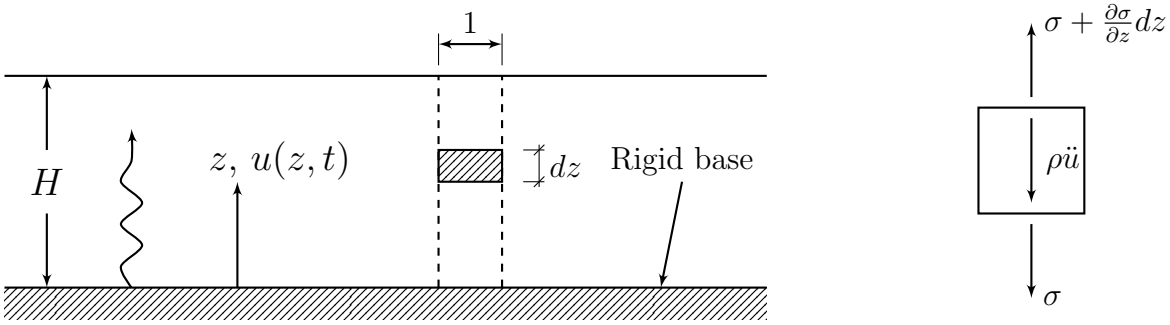

Figure 2.7. Vertically propagating pressure wave in a 1D-medium.

A one-dimensional idealization of an unbounded medium is considered. The medium can be represented by an infinitely long rod. It is assumed that the rod is constrained against deformation in the radial direction. Thus, the displacement of particles caused by a longitudinal wave will be parallel with the orientation of the rod. Considering the equilibrium of forces in fig. 2.7 yields

$$\frac{\partial \sigma}{\partial z} - \rho\ddot{u} = 0 \quad \text{where} \quad \sigma = K_s \cdot \varepsilon = K_s \frac{\partial u}{\partial z} \tag{2.30}$$

The wave equation can then be obtained:

$$\frac{\partial^2 u}{\partial t^2} = v_p^2 \frac{\partial^2 u}{\partial z^2} \tag{2.31}$$

where: $v_p = \sqrt{\frac{K_s}{\rho}}$ = Pressure wave velocity
K_s = Bulk modulus
ρ = Density

The following solution is assumed.

$$u(z,t) = \bar{u}e^{i\omega t} \tag{2.32}$$

This then gives.

$$\frac{\partial^2 \bar{u}}{\partial z^2} + \left(\frac{\omega}{v_p}\right)^2 = 0 \quad \Rightarrow \quad \bar{u} = A \cdot \cos\left(\frac{\omega z}{v_p}\right) + B \cdot \sin\left(\frac{\omega z}{v_p}\right) = A \cdot \cos(kz) + B \cdot \sin(kz) \tag{2.33}$$

where: $k = \frac{\omega}{v_p}$ = wave number
ω = angular frequency

The boundary conditions are used to determine an analytical solution.

$$\bar{u}(z=0) = u_0 \quad \Rightarrow \quad A = u_0 \tag{2.34}$$

$$\bar{u}(z=H) = 0 \quad \Rightarrow \quad B = \frac{-u_0}{\tan(kH)} \tag{2.35}$$

The analytical solution is then

$$u(z,t) = u_0 \left(\cos(kz) - \frac{\sin(kz)}{\tan(kH)}\right) e^{i\omega t} \tag{2.36}$$

A transfer function for the pressure at $z = H$ can then be determined.

$$H_1(\omega) = \frac{\sigma_{\max}|_{z=h}}{u_{\max}|_{z=0}} = \frac{K_s k}{\sin(kH)} \tag{2.37}$$

Undamped case with zero pressure at one end

The top of the medium is now assumed to have a pressure equal to zero. The boundary conditions are once again used to determine $\bar{u}$.

$$\bar{u}(z=0) = u_0 \quad \Rightarrow \quad A = u_0 \tag{2.38}$$

$$\sigma(z=H,t) = 0 \quad \Rightarrow \quad \frac{\partial \bar{u}}{\partial z}|_{z=h} = 0 \quad \Rightarrow \quad B = u_0 \cdot \tan(kH) \tag{2.39}$$

The following analytical solution is then obtained.

$$u(z,t) = u_0(\cos(kz) + \tan(kH) \cdot \sin(kz))e^{i\omega t} \tag{2.40}$$

A transfer function for the pressure at $z = z'$ can be determined.

$$H_2(\omega) = \frac{\sigma_{\max}|_{z=z'}}{u_{\max}|_{z=0}} = K_s k(-\sin(kz') + \tan(kH)\cos(kz')) \tag{2.41}$$

Introducing damping

A frequency independent damping is introduced. The damping is represented through the use of a complex bulk modulus K_s^*.

$$K_s^* = K_s(1 + i2\xi) \tag{2.42}$$

A complex pressure wave velocity and wave number can then be determined. Quadratic terms of ξ are assumed to negligible.

$$v_p^* = \sqrt{\frac{K_s^*}{\rho}} = \sqrt{\frac{K_s(1+i2\xi)}{\rho}} \approx \sqrt{\frac{K_s}{\rho}}(1+i\xi) = v_p(1+i\xi) \tag{2.43}$$

$$k^* = \frac{\omega}{v_p^*} = \frac{\omega}{v_p(1+i\xi)} = \frac{\omega(1-i\xi)}{v_p(1+\xi^2)} \approx \frac{\omega(1-i\xi)}{v_p} = k(1-i\xi) \tag{2.44}$$

The transfer functions then become:

$$H_1(\omega) = \frac{K_s(1+i2\xi)k(1-i\xi)}{\sin(k(1-i\xi)H)} = \frac{K_s k(1+i\xi+2\xi^2)}{\sin(k(1-i\xi)H)} \approx \frac{K_s k(1+i\xi)}{\sin(k(1-i\xi)H)} \tag{2.45}$$

$$H_2(\omega) = K_s k(1+i\xi)(-\sin(k(1-i\xi)) + \tan(k(1-i\xi)H)\cos(k(1-i\xi)z')) \tag{2.46}$$

2.2.4 Propagation of shear waves in soil

For a one-dimensional ground response analysis, the bedrock and soil layers are assumed to extend infinitely in the horizontal directions. It is also assumed that all boundaries are horizontal and that the response of a soil deposit is mainly caused by horizontal shear waves, which propagate vertically from bedrock (Kramer, 1996). One way to obtain different response quantities of the ground is to use transfer functions. This relies on superposition, and is therefore limited to linear analysis.

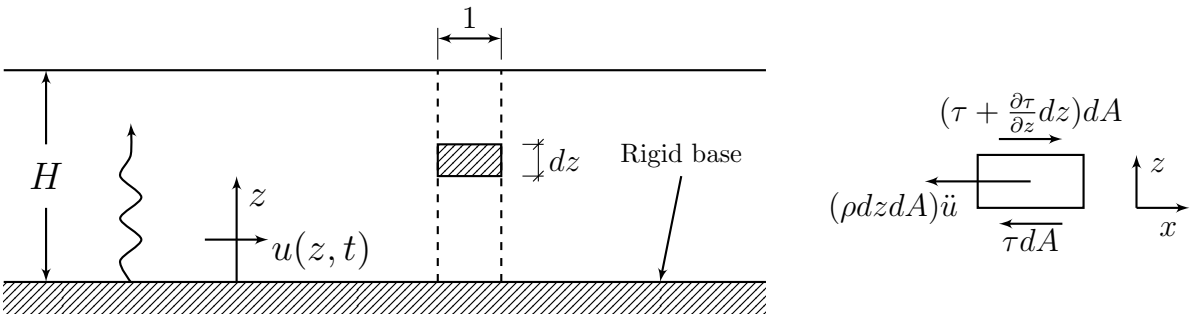

Figure 2.8. Vertically propagating shear waves in a uniform soil medium.

For a linear elastic soil deposit over bedrock, horizontal harmonic motion of the bedrock will result in vertically propagating shear waves through the soil layer. The horizontal motion through the soil can be expressed through a simple equilibrium consideration of the infinitesimal element in fig. 2.8

$$\sum F_x = 0 \implies \frac{\partial \tau}{\partial z} - \rho \ddot{u} = 0 \tag{2.47}$$

Introducing the following relations

$$\tau = G\gamma = G\frac{\partial u}{\partial z} \qquad \text{and} \qquad v_s = \sqrt{\frac{G}{\rho}}$$

yields

$$\frac{\partial^2 u}{\partial z^2} - \frac{1}{v_s^2}\ddot{u} = 0 \tag{2.48}$$

The response is assumed to be a trigonometric function of time.

$$u(z,t) = \bar{u}(z)\cos\omega t \tag{2.49}$$

The following equation is then obtained.

$$\frac{\partial^2 \bar{u}}{\partial z^2}\cos\omega t + \left(\frac{\omega}{v_s}\right)^2 \cos\omega t\ \bar{u} = 0 \implies \frac{\partial^2 \bar{u}}{\partial z^2} + \left(\frac{\omega}{v_s}\right)^2 \bar{u} = 0 \tag{2.50}$$

The solution of eq. (2.50) is given by

$$\bar{u} = A\cos\frac{\omega}{v_s}z + B\sin\frac{\omega}{v_s}z \tag{2.51}$$

Introducing the following boundary conditions

$$\bar{u}(z=0) = u_0 \qquad \text{and} \qquad \tau(z=H) = G\frac{\partial \bar{u}}{\partial z}\Big|_{z=H}\cos\omega t = 0$$

yields

$$\bar{u} = u_0\cos\frac{\omega}{v_s}z + u_0\tan\frac{\omega H}{v_s}\sin\frac{\omega}{v_s}z \tag{2.52}$$

where: ω = base excitation circular frequency
v_s = shear wave velocity ($= \sqrt{\frac{G}{\rho}}$)
G = shear modulus
ρ = density

eq. (2.52) can be used to produce a transfer function $H(\omega)$ which expresses the ratio between displacement amplitude at the bottom, and the top of the soil layer

$$H(\omega) = \frac{|u(H,t)|}{|u(0,t)|} = \frac{|\bar{u}(H)|}{|\bar{u}(0)|} = \frac{1}{|\cos(\omega H/v_s)|} \tag{2.53}$$

The expression in eq. (2.53) shows that the displacement amplitude at the free surface will always be equal to or greater than the displacement amplitude at the bottom. As the denominator of eq. (2.53) approaches zero ($\frac{\omega H}{v_s} \to \frac{\pi}{2} + n\pi$), the amplification goes toward infinity and the soil layer is in resonance. This shows the importance of the excitation frequency at the base and the material properties of the soil on the resulting surface response. This relation is further illustrated in fig. 2.9.

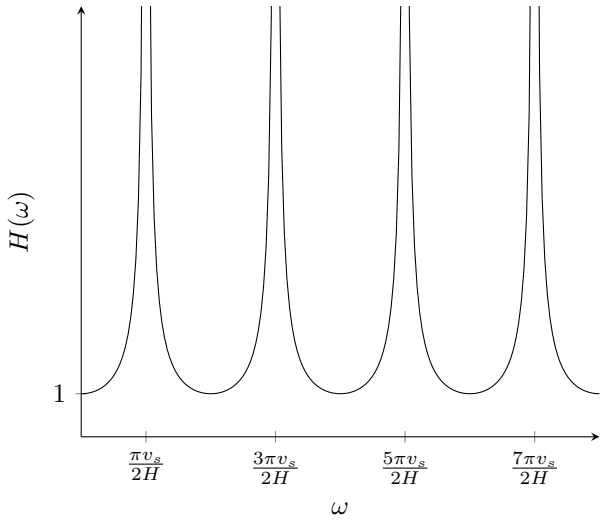

Figure 2.9. Amplification of harmonic base motion for *undamped* soil.

To compute the natural frequencies ω_n of the soil layer, eq. (2.51) has to be solved for no ground excitation, i.e. $\bar{u}(z=0) = 0$ which implies $A = 0$. As previously, the boundary condition $\tau(z = H) = 0$ is introduced:

$$\left.\frac{\partial \bar{u}}{\partial z}\right|_{z=H} = 0 \implies B\frac{\omega}{v_s}\cos\frac{\omega H}{v_s} = 0 \implies \frac{\omega H}{v_s} = \frac{\pi}{2}(2n-1) \qquad n \in \mathbb{N} \implies \omega_n = \frac{\pi v_s}{2H}(2n-1) \tag{2.54}$$

The mode shapes of the soil layer can then be obtained

$$\bar{u}(z) = B\sin\frac{\omega_n}{v_s}z = B\sin\left(\frac{\pi z}{2H}(2n-1)\right) \quad \therefore \phi_n = \sin\left(\frac{\pi z}{2H}(2n-1)\right) \tag{2.55}$$

The three lowest natural frequencies are given in eq. (2.56), along with the corresponding mode shapes, which are illustrated in fig. 2.10

$$\begin{aligned} \omega_1 &= \frac{\pi v_s}{2H} \quad \Longleftrightarrow \quad \phi_1 = \sin\frac{\pi z}{2H} \\ \omega_2 &= \frac{3\pi v_s}{2H} \quad \Longleftrightarrow \quad \phi_2 = \sin\frac{3\pi z}{2H} \\ \omega_3 &= \frac{5\pi v_s}{2H} \quad \Longleftrightarrow \quad \phi_3 = \sin\frac{5\pi z}{2H} \end{aligned} \tag{2.56}$$

The infinite amplification depicted in fig. 2.9 is of course not realistic, as there will always exist some kind of damping reducing it. The wave equation can be rewritten to include damping.

$$\rho\frac{\partial^2 u}{\partial t^2} = G\frac{\partial^2 u}{\partial z^2} + \eta\frac{\partial^3 u}{\partial z^2 \partial t} \tag{2.57}$$

This is assuming that the soil has the shearing characteristics of a Kelvin-Voigt solid. Solving eq. (2.57) yields

$$u(z,t) = Ae^{i(\omega t + k^* z)} + Be^{i(\omega t - k^* z)} \tag{2.58}$$

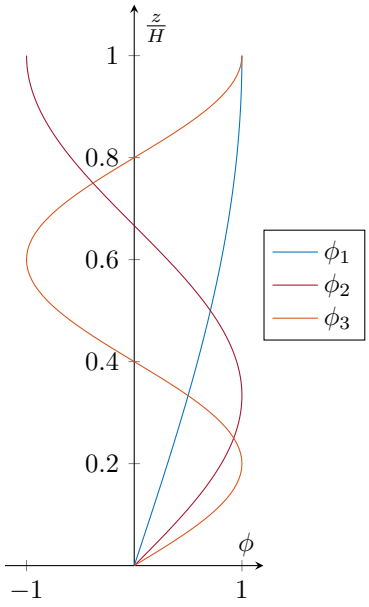

Figure 2.10. Soil layer mode shapes.

The parameter k^* is a complex wave number. From this, a transfer function for damped soil over rigid rock can be obtained.

$$H(\omega) = \frac{1}{\cos k^* H} = \frac{1}{\cos\left({}^{\omega H}/_{v_s^*}\right)} \tag{2.59}$$

where, for small damping ratios ξ.

$$v_s^* = \sqrt{\frac{G^*}{\rho}} = \sqrt{\frac{G(1+i2\xi)}{\rho}} \approx \sqrt{\frac{G}{\rho}}(1+i\xi) = v_s(1+i\xi) \tag{2.60}$$

$$k^* = \frac{\omega}{v_s^*} = \frac{\omega}{v_s(1+i\xi)} \approx \frac{\omega}{v_s}(1-i\xi) = k(1-i\xi) \tag{2.61}$$

Following these approximations, the transfer function from eq. (2.59) can be expressed as

$$H(\omega) = \frac{1}{\cos k(1-i\xi)H} = \frac{1}{\cos\left[{}^{\omega H}/_{v_s}(1+i\xi)\right]} \tag{2.62}$$

The transfer function is expressed in eq. (2.63), using the identity $|\cos(x+iy)| = \sqrt{\cos^2 x + \sinh^2 y}$ and $\sinh^2 y \approx y^2$ for small values of y.

$$H(\omega) = \frac{1}{\sqrt{\cos^2 kH + (\xi kH)^2}} = \frac{1}{\sqrt{\cos^2\left({}^{\omega H}/_{v_s}\right) + \left[\xi\left({}^{\omega H}/_{v_s}\right)\right]^2}} \tag{2.63}$$

As shown in fig. 2.11, the amplification reaches a local maximum value when $\omega \approx (\frac{\pi}{2} + n\pi)\frac{v_s}{H}$, which is always finite due to damping.

The largest amplification of motion occurs close to the lowest natural frequency of the soil layer, known as the *fundamental frequency*

$$\omega_0 = \frac{\pi v_s}{2H} \tag{2.64}$$

A commonly used descriptive number of a soil layer at a certain location is called the *characteristic site period*, which is related to the fundamental frequency by the following.

$$T_s = \frac{2\pi}{\omega_0} = \frac{4H}{v_s} \tag{2.65}$$

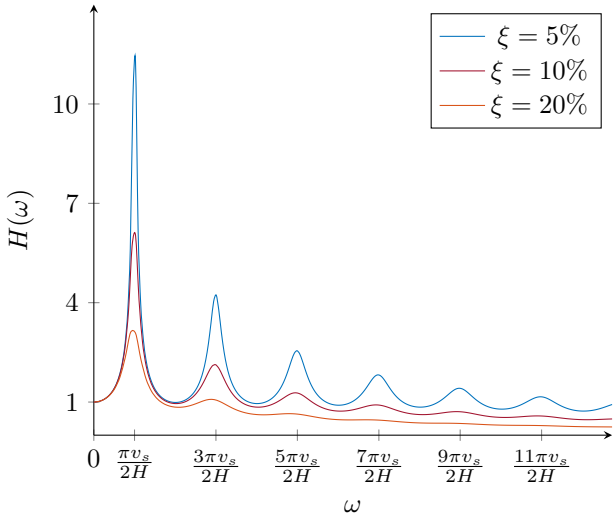

Figure 2.11. Amplification of harmonic base motion for *damped* soil.

2.2.5 Soil-Structure Interaction

Free-field motions are defined as ground motions that are not influenced by the presence of structures. For a structure founded on solid rock, the large stiffness of the rock will constrain the motion of the soil, and the motion will be similar to the free-field motion. A structure founded on rock can be referred to as a fixed-base structure. On the other hand, for a structure founded on a soft soil deposit, this will not be the case. Two important mechanisms occur for such cases. The stiffness of the foundation prevents it from following the free-field motion. The structure will deviate from the free-field motion. The soil experiences deformation due to the dynamic response of the structure. This process is referred to as soil-structure interaction (SSI).

Kinematic interaction refers to the first source of SSI, i.e. the inability of the foundation to follow the free-field motion. This process is illustrated in fig. 2.12. The curved line represents a vertical free-field motion. The surface foundation is prevented by its bending stiffness to conform to the motion of the soil.

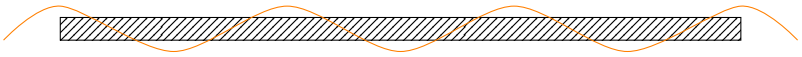

Figure 2.12. A stiff surface foundation unable to conform to free-field motion.

The effects of SSI on structures depend on the problem of interest. One of the most important effects of SSI is the reduction of the natural frequency of the combined system consisting of the soil and structure. If a SDOF system is considered, the following expression can be derived (Kramer, 1996, p.297).

$$\frac{1}{\omega_{\text{eq}}^2} = \frac{1}{\omega_0^2} + \frac{1}{\omega_h^2} + \frac{1}{\omega_r^2} \tag{2.66}$$

where: ω_{eq} = Equivalent natural frequency of combined system
ω_0 = Natural frequency of fixed-base system
ω_h = Translational natural frequency of foundation
ω_r = Rocking natural frequency from rocking of foundation

The inclusion of SSI in the design of a structure will depend upon the problem at hand. The reduction of the natural frequency will in most cases lead to favourable effects such as reduction of accelerations in the system. However, for some cases including SSI can cause unfavourable consequences.

Methods for analyzing SSI are divided into two main categories: *direct methods* and *multistep methods*. Multistep methods apply superposition to focus on the primary causes of SSI. These methods are limited to the analysis of linear systems. Direct methods consider and analyze in one step the entire soil-foundation-structure system. The free-field input motions are specified along the boundaries of

the system. The response of the entire system is obtained using FE simulations in an appropriate FE program. An example of a soil-foundation-structure model is shown in fig. 2.13.

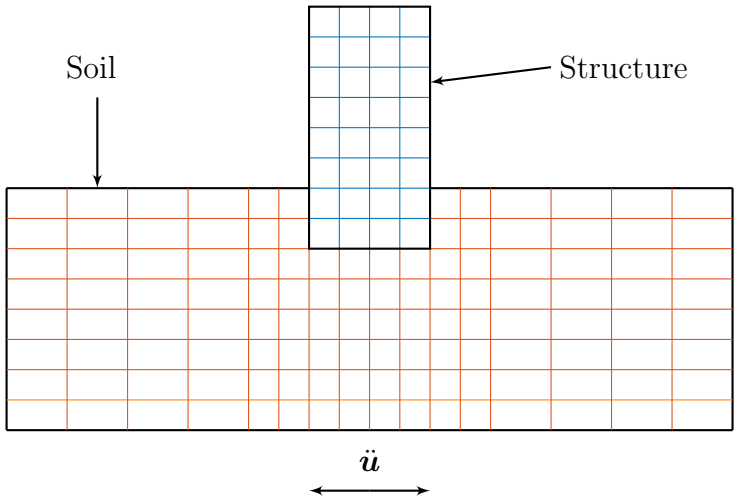

Figure 2.13. Direct SSI method.

2.2.6 Mohr-Coulomb plasticity

The Mohr-Coulomb failure criterion is given by the following expression (Emdal et al., 2016):

$$\tau = c - \sigma \cdot \tan(\phi) \tag{2.67}$$

where: c = cohesion of the material
ϕ = friction angle of the material
σ = normal stress
τ = shear stress

A graphical representation of the failure criterion is presented in fig. 2.14. The Mohr-Coulomb failure criterion is based on plots of Mohr's circles. The failure line is a straight line which touches the circles. Failure occurs when the shear stress at any point in the material reaches a certain limit value. This value depends linearly on the normal stress in the same plane.

In order to implement a Mohr-Coulomb plasticity model in Abaqus, the following properties must be defined (Dassault Systèmes Simulia Corp., 2014):

- Friction angle
- Dilation angle
- Cohesion yield stress and the corresponding absolute plastic strain

The dilation angle controls some of the plastic strain developed during plastic shearing. It is assumed to be constant during yielding. For clay, it is typically equal to zero.

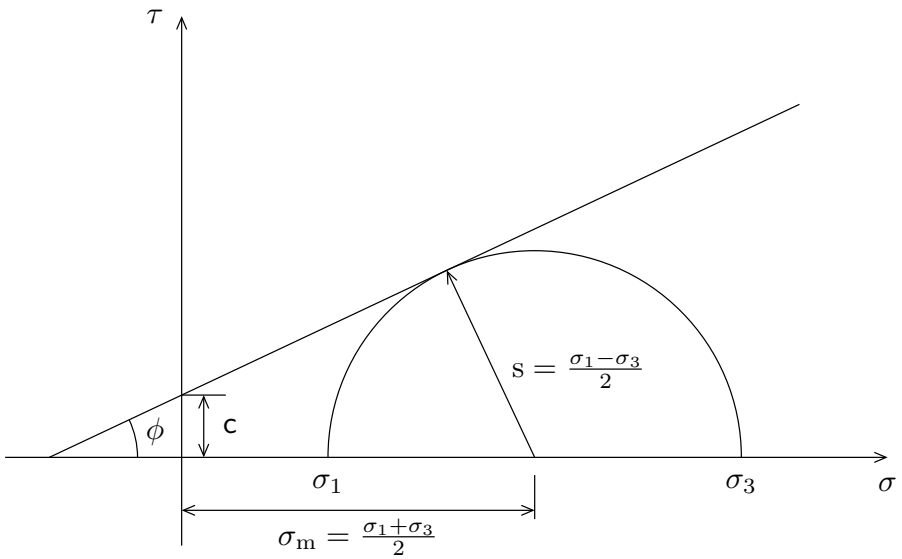

Figure 2.14. A graphical representation of the Mohr-Coulomb failure criterion.

2.3 Fluid modeling

The definition of a fluid is a substance that will continuously deform, when subjected to a shear stress.

2.3.1 Fluid mechanics

An important property which describes the behaviour of fluids is called the *viscosity*. It is a measure of how resistant the fluid is against deformation due to shear stress, and it relates the rate of strain to the shear stress. The velocity profile of a fluid, flowing against a solid stationary boundary, is shown in fig. 2.15. $\frac{dV}{dy}$ is called the velocity gradient. The curve can not lie tangent to the boundary, as this would imply an infinite gradient and shear stress. $V = 0$ at the boundary is called a no-slip condition.

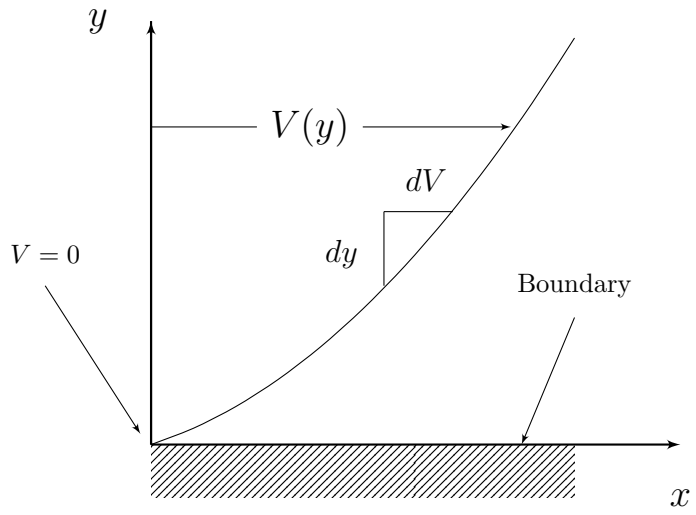

Figure 2.15. Velocity profile.

The shear stress is expressed as

$$\tau = \mu \frac{dV}{dy} \tag{2.68}$$

where: μ = absolute viscosity [m]

Often in fluid mechanics, the ratio μ/ρ occurs, which is called the *kinematic viscosity*

$$\nu = \frac{\mu}{\rho} \tag{2.69}$$

Bulk modulus of elasticity

The *bulk modulus of elasticity* is often referred to as the compressibility of the fluid

$$\begin{aligned} K_s &= -\frac{dp}{dV/V} \\ &= \rho \frac{dp}{d\rho} \end{aligned} \tag{2.70}$$

It relates the change in pressure to the change in volume. Water is often assumed to be incompressible, because water has a very high bulk modulus of elasticity ($K_s \approx 2.2^{\mathrm{GN}}/_{\mathrm{m}^2}$)(Crowe et al., 2010).

Dynamic motion of fluids

The dynamics of rigid bodies are governed by the opposing actions of different forces, where the forces may be regarded as acting on discrete points of the system. The former statement is also true for the dynamic motions of fluids, but in this case the forces have to be distributed in a relatively smooth way between the fluid particles (Newman, 2017). Important force mechanisms acting on the fluid are inertia, weight, and viscous stresses. The velocity of the fluid can be expressed as a vector:

$$\dot{\boldsymbol{u}}(x,y,z,t) = \dot{u}(x,y,z,t)\boldsymbol{i} + \dot{v}(x,y,z,t)\boldsymbol{j} + \dot{w}(x,y,z,t)\boldsymbol{k} \tag{2.71}$$

Where $\dot{u}$, $\dot{v}$ and $\dot{w}$ are the velocity components in x-, y- and z-direction, respectively. The pressure $p(x,y,z,t)$ is equal in every direction for a point within the fluid, and is therefore a scalar quantity (Pettersen, 2020). The local variation of velocity in the x-direction of a fluid particle w.r.t. time is

$$\frac{\partial \dot{u}}{\partial t} dt \tag{2.72}$$

Between two points within the fluid the variation is

$$\frac{\partial \dot{u}}{\partial x} dx + \frac{\partial \dot{u}}{\partial y} dy + \frac{\partial \dot{u}}{\partial z} dz \tag{2.73}$$

Which is equal to

$$\frac{\partial \dot{u}}{\partial x} \dot{u} dt + \frac{\partial \dot{u}}{\partial y} \dot{v} dt + \frac{\partial \dot{u}}{\partial z} \dot{w} dt \tag{2.74}$$

Combining eq. (2.72) and eq. (2.74) yields the particle's total acceleration in the x-direction

$$\frac{D\dot{u}}{Dt} = \frac{\partial \dot{u}}{\partial t} + \dot{u}\frac{\partial \dot{u}}{\partial x} + \dot{v}\frac{\partial \dot{u}}{\partial y} + \dot{w}\frac{\partial \dot{u}}{\partial z} \tag{2.75}$$

Acceleration in the y- and z-direction may be obtained in a similar fashion. The acceleration of the fluid may then be expressed as a vector.

$$\begin{aligned} \ddot{\boldsymbol{u}} = \frac{D\dot{\boldsymbol{u}}}{Dt} &= \frac{\partial \dot{\boldsymbol{u}}}{\partial t} + (\dot{\boldsymbol{u}} \cdot \nabla)\, \dot{\boldsymbol{u}} \\ &= \frac{\partial \dot{\boldsymbol{u}}}{\partial t} + \left(\dot{u}\frac{\partial}{\partial x} + \dot{v}\frac{\partial}{\partial y} + \dot{w}\frac{\partial}{\partial z} \right) \dot{\boldsymbol{u}} \\ &= \underbrace{\frac{\partial \dot{\boldsymbol{u}}}{\partial t}}_{\text{local acc.}} + \underbrace{\dot{u}\frac{\partial \dot{\boldsymbol{u}}}{\partial x} + \dot{v}\frac{\partial \dot{\boldsymbol{u}}}{\partial y} + \dot{w}\frac{\partial \dot{\boldsymbol{u}}}{\partial z}}_{\text{convective acceleration}} \end{aligned} \tag{2.76}$$

The convective acceleration is due to spatial variation of velocity within the fluid, and the local acceleration is zero for steady flow.

Reynolds number

A number used to describe the ratio between inertial- and viscous forces in a fluid is the Reynolds number. This dimensionless parameter, used to describe and compare viscous flow, is defined as (Pettersen, 2020)

$$\mathrm{Re} = \frac{UL}{\nu} \tag{2.77}$$

where: U = flow speed $\left[\frac{\mathrm{m}}{\mathrm{s}}\right]$
L = characteristic length [m]

The equation of continuity

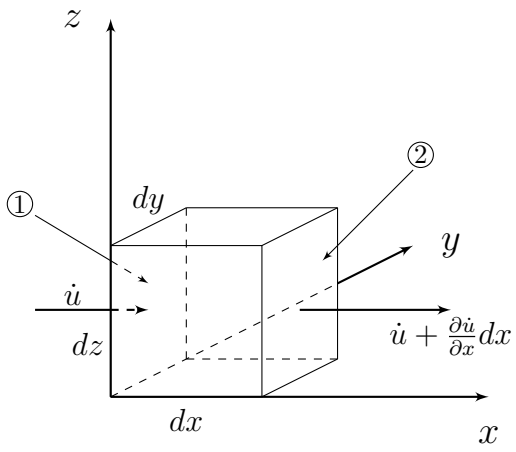

Figure 2.16. A fluid flowing through a cube.

Fig. 2.16 shows flow in the x-direction through a cube with side lengths dx, dy and dz. The instantaneous amount of fluid passing through surface ① is

$$\rho\, \dot{u}\, dy\, dz \tag{2.78}$$

Assuming that the density and velocity of the fluid change w.r.t. time, the instantaneous flow through surface ② at the same instant is

$$\left(\rho + \frac{\partial \rho}{\partial x} dx\right)\left(\dot{u} + \frac{\partial \dot{u}}{\partial x} dx\right) dy\, dz \tag{2.79}$$

Subtracting the latter equation from the former yields the instantaneous change of mass due to flow in the x-direction

$$\begin{aligned} \rho\, \dot{u}\, dy\, dz - \left(\rho + \frac{\partial \rho}{\partial x} dx\right)\left(\dot{u} + \frac{\partial \dot{u}}{\partial x} dx\right) dy\, dz &= \left(-\dot{u}\frac{\partial \rho}{\partial x} dx - \rho \frac{\partial \dot{u}}{\partial x} dx\right) dy\, dz \\ &= -\frac{\partial (\rho \dot{u})}{\partial x} dx\, dy\, dz \end{aligned} \tag{2.80}$$

This can be obtained for the y- and z-direction in a similar fashion. Since the rate at which mass enters the volume has to be equal to the rate at which mass leaves the volume in addition to the accumulation of mass within the volume, the following equation has to be satisfied.

$$\begin{aligned} \frac{\partial \rho}{\partial t} dx\, dy\, dz &= -\left[\frac{\partial (\rho \dot{u})}{\partial x} + \frac{\partial (\rho \dot{v})}{\partial y} + \frac{\partial (\rho \dot{w})}{\partial z}\right] dx\, dy\, dz \\ \implies \frac{\partial \rho}{\partial t} + \frac{\partial (\rho \dot{u})}{\partial x} + \frac{\partial (\rho \dot{v})}{\partial y} + \frac{\partial (\rho \dot{w})}{\partial z} &= 0 \end{aligned} \tag{2.81}$$

The equation is called an equation of continuity. This may be written more compactly using del-operator notation.

$$\frac{\partial \rho}{\partial t} + \nabla \cdot (\rho \dot{\boldsymbol{u}}) = 0 \tag{2.82}$$

If the density of the fluid is assumed to remain constant, the continuity equation simplifies to

$$\begin{aligned} \frac{\partial \dot{u}}{\partial x} + \frac{\partial \dot{v}}{\partial y} + \frac{\partial \dot{w}}{\partial z} &= 0 \\ \therefore \nabla \cdot \dot{\boldsymbol{u}} &= 0 \end{aligned} \tag{2.83}$$

2.3.2 Wave spectra

The accelerations, velocities and pressures within the fluid as functions of the surface elevation can be described by several wave theories. The most commonly used theory is Airy's wave theory, which assumes a sinusoidal wave form and a small wave height (H_w) compared to the wavelength (λ) and the water depth (Chandrasekaran, 2018). Ocean waves are random, generated mainly by wind interacting with the water surface (Newman, 2017). The randomness is amplified by the long distances travelled by waves, where they encounter obstacles and other influencing factors along the way. The waves should therefore be modelled in a probabilistic way. The elevation of the sea surface may, however, be represented by combining several regular waves with different directions and magnitudes. A wave spectrum describes how the energy of the waves are distributed among different frequencies for a certain sea state. An example of a wave spectrum is the Pierson-Moskiwitz (PM) spectrum. This spectrum is used for fully developed sea states, generated by wind over large fetches. The PM spectrum is given by (DNV GL, 2010)

$$S_{\mathrm{PM}}(\omega) = \frac{5}{16} \cdot H_{\mathrm{s}}^2 \omega_{\mathrm{p}}^4 \cdot \omega^{-5} \exp\left(-\frac{5}{4}\left(\frac{\omega}{\omega_{\mathrm{p}}}\right)^{-4}\right) \tag{2.84}$$

where: H_{s} = significant wave height
$\omega_{\mathrm{p}} = \frac{2\pi}{T_{\mathrm{p}}}$ = angular spectral peak frequency

The JONSWAP spectrum is defined as

$$S_{\mathrm{J}}(\omega) = A_\gamma S_{\mathrm{PM}}(\omega)\, \gamma^{\exp\left(-0.5\left(\frac{\omega-\omega_p}{\sigma\omega_p}\right)^2\right)} \tag{2.85}$$

where: $A_\gamma = 1 - 0.287 \ln(\gamma)$ = normalizing factor
σ = spectral width parameter
γ = peak-shape parameter

For $\gamma = 1$ the spectrum reduces to the Pierson-Moskowitz spectrum. The average value of γ from the JONSWAP experiment data is 3.3. To describe the response of a floating structure resulting from wave loading, a nomenclature for motion in different directions, as described in fig. 2.17 is useful.

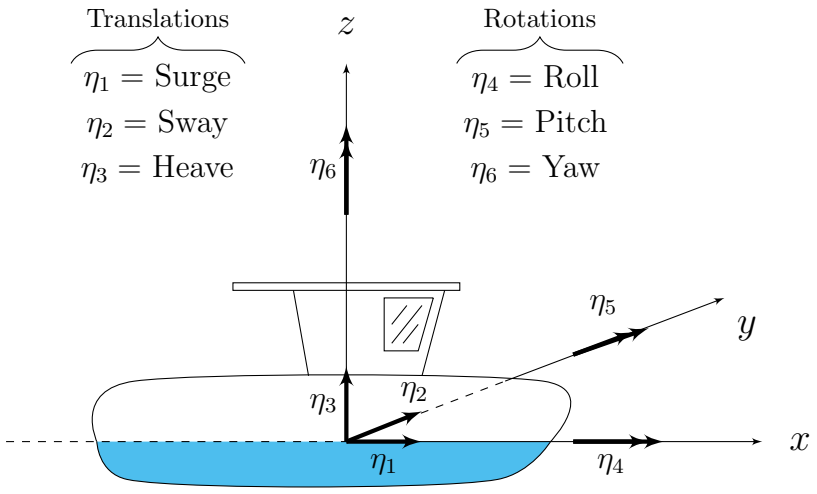

Figure 2.17. Nomenclature for motions of a floating vessel.

2.3.3 Fluid-Structure Interaction

It is important to consider fluid-structure interaction for structures in a fluid, such as offshore structures. The structure's presence in the water will affect the flow field around the structure. Offshore structures experience large oscillating forces in the flow direction of the water, which depends on the sea state. Important mechanisms related to fluid-structure interaction are added mass and hydrodynamic damping. Damping mechanisms occur in a fluid when it is set into motion by an oscillating structure. Drag forces are one of these restraining mechanisms (Chandrasekaran, 2018, p.283).

Added mass

The inertia forces experienced when trying to accelerate a body surrounded by a fluid, are larger than for a body in a vacuum. This is an effect referred to as added mass. The reason for the larger inertia forces is that some of the surrounding fluid is accelerated along with the body, which effectively adds to the total mass of the system. Added mass coefficients can be considered, from a physical point of view, as the amount of fluid accelerated by a body. These coefficients depend on the considered DOF of the body. All of the fluid particles around a body will accelerate to some extent when the body is in motion. Therefore, the added mass will be an integration of the mass of all of these fluid particles (Newman, 2017, p.147).

The added mass coefficient will depend on the size and shape of the body. As previously mentioned, the coefficient depends on the motion direction. This is especially the case for non-symmetrically shaped bodies. Theoretical added mass coefficients for 2D bodies with a simple geometrical shape can be determined. One underlying assumption for these coefficients is that the dimension out of the plane is large compared to the other dimensions, and that the body is stiff. A second assumption is that the body is located in an approximately infinite fluid. As no fluid is truly infinite, this second assumption requires that the body is relatively small compared to the fluid it is in. When these assumptions are valid, the different sections of the body can be approximated locally as two-dimensional bodies. A few examples of bodies, where two-dimensional added mass coefficients can be used, are ship hulls and mooring cables. Examples of structures, where the basic assumptions are not satisfied, could be structures in a confined fluid or a soft structure (Newman, 2017, p.151). Some theoretical added mass coefficients, m_{ij} , for a square and a circle are shown in fig. 2.18. Due to symmetry, the remaining added mass coefficients for the presented shapes are equal to zero.

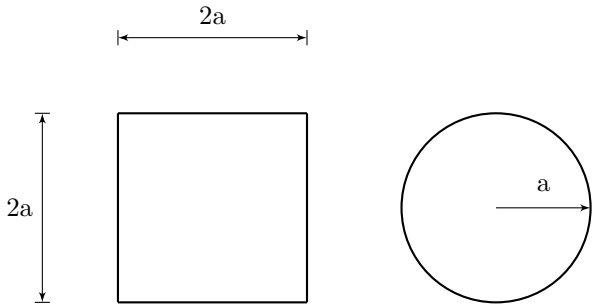

Figure 2.18. Added mass coefficients for a square and a circular section, taken from Table 4.3 in J. N. Newman's *Marine Hydrodynamics* (Newman, 2017, p.152). The indices refer to the nomenclature in fig. 2.17.

As added mass increases the total mass of a body in motion in a fluid, it will affect the structural behaviour of a body. More specifically, the dynamic properties of the body. A change in the system mass would affect the natural frequencies of the structure. For a SDOF system, the natural frequency is given by:

$$\omega_n = \sqrt{\frac{k_{\text{tot}}}{m_{\text{tot}}}} \quad \Rightarrow \quad \omega_n = \sqrt{\frac{k_{\text{tot}}}{m_{\text{structure}} + m_{\text{added}}}} \tag{2.86}$$

It is important to consider the effects of added mass when considering the dynamic properties of floating bodies, such as a floating wind turbine.

Hydrodynamic damping

Hydrodynamic damping can be considered as the sum of the effects of radiation damping and viscous damping. It is expected that the hydrodynamic damping on offshore structures results in larger total damping, than for corresponding structures in air (Chandrasekaran, 2018, p.94).

Radiation damping occurs due to a coupling of the motion of the body and the surrounding fluid. This coupling creates waves radiating out from the body in the fluid. Radiation damping depends highly on the frequencies of the fluid motion and effects related to submergence of the body. When water is considered as the fluid, some of these submergence effects are the water density, the water depth and relative velocity of the body. Radiation damping is also referred to as potential damping, since potential theory is usually used to calculate the damping effects related to radiating waves (DNV-GL, 2017, p.18).

Viscous damping occurs when a body vibrates in a viscous medium. The property of the fluid, which creates a resistance to the motion of a fluid layer over another layer, is known as the viscosity of the fluid. More specifically, the viscosity creates a resistance against shear deformation or motion between two fluid layers (Chandrasekaran, 2018, p.136). Viscous damping depends on the geometry of the body and the flow direction relative to the body. The effects related to viscous damping are more important for long and slender bodies (Newman, 2017, p.17).

As explained in 2.1.2, within structural engineering, the dissipation of energy within a system, known as damping, is represented by one or multiple viscous dampers or dashpots. These are assigned damping ratios which represent all of the different energy dissipation mechanisms within the system. The damping forces related to these viscous dampers are proportional with the velocity of the system.

$$F_{\mathrm{D}} = c \cdot \dot{u} \tag{2.87}$$

Within hydrodynamics, the drag force from a fluid on a body will also be a function of the velocity of the body. More specifically, the drag force depends on the relative velocity of the body w.r.t. the fluid. The drag force on a sphere will be a function of the diameter, the relative velocity, the fluid density and the kinematic viscosity (Newman, 2017, p.14).

$$F_{\mathrm{D}}^{\mathrm{drag}} = f(d, U, \rho, \nu) \tag{2.88}$$

where:
$F_{\mathrm{D}}^{\mathrm{drag}}$ = Drag force
d = Diameter
U = Flow speed
ρ = Fluid density
ν = Kinematic viscosity coefficient

2.3.4 Extreme value statistics

If a sequence of independently and identically distributed random variables $X_1, X_2, X_3 \ldots$ has a common distribution function $F_X(x)$, the extreme value for a finite number of random variables $X_1, X_2, \ldots, X_n$ is $X_{\max,n} = \max\{X_1, X_2, \ldots, X_n\}$. The distribution of $X_{\max,n}$ can then be obtained as:

$$F_{X_{\max,n}}(x) = \mathrm{Prob}\left(X_{\max,n} \leq x\right) = \left(F_X(x)\right)^n \tag{2.89}$$

In practice, accurate estimates of $F_X(x)$ can be hard to obtain. For response processes relevant to marine structures, the Gumbel distribution is usually the appropriate extreme value distribution (Næss, 2013). Performing N simulations of the response process $X(t)$, each of duration T with the same environmental conditions, the extreme response value for each time history can then be identified. The N different extreme response values are then assumed to be Gumbel distributed. The Gumbel distribution of the extreme value $X_{\max}(T)$ can be written as:

$$\mathrm{Prob}\left(X_{\max}(T) \leq \zeta\right) = \exp\left\{-\exp\left(-a_1\left(\zeta - a_2\right)\right)\right\} \tag{2.90}$$

Where a_1 and a_2 are related to the mean value m_M and standard deviation σ_M, respectively, as:

$$a_1 = \frac{1.28255}{\sigma_M} \qquad \text{and} \qquad a_2 = m_M - \frac{0.57722}{a_1} \tag{2.91}$$

Estimates of m_M and σ_M may be obtained from the extreme samples gathered from the simulations.

2.4 Numerical solution of acoustic problems in Abaqus

All of the information presented in this section can be found in the Abaqus user manual version 6.14 (Dassault Systèmes Simulia Corp., 2014).

2.4.1 Acoustic equations

The propagation of pressure waves in a fluid or a solid medium can be solved numerically in Abaqus through the use of acoustic elements. Acoustic elements are often used for modelling of sound propagation problems or for problems involving calculating of shock waves in fluids. The second case corresponds well with the intent of this thesis, which is to model propagation of pressure waves in water due to a seaquake.

The only active DOF in acoustic elements is pressure, which is denoted POR in Abaqus. Thus the only nodal output obtained from this kind of element is pressure. Acoustic mediums are usually fluids such as water or air. For fluids (elastic mediums) the stress is solely hydrostatic, which means that there is no shear stress. The pressure is proportional to the volumetric strain.

When considering small motions of a compressible, inviscid fluid (zero viscosity) the equilibrium equations employed in acoustic simulations are obtained.

$$\frac{\partial p}{\partial x} + \gamma \dot{u}^f + \rho_f \ddot{u}^f = 0 \tag{2.92}$$

where: p = dynamic pressure in the fluid
x = spatial position
$\dot{u}^f$ = fluid particle velocity
$\ddot{u}^f$ = fluid particle acceleration
ρ_f = fluid density
γ = volumetric drag

As mentioned previously, the fluid is assumed to be inviscid and also compressible. The product between the bulk modulus K_s and the volumetric strain ε_v gives the dynamic pressure.

$$p = -K_s \varepsilon_v \tag{2.93}$$

2.4.2 Mesh refinement

In order to obtain accurate results, it is necessary to use a mesh with sufficient refinement, as is generally the case for any FE-analysis. For acoustic analyses, it is recommended that at least six internodal intervals of the acoustic mesh fit into the shortest acoustic wavelength. The accuracy is highly improved if ten or more internodal intervals are used at the smallest wavelength. The internodal interval is defined as the distance from a node to its nearest neighbouring node in another element. For a linear element this is the element size and for quadratic elements it is equivalent to half of the element size. The acoustic wavelength will decrease with increasing frequency. The maximum internodal interval of an element, denoted $L_{\max}$ is given by

$$L_{\max} < \frac{c_{\mathrm{d}}}{n_{\min} f_{\max}} \tag{2.94}$$

where: c_{d} = speed of sound in medium
$n_{\min}$ = number of internodal intervals per acoustic wavelength
$f_{\max}$ = cyclical frequency of excitation

The speed of sound in the medium is a function of the bulk modulus and the fluid density.

$$c_{\mathrm{d}} = \sqrt{\frac{K_s}{\rho_f}} \tag{2.95}$$

For time domain analysis, it is reasonable to estimate the shortest wave length using the highest frequency in the loading (pressure or acceleration).

2.4.3 Loads and boundary conditions

One of the boundary conditions available for acoustic elements in Abaqus is prescribed pressure. Pressure, which is the only variable in the acoustic medium, can be prescribed at a node or surface. This is useful to represent a so-called free surface where the pressure does not vary due to the motion of the surface.

Pressure waves can be applied to a model through the use of an incident wave loading. Incident wave loading can occur due to for instance an underwater explosion or a seaquake. The requirements for using this option is to define a source node, which acts as the source of the wave, a standoff point, which is a chosen point on the surface which is to be loaded. The variation of the incident wave is defined through a predefined amplitude. An incident wave can either be given as a series of pressure or acceleration values. The source of the wave can be given as a single plane (planar) or a series of multiple planes emitting waves from different angles (diffuse).

In order to model the loss of pressure when waves hit the boundaries surrounding an acoustic medium, an acoustic impedance can be employed. The impedance can either be reflecting or non-reflecting. When the second option is chosen, the waves propagating towards the surface with the impedance will not be reflected. As waves propagate back and forth in the model, the energy within the acoustic model will slowly diminish towards zero.

One of the disadvantages of using incident waves in acoustic models is the application of an incident wave at a boundary between finite or infinite acoustic elements. An incident wave results in a pressure jump at a given surface. For a surface between finite or infinite elements, this jump will not be modelled correctly since the pressure is continuous between acoustic elements. The result is then that the initial pressure near the surface, shortly after application of the incident wave, will not be equal to the pressure of the load.

2.4.4 Theoretical impedance and wave reflection coefficient

When an acoustic wave propagates towards a boundary, a part of the wave will be transmitted through it and the other part will be reflected by the boundary. The acoustic impedance of a medium Z can be interpreted as the resistance against pressure excitation (Vorländer, 2008, p.14). The ratio between the initial wave and the part of it reflected by the boundary is denoted as the reflection coefficient R. This is determined by the density and speed of sound of the two mediums (Vorländer, 2008, p.36).

$$Z = \frac{p}{\dot{u}} = \rho c \tag{2.96}$$

$$R = \frac{Z_1 - Z_0}{Z_1 + Z_0} = \frac{\rho_1 c_1 - \rho_0 c_0}{\rho_1 c_1 + \rho_0 c_0} \tag{2.97}$$

The subscript "0" denotes the initial medium of propagation of the wave. The subscript "1" denotes the medium on the other side of the boundary. The sign of R determines whether the reflected wave changes sign compared to the initial wave. A negative reflection coefficient indicates that the wave changes sign after being reflected.

2.4.5 Numerical instability and signal sampling

Numerical instability is a possible issue for explicit numerical integration methods. In order to obtain a bounded numerical solution from an acoustic analysis, the chosen time step must be smaller than a critical time step Δt_{cr} (Cook et al., 2001, p.413). The time step must be small enough that information does not propagate more than the distance between adjacent nodes during a time step.

$$\Delta t_{\mathrm{cr}} = \frac{L^e}{c_d} \tag{2.98}$$

where: L^e = characteristic length of the smallest element in the mesh
c_{d} = speed of sound in medium

The Nyquist sampling theorem states that in order to avoid aliasing of a signal, such as an earthquake

acceleration-time history, the employed sampling frequency should be at least twice the highest frequency contained in the signal (Vorländer, 2008, p.113)

$$2f_{\mathrm{c}} \leqslant f_{\mathrm{s}} \tag{2.99}$$

Chapter 3

Case study of an FWT

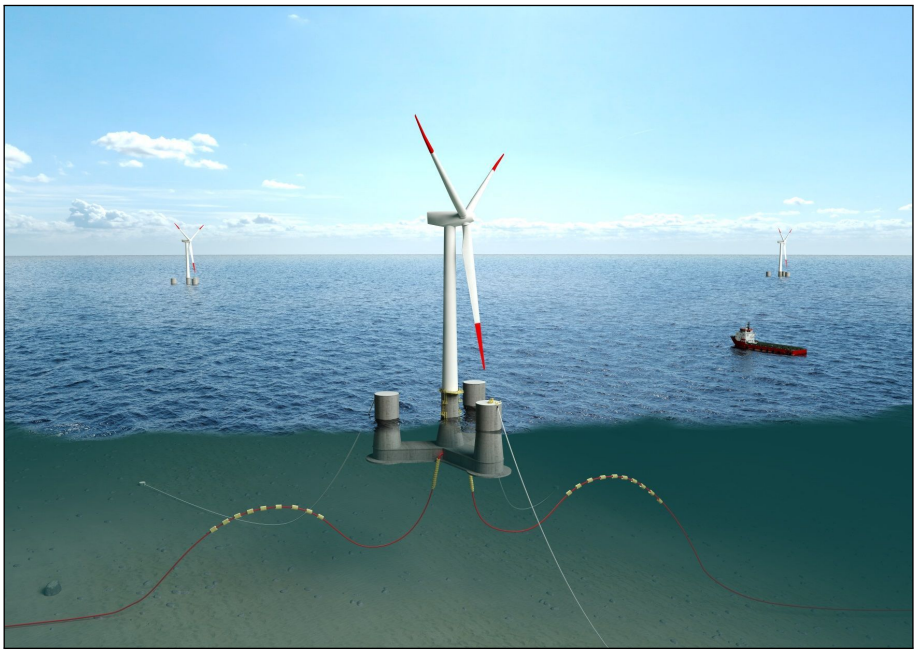

Figure 3.1. An illustration of the OO-Star Wind Floater, developed by Dr.techn. Olav Olsen (Dr. techn. Olav Olsen, 2020a).

A concept of a semi-submersible wind turbine platform developed by Dr. techn. Olav Olsen (OO), called the "OO-Star Wind Floater", is considered in the analyses. The platform comprises three outer columns connected to a central column by submerged pontoons. The platform is intended to be built using post-tensioned concrete, moored to the seabed by a catenary system comprising three mooring lines. The large bottom surface area of this platform design is thought to make the FWT more prone to effects of seaquake pressure compared to other substructures, e.g. a spar design.

3.1 LIFES50+ OO-Star Wind Floater Semi 10MW

3.1.1 Structural properties

Structural properties of the LIFES50+ version of the OO-Star platform are gathered from the LIFES50+ deliverable D4.2. The wind turbine is based on the DTU 10MW Reference Wind Turbine, with structural properties collected from a LIFES50+ report (Bak et al., 2013).

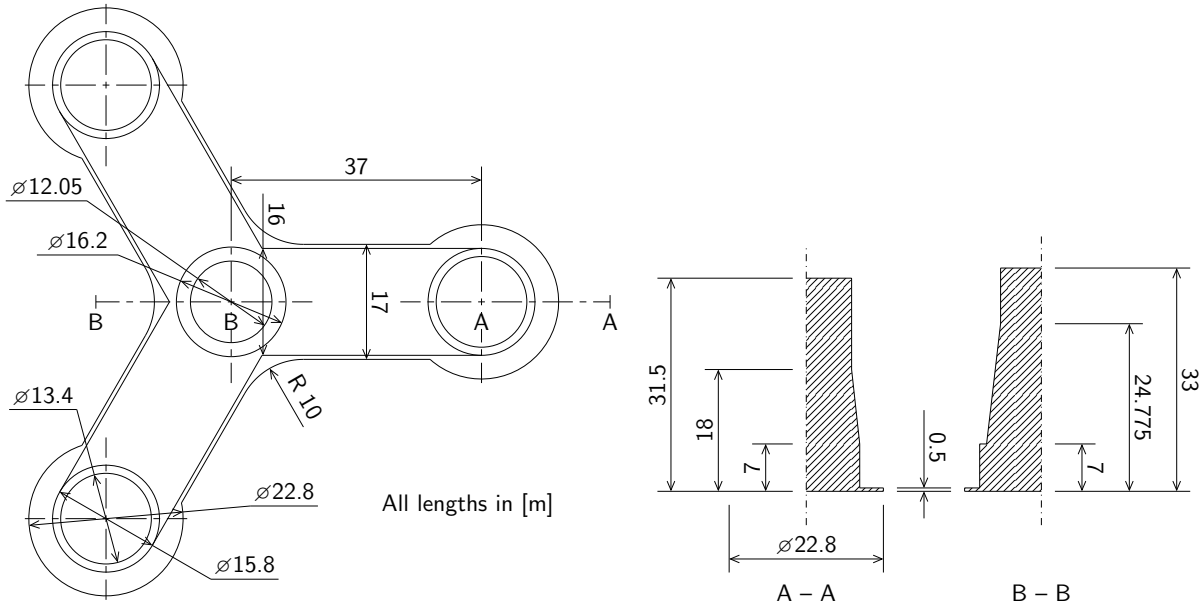

Figure 3.2. OO-Star Wind Floater LIFES50+ dimensions.

Table 3.1: Properties of the OO-Star semi-submersible platform.

Property	Unit	Value
Total platform mass	[kg]	$2.1709 \cdot 10^7$
Centre of mass below SWL	[m]	15.225
Tower base interface above SWL	[m]	11.0
Draft at equilibrium position including mooring	[m]	22.0
Displaced water volume	[m^3]	$2.3509 \cdot 10^4$
Centre of buoyancy below SWL	[m]	14.236

Table 3.2: Properties of the wind turbine tower.

Property	Unit	Value
Total mass	[kg]	$1.257 \cdot 10^6$
Tower base elevation above SWL	[m]	11.0
Tower top elevation above SWL	[m]	115.63
Vertical centre of mass above SWL	[m]	49.8
Density, ρ	[kg/m^3]	$8.243 \cdot 10^3$
Modulus of elasticity, E	[N/m^2]	$2.1 \cdot 10^{11}$

Additional information regarding the structural properties of the tower is given in table C.1.

Table 3.3: Properties of the DTU 10MW reference wind turbine.

Property	**Unit**	**Value**
Rotor mass	[kg]	230 717
Rotor centre of mass	[m]	[-7.07,0,119]
Nacelle mass	[kg]	446 006
Nacelle centre of mass	[m]	[2.69,0,118.08]

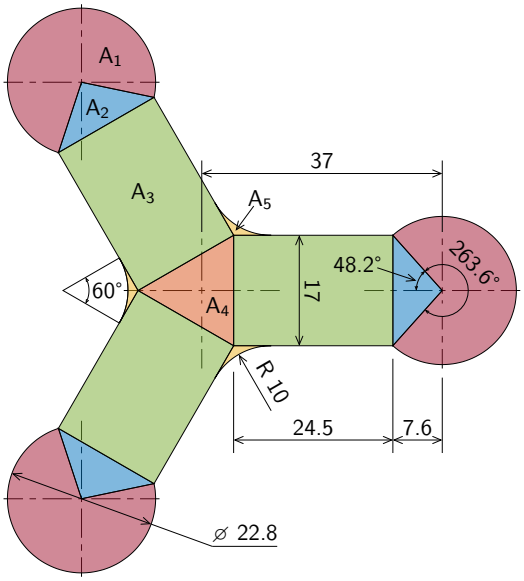

Surface area calculation

$$A_1 = 0.25 \cdot \pi \cdot (22.8)^2 \cdot \frac{263.6^\circ}{360^\circ} = 298.95\text{m}^2$$

$$A_2 = 0.5 \cdot 17 \cdot 7.6 = 64.60\text{m}^2$$

$$A_3 = 17 \cdot 24.5 = 416.50\text{m}^2$$

$$A_4 = 0.5 \cdot 17^2 \cdot \sin 60^\circ = 125.14\text{m}^2$$

$$A_5 = 10^2 \cdot \tan 30^\circ - \pi \cdot 10^2 \cdot \frac{60^\circ}{360^\circ} = 5.38\text{m}^2$$

$$\sum A = 3 \cdot (A_1 + A_2 + A_3 + A_5) + A_4 = 2479\text{m}^2$$

Figure 3.3. OO-Star Wind Floater LIFES50+ bottom surface area.

3.2 Soil properties

A general soil profile not specific to any geographic site is considered. It is taken from a study performed by Norges Geotekniske Institutt (NGI) (see C.1). The soil consists of clay with a linearly increasing undrained shear strength with the depth. As linearly varying material properties such as the shear modulus and Young's modulus cannot be included in Abaqus, the soil profile must be divided into several soil slices with constant shear and Young's moduli. An illustration of the soil profile along with material properties is shown in fig. 3.4.

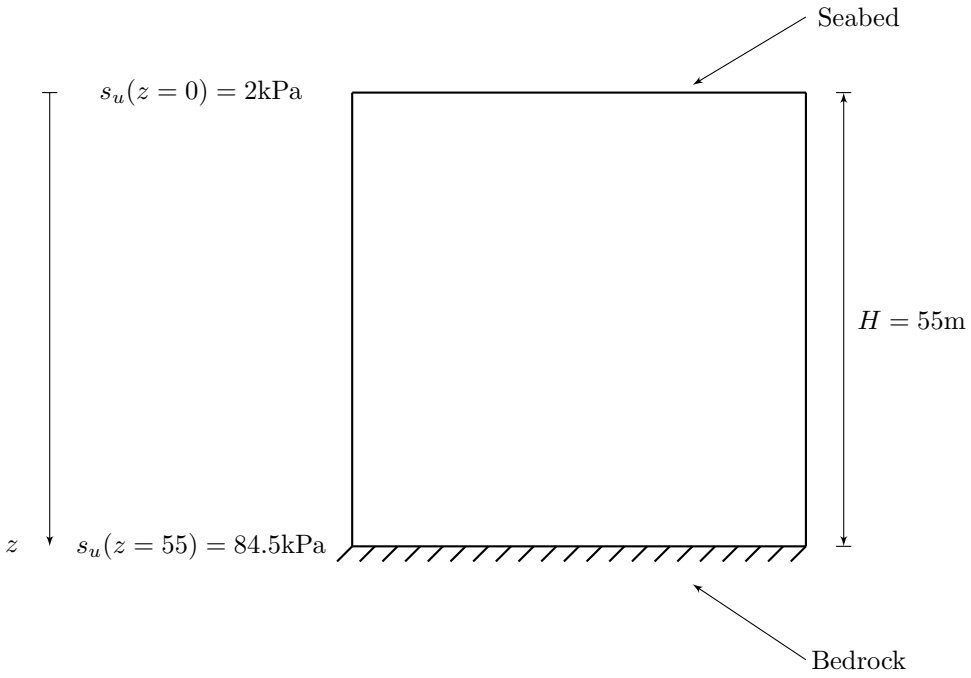

Figure 3.4. Properties of the general soil profile.

In the initial study performed by NGI, the soil profile has a depth of 100m. For this thesis only the upper 55m are considered, in order to reduce the computational time of FE simulations. The bedrock is therefore considered to begin at a depth of 55m. It is assumed that the bedrock consists of granite. For the acoustic models in the thesis, the layers of clay are not considered. Thus, the seabed will be composed solely of the bedrock layer. As no specific location is studied and the intention of the thesis is to investigate the general effects of a seaquake on floating wind turbines, a seabed consisting of a rock material could be as realistic as one consisting of clay. For the SSI analysis however, the clay layer is included in the models.

3.3 Earthquake time histories

Three earthquake time histories are used to study the effects on the floater (seaquake) and the connected anchor (SSI). Among these, two correspond to horizontal accelerations and the last one is a vertical acceleration. The two horizontal series correspond to two directions with an angle of 90° in between. These directions will be referred to as an x- and y-direction since they do not correspond to the East-West and North-South directions. All accelerations originate from an earthquake called the Loma Prieta earthquake recorded at Point Bonita, California on October 18th in 1989. The three time series are shown in fig. 3.5. The peak ground accelerations (PGA) for the x-, y- and vertical time histories are 0.7038m/s^2, 0.7215m/s^2 and 0.3381m/s^2, respectively. The pseudo-acceleration response spectra of the three accelerations are shown in fig. 3.6.

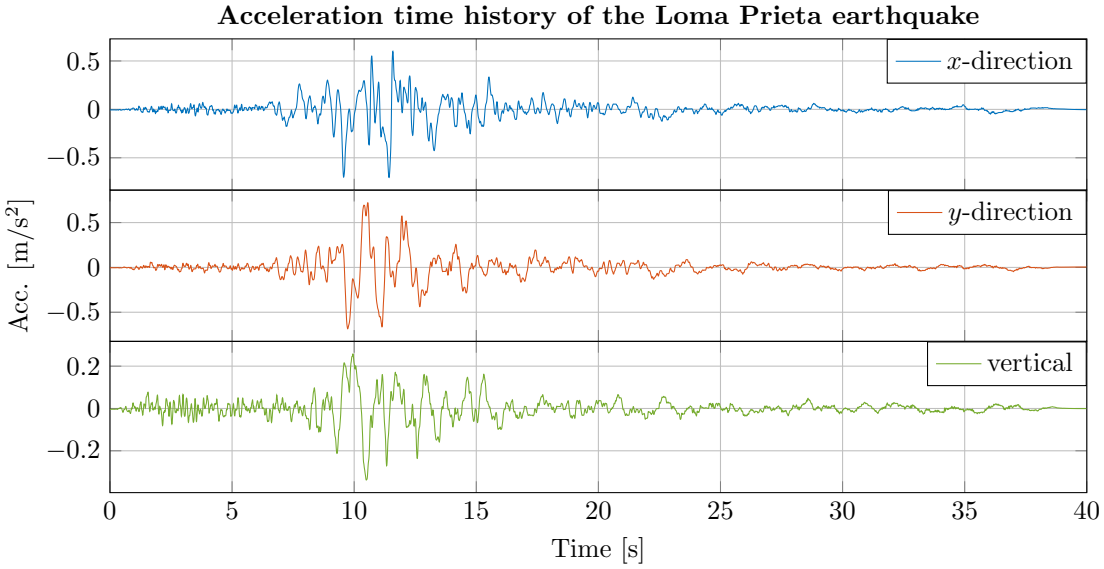

Figure 3.5. Acceleration-time histories, x-direction at the top (PGA=0.7038m/s^2), y-direction in the middle (PGA=0.7215m/s^2) and vertical direction at the bottom (PGA=0.3381m/s^2).

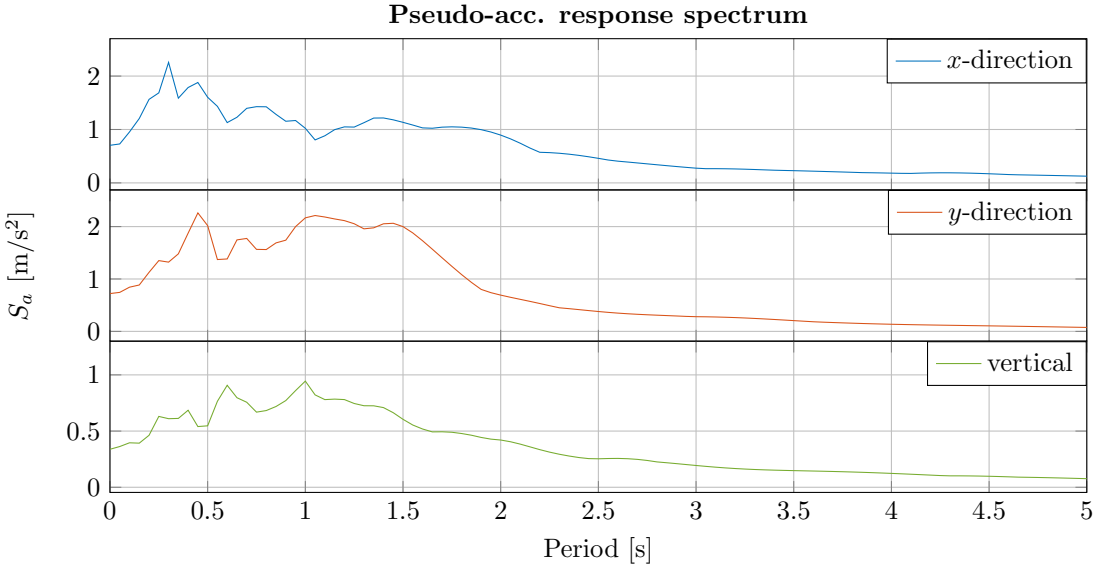

Figure 3.6. Pseudo acceleration spectra for the three time histories, x-direction at the top, y-direction in the middle and vertical direction at the bottom.

The frequency content of the acceleration-time series determines the smallest wavelengths of the earthquake waves. When conducting FE analyses which consider earthquake accelerations, a sufficient amount of elements must be used per wavelength. The maximum element size is then determined by the largest frequency present in the acceleration-time histories. The frequency content can be determined using the Fourier transform of the accelerations. More specifically, a fast Fourier transform (FFT) algorithm is employed. The one-sided Fourier amplitudes are shown in fig. 3.7. The maximum frequency is assumed to be equal to 6Hz. The majority of the frequency content for the three series is located between 0 and 5 Hz.

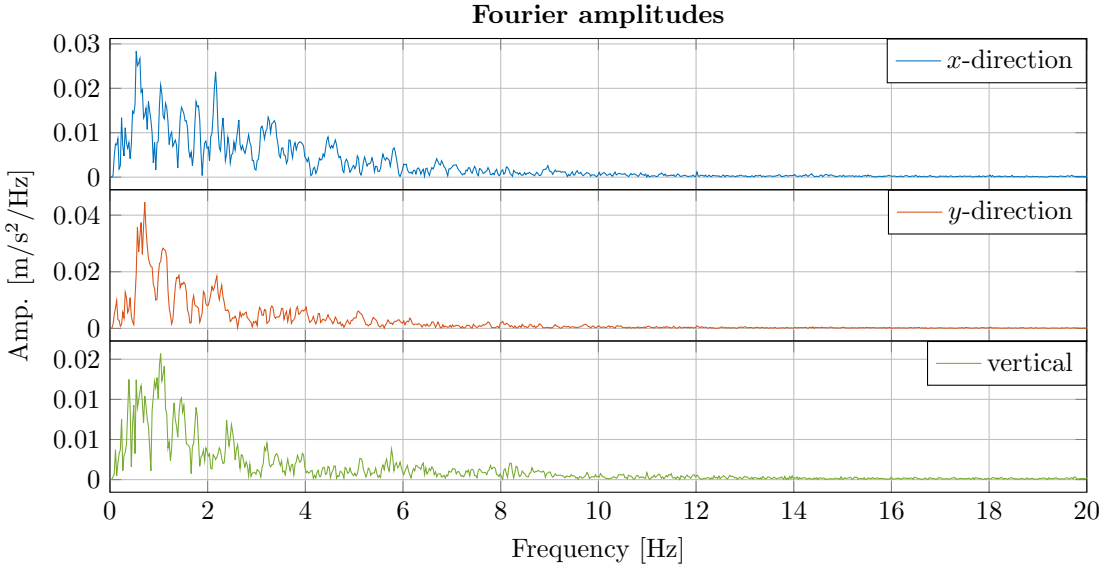

Figure 3.7. Fourier amplitudes obtained using a FFT algorithm, x-direction at the top, y-direction in the middle and vertical direction at the bottom.

3.3.1 Strong motion acceleration

In order to reduce the required computational time for the numerical simulations based on the earthquake accelerations, these are shortened. Only a period of around 17s with the largest acceleration values is considered. The reduced acceleration components are shown in fig. 3.8. Some small values are added at the beginning and the end of the reduced time histories in order to have zero acceleration at the start and the end of the numerical simulations. More specifically, the acceleration decreases towards zero over 0.1s at the beginning and the end of the time histories. This increases the total length of the acceleration histories by 0.2s, making it 17.2s.

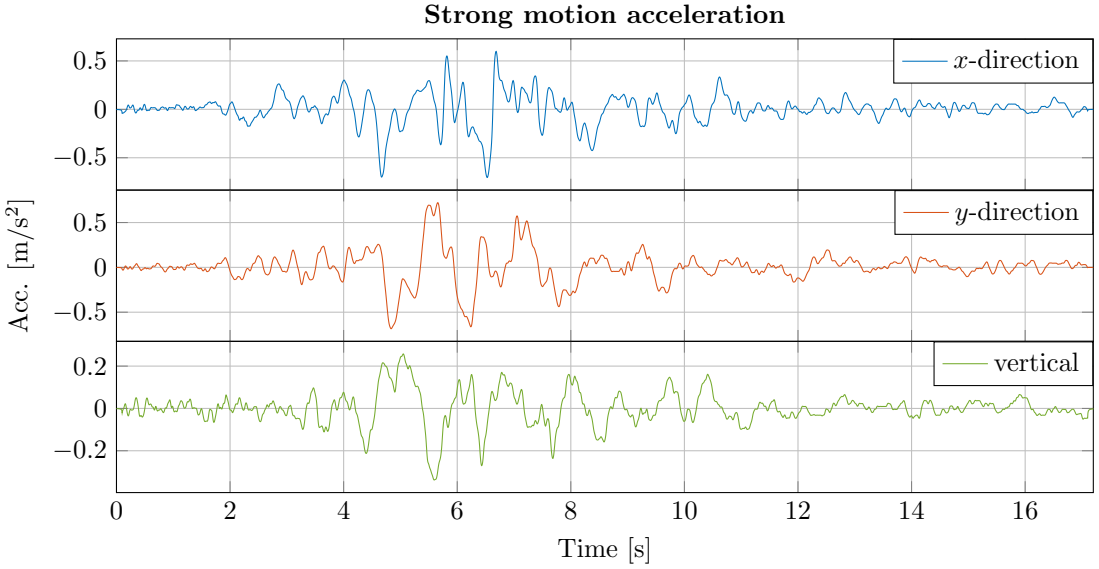

Figure 3.8. Acceleration-time histories with reduced length (17.2s), x-direction at the top, y-direction in the middle and vertical direction at the bottom.

3.4 Anchor design

OO has developed a design for an anchor, called the "OO-Anchor", which is intended to be used in the anchoring system of the OO-Star Wind Floater. The shape of the anchor is presented in fig. 3.9. Some initial choices for the height, width and side lengths are made. These are shown in fig. 3.10. The thicknesses are not specified and will be assessed in this thesis. The top of the anchor will be located at the same level as the seabed.

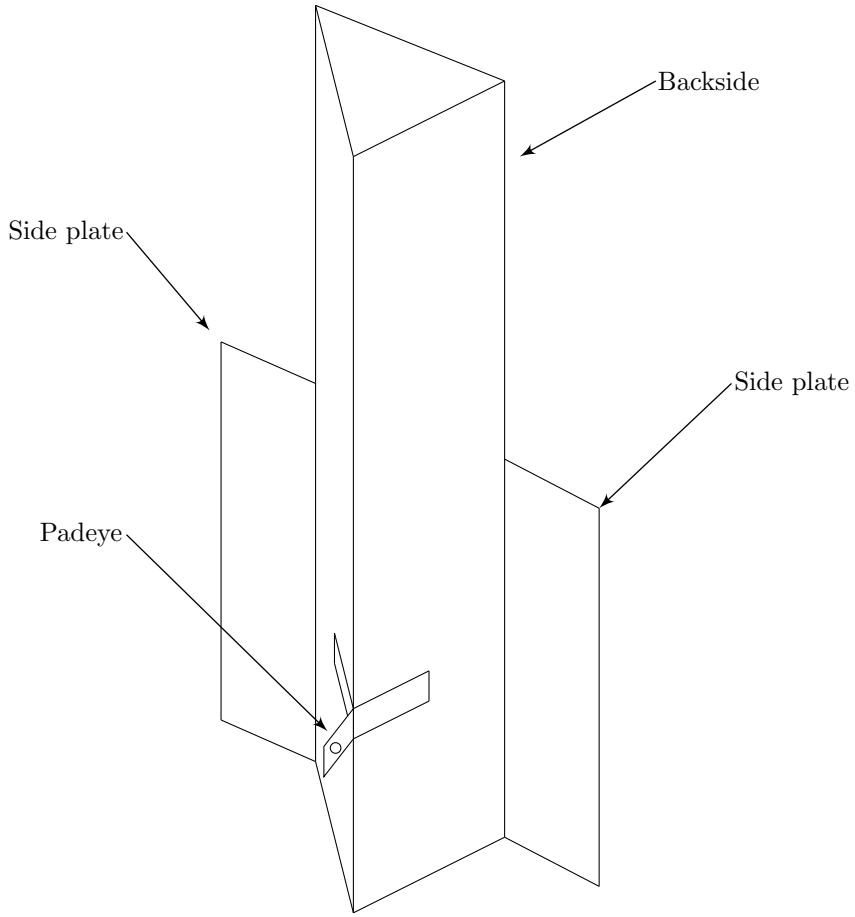

Figure 3.9. A 3D illustration of the intended geometry of the OO-Anchor. The figure is not to scale. Thicknesses are not shown.

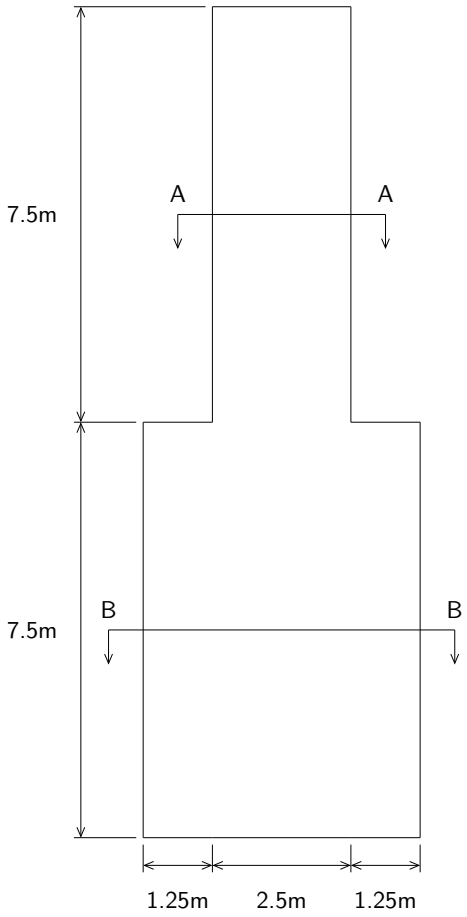

(a) Geometry of the back of the anchor.

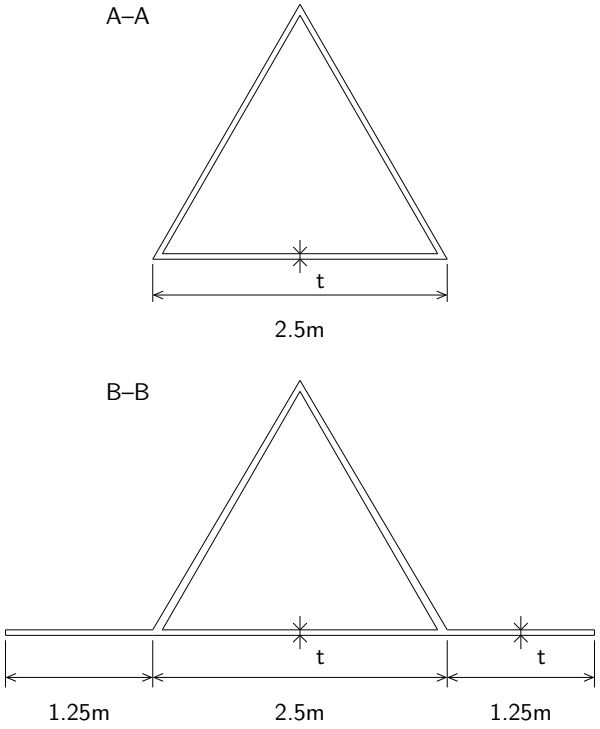

(b) Cross section consisting of a hollow triangle with equal side lengths (A-A). The cross section for the lower part is also shown (B-B). The required thickness is not yet determined.

Figure 3.10. Geometry of the backside and the cross sections of the anchor.

Chapter 4

Acoustic modelling in Abaqus

In this chapter, available options in Abaqus for modelling of propagation of pressure through a water column, using acoustic elements, will be explored. Two boundary conditions for the top of the water column will be considered: zero pressure and zero displacement. These represent the upper and lower limit for the expected pressure under the platform during a seaquake. After having validated the chosen elements and boundary conditions, analytical solutions using transfer functions and calculations in the frequency domain will be derived. The results for the limit cases from the acoustic modelling in Abaqus, using the water depth of interest, will then be compared with these analytical solutions. Then, a third acoustic model which combines the boundary conditions of the two limit cases will be considered. Finally, a 2D model will also be studied to verify if the chosen modelling options are able to only represent propagation of pressure through a 1D medium or not. The development of the acoustic models in this chapter is inspired by the work carried out by L. A. Nerland and M. Røsvik, who used 1D acoustic models to represent the pressure from a seaquake on a submerged floating tunnel (Nerland & Røsvik, 2017).

4.1 Validation of a simple acoustic model

A simple model of a column consisting of acoustic elements is established in order to verify and validate different options for element types, boundary conditions and numerical integration methods. An illustration of this model is shown in fig. 4.1. The acoustic elements are assigned properties which correspond to relevant acoustic properties of seawater. The two main acoustic material properties which are required when using acoustic elements are the fluid density and bulk modulus. The initial model contains no boundary conditions on the sides, at the top or the bottom. This means that there will be no absorption of energy anywhere in the column and all the energy from an applied incident wave will be kept in the system. A pressure wave is applied at the bottom of the column as a planar incident wave. Even though the simple model uses 3D elements, it will behave as a 1D model due to the lack of absorption of pressure from the sides, the small column area (5x5m^2) which will be considered and the pressure propagation along only one direction.

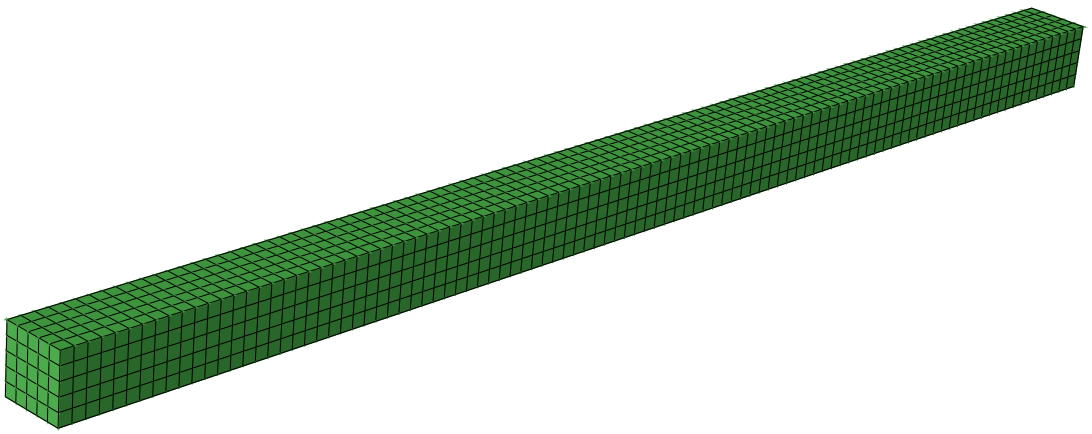

Figure 4.1. Simple acoustic model of a 100m water column with base area 5x5m^2 using solid acoustic elements with mesh size of 1x1x1m^3.

A generic pressure wave is created in order to verify the properties of the acoustic elements, the boundary conditions of the model and how well the wave propagation through the acoustic medium is represented

in the model. An illustration of the wave is shown in fig. 4.2. Initially, the wave has zero amplitude. This allows for validation of the behaviour of the acoustic model by considering if the pressure is equal to zero everywhere in the model. Besides considering the simple model of a water column with no

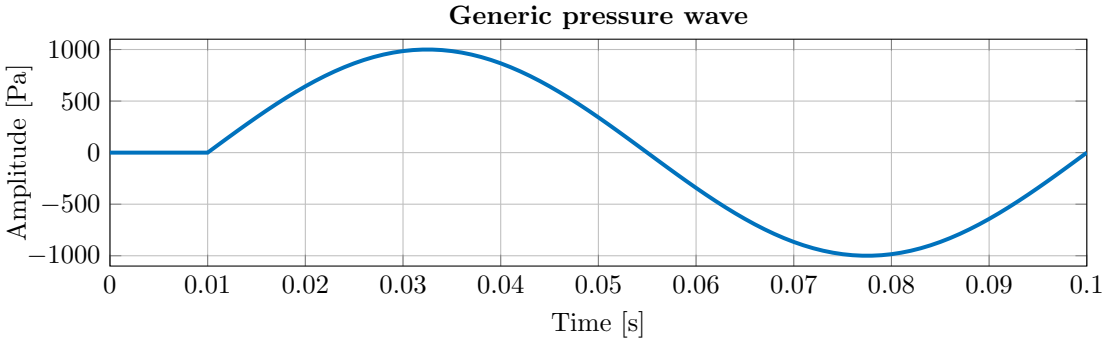

Figure 4.2. A generic pressure wave consisting of a full sine-wave with amplitude set to zero for the initial 0.01s.

boundary conditions, other models with boundary conditions and another acoustic medium, representing the seabed, are also investigated in this chapter. The seabed is assumed to only consist of bedrock with acoustic properties corresponding to granite. The assumed acoustic properties of all the mediums are shown in table 4.1.

Table 4.1: Acoustic properties of the considered mediums.

Property	**Value**
Density of seawater	1024 kg/m^3
Bulk modulus of seawater	2.34 GPa
Speed of sound in seawater	1500 m/s
Density of bedrock	2700 kg/m^3
Bulk modulus of bedrock	81.675 GPa
Speed of sound in bedrock	5500 m/s
Reflection ratio between seawater and bedrock (theoretical value)	0.813

The properties of the different models used to examine the different water column models are shown in table 4.2. According to the Abaqus user's manual (Dassault Systèmes Simulia Corp., 2014), the theoretical estimate for the critical time step is in most cases not conservative. The actual stable time increment may be reduced by a factor between 1 and $1/\sqrt{2}$. It can be reduced further to account for any stiffness behaviour in a model with imposed contact. The given critical time steps correspond to the chosen mesh size and not the maximum element length given in 2.4.2. The maximum element length is determined by assuming a minimum number internodal intervals per wavelength equal to 10. Seawater is the medium with the lowest speed of sound which means it will determine the maximum element length $L_{\max}$.
The initial model with no boundary conditions and the generic pressure wave from fig. 4.2 applied as an incident wave at the bottom, is analyzed using an explicit numerical solver. With the chosen column height, there are 100 layers of elements along the height. The pressure is extracted at a node near the middle of each layer. This results in 100 pressure-time histories for the pressure along the column. These are shown in fig. 4.3.
The lack of boundary conditions results in full reflection of waves at the upper and lower boundaries. A consequence of this is that the pressure will be doubled at the top of the column. This is indicated in fig. 4.3. The Abaqus results correspond well with the expectations given by theoretical solutions. The speed of sound in the model can be verified by comparing two curves with a known distance between their two corresponding nodes in the model. More specifically, the distance between two points with the same amplitude needs to be considered. The estimated speed of sound in the model corresponds well with the assumed input value.

Table 4.2: Abaqus model properties.

Property	**Value**
Column height	100m
Column base area	5x5m^2
Chosen mesh size	1x1x1m^3
Acoustic solid element	AC3D8R (explicit) or AC3D8 (implicit)
Theoretical critical time step for aliasing of acceleration input	$2.5 \cdot 10^{-3}$s
Theoretical critical time step for water	0.00067s
Theoretical critical time step for bedrock	0.00018s
Critical time step from Abaqus for seawater medium	0.000344s
Critical time step from Abaqus for bedrock medium	$9.45 \cdot 10^{-5}$s
Chosen time step for explicit analysis	$9.0 \cdot 10^{-5}$s
Maximum element length with n_{min} equal to 10	25m
Number of internodal intervals per wavelength with chosen element size	250

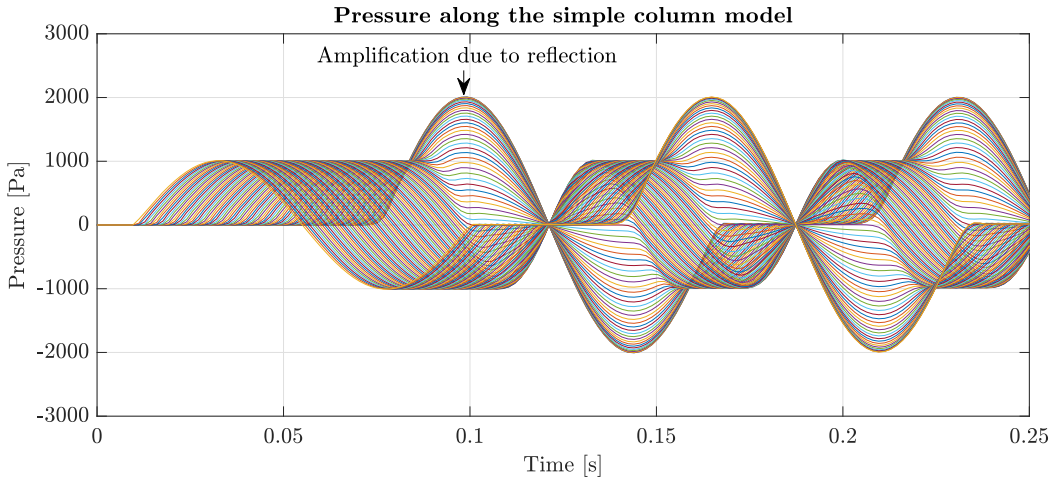

Figure 4.3. Propagation of the incident wave up and down through the water column. Each curve represents the pressure at different heights along the column as a function of time, obtained with an explicit method.

4.2 Addition of boundary conditions

Two types of boundary conditions for the top surface of the water column will be considered. The first one imposes the acoustic pressure to be equal to zero. This is achieved in Abaqus by directly imposing the pressure at the upper surface of the column to be zero. The second one will represent a rigid reflector. A rigid surface will be equivalent to zero displacement at the top of the model. As the only active DOF for acoustic elements is pressure, displacement cannot be specified. Since all the pressure waves hitting a rigid body will be reflected back, no boundary conditions are required at the top of the column. The reflection coefficient will then be -1 which corresponds with the previously described effect of a rigid body. All the energy will then be reflected from the upper surface of the column, which represents the bottom of the platform. The rigid reflector model will represent an upper limit of the pressure acting on the platform, while the free-field model will represent a lower limit.

A layer with the corresponding acoustic properties of bedrock is introduced beneath the water column. The sediment layer presented in section 3.2 is not included in the acoustic model. The thickness of this bedrock layer is 10m. The two acoustic mediums are connected using a tie constraint. It is likely that this constraint is one of the reasons for the difference between the theoretical and actual critical time steps in table 4.2. Some of the energy of a wave travelling downwards in the water will be reflected by the surface between the two acoustic mediums. The remaining part of the wave, which passes through the surface, should not be reflected at the bottom of the bedrock layer. This is achieved by implementing a non-reflective acoustic impedance. The chosen thickness for the acoustic bedrock layer is not important as the energy should not be reflected by the bottom of it. One probable disadvantage of the acoustic model is that the amplitude of the incident wave will not be represented correctly if the wave is applied at the surface at the bottom of the column, between two separate acoustic mediums. As explained in 2.4.3, the pressure must be continuous over a boundary and this will result in a reduction of the initial amplitude of the incident wave. An illustration of the two models is shown in fig. 4.4.

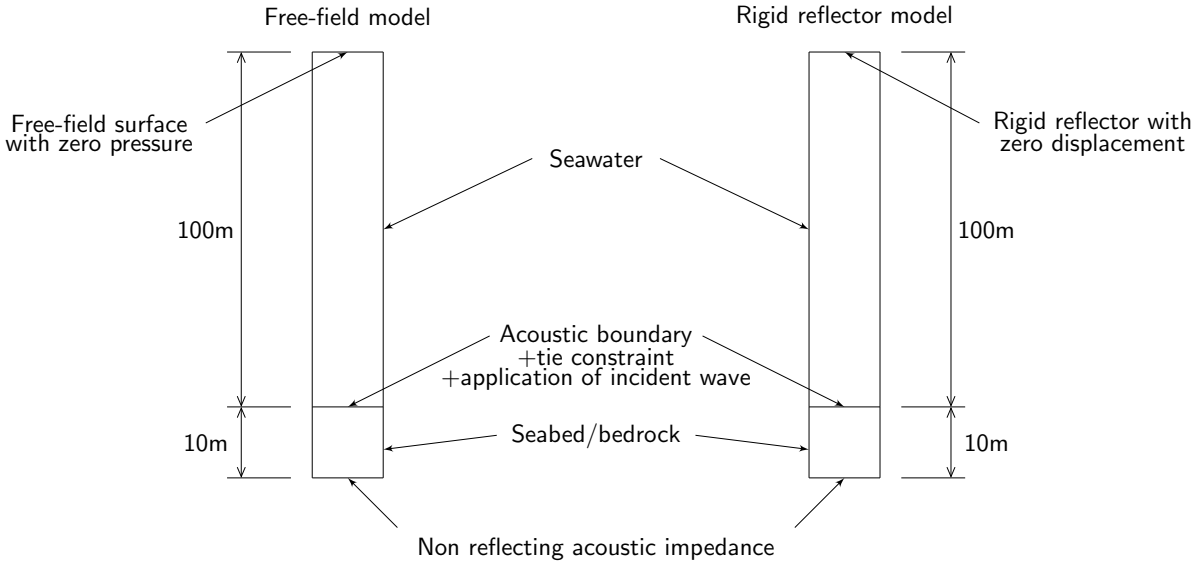

Figure 4.4. An illustration of the two considered models with the applied boundary conditions and acoustic interactions.

The results obtained from applying the generic pressure wave on the new models, containing relevant boundary conditions and impedances, are shown in fig. 4.5 and fig. 4.6.
The ratio between two adjacent pressure peak values should be close to the theoretical reflection coefficient which is approximately equal to 0.81. For the explicit analyses, the reflection coefficient is approximately 0.81 for the model with zero pressure at the top, and around 0.80 for the model with a rigid top reflector. For the implicit analyses, it is approximately 0.81 for both models. The two integration methods yield similar magnitudes for the results and their respective reflection coefficients correspond well with the theoretical value. For both integration methods, the pressure seems to diminish towards zero with increasing time. This is an indication that the non-reflective impedance is working

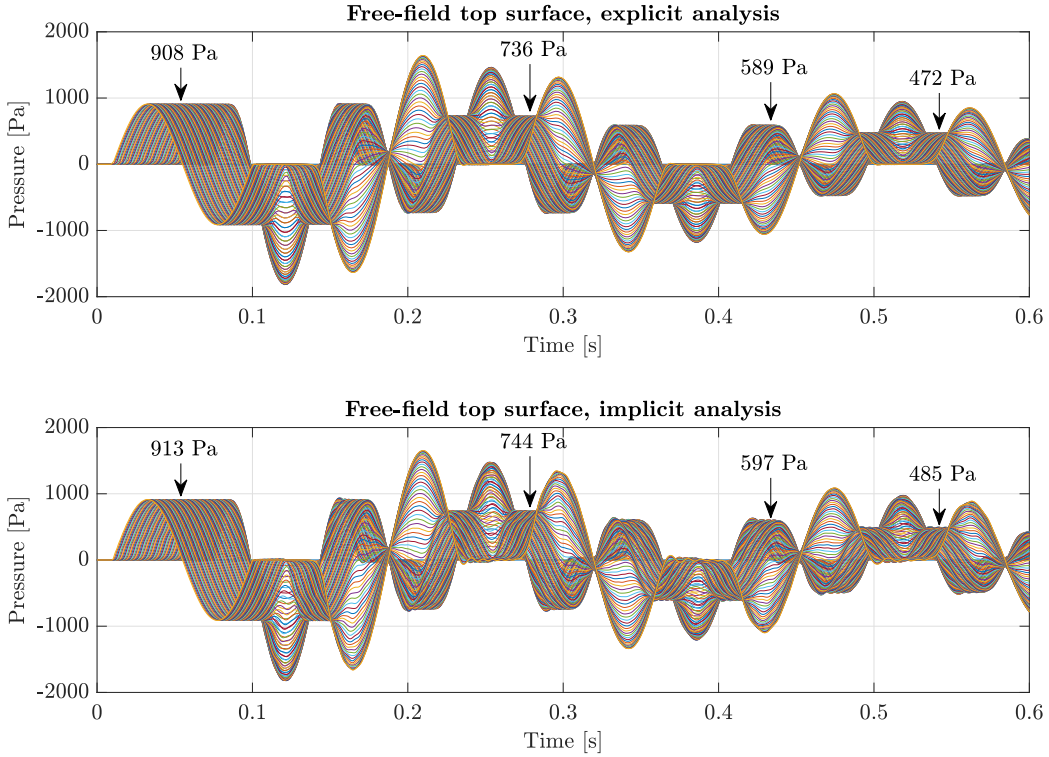

Figure 4.5. An explicit and implicit ($\Delta t = 0.0005$s) analysis with zero acoustic pressure imposed at the column top, two different acoustic mediums (seawater and seabed) and a non-reflective acoustic impedance at the bottom. Each curve represents the pressure at different heights along the column as a function of time.

as intended. In order to achieve an adequate accuracy with an implicit method, the time step must be small enough. One important disadvantage of using an explicit method is the very small critical time step which occurs with the chosen mesh size (order of 10^{-5}s). The strong motion earthquake accelerations have a length of approximately 17s. The computational effort would then be considerably large for an explicit method. Implicit integration allows for a larger time step. However, the time step will still be limited by the risk of aliasing of the acceleration input. Another limiting factor is the accurate representation of pressure peaks. More specifically, a sufficiently small time step must be employed to ensure that the peaks are included in the solution from the FE simulations. An implicit method is chosen for the acoustic FE simulations presented later in this chapter.

By considering the initial amplitudes in fig. 4.5 and fig. 4.6, one can observe that these are smaller than the amplitude of the incident wave in fig. 4.2. As explained previously, the acoustic pressure across a boundary or surface must be continuous. When a pressure jump is introduced through the use of an incident wave, Abaqus reduces the pressure in the water column and the remaining pressure is introduced in the seabed medium. Another possible explanation is a numerical phenomenon caused by the acoustic impedance introduced at the bottom. To account for the reduction of the initial pressure amplitude in future simulations, the results are scaled with a factor according to fig. 4.5 and fig. 4.6 (approximately equal to 1.095 for both of the implicit analyses). The initial pressure in the water medium will then correspond to the initial pressure magnitude caused by the earthquake input (acceleration).

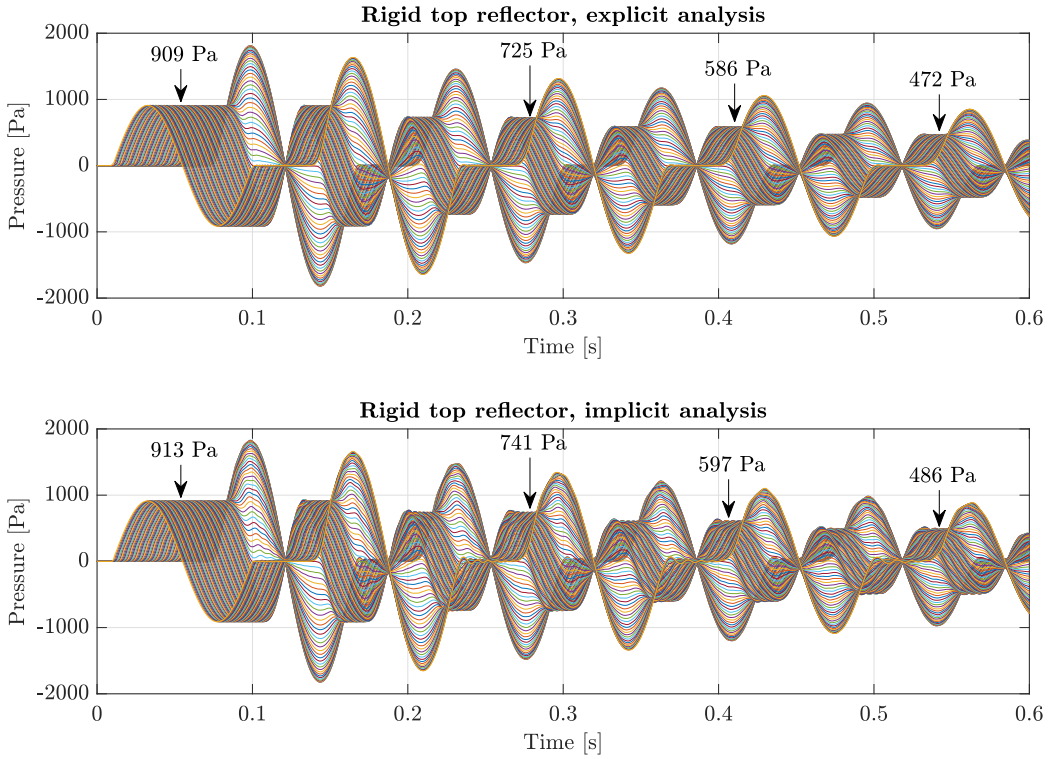

Figure 4.6. An explicit and implicit ($\Delta t = 0.0005s$) analysis with full reflection at the column top, two different acoustic mediums (seawater and seabed) and a non-reflective acoustic impedance at the bottom. Each curve represents the pressure at different heights along the column as a function of time.

4.3 Analytical solutions

Analytical solutions for the pressure propagation in the two models can be determined using the transfer functions in 2.2.3. The acoustic properties used to calculate the two transfer functions are taken from table 4.1, as for the previous acoustic models. The height of the water columns is based on a report concerning environmental conditions at a site suitable for offshore wind development (Gómez et al., 2018). In this report, the design depth for a site on the east coast of the United States is set to 130m. The bottom of the platform is located 22m beneath the water surface. For the first model with zero pressure at the top surface, a height of $H = 130$m is used for the water column part and the pressure is collected at a point 108m above the seabed. For the second model with zero displacement at the top, a height of $H = 108$m (for the water column part) is considered and the pressure is extracted at the top of the column.

The two considered models will yield different magnitudes for the pressure acting at the bottom of the platform. For the model with zero pressure at the top, the pressure will be reduced when it reaches the top of the column due to the imposed boundary condition of zero pressure. This will result in a part of the pressure not being reflected by the upper surface. For the second model with a rigid reflector giving zero displacement at the top, the pressure will be fully reflected when it reaches the top surface. The resulting reflection coefficient will then be -1. The second model is therefore expected to yield larger pressures than the first one. The first option is considered as a lower boundary for the pressure due to seaquake. The second model is considered as an upper boundary.

The analytical pressures are calculated using Matlab. The full length vertical acceleration is used to determine the analytical solutions. The corresponding displacement is derived using numerical trapezoidal integration twice on the considered acceleration-time history. A FFT algorithm is employed to obtain the transform of the displacement and its corresponding frequency values. The transfer functions, relating the displacement at the bottom and the pressure at the specific points for the pressure extraction, are utilized to determine the pressure transform of interest. In order to obtain time domain pressure for the two cases, an inverse FFT algorithm is used. A damping ratio of 5% is introduced in the transfer functions to achieve finite transfer function values around natural frequencies given by the analytical solutions. The pressure-time histories are shown in fig. 4.7. As expected, the pressure for the

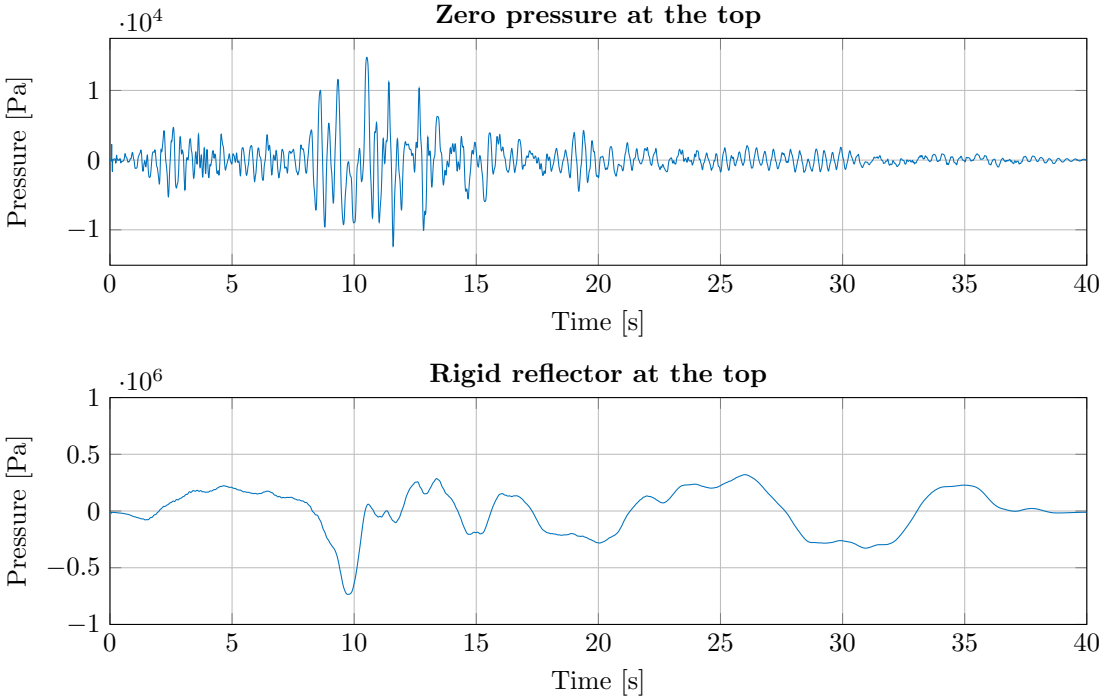

Figure 4.7. Analytical pressure-time histories for cases with zero pressure imposed at the top of the 1D water column (1st plot) and with a rigid reflector at the top (2nd plot). The full length vertical acceleration is considered.

case with a free-field upper surface yields lower pressures than the case with a rigid reflector. It should be mentioned that the amplitude of the pressure obtained with a rigid top reflector is conservative and is expected to be larger than what is realistic to expect for a more detailed model. For the less conservative case with a free-field top surface, the results have a magnitude of 10^4 Pa. For the more conservative case, the results are in the range of 10^5 to 10^6 Pa.

4.4 Results from numerical simulations

The resulting load on the platform due to pressure propagating upwards from the seabed depends on the size and mass of the structure. More specifically, the area of the bottom of the structure is important. In order to get an accurate representation of the load, a coupled analysis between the structure and the surrounding fluid (water) should be performed. Ideally a 2D or even 3D analysis using potential flow theory should be performed. A 2D or 3D acoustic analysis could also be carried out using Abaqus. For this alternative, the floater and surrounding water medium must be discretized using finite elements and a coupling between the acoustic mesh representing the fluid and the structural mesh representing the floater must be established.

As explained in previous sections, much simpler uncoupled models are considered herein for the calculations of the seaquake pressure acting on the bottom of the platform. These simplified models ignore any interaction between the pressure in the fluid and the motion of the structure. As for the previously described analytical solutions, the height of the first model with zero pressure at the top is 130m, and the pressure is extracted at a point 22m beneath the top surface. For the model with a rigid top reflector, the model height is 108m and the pressure is collected at the top of the water column. The acoustic properties of the mediums (seabed and seawater) in the models are the same as in table 4.1. The element size is the same as in table 4.2. The time step used for the implicit analyses is 0.0025s.

The strong motion part of the vertical component of the Loma Prieta earthquake accelerations (see fig. 3.8) is applied at the bottom of the water column models. The resulting pressures are shown in fig. 4.8.

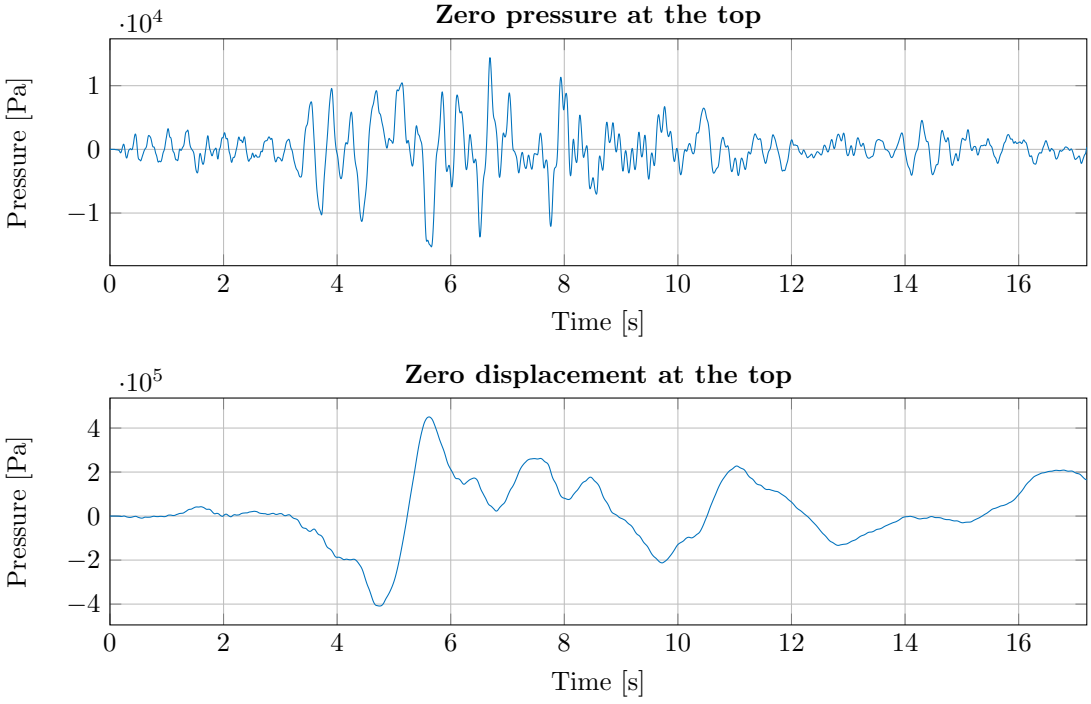

Figure 4.8. Pressure obtained from the two different 1D Abaqus acoustic models. The model with an upper free field surface at the top, and the model a rigid top reflector.

The pressure-time history, obtained from the model with zero pressure at the top surface, has a magnitude of $\approx 10^4$Pa. For the second model, with zero displacement and full reflection at the top surface, the magnitude of the results is between 10^5Pa and 10^6Pa. Even though the analytical solutions are based on the full length vertical acceleration, and the numerical results are based on the strong motion acceleration, the amplitudes of the numerical results for both models are similar to the corresponding analytical solutions. The pressure obtained from the free-field model has much lower amplitudes than the pressure from the model with a rigid top reflector. The amplitudes of the pressure from the free-field model compared with the ones from the rigid reflector model corresponds well with the corresponding ratio for

the analytical results. This indicates that the chosen acoustic FE models are reasonable and sufficiently accurate.

4.5 A third 1D acoustic model

4.5.1 Model description

As the previously presented models have been validated by comparing their results with corresponding analytical solutions, the same modelling options will be used to establish a third acoustic model. This 1D water column model will have a surface at the top with a part with full reflection and another with zero acoustic pressure. The effect from the water surrounding a floating structure on the pressure will then be included as well as the amplification of the pressure from a structure acting as a rigid reflector.

The properties of the two acoustic mediums in this third model correspond to the ones given in table 4.1. The column base area and the mesh size are the same as in the previous models (given in table 4.2). The time step for the implicit analysis is the same as before (0.0025s). The acoustic impedance and the incident wave are identical to the previously used ones. As this third acoustic 1D model combines the boundary conditions of the two limit cases, it is referred to as a hybrid model. An illustration of top surface of the hybrid model along with the top of the Abaqus model is shown in fig. 4.9. The height of the bedrock layer is 10m. The total height of the water column is 130m, where the first 108m have a "filled" surface, and the remaining 22m at the top have a surface with an extrusion. The missing part of the top of the column model represents the floater. The remaining part represents the water around the structure. Zero acoustic pressure is imposed at the top of the model on the remaining surface. The pressure is fully reflected on the surface, representing the bottom of the platform, at a height of 108m above the seabed.

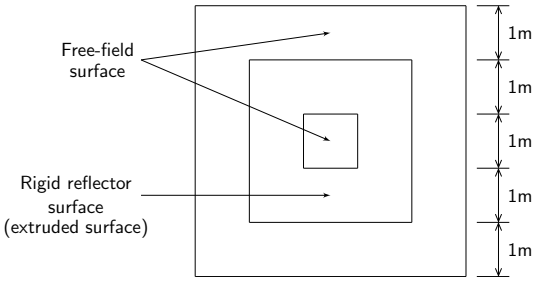

(a) The projection of the top surface of the hybrid acoustic FE model. The geometry of the extruded and non extruded surfaces is indicated.

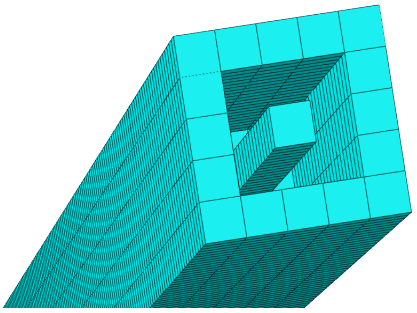

(b) The top part of the hybrid acoustic model from Abaqus. The remaining non extruded surface represents the water around the floater. The extruded part represents the floater.

Figure 4.9. An illustration of the projection of the top surface of the hybrid model, along with the top of the corresponding Abaqus model.

4.5.2 Results

As the hybrid model combines the boundary conditions of the limit cases, it could be expected that the pressure will vary over a surface horizontally at a given height. A model based on potential-flow theory will most likely have a pressure variation both vertically and horizontally. The horizontal pressure variation of the hybrid model can be verified by plotting the pressure at certain points all at the same height. Contour plots of the pressure along the model, around the surface representing the bottom of the floater, can also be assessed. The pressure is extracted at the points shown in fig. 4.10. The strong motion vertical acceleration is applied at the bottom of the model. The resulting pressure-time histories for three points are shown in fig. 4.11.
The pressure over time is almost identical for each of the three points. This indicates that there is almost no horizontal variation for the pressure along the bottom of the floating platform obtained with the hybrid model. This can also be deduced from the contour plots presented in fig. 4.12. These figures indicate the pressure variation of the upper 22m of the model. This area corresponds to the location of the platform and the water around it. It is expected that the actual pressure from a seaquake will not be constant horizontally close to the bottom of the platform.

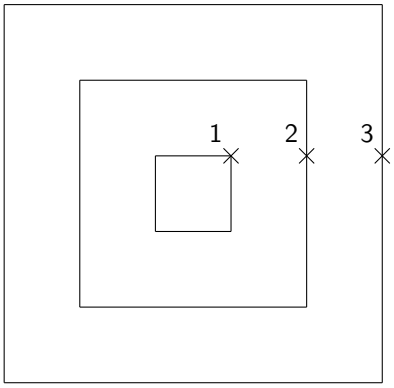

Figure 4.10. The pressure is extracted at the indicated points at a height of 108m.

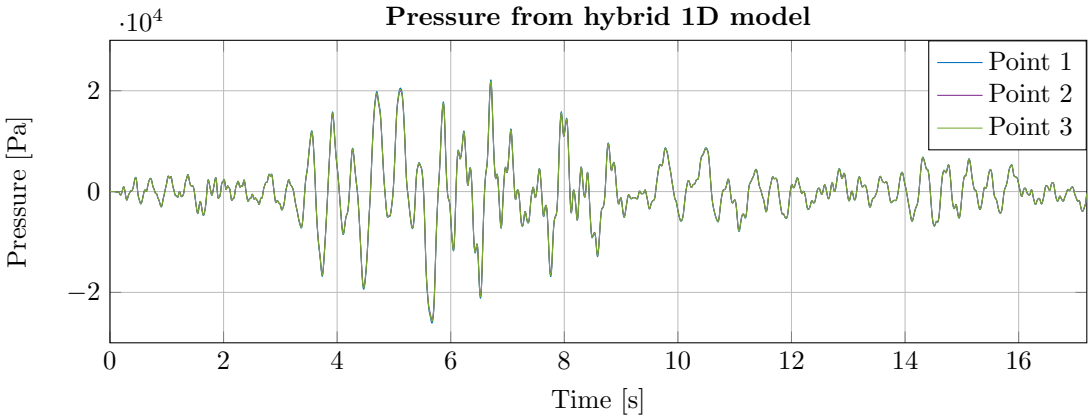

Figure 4.11. Pressure-time histories for the three chosen points at a height corresponding to the bottom of platform. The three curves are almost identical.

The amplitude of the pressure presented in fig. 4.11 is around $2 \cdot 10^4$ Pa. By comparing the results with the pressure from the limit cases, presented in fig. 4.8, the obtained pressure seems reasonable as the magnitude of the results is lower than for the model with a rigid top reflector, and larger than the ones from the model with a free-field top surface.

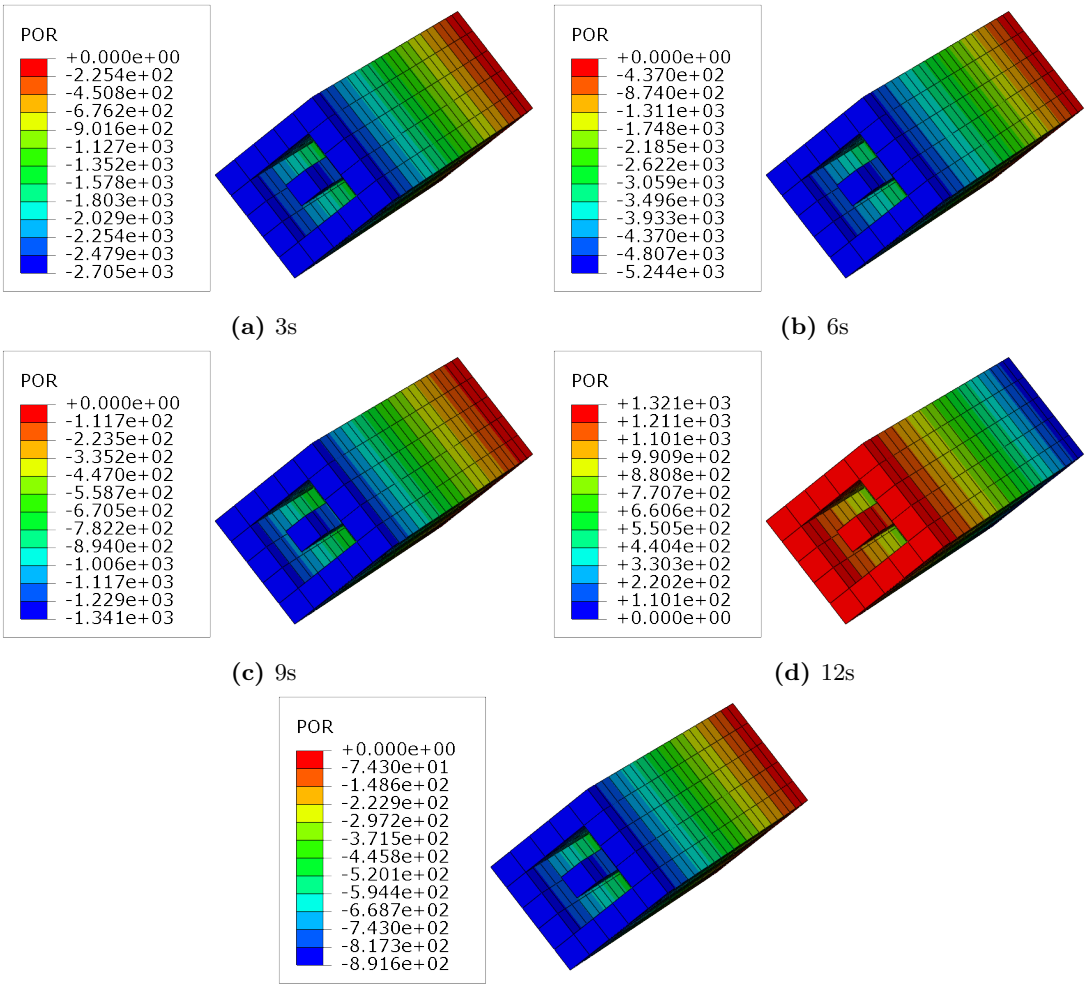

(a) 3s **(b)** 6s **(c)** 9s **(d)** 12s **(e)** 15s

Figure 4.12. Contour plots for the pressure of the upper 22m of the model after 3s, 6s, 9s, 12s, and 15s. A section at a height of 108m is studied. The part of the model above the section is seen from below. The free-field surface is located on the side with zero pressure. The unit of the pressure is Pa.

4.6 A 2D acoustic model

4.6.1 Model description

In order to attempt to obtain an acoustic model with a horizontal variation of the pressure, a 2D model is developed. An illustration of the model is shown in fig. 4.13. The area of the bottom of the OO-Star Wind Floater, shown in fig. 3.3, is approximately 2500m^2. Therefore, the width of the rigid reflector, which represents the floater, is chosen to be 50m. The thickness of the model is 1m. Non-reflective acoustic impedances are assigned to the bottom surface of the bedrock layer as previously, and to the surfaces on both vertical ends of the model. These new impedances account for the loss of pressure horizontally which will occur when a large domain is considered. When pressure waves hit the platform, some of these will be reflected horizontally and will not be reflected by the vertical boundaries on the sides. A flat surface is used to represent the seabed, and it is assumed that all points along the seabed experience the same vertical motion. This is achieved in the 2D acoustic model by using a planar incident wave to represent the vertical earthquake acceleration. No changes are made for the acoustic material properties, time step, integration method or the element type compared to previous acoustic models. The FE 2D model, along with the employed mesh, are shown in fig. 4.14. .

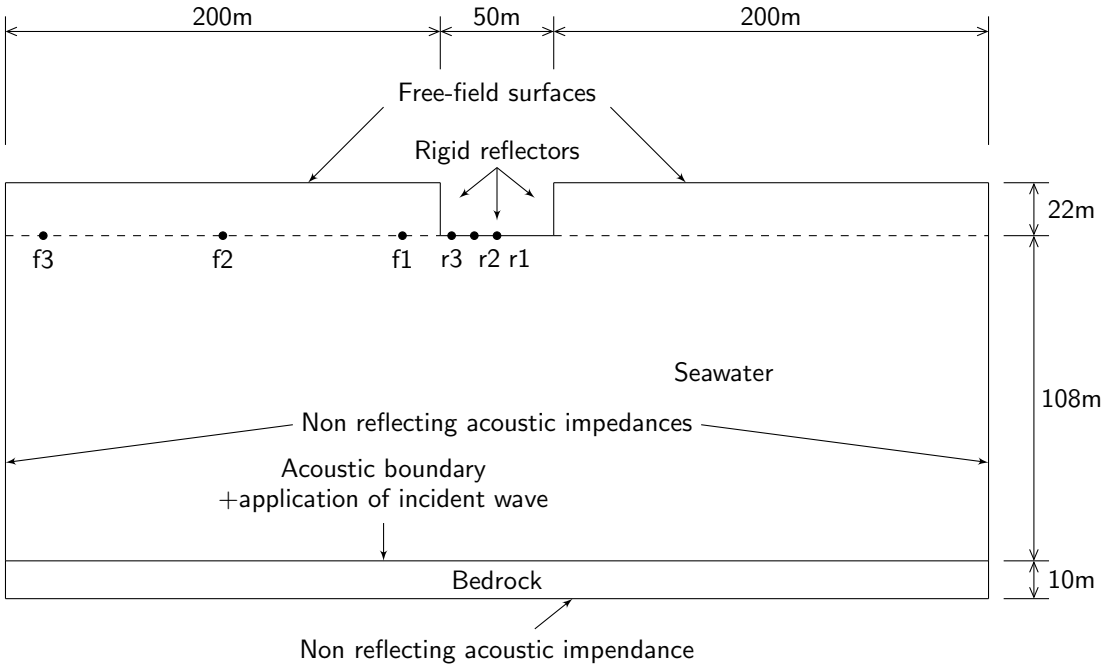

Figure 4.13. An illustration of the 2D acoustic model. Acoustic properties, boundary conditions and dimensions are indicated. The incident wave is applied on the entire surface between the two acoustic mediums. Points at which the pressure is studied are also indicated. The thickness of the model inwards is 1m. For visualization purposes the model is not drawn to scale.

4.6.2 Results

The acoustic pressure is plotted at six points located at a height of 108m over the seabed in the model. These nodes are shown in fig. 4.13. The results are shown in fig. 4.15 and fig. 4.16. The chosen nodes are also described in table 4.3.

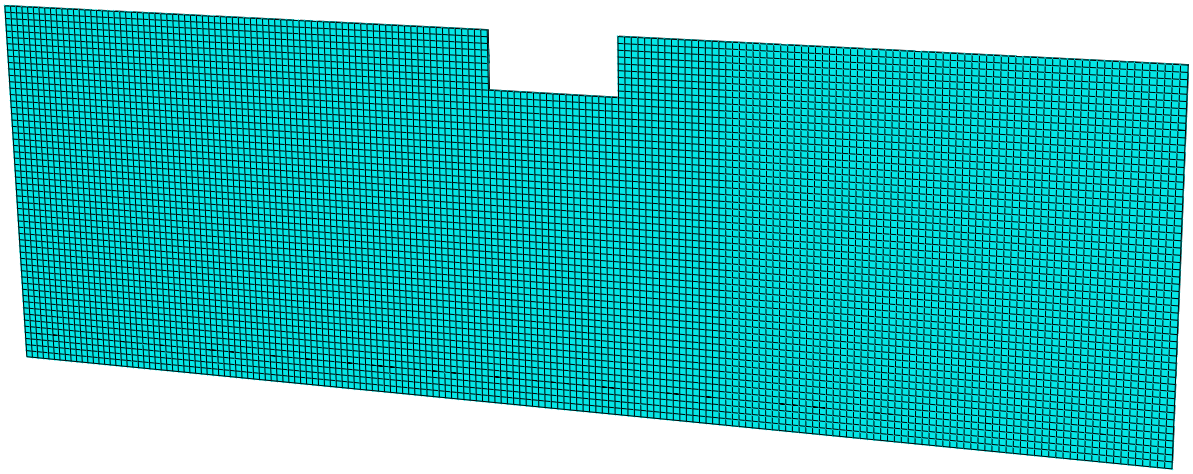

Figure 4.14. The 2D FE acoustic model with the chosen mesh. A uniform mesh with an element size of 2.5m is used.

Table 4.3: The nodes from the 2D model for which the pressure is extracted.

Node	**Distance from left end of model**[m]	**Distance from left rigid reflector** [m]
f1	190	-
f2	100	-
f3	10	-
r1	225	25
r2	215	15
r3	205	5

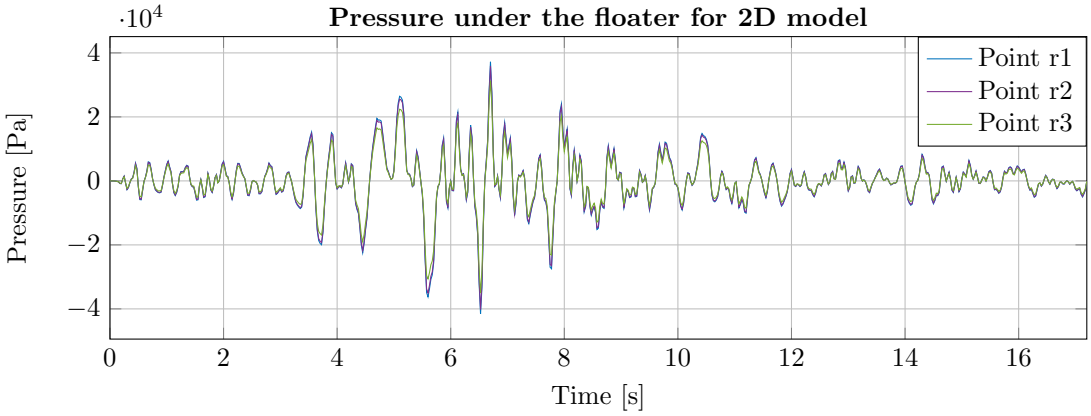

Figure 4.15. The pressure-time histories for the chosen nodes at the horizontal rigid reflector surface in the 2D model.

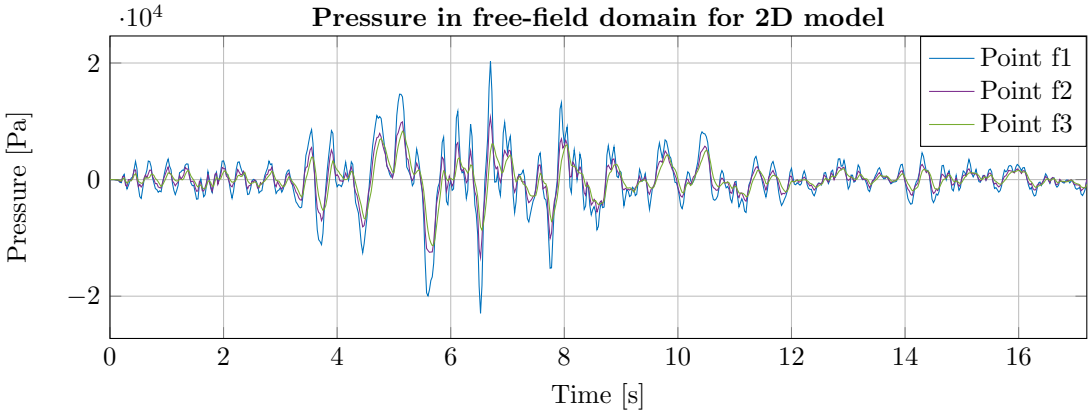

Figure 4.16. The pressure-time histories for the chosen nodes in the free-field domain in the 2D model.

The pressure-time histories for the chosen points show that the pressure obtained by the 2D model varies horizontally. The magnitude of the results is in the order of 10^4Pa, which seems reasonable when compared with the results for the previous 1D models. Once again, contour plots of the pressure in the model can be considered to verify the pressure distribution. Such plots are shown in fig. 4.17. The previously stated observation about the horizontal pressure variation is confirmed by these plots.

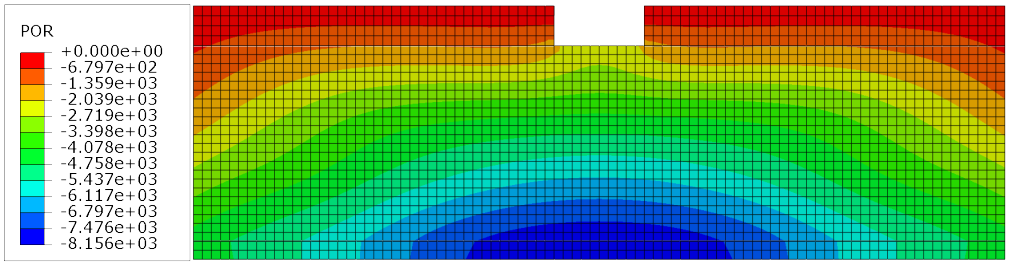

(a) 3s

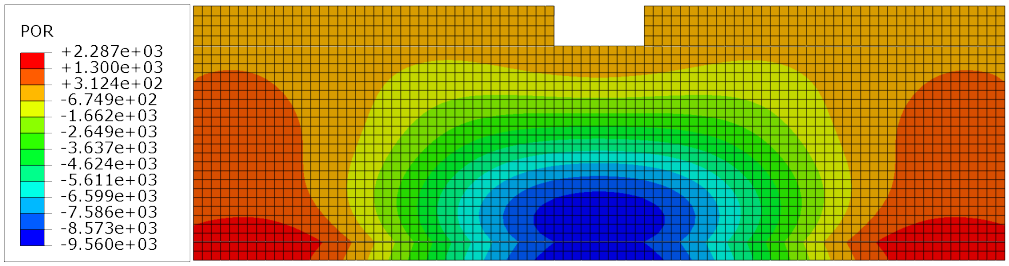

(b) 6s

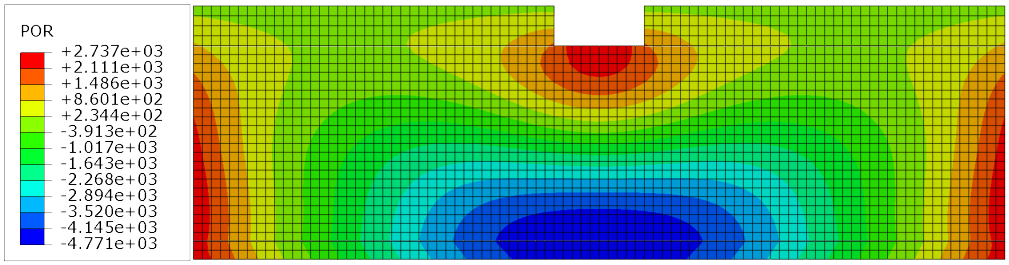

(c) 9s

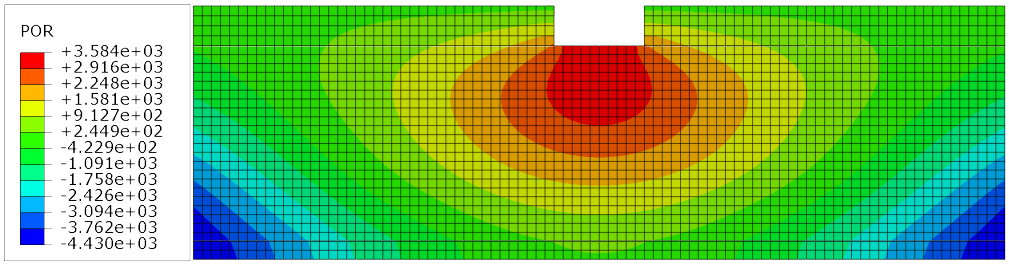

(d) 12s

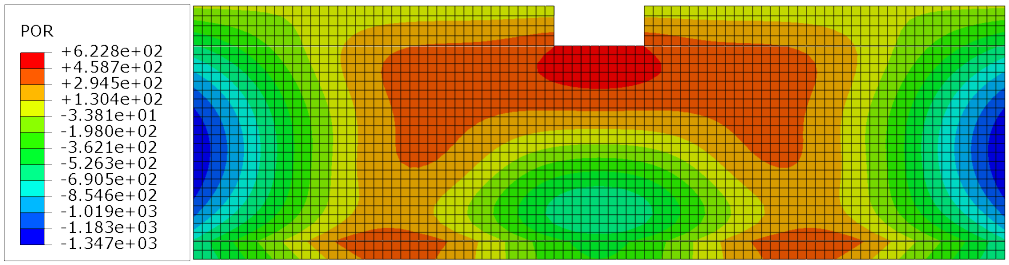

(e) 15s

Figure 4.17. Contour plots for the acoustic pressure after 3s, 6s, 9s, 12s and 15s for the 2D model. The pressure is given in Pa.

Chapter 5

Response of an FWT subjected to initial conditions and environmental loads

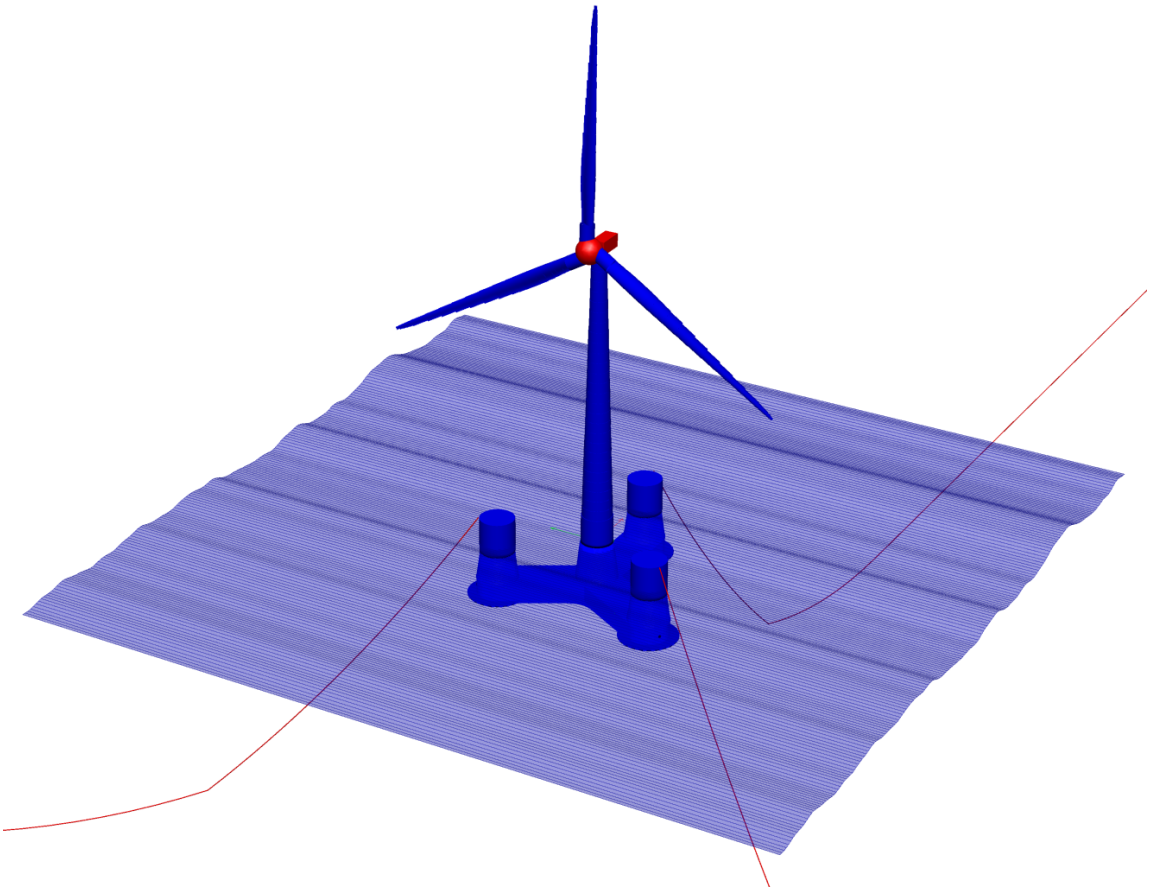

Figure 5.1. The LIFES50+ OO-Star Wind Floater Semi 10MW modelled in SIMA.

A SIMA model of an FWT was provided by SINTEF Ocean. SIMA is a graphical user interface which executes different dynamic response solvers like SIMO and RIFLEX. The response of the provided model is solved by a coupled SIMO-RIFLEX analysis in SIMA. The response of flexible parts like the rotor blades, the tower, and the mooring lines are solved using the FE program RIFLEX, which is well suited to model the non-linear behaviour of slender structures. The platform, nacelle, and hub are modelled as rigid bodies, and their response is solved in SIMO. The model was initially developed as a contribution to the Horizon 2020 funded LIFES50+ research project. The model comprises a wind turbine based on the DTU 10-MW reference wind turbine (Bak et al., 2013), mounted on the OO-Star semi-submersible platform. The FWT is kept stationary by a catenary mooring system, comprising chain anchor lines. In this chapter, the dynamic behaviour of the SIMA model following initial conditions, and during environmental loading, is studied.

5.1 Response to initial conditions

5.1.1 Performing free decay analyses in SIMA

A free decay analysis is conducted to study the dynamic behaviour of the FWT. Six analyses are conducted separately, each by giving the turbine an initial displacement in the considered degree of freedom. The FWT is then released from the initial displacement, which yields the free decaying oscillations shown in fig. 5.3. The initial disturbances from static equilibrium are obtained by applying concentrated forces and moments, F_{η_i} and M_{η_i}. As a remedy to reduce oscillations resulting from sudden force application, the forces and moments are gradually applied as shown in fig. 5.2. Forces and moments are iteratively re-positioned and their magnitudes are adjusted, to obtain the desired displacement and reduce motion in the remaining five degrees of freedom. From fig. 5.3 it can be seen that the free decay in roll and pitch do not follow a smooth exponential decay. One reason for this noise is likely the forces acting on the platform from the mooring lines. This is illustrated in fig. B.1, where the motion in remaining degrees of freedom are shown during the pitch decay. This added noise to the pitch and roll will likely compromise the accuracy of the calculated damping ratios, shown in table 5.1, because the damping is based on the peak values.

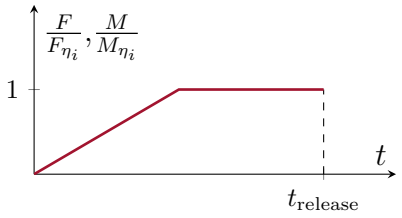

Figure 5.2. Force/moment applied to initialize turbine displacement/rotation.

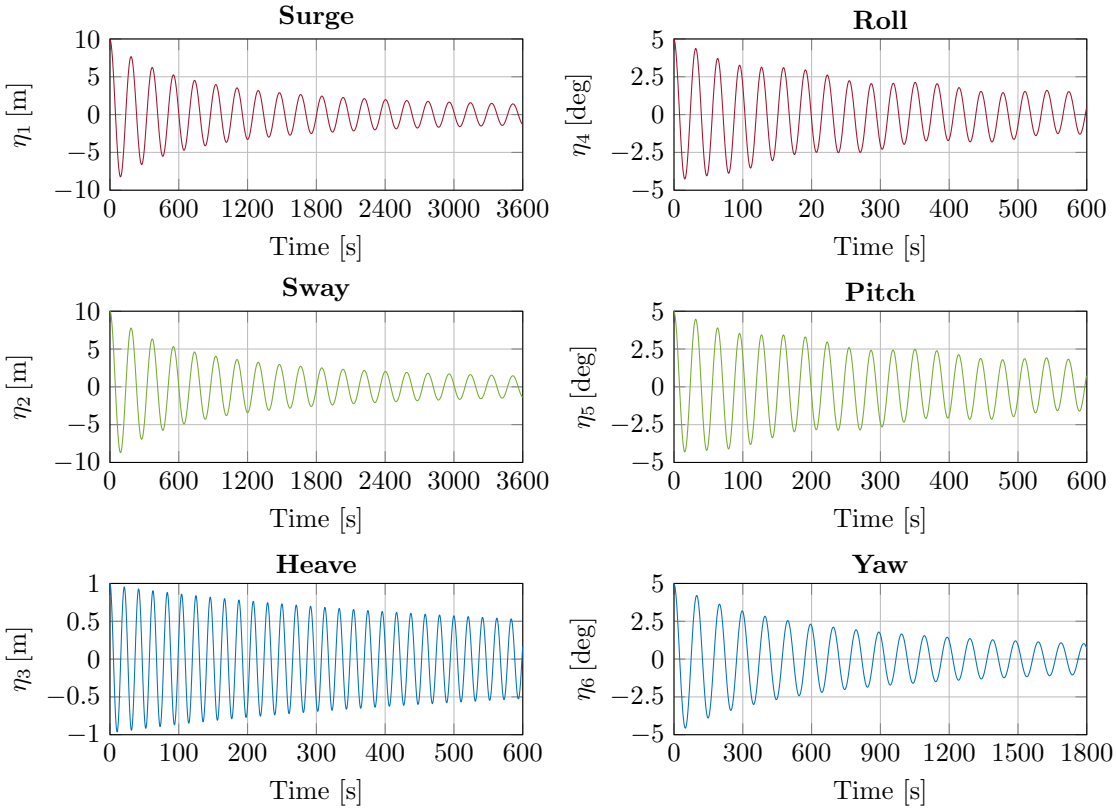

Figure 5.3. Motion of the platform in free decay. Individual analyses are performed for each degree of freedom, giving the FWT an initial displacement or rotation.

The free-decay response of the platform obtained in SIMA is saved and exported to Matlab, where damped natural periods and damping rations in all six degrees of freedom are computed. Damping ratios are calculated using eq. (2.16b). As shown in table 5.1, where the damping ratios are calculated based on different numbers of displacement peaks, the damping is highly dependent on velocity.
The computed natural periods from table 5.1 correspond well with information given in the LIFES50+ D4.2 report, except in yaw where the computed natural period deviates by 14.6% compared to the

Table 5.1: Free decay motion characteristics obtained in the SIMA analyses.

DOF	**Damped natural period** T_D [s]		**Computed damping ratio** ξ [%]			
	SIMA	LIFES50+ D4.2	Number of peaks after first			
			3	6	9	12
Surge	185.03	$1/0.0055 = 181.82$	2.796	2.337	2.021	1.800
Sway	184.97	-	2.781	2.316	2.004	1.783
Heave	20.83	$1/0.049 = 20.41$	0.419	0.406	0.395	0.385
Roll	31.84	-	2.193	1.339	1.512	1.144
Pitch	31.80	$1/0.032 = 31.25$	1.768	1.047	1.214	0.930
Yaw	99.29	$1/0.0086 = 116.28$	2.096	1.833	1.645	1.503

reference value. Since the only restoring forces involved in the yaw decay motion come from the mooring lines, the deviation may be explained by a slightly different mooring configuration.

5.1.2 Heave motion modelled by a SDOF system

In general, the stiffness- and mass contribution from the mooring system in heave motion are small compared to the hydrostatic restoring forces for catenary moored floating structures (Karimirad, 2014). As a simplification, the heave motion may therefore be idealized as a simple SDOF system as shown in fig. 5.4. If the contribution from the mooring system related to heave motion is neglected, the stiffness of the system only comes from the hydrostatic restoring forces. If the weight of the mooring is neglected, the equilibrium heave position is where the hydrostatic restoring force is equal to the total weight of the FWT. If the cross sectional area of the platform around this equilibrium position has a small enough variation, the hydrostatic stiffness in heave may further be simplified based on the cross sectional area of the platform at still water level (SWL). The mass of the SDOF model has a contribution from the structural mass of the FWT as well as the hydrodynamic mass, as described in section 2.3. The motion of the simplified SDOF system may then be described by the following equation:

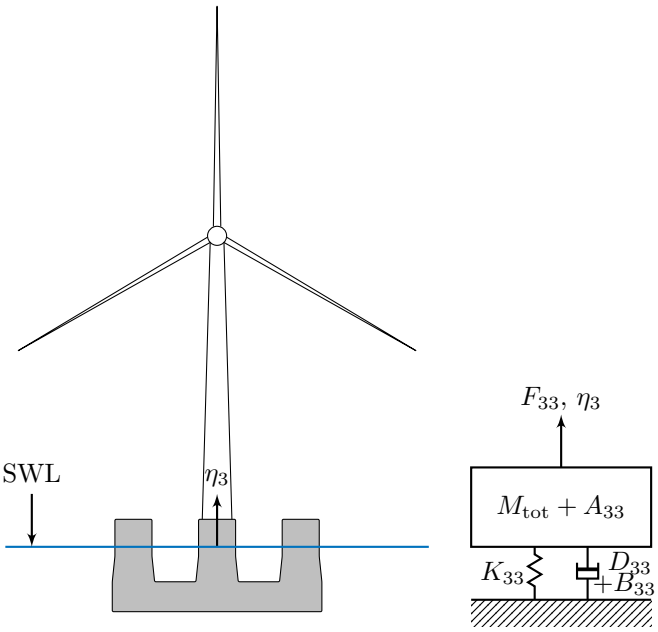

Figure 5.4. Heave motion modelled as a SDOF system.

$$(M_{tot} + A_{33})\,\ddot{\eta}_3 + (D_{33} + B_{33})\,\dot{\eta}_3 + K_{33}\eta_3 = F_{33} \tag{5.1}$$

where:
- M_{tot} = total mass of the FWT
- A_{33} = added mass in heave
- D_{33} = potential damping
- B_{33} = viscous damping
- $K_{33} = \rho_w g A_{SWL}$ = hydrostatic stiffness in heave
- A_{SWL} = cross sectional area of the platform at SWL
- F_{33} = external force

Subjected to $F_{33} = 0$, eq. (5.1) describes free vibration of a viscously damped system

$$(M_{tot} + A_{33})\,\ddot{\eta}_3 + (D_{33} + B_{33})\,\dot{\eta}_3 + K_{33}\eta_3 = 0 \tag{5.2}$$

Assuming that the system is underdamped, with zero initial velocity and an initial position of 1m, eq. (5.2) has the following solution (Chopra, 2012, Ch.2.2)

$$\eta_3(t) = e^{-\xi\omega_n t}\left[\cos\omega_{\mathrm{D}}t + \frac{\xi\omega_{\mathrm{n}}}{\omega_{\mathrm{D}}}\sin\omega_{\mathrm{D}}t\right]\,[\mathrm{m}] \tag{5.3}$$

where: $\omega_n = \sqrt{\frac{K_{33}}{M_{\mathrm{tot}}+A_{33}}}$ = natural frequency

ξ = damping ratio

$\omega_{\mathrm{D}} = \frac{2\pi}{T_{\mathrm{D}}} = \omega_{\mathrm{n}}\sqrt{1-\xi^2}$ = damped natural frequency

The hydrostatic stiffness in heave is calculated using the area from fig. 5.5

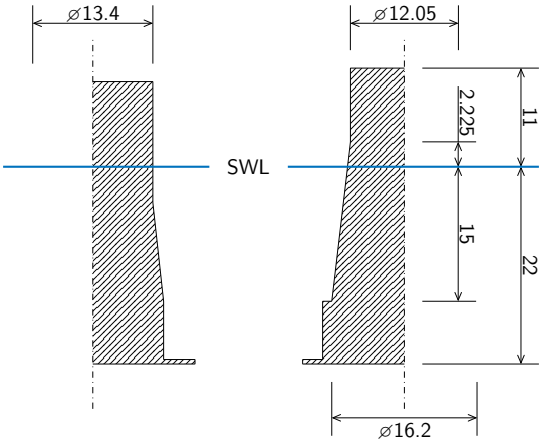

Cross sectional area of columns at SWL		
Outer:	$\pi \cdot 6.7^2$	$= 141.026\mathrm{m}^2$
Shaft:	$\pi \cdot \left(6.025 + 2.075 \cdot \frac{2.225}{17.225}\right)^2$	$= 124.414\mathrm{m}^2$
Total:	$3 \cdot 141.026 + 124.414$	$= 547.492\mathrm{m}^2$

Figure 5.5. OO-Star cross sectional area at SWL.

$$K_{33} = \rho_w \cdot g \cdot A_{\mathrm{SWL}} = 1023^{\mathrm{kg}}/_{\mathrm{m}^3} \cdot 9.81^{\mathrm{m}}/_{\mathrm{s}^2} \cdot 547.492\mathrm{m}^2 = 5.4944 \cdot 10^{6\,\mathrm{N}}/_{\mathrm{m}} \tag{5.4}$$

An estimate of the natural period of the system may be calculated using the sum of the structural masses of the system, given in section 3.1.1, plus added mass in heave and the hydrostatic stiffness. Added mass in heave is based on a frequency depended added mass function gathered from the SIMA model. Using the natural period from table 5.1, A_{33} is found as shown in fig. 5.6.

$$\begin{aligned} M_{\mathrm{tot}} &= M_{\mathrm{semi}} + M_{\mathrm{rotor}} + M_{\mathrm{nacelle}} + M_{\mathrm{tower}} \\ &= (2.1709 + 0.0231 + 0.0446 + 0.1257) \cdot 10^7\mathrm{kg} = 2.3643 \cdot 10^7\mathrm{kg} \end{aligned} \tag{5.5}$$

$$T_{\mathrm{D}} \approx 2\pi \cdot \sqrt{\frac{M_{\mathrm{tot}} + A_{33}}{K_{33}}} = 2\pi\sqrt{\frac{2.3643 \cdot 10^7 + 3.58 \cdot 10^7}{5.4944 \cdot 10^6}} = 19.86\mathrm{s} \tag{5.6}$$

This deviates by around 5% from the natural period obtained during the free decay analysis, and 3% from the value given i the LIFES50+ D4.2. report. The frequency dependent damping in heave, shown in fig. 5.6, decays quickly towards zero for periods above 15s. As the natural period in heave is around 20s, this explains why the heave motion in fig. 5.3 decays quite slowly.

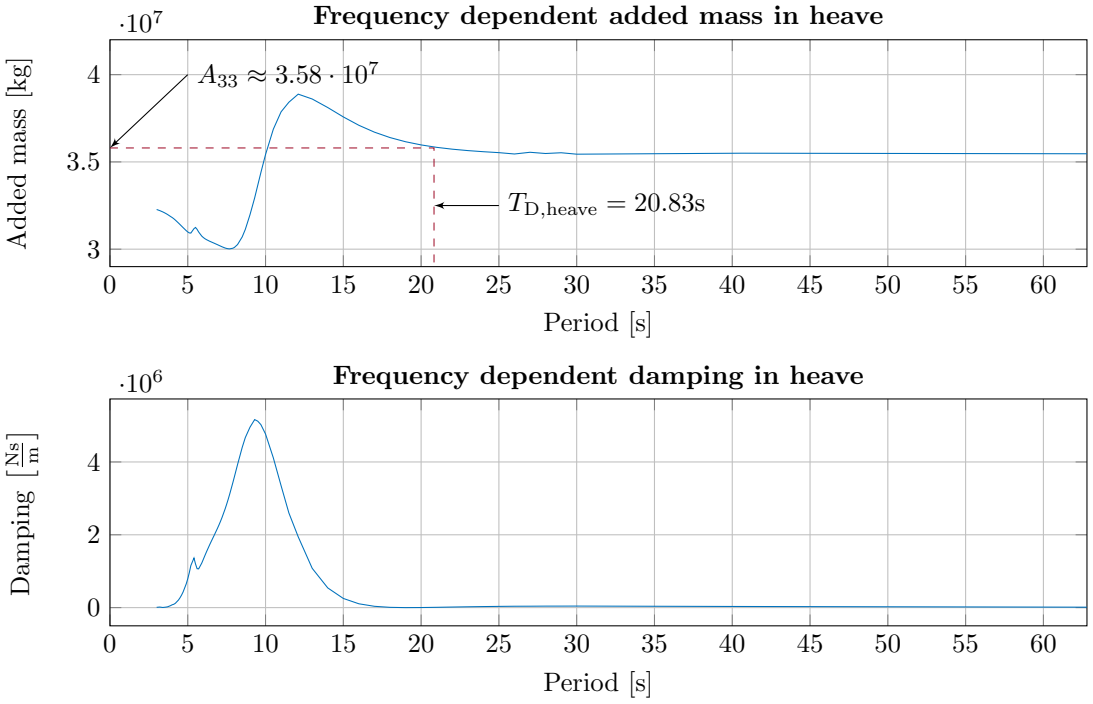

Figure 5.6. Frequency dependent added mass and -damping of the platform in heave motion taken from the SIMA model.

5.2 Response to environmental loading

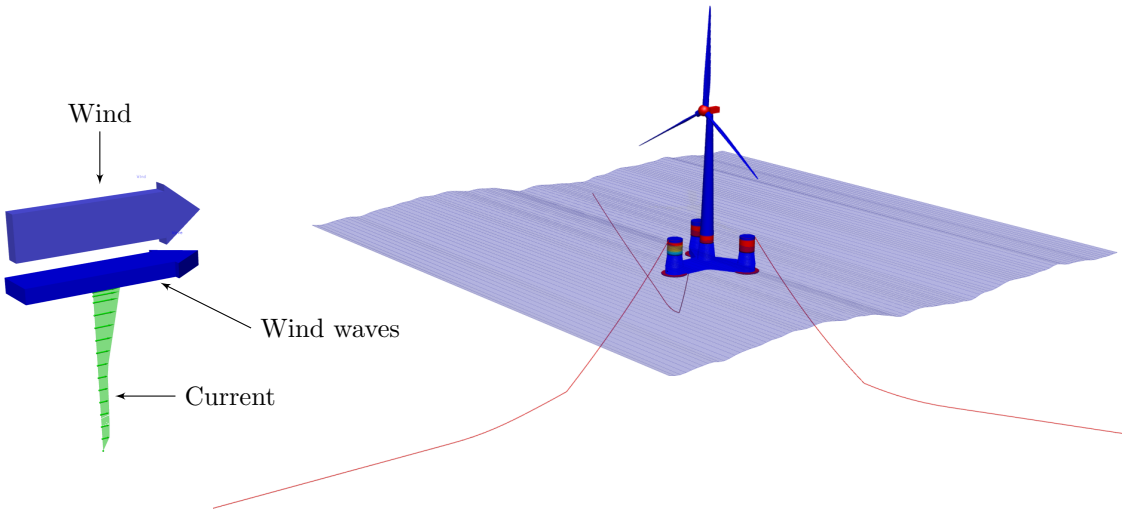

Figure 5.7. Configuration of the SIMA model during environmental loading. Wind, waves and current are applied parallel to one of the three mooring lines, with the hub facing the wind, and the rotor in the parked configuration.

In order to have a basis for comparison, regarding the effect of a seaquake on the response of an FWT, analyses containing wind-, wave- and current loading are performed in SIMA. Parameters describing wind, wave and current acting on the floating wind turbine are gathered from a LIFES50+ report describing oceanographic and meteorological conditions at three different sites suitable for offshore wind development (Gómez et al., 2018).

5.2.1 Selected site and environmental parameters

The chosen site is the Gulf of Maine on the east coast of the United States. This site has a mean depth of 130 meters, which is the same depth used in the provided SIMA model. Analyses are performed applying wind, waves and current parallel to one of the three mooring lines, with the hub facing the wind. The wind velocity is far above the cut-out limit for power production, and the wind turbine is therefore set to the parked configuration, with the blades adjusted to reduce drag from the wind. The irregular waves are generated using the JONSWAP spectrum in SIMA, which is given in eq. (2.85). Sea states using three different values of the peak shape parameter γ are considered. Initially, analyses ware performed with $\gamma = 1.0$ and $\gamma = 3.3$. Finally, a more comprehensive study using γ based on a recommended value from DNV-RP-C205 (DNV GL, 2010, Section 3.5.5) is considered. It is stated that if no particular values are given for γ, the following may be applied:

$$\gamma = \exp\left(5.75 - 1.15\frac{T_p}{\sqrt{H_s}}\right) \quad \text{for} \quad 3.6 < \frac{T_p}{\sqrt{H_s}} < 5 \tag{5.7}$$

H_s is the *significant wave height*, with a *peak period* described by T_p. To obtain an adequate basis for design of the wind turbine, several combinations of H_s and T_p likely to occur at the site should be analyzed. However, design is not the main focus of this thesis, and a combination of H_s and T_p to obtain a sufficiently accurate mooring line design tension for this site is based on advice from OO to be 10.9m and 14.8s, respectively. Based on these values, the peak shape parameter γ is calculated using eq. (5.7).

$$H_s = 10.9 \quad \text{and} \quad T_p = 14.8 \implies \frac{T_p}{\sqrt{H_s}} = \frac{14.8}{\sqrt{10.9}} = 4.483 \tag{5.8}$$

$$\implies \gamma = \exp\left(5.75 - 1.15 \cdot 4.483\right) = 1.813 \tag{5.9}$$

Wind and current acting on the wind turbine during the design situation are defined by uniform speed profiles, as shown in fig. 5.9, with no fluctuating part. These profiles are based on information from the

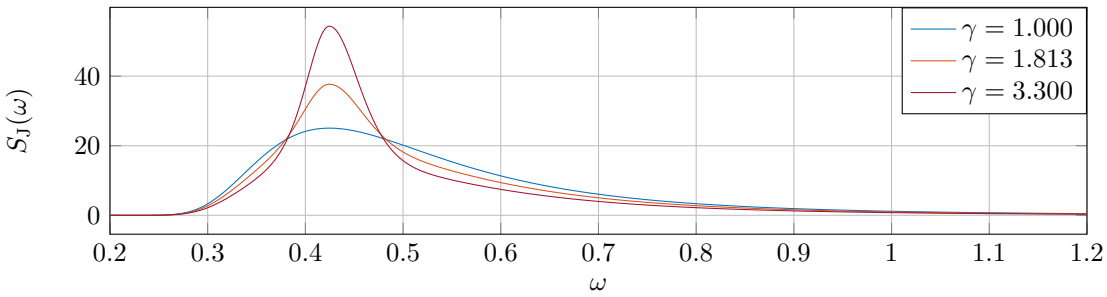

Figure 5.8. Shape of the JONSWAP spectrum at different peakedness values.

Table 5.2: SIMA parameters used during analyses of environmental loads.

Parameter	Value	Unit
Significant wave height H_s	10.9	[m]
Peak period T_p	14.8	[s]
Peak shape γ	1.0, 1.813 & 3.3	[-]

LIFES50+ D1.1 report (Gómez et al., 2018). A "0.11 Potential Profile" is used for the extreme wind condition, with a 50-year reference wind speed at 4m of 30.3m/s. This leads to a wind speed of 44m/s at the hub.

$$u_{10}(z) = u_{10}(H)\left(\frac{z}{H}\right)^{0.11} \tag{5.10}$$

where: u_{10} = wind speed with an averaging period of 10 minutes

The speed profile for the current is calculated as a sum of the wind- and the tide-induced current speed profiles. The profile for current speed induced by wind is linear, and is calculated using the following equation:

$$v_{c,\text{wind}}(z) = v_{c,\text{wind}}(0) \cdot \left(\frac{D_0 + z}{D_0}\right) \quad \text{for} \quad -D_0 \leq z \leq 0 \tag{5.11}$$

where: $v_{c,\text{wind}}(0)$ = wind induced current speed at the surface
D_0 = 65m (Half of the water depth at Gulf of Maine)

The current speed profile due to tide induced current is represented by a potential profile:

$$v_{c,\text{tide}}(z) = v_{c,\text{tide}}(0) \cdot \left(\frac{D + z}{D}\right)^{0.14} \quad \text{for} \quad -D \leq z \leq 0 \tag{5.12}$$

where: $v_{c,\text{tide}}(0)$ = tide induced current speed at the surface
D = water depth

To construct the current speed profiles, extreme current speed reference values at the surface with a 50 year return period have been used. The values are 0.7m/s and 0.43m/s for the wind- and the tide induced current speed, respectively. Inserting these values into eq. (5.11) and eq. (5.12) yields the current profile shown in fig. 5.9. The design tension T_d in the mooring lines is calculated using eq. (5.13), which is found in the DNVGL-ST-0119 standard (DNV GL, 2018b, Ch. 8.2)

$$T_d = \gamma_{\text{mean}} \cdot T_{c,\text{mean}} + \gamma_{\text{dyn}} \cdot T_{c,\text{dyn}} \tag{5.13}$$

where: $T_{c,\text{mean}}$ = characteristic mean tension
$T_{c,\text{dyn}}$ = characteristic dynamic tension
$\gamma_{\text{mean}}, \gamma_{\text{dyn}}$ = load factors

In the ultimate limit state (ULS), for structures in consequence class 1, the load factors γ_{mean} and γ_{dyn} are, according to DNVGL-ST-0119, required to be 1.3 and 1.75, respectively. To estimate $T_{c,\text{mean}}$ and $T_{c,\text{dyn}}$, several simulations with different sea states defined by H_s and T_p should be performed along a

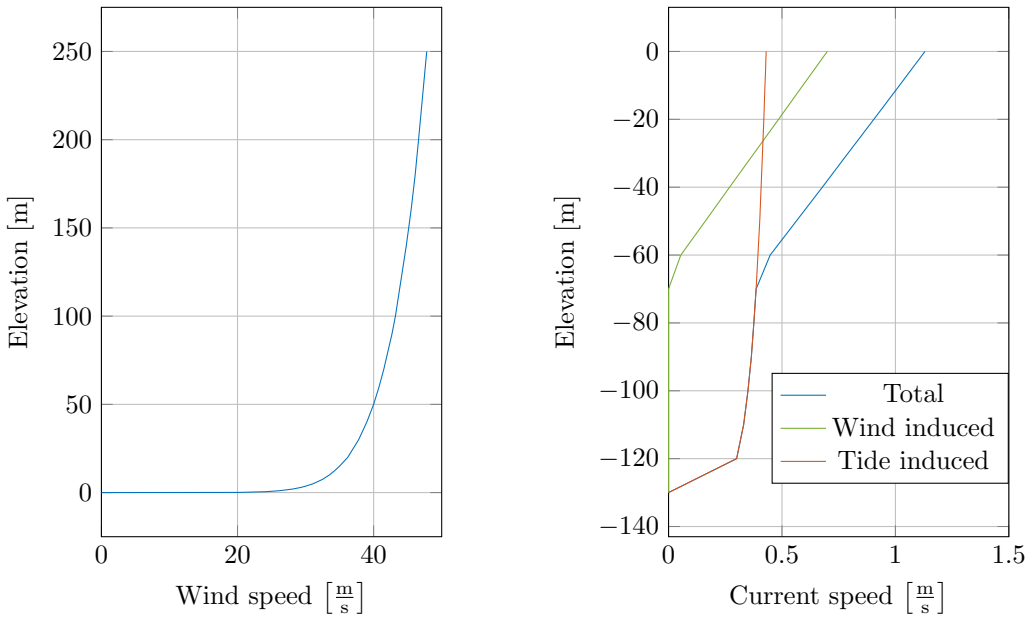

Figure 5.9. Extreme condition wind- and current profiles.

50-year contour. Then, $T_{\text{c,mean}}$ and $T_{\text{c,dyn}}$ can be based upon analyses with the sea state which yield the largest mooring line tension (DNV GL, 2018b). As already mentioned, different sea states will not be considered and the largest mooring line tension is based on the provided parameters in table 5.2. As an alternative to performing a single long time domain analysis, several realisations with a duration of three hours can be performed to establish an extreme value distribution (DNV GL, 2018c, Ch. 2.2). The extreme samples are then gathered from the maximum values observed from each simulation, and an extreme value distribution is then fitted to these samples as described in 2.3.4. $T_{\text{c,mean}}$ is calculated taking the average of the mean tension from all the performed simulations.

$$T_{\text{c,mean}} = \frac{1}{N}\sum_{i=1}^{N}\bar{T}_i \tag{5.14}$$

where: N = number of simulations
$\bar{T}_i$ = Mean mooring tension during simulation i

$T_{\text{c,dyn}}$ is then calculated using the most probable max (MPM) of the mooring tension, which is based on a Gumbel distribution fitted to the max tensions gathered from multiple three-hour simulations.

$$T_{\text{c,dyn}} = \text{MPM} - T_{\text{c,mean}} \tag{5.15}$$

The MPM of the mooring tension is calculated by fitting the maximum values of the different simulations to a Gumbel distribution. According to DVNGL-OS-E301, the MPM value of a Gumbel distributed variable corresponds to the 37% percentile (DNV GL, 2018c, Ch. 2.2).

5.2.2 Mooring response during environmental loads

In order to obtain a design mooring tension, several analyses were performed in SIMA with different seed numbers to generate different wave-time histories. The wave seed number is an arbitrary number which is fed into the algorithm producing the waves in SIMA. Using different wave seed numbers, different time histories of wave elevation are generated. Ten three-hour simulations are performed, each with a different wave seed number, for each of the three peak shape parameters. Since the peak shape parameter based on the recommendation from DNV GL is expected to yield the most accurate representation of the waves ($\gamma = 1.813$), 20 additional simulations are performed using this value, i.e. 30 simulations in total. The increased number of simulations give a better foundation for the extreme value statistics, which the design tension of the mooring lines is based on. Since the environmental loads are applied quite suddenly, all in one dominant direction, the model will experience a transient response phase before it settles at a

new position once the loaded anchor line is tightened. Therefore, the first 400 seconds of the simulations are ignored, as they are not representative of the true response. The simulation length of the analyses is based on advice from OO and is set equal to 11200s, to obtain three hours of simulation in addition to the initial 400s of transient response.

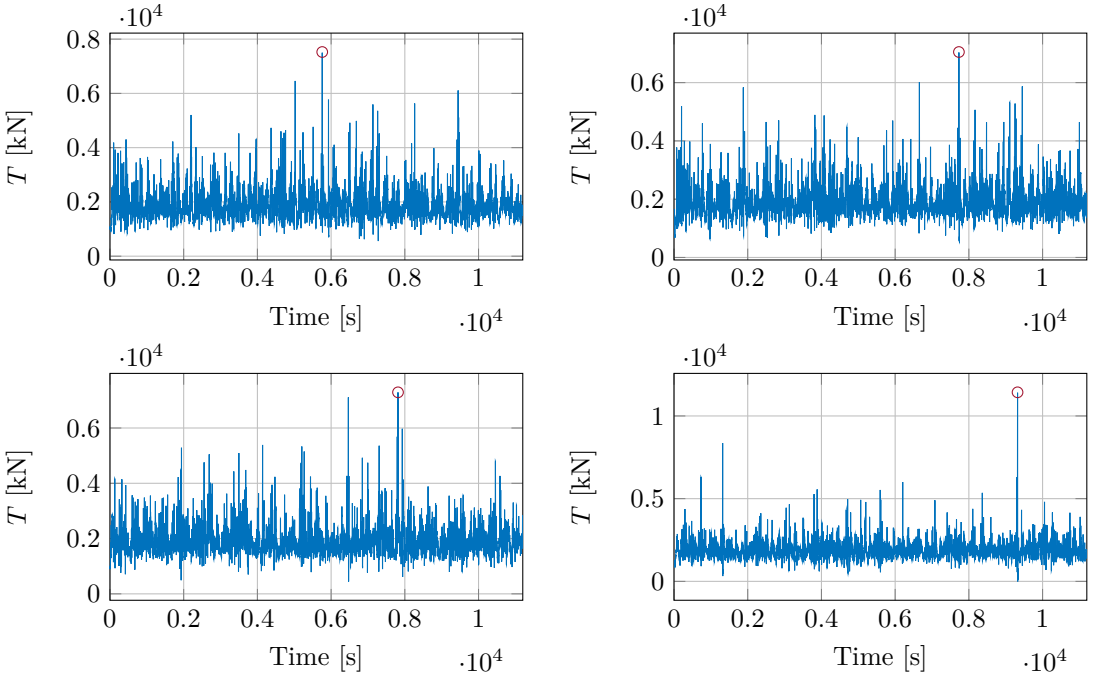

Figure 5.10. Tension in the mooring line element, connected to the seabed, in the loaded mooring line during environmental loading with waves generated by four different seed numbers. The peak tensions, indicated by red circles, are used to create the extreme value distribution which the design tension T_d is based upon.

Fig.5.10 shows time histories of the mooring line tension during four of the 30 different three-hour simulations with $\gamma = 1.813$. The maximal- and the mean value of mooring line tension, during the last three hours of each simulation, are determined for each simulation. The results from 10 of the employed wave seeds, for the three different values of γ, are shown in table 5.3. The analyses using lower peakedness yield higher mean tensions and higher peak tensions. The complete list of peak and mean tensions during the 30 simulations with $\gamma = 1.813$ is given in table B.1. The maximum values are then used to establish the extreme value distribution of mooring tension, shown in fig. 5.11. The design mooring tension is then calculated using eqs. (5.13) and (5.15)

$$T_{\mathrm{c,dyn}} = 6744\mathrm{kN} - 1947\mathrm{kN} = 4797\mathrm{kN} \tag{5.16}$$

$$T_{\mathrm{d}} = 1.3 \cdot 1947\mathrm{kN} + 1.75 \cdot 4797\mathrm{kN} = 10926\mathrm{kN} \tag{5.17}$$

Table 5.3: Tension in the loaded mooring line during waves generated by 10 different wave seed numbers, for three different values of the peak shape parameter γ. The tension is collected from the RIFLEX mooring line element connected to the seabed in the SIMA model.

Seed	$T_{\max,i}$ [kN]			$\bar{T}_i$ [kN]		
number	$\gamma = 3.3$	$\gamma = 1.813$	$\gamma = 1.0$	$\gamma = 3.3$	$\gamma = 1.813$	$\gamma = 1.0$
1001	6318	7525	7995	1847	1930	2015
1002	6163	7051	7541	1850	1937	2027
1003	6500	7291	8069	1863	1951	2042
1004	10233	11433	12344	1858	1941	2029
1005	8068	10337	11656	1853	1943	2034
1006	6004	6397	7991	1868	1955	2042
1007	6105	6186	6584	1855	1941	2028
1008	7730	7806	8058	1874	1963	2053
1009	6036	6728	7586	1851	1936	2020
1010	6575	6429	6172	1846	1927	2012

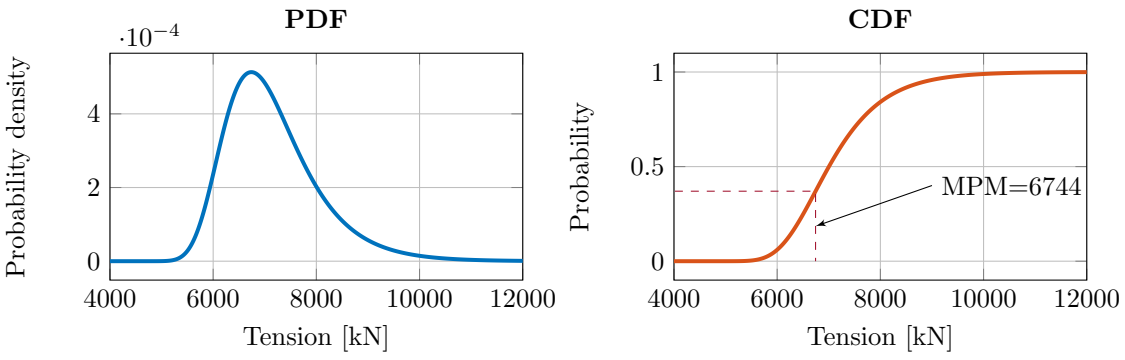

Figure 5.11. Gumbel distribution fitted to the maximum mooring line tensions at the anchor from the different simulations with $\gamma = 1.813$, given in table 5.3. The distribution is fitted using the built in extreme value distribution function in Matlab.

Chapter 6

Seaquake response of an FWT

In this chapter, the response of the SIMA modelled FWT, due to seaquake pressure at the bottom of the platform, is presented. Initially, seaquake analyses are performed with the turbine in the parked configuration in still water with neither wind nor current applied. The response of the FWT due to seaquake during power production in strong winds is considered at the end of the chapter.

6.1 Preparing the SIMA model for seaquake loading

At the start of the dynamic analyses in SIMA, the buoyant forces described by the hydrostatic stiffness matrix, the weight of the structure, and the forces acting on the platform from the mooring are not completely in equilibrium. This yields an initial movement of the wind turbine which slowly decays with time. As a remedy to obtain a wind turbine at rest when the seaquake loading is applied, without having to run the analysis for a long time to wait for the initial motion to decay, additional damping is added to the model as illustrated in fig. 6.1. In addition to the dampers shown in fig. 6.1, yaw damping is also incorporated by a pair of dampers placed at a distance of ±500m in the y-direction lying in the horizontal plane $z = 0$ to act as a "rotational damper". Damping is added by a force-elongation model (SINTEF Ocean, 2019c, Ch. 4.4.4). The axial force acting on the wind turbine from each of the force elongation models is given by:

$$F_a = F_{as} + C_a(u)\,|\dot{u}|^r \operatorname{sign}(\dot{u}) \tag{6.1}$$

where: u = displacement
F_{as} = axial stiffness force
$C_a(u)$ = axial damping coefficient
r = exponent of velocity

The force-elongation model added in SIMA is obtained by eq. (6.1) with $r = 1$, no axial stiffness, and a constant damping coefficient:

$$F_a = C_a \dot{u} \tag{6.2}$$

Damping coefficients used to damp the initial motion, in respective DOFs are given in table 6.1. This additional damping is set to vanish after the first 200 seconds of the analyses, the same instant as the seaquake loading is applied, to avoid that the added damping influences the seaquake response. In order to verify that the added damping functions as intended, an analysis is conducted where the turbine is left to decay over the first 200 seconds until the damping is set to vanish. The turbine is then lifted back to the initial position and is left to decay once again. The resulting heave motion and the heave motion of the original model are illustrated in fig. 6.2. This clearly shows the effect of the added damping on the initial motion, and that it vanishes for $t > 200$s as intended. The provided Loma Prieta earthquake time

Table 6.1: Added damping coefficients in each degree of freedom.

DOF	**Damping coefficient** $C_a\left[\frac{\text{Ns}}{\text{m}}\right]$
Surge	$2.0 \cdot 10^6$
Sway	$2.0 \cdot 10^6$
Heave	$5.0 \cdot 10^6$
Roll	$2.5 \cdot 10^5$
Pitch	$2.5 \cdot 10^5$
Yaw	$7.0 \cdot 10^3$ (for each)

history has a sampling period $T_s = 0.0050$s, which gives a sampling frequency $f_s = {}^1/_{0.0050\text{s}} = 200$Hz. To adequately capture the earthquake signal, the time step in the acoustic analyses in Abaqus is set to 0.0025s, storing the pressure at each step. The time step for the SIMA analyses is in turn set to 0.00125s in order to use a sampling frequency corresponding to the Nyquist frequency.

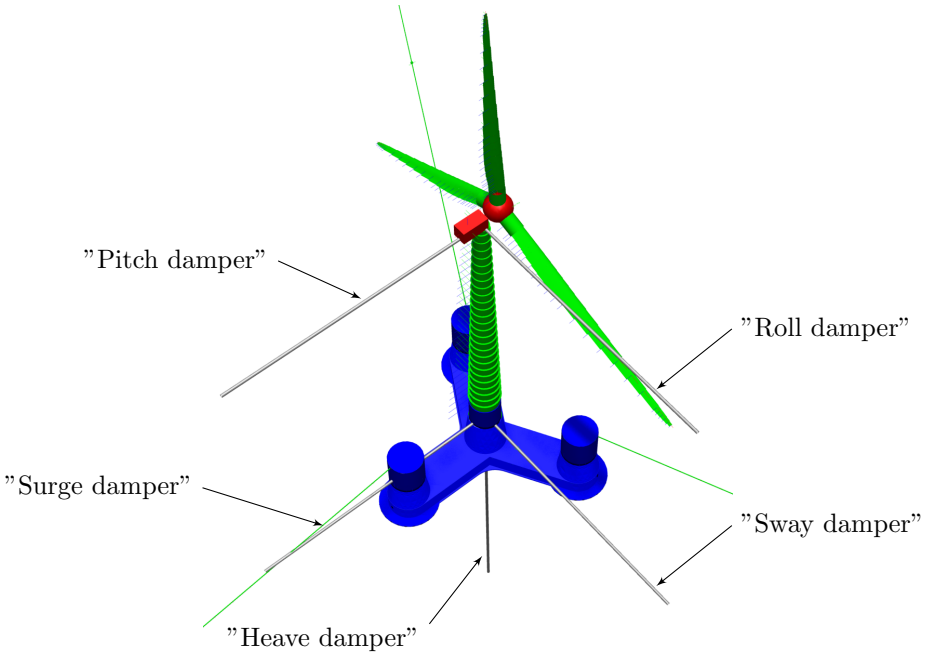

Figure 6.1. Dampers added to the SIMA model to decrease initial motion, before applying the seaquake loading.

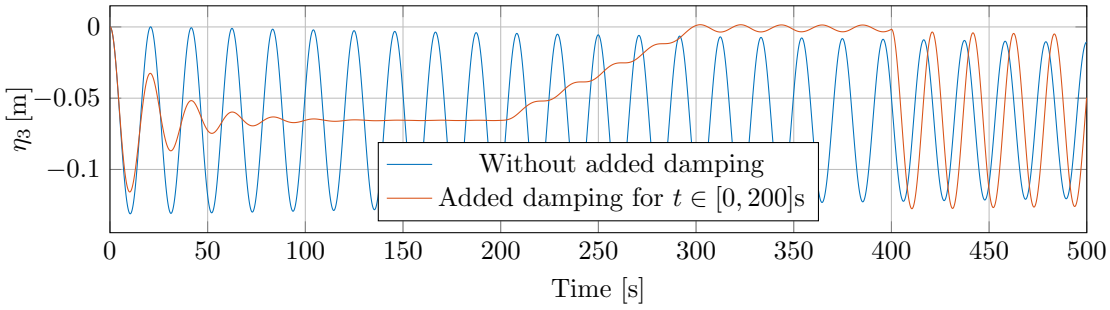

Figure 6.2. Platform heave motion without any external forces applied. Comparing the first- to the last one hundred seconds of the heave motion of the model with added damping, clearly shows that the damping vanishes after 200s as intended.

6.2 Platform response during seaquake

In this section, the pressure-time histories obtained from the different Abaqus acoustic models are applied to the bottom of the wind turbine platform in the SIMA model. The strong motion part of the vertical component of the Loma Prieta earthquake acceleration, shown in fig. 3.8, is applied at the bottom of the acoustic models. The different pressures are applied in the SIMA model as concentrated time-varying forces. The seaquake forces are calculated by multiplying the pressures by the total area of the bottom of the platform. The concentrated forces are introduced to the SIMA model as external forces from input files. In the provided SIMA model, the water depth is set to 130m. This is the design depth of the Gulf of Maine site, from the LIFES50+ D1.1 report (Gómez et al., 2018). In the acoustic models, the bottom of the platform is considered to sit 22m beneath the sea surface, as shown in fig. 5.5. For the conservative 1D model with a rigid reflector at the top of the model, the total column height is 108m and the pressure is extracted at a height corresponding to the bottom of the floater (which is the top of this model). For the second and less conservative 1D alternative, the model height is 130m and the pressure is extracted 22m beneath the top of the model. For the hybrid 1D model and the 2D model, the total water depth is 130m and the pressure is extracted 22m beneath the top surface of the models. Only motion in heave is considered during the seaquake. Since the seaquake is applied vertically by a force acting at the centroid of the bottom of the platform, motions in the remaining degrees of freedom are small in comparison.

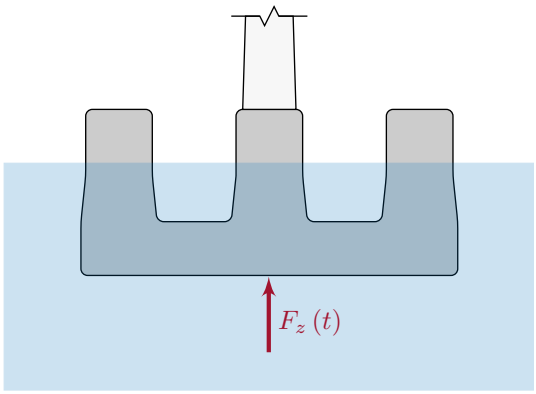

Figure 6.3. Applying the seaquake pressure to the bottom of the platform by integrating the pressure over the surface.

The natural frequency for the heave motion of the wind turbine is approximately 0.049Hz, as indicated in table 5.1. The vertical component of the Loma Prieta earthquake has a frequency content which is concentrated between 0 and 5Hz, as shown in fig. 3.7. The frequencies in the vertical acceleration and corresponding pressure will be much larger than the natural frequency of the heave motion. The phase lag between the response of the floater and the initial pressure will be large. This means that the response is in the mass controlled domain. The heave response of the wind turbine is consequently expected to be small. The assumption of a rigid surface representing the bottom of the floater could then be reasonable. The acoustic models in Abaqus do not consider or include the interaction between pressure waves and the motion of the bottom of the structure. In reality, the pressure acting on the platform from the seaquake would set the wind turbine in motion, which in turn would generate pressure waves radiating out from the platform towards the seabed. This effect is not captured by the uncoupled analyses between Abaqus and SIMA.

As previously explained, the 1D model with a rigid top reflector represents an upper conservative limit for the pressure at the bottom of the floating structure. The second 1D model with a free-field top surface represents a lower limit for the pressure. The results from the less conservative model are expected to be smaller than the real pressure from a seaquake, when assuming a uniform displacement along the entire seabed. It is important to verify the resulting accelerations in the floater for both alternatives. It is especially important to verify if the conservative model yields realistic results.

6.2.1 Applying pressure from the 1D rigid top acoustic model

Applying the pressure obtained from the 1D rigid top Abaqus acoustic analysis in the SIMA model, yields the vertical platform response shown in fig. 6.4. The maximum heave of nearly 40m, in addition to the maximum acceleration of more than 20 $^{m}/_{s^2}$, indicate that the acoustic model with a rigid top reflector yields a much too conservative pressure, compared to what could be expected to act on a floating structure during a seaquake. The peak pressure of more than 0.4MPa, shown in section 4.4, is in fact approaching 25% of the mean value of axial tensile strength of a weak concrete type, which seems unlikely. A reasonable pressure is expected to be somewhere between this and the one obtained from the free-field acoustic analysis considered next. The pressure from the rigid top acoustic model will not be considered further.

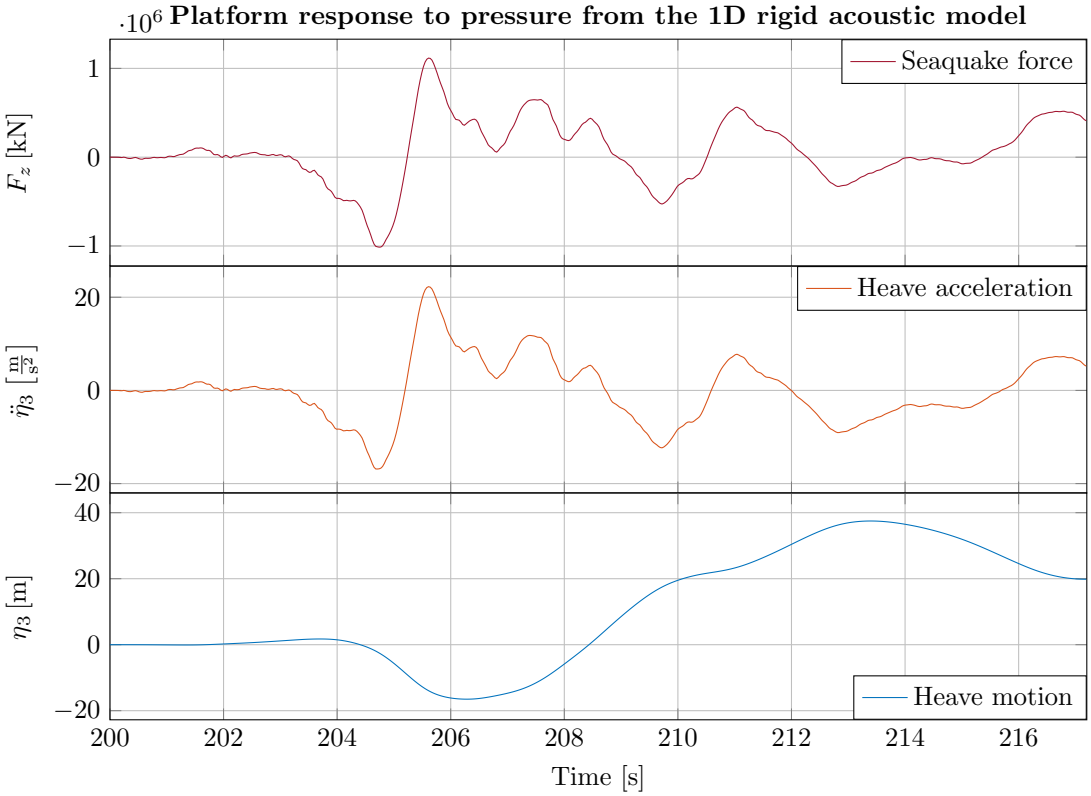

Figure 6.4. Platform response to seaquake pressure obtained from the Abaqus acoustic model with a rigid top reflector.

6.2.2 Applying pressure from the 1D free-field acoustic model

As for the 1D rigid top acoustic model, the less conservative pressure from the free-field acoustic model is applied to the bottom of the platform. The resulting vertical response is presented in fig. 6.5. The magnitude of these results seems more realistic than the previous response obtained from the conservative acoustic model. However, a free-field top surface is most likely not conservative enough when it comes to representing the actual pressure which could act on the bottom of a floating structure during a seaquake. The constrained movement of the water near the bottom of the platform is expected to yield a higher peak pressure.

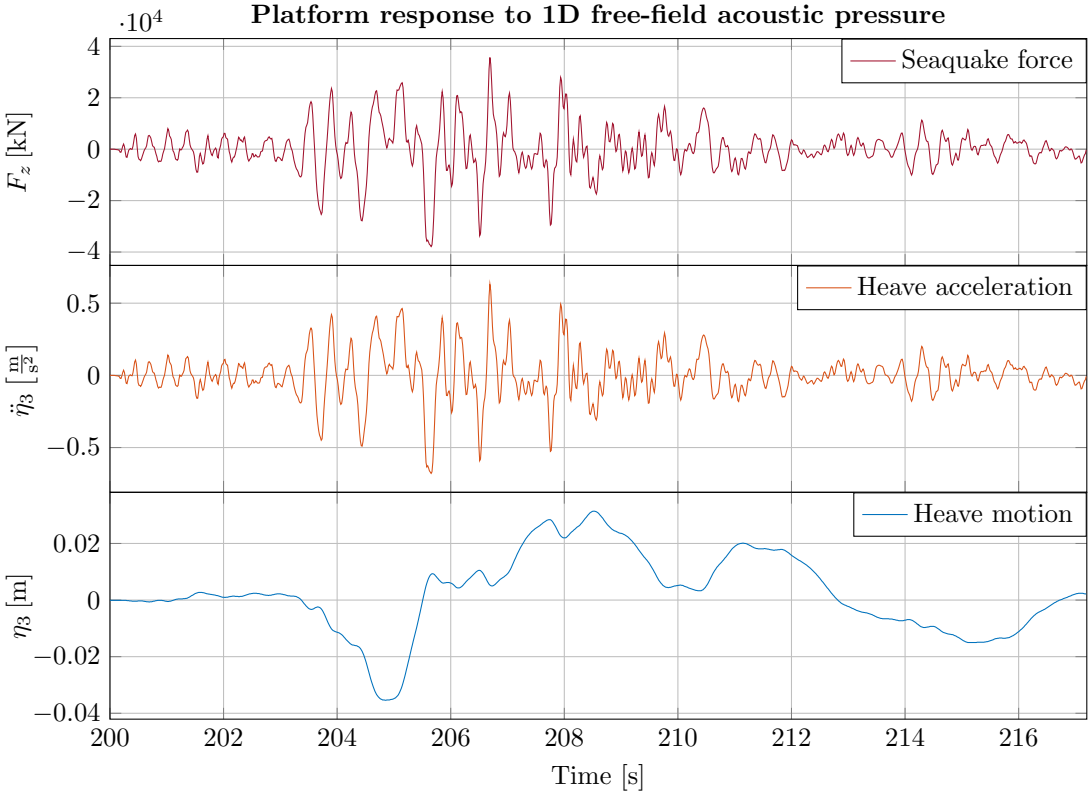

Figure 6.5. Platform response to unscaled seaquake pressure from the free-field 1D Abaqus model.

6.2.3 Applying pressure from the hybrid acoustic model

As previously explained, the pressure obtained by the 1D model with a rigid top reflector yields a response of the wind turbine platform which indicates a far too conservative modelling of pressure. The model with a free-field top surface yields a response which intuitively seems more reasonable. The motivation for the development of the hybrid model, described in section 4.5.1, is that the real pressure acting on the platform is expected to lie somewhere between the ones obtained by these two limiting cases. This is because the presence of the floating structure will result in a larger pressure reflection than a free-field case would.

The pressure from the Abaqus hybrid model used to study the response of the platform in SIMA, is collected at point 1 according to fig. 4.10 and illustrated in fig. 4.11. The vertical response of the platform is presented in fig. 6.6. As expected, the peak values of the response is somewhere between the previous responses obtained by the limiting 1D cases.

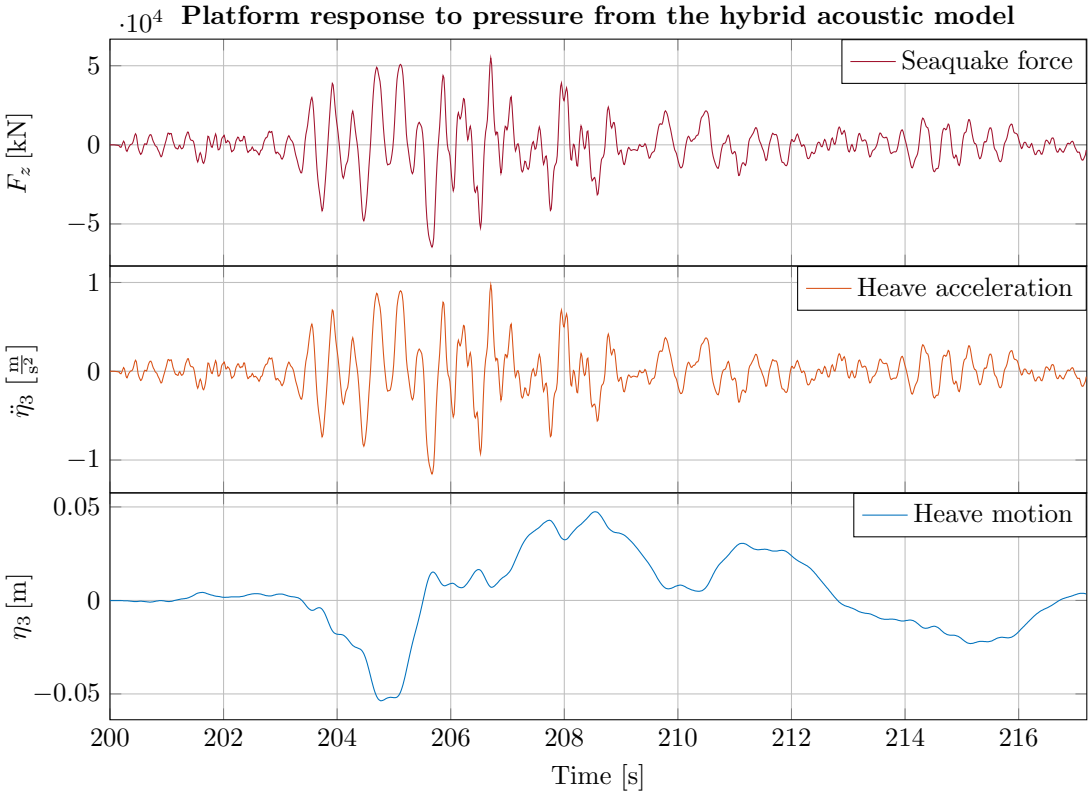

Figure 6.6. Response of the wind turbine platform subjected to the pressure obtained from the Abaqus 1D hybrid acoustic model.

6.2.4 Applying pressure from the 2D acoustic model

The main difference between the 1D and 2D acoustic models is that the 2D model yields horizontally varying pressure, as illustrated in 4.6. A unique time-varying pressure is then obtained at each node in the mesh of the acoustic model, along the bottom of the platform. In order to apply these pressures on the SIMA model, the pressure has to be converted to concentrated forces. One could imagine that each pressure-time history should be multiplied by a small area of the platform which it acts upon, and then apply all of these forces in SIMA. However, since the platform geometry is not represented accurately in the 2D acoustic model, and because the SIMO body representing the platform in SIMA is modeled as a rigid body, the pressure series are averaged along the bottom of the platform and applied as a single concentrated time-varying force. The averaged pressure-time history acting the bottom of the platform is presented in fig. 6.7. The resulting vertical response is shown in fig. 6.8.

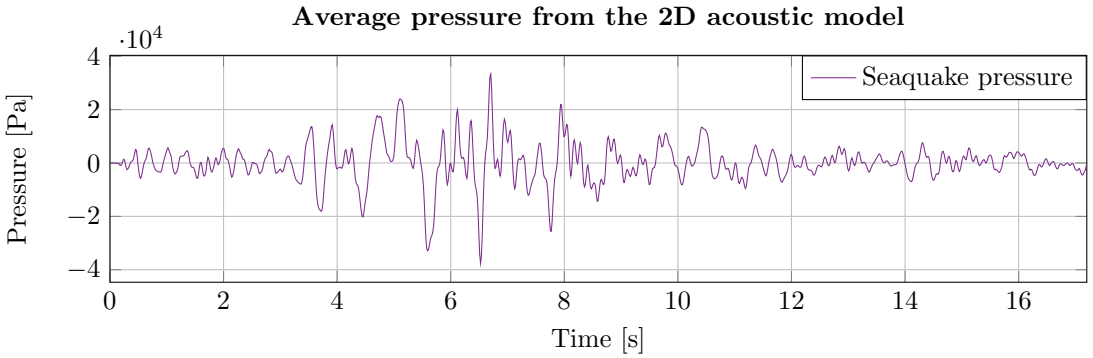

Figure 6.7. The average pressure under the horizontal rigid reflector surface representing the bottom of the platform in the 2D acoustic model.

The seaquake pressure from the 2D acoustic model causes a maximal heave displacement of 0.083m from the static equilibrium position of the platform. This is about 2.3 times larger than the response due to the 1D free-field pressure, and about 1.5 times larger than the response due to pressure from the hybrid acoustic model. The 2D model and the hybrid model are expected to provide the pressure closest to reality of the four different acoustic models. Since the pressure obtained from the 2D model provides the largest pressure between the two models, this pressure is considered to be the best candidate for further study of the wind turbine response during a seaquake. The pressure from the 2D model will be used to investigate the response of the remaining parts of the wind turbine model during a seaquake.

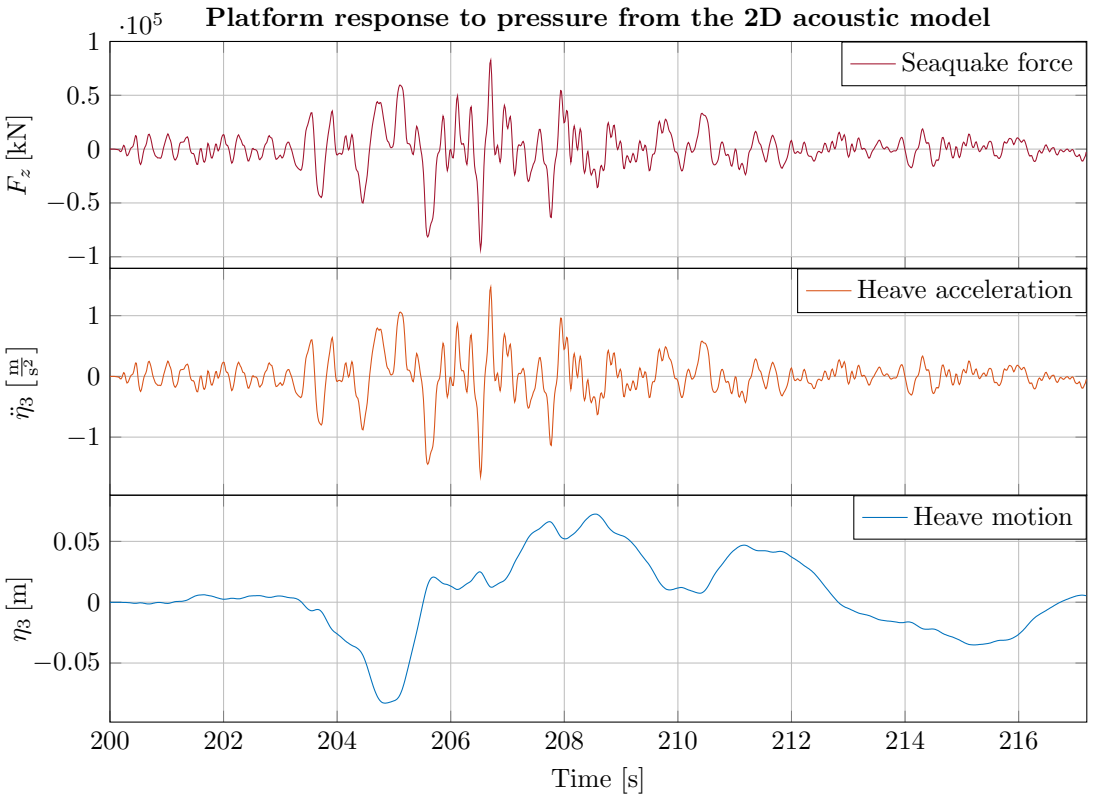

Figure 6.8. Response of the wind turbine platform subjected to the average seaquake pressure from the 2D acoustic model.

6.2.5 Applying scaled seaquake pressures from the 2D acoustic model

The pressure in fig. 6.7 is the result of applying the strong motion part of the vertical acceleration of the Loma Prieta earthquake at the seabed. To study the effect of a more severe seaquake on the response of the wind turbine, this pressure is scaled up to represent a higher peak vertical acceleration (PVA) of the seabed, assuming a linear relationship between ground acceleration and seaquake pressure. Each of the scaled pressures is then applied to the platform in separate SIMA analyses. The scaling factors for PVA levels are presented in table 6.2. The seaquake pressure resulting from a vertical earthquake excitation of the seabed with a PVA of 0.3g is presented in fig. 6.9. The response of the platform due to this scaled seaquake pressure is presented in fig. 6.10. The results show a maximum heave acceleration larger than $10^{m}/_{s^2}$. The maximum heave displacement is slightly larger than 0.5m. The response of the platform to unscaled seaquake pressure, shown in fig. 6.8, exhibits a maximum heave acceleration of approximately $1.6^{m}/_{s^2}$, and a maximum heave displacement of around 0.075m.

Table 6.2: Scaling factors applied to the average pressure from the Abaqus 2D acoustic model.

Earthquake history	**PVA** $\left[\frac{m}{s^2}\right]$	**PVA** [g]	**Scaling factor**
Loma Prieta (L.P.) unscaled	0.3381	0.0345	1.0000
L.P. scaled to 0.05g	0.4905	0.0500	1.4508
L.P. scaled to 0.10g	0.9810	0.1000	2.9015
L.P. scaled to 0.15g	1.4715	0.1500	4.3523
L.P. scaled to 0.20g	1.9620	0.2000	5.8030
L.P. scaled to 0.25g	2.4525	0.2500	7.2538
L.P. scaled to 0.30g	2.9430	0.3000	8.7045

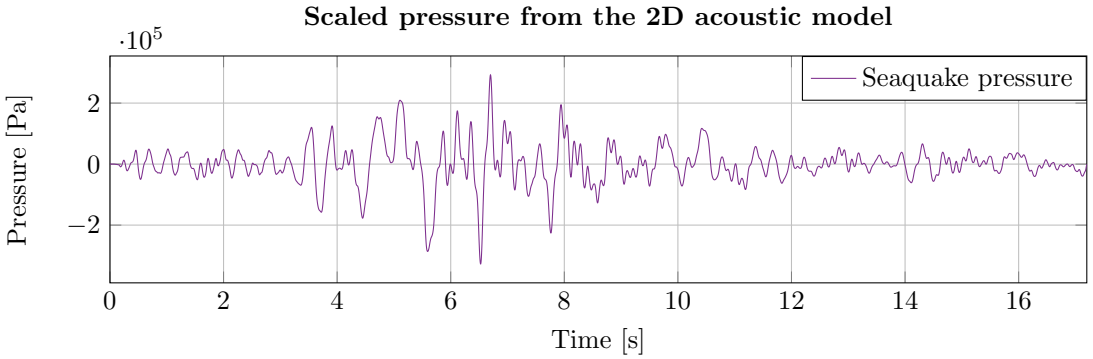

Figure 6.9. Average seaquake pressure from the Abaqus 2D acoustic model scaled by a factor of 8.7045, as described in table 6.2, to correspond to a PVA of the seabed of 0.3g.

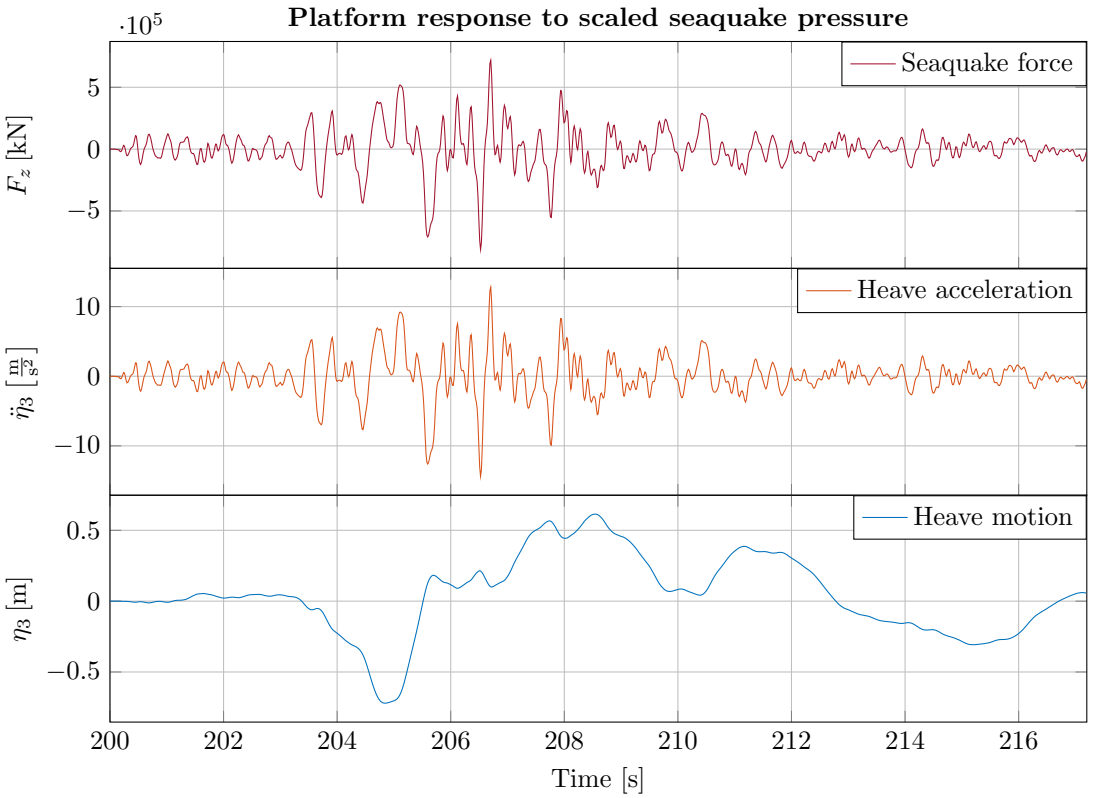

Figure 6.10. Seaquake response of the platform subjected to the Abaqus 2D acoustic pressure scaled to correspond to a seabed PVA of 0.3g.

6.3 Nacelle seaquake response

The nacelle contains equipment which may be sensitive to the vertical accelerations experienced by the FWT during a seaquake. During design of floating offshore wind turbines, a common industrial practice is to set an operational limit for the tower top accelerations. This limit is normally in the range of 0.2-0.3g (Nejad et al., 2017). Due to amplification related to the natural frequencies of the tower, the nacelle will experience larger acceleration levels than the ones experienced by the platform.

6.3.1 Response to pressure from the 2D acoustic model

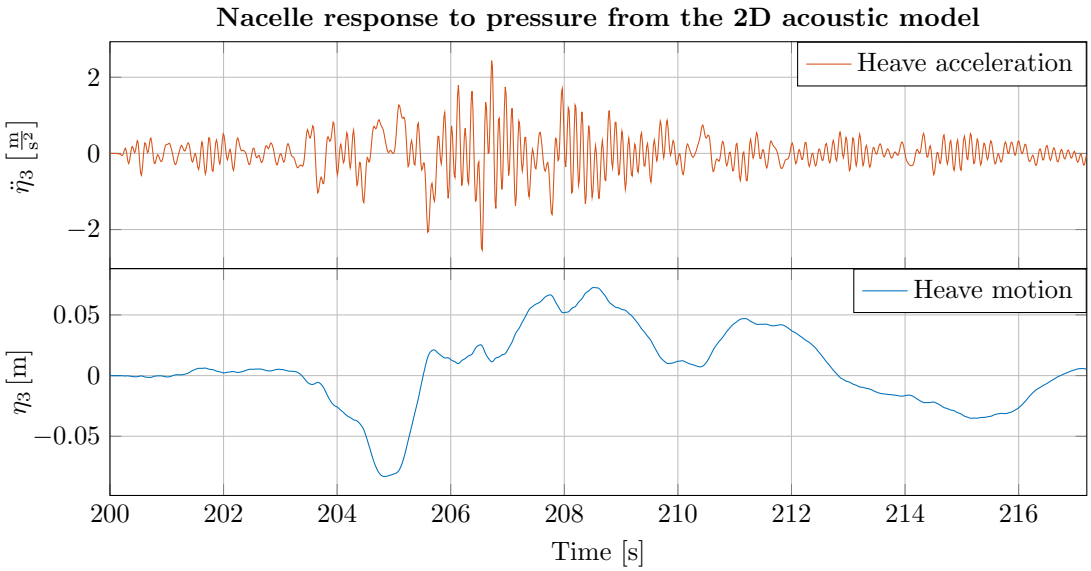

Figure 6.11. Response of the nacelle during seaquake excitation on the platform from the 2D Abaqus acoustic pressure.

The response of the nacelle, shown in fig. 6.11, indicates a moderate heave motion of less than 0.1m. The vertical acceleration levels are however in the operational limit range. The maximum acceleration experienced by the nacelle is 0.2650g, which indicates an amplification between the seabed and nacelle accelerations of 7.68. This suggests that a seaquake can have an important effect on the components in the nacelle. Peak nacelle- and platform accelerations during scaled seaquake pressures, as described in section 6.2.5, are presented next in addition to amplification of accelerations between the seabed and the nacelle.

6.3.2 Amplification of seabed acceleration through the FWT

The seaquake pressure acting on the platform is scaled according to table 6.2. The maximum accelerations in the platform and the nacelle are presented in table 6.3. For all of the considered PVA's of the seabed, the peak nacelle acceleration is either equal to or above the operational acceleration limit described in the beginning of the section (0.2-0.3g). The amplification between the seabed and the platform, as well as between the seabed and the nacelle, is nearly constant for the different PVA levels. It seems that the amplifications increase slightly for increasing PVA's. The average amplification between the accelerations at the seabed and the platform is 4.8816. The average amplification between the seabed and the nacelle is 7.6956. It could be expected that the amplification would decrease for higher PVA's as the velocity proportional damping (viscous damping) would increase. This is however not the case. For the following sections, the two amplifications are assumed to be constant.
The amplification of the seabed acceleration through the platform to the nacelle is illustrated in fig. 6.13. The accelerations in the nacelle and the platform are due to the seaquake excitation of the platform applying the pressure from the 2D acoustic model. The amplification of platform acceleration is clearly visible around the maximum nacelle acceleration. The larger amplification obtained around 207s is likely due to the frequency content of the platform acceleration approaching one of the natural frequencies of the tower. The amplifications for the considered PVA's are given in table 6.3.

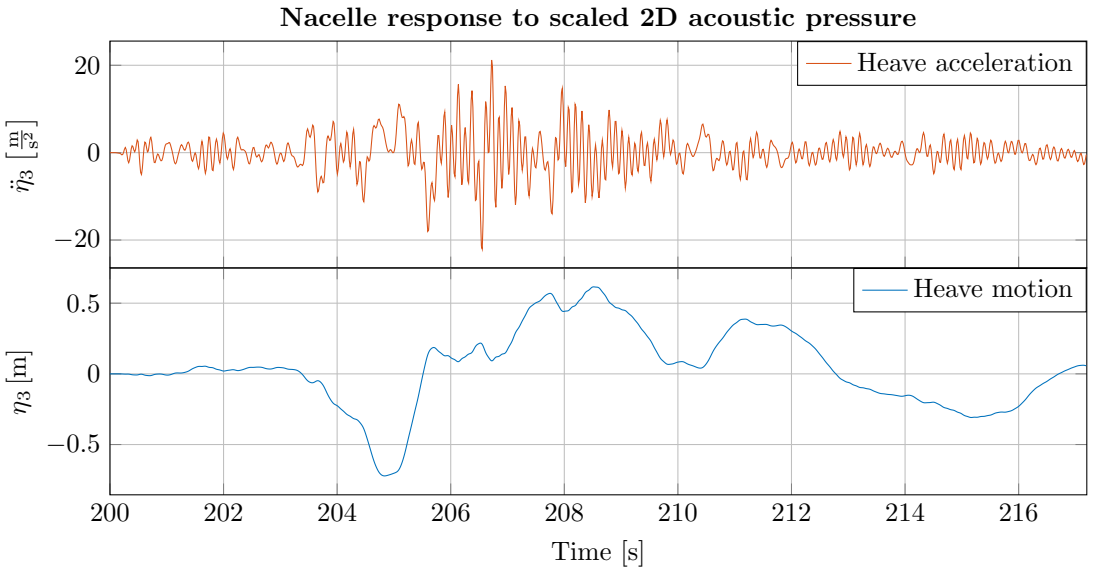

Figure 6.12. Nacelle response during seaquake excitation of the platform, using the 2D Abaqus acoustic pressure, scaled to correspond to a seabed PVA of 0.3g.

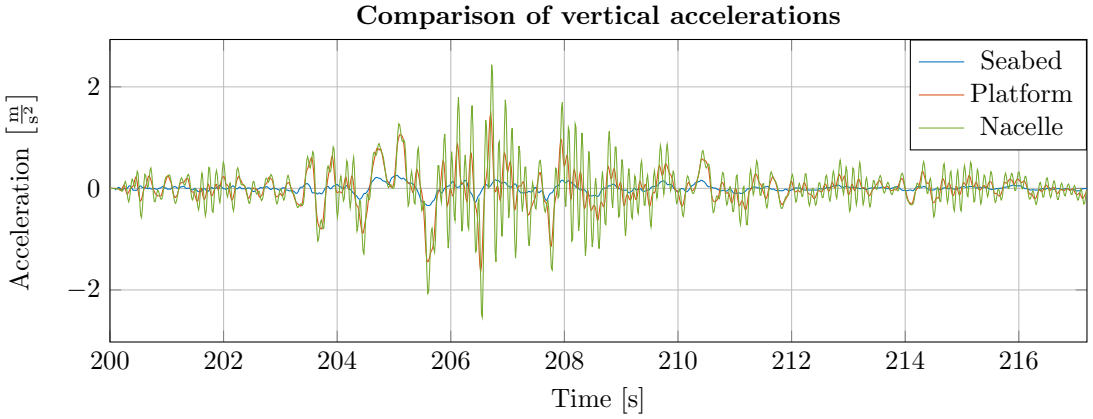

Figure 6.13. Unscaled strong motion vertical acceleration at the seabed compared with the vertical accelerations in the platform and the nacelle.

Table 6.3: PVA of the nacelle and the platform due to seaquake pressures resulting from different seabed PVA's.

PVA of the seabed		**PVA of the platform**		**PVA of the nacelle**		**Platform amplification**	**Nacelle amplification**
[g]	[$\frac{m}{s^2}$]	[g]	[$\frac{m}{s^2}$]	[g]	[$\frac{m}{s^2}$]	[−]	[−]
0.0345	0.3381	0.1680	1.6484	0.2650	2.5997	4.8755	7.6891
0.0500	0.4905	0.2438	2.3915	0.3845	3.7715	4.8756	7.6891
0.1000	0.9810	0.4876	4.7834	0.7690	7.5435	4.8760	7.6896
0.1500	1.4715	0.7317	7.1782	1.1539	11.3193	4.8782	7.6924
0.2000	1.9620	0.9770	9.5845	1.5399	15.1063	4.8851	7.6994
0.2500	2.4525	1.2223	11.9909	1.9259	18.8933	4.8893	7.7037
0.3000	2.9430	1.4675	14.3965	2.3119	22.6793	4.8918	7.7062

6.4 Response of the wind turbine tower during seaquake

The force-response of the wind turbine tower during seaquake loading is obtained in SIMA and exported to Matlab for post-processing. The tower model in SIMA is discretized into 27 circular tube segments with a constant diameter and wall thickness within each segment. In reality, each segment would have a linearly varying diameter along the height, with a constant wall thickness (see fig. C.1). The complete description of the tower discretization is given in table C.1. Each of the 27 segments of the tower are represented by one beam element. The response quantities available for each beam element are the axial force, torsional moment, moment about the local y- and z-axes for each element end, in addition to shear force in the y- and z-direction for each element end, i.e. 10 in total. The resulting dimension of the matrix of stored RIFLEX response then becomes $[n_{\text{step}} \times 10 \cdot n_{\text{els}}]$, where n_{step} is the number of time steps stored from the SIMA analyses, and n_{els} is the number of beam elements. The axial forces and bending moments in three selected beam elements of the tower are extracted and presented. The selected elements are shown in fig. 6.15.

6.4.1 Applying seaquake pressure from the 2D acoustic model

The tower response obtained from RIFLEX due to seaquake pressure from the 2D acoustic model, applied at the bottom of the platform, is presented. The seaquake pressure corresponds to the unscaled vertical acceleration of the seabed. To study the effect of a seaquake on the wind turbine tower, the force-response of each RIFLEX modelled beam element comprising the turbine tower is saved and post-processed in Matlab. As the wind turbine model, in the parked configuration, is symmetric about the global xz-plane, and the seaquake excitation is only acting vertically, the bending moment about the global x-axis is negligible compared to the bending about the global y-axis. The response quantities of interest are assumed to be the bending about the global y-axis and the axial force. Bending about the global y-axis is due to the eccentricity of the center of mass of the rotor-nacelle assembly (RNA). As previously, the seaquake loading is applied to the SIMA model after 200s of transient response. The static part of the axial force and the bending moment, due to the weight of the RNA and the tower itself, is calculated taking the average value during the interval $t \in [100, 200]$s. The dynamic axial force and -moment are obtained by subtracting the static axial force and -moment from the total. The dynamic part of the axial force and bending moment during the seaquake from the 2D acoustic model, for the three selected elements, are presented in fig. 6.14. The normal stress, sampled at the left edge of the tower, according to fig. 6.15, during seaquake is also presented in the same figure. The dynamic part of the normal stress within beam element i is calculated using the following expression:

$$\sigma^i_{\text{dynamic}} = \frac{N^i_{\text{dynamic}}}{A^i_{\text{cs}}} + \frac{M^i_{\text{y1,dynamic}}}{I^i} \cdot R^i_{\text{out}} \tag{6.3}$$

where:
- N^i_{dynamic} = dynamic part of the axial force in element i
- A^i_{cs} = cross-sectional area of element i
- $M^i_{\text{y1,dynamic}}$ = dynamic bending moment about local y-axis at end 1 (the bottom) for element i
- I^i = second moment of area for element i
- R^i_{out} = outer radius of element i

The maximum dynamic stress occurs for element 27 since the amplification of vertical accelerations is the largest at the top of the tower. The maximum additional stress is approximately 5MPa. By considering the nacelle and platform amplifications from table 6.3, it is assumed that the amplification between the acceleration at the seabed and a given point along the tower is constant. Therefore, the maximum dynamic stress can be scaled according to the PVA of the seabed. The maximum dynamic stress for the three considered elements for different PVA levels is presented in table 6.4.
The static response along the tower is shown in table 6.5. The static stresses are determined using eq. (6.3) with the static axial forces and -moments.
A comparison between the maximum dynamic stresses from table 6.4 and the static stresses from table 6.5 indicates that the effects of a seaquake are not critical for the capacity of the tower. As the dynamic amplification is the largest and the cross section is the smallest at the top of the tower, this location experiences the largest dynamic stresses. The static stress is also the largest in the top of the tower. For a vertical PGA of 0.3g, the total (static+dynamic) compressive stress is approximately 69.8 MPa. As the tower is made of steel, it is expected that the design yield stress is at least larger than 200

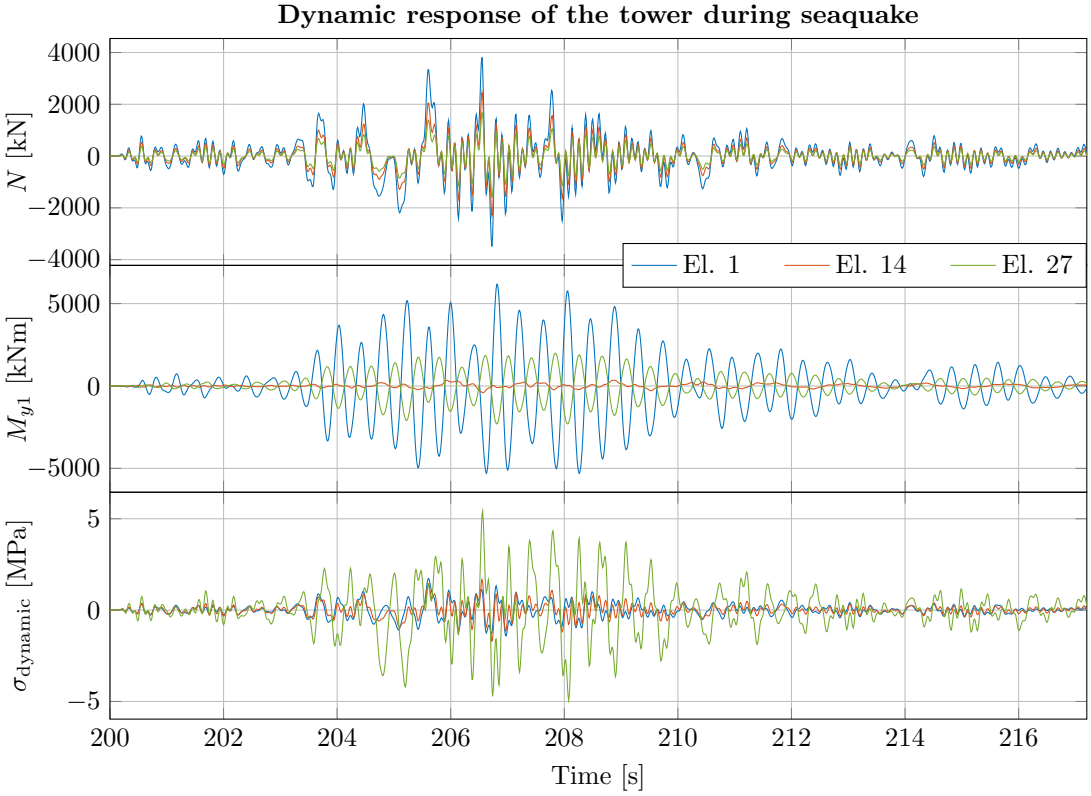

Figure 6.14. Dynamic part of tower response during seaquake excitation of the platform. The unscaled vertical acceleration at the seabed is considered. The static response has been subtracted.

Table 6.4: Maximum dynamic stress for the three tower elements for different PVA's of the seabed.

Element number	**Maximum dynamic stress** [MPa] **at different seabed PVA's** [g]						
	0.0345	0.05	0.1	0.15	0.2	0.25	0.3
1	1.725	2.499	4.999	7.498	9.998	12.497	14.997
14	1.662	2.409	4.818	7.227	9.635	12.044	14.453
27	5.417	7.851	15.701	23.552	31.403	39.254	47.104

Table 6.5: Static response of the tower due to self-weight. The axial forces are all compressive forces.

Element	**Cross section properties**			**Static response**		
number	$A\,[\text{m}^2]$	$I\,[\text{m}^4]$	R_{out} [m]	N_{static} [kN]	$M_{y1,\text{static}}$ [kNm]	σ_{static} [MPa]
1	2.665	42.61	5.6925	18536	10634	8.38
14	1.361	11.82	4.1925	10303	7710	10.3
27	0.484	1.805	2.7205	6676	5935	22.74

MPa. Therefore, a seaquake will most likely not result in issues for the capacity of the cross sections along the tower, when comparing the seaquake stresses with the static stresses. Especially since a PVA of 0.3g for the seabed is expected to rarely occur. However, the buckling capacity should perhaps be considered as the wall thicknesses are small compared to the diameter of the sections. By assessing the results from tables 6.4 and 6.5, it is observed that at a PVA of the seabed equal to 0.15g, the dynamic stresses at top of the tower are approximately equal to the static stresses due to self weight.

To verify the static tower response, the static axial force in element 1 from table 6.5 is compared with the combined weight of the RNA and the tower, using properties from table 3.3 and table C.1.

$$\begin{aligned} W_{\text{Tower+RNA}} &= (m_{\text{Tower}} + m_{\text{RNA}}) \cdot \text{g} \\ &= (0.677 + 1.257) \cdot 10^6 \text{kg} \cdot 9.81 \frac{\text{m}}{\text{s}^2} = 18970 \text{kN} \end{aligned} \tag{6.4}$$

Subtracting half of the weight of element 1 yields

$$18970 \text{kN} - \frac{8.667}{2} \cdot 10^4 \text{kg} \cdot 9.81 \frac{\text{m}}{\text{s}^2} = 18545 \text{kN} \tag{6.5}$$

which corresponds well with the static axial force obtained in table 6.5.

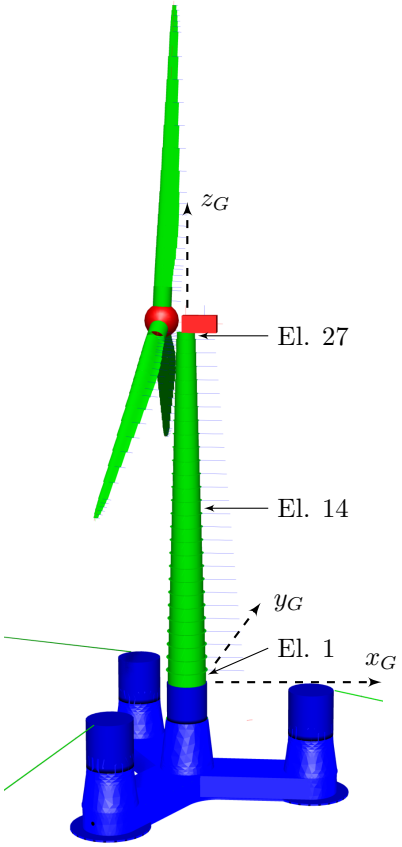

Figure 6.15. Graphical representation of the wind turbine tower from the SIMA model, including element numbering and the global coordinate system.

6.4.2 Simplified beam model of wind turbine tower

In order to verify the tower response results obtained from the RIFLEX modeled tower in SIMA, a simplified plane beam model of the tower is implemented in Matlab. The tower is composed of 27 tubular beam sections with different radii and wall thicknesses as described in table C.1. The mode shapes and natural frequencies of the simplified tower model are studied.

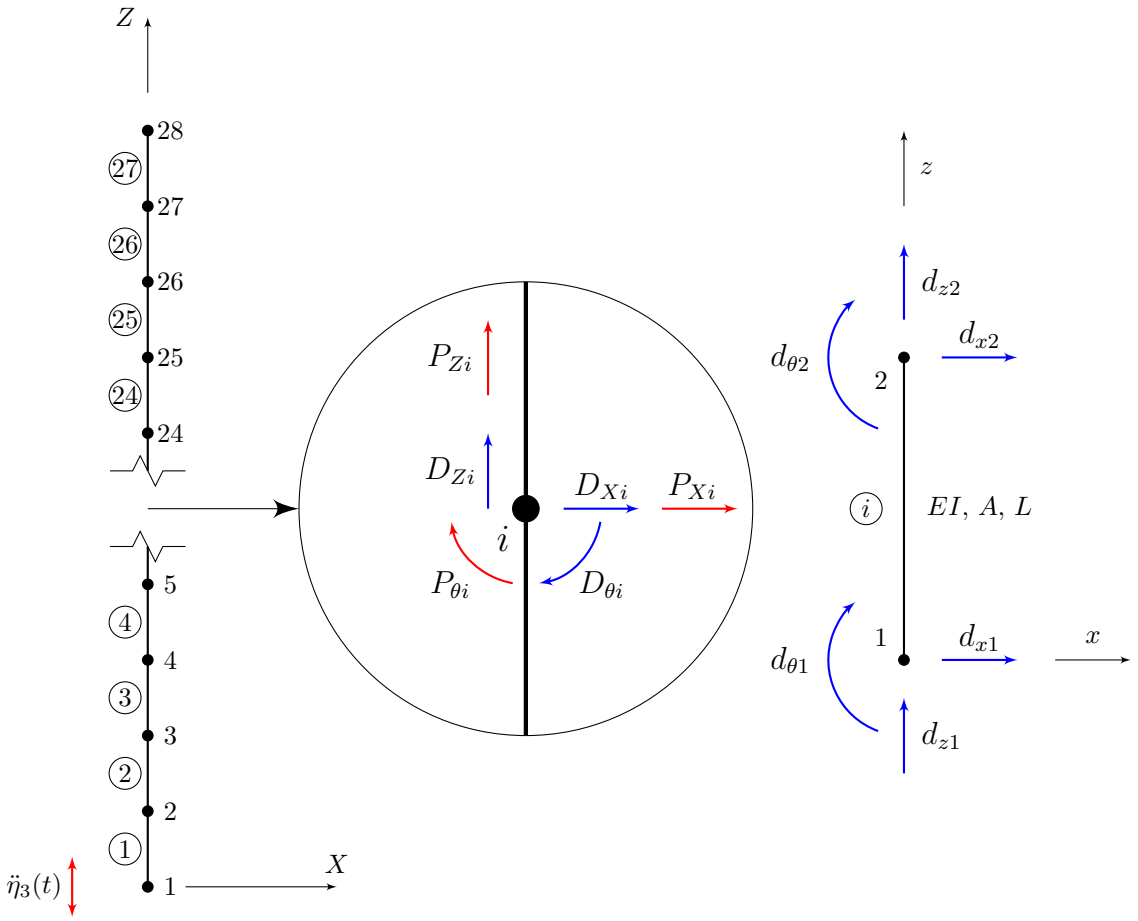

Figure 6.16. Illustration of simplified plane beam model.

Element stiffness- and mass matrices for each six dof beam element comprising the tower model are computed using eqs. (6.6) and (6.7).

$$\boldsymbol{k}^{(i)} = \begin{bmatrix} \frac{EA}{L} & 0 & 0 & -\frac{EA}{L} & 0 & 0 \\ 0 & \frac{12EI}{L^3} & \frac{6EI}{L^2} & 0 & -\frac{12EI}{L^3} & \frac{6EI}{L^2} \\ 0 & \frac{6EI}{L^2} & \frac{4EI}{L} & 0 & -\frac{6EI}{L^2} & \frac{2EI}{L} \\ -\frac{EA}{L} & 0 & 0 & \frac{EA}{L} & 0 & 0 \\ 0 & -\frac{12EI}{L^3} & -\frac{6EI}{L^2} & 0 & \frac{12EI}{L^3} & -\frac{6EI}{L^3} \\ 0 & \frac{6EI}{L^2} & \frac{2EI}{L} & 0 & -\frac{6EI}{L^2} & \frac{4EI}{L} \end{bmatrix} \tag{6.6}$$

$$\boldsymbol{m}^{(i)} = \frac{\rho AL}{420} \begin{bmatrix} 140 & 0 & 0 & 70 & 0 & 0 \\ 0 & 156 & 22L & 0 & 54 & -13L \\ 0 & 22L & 4L^2 & 0 & 13L & -3L^2 \\ 70 & 0 & 0 & 140 & 0 & 0 \\ 0 & 54 & 13L & 0 & 156 & -22L \\ 0 & -13L & -3L^2 & 0 & -22L & 4L^2 \end{bmatrix} \tag{6.7}$$

No transformation is performed on local element matrices. They are directly substituted into the global 84 by 84 stiffness- and mass matrices $\boldsymbol{K}$ and $\boldsymbol{M}$ as shown in eq. (6.8)

$$\boldsymbol{K} = \boldsymbol{K}^{①} + \boldsymbol{K}^{②} + \cdots + \boldsymbol{K}^{ⓘ} + \cdots + \boldsymbol{K}^{㉗} \qquad \text{where} \qquad \boldsymbol{K}^{ⓘ} = \begin{bmatrix} 0 & \cdots & 0 & \cdots & 0 \\ \vdots & \ddots & \vdots & \iddots & \vdots \\ 0 & \cdots & \boldsymbol{k}^{ⓘ} & \cdots & 0 \\ \vdots & \iddots & \vdots & \ddots & \vdots \\ 0 & \cdots & 0 & \cdots & 0 \end{bmatrix} \tag{6.8}$$

The tower description given in the LIFES50+ report (Yu et al., 2018) is used as reference for the investigation of the accuracy of the simplified beam model. In order to be able to compare the two models, the coefficient matrices $\boldsymbol{K}$ and $\boldsymbol{M}$ are altered to impose zero displacement and rotation at the bottom of the beam model as in the reference. The mass and the mass moment of inertia of the RNA are also added into the global mass matrix. The eigenvalue problem involving the altered matrices is then solved to obtain mode shapes and natural frequencies of the clamped tower. The natural frequencies obtained from the Matlab model are compared with the ones given in the reference report in table 6.6. The frequencies obtained with the simplified model correspond well with the reference values. This suggests that the RIFLEX model of the turbine tower behaves reasonably.

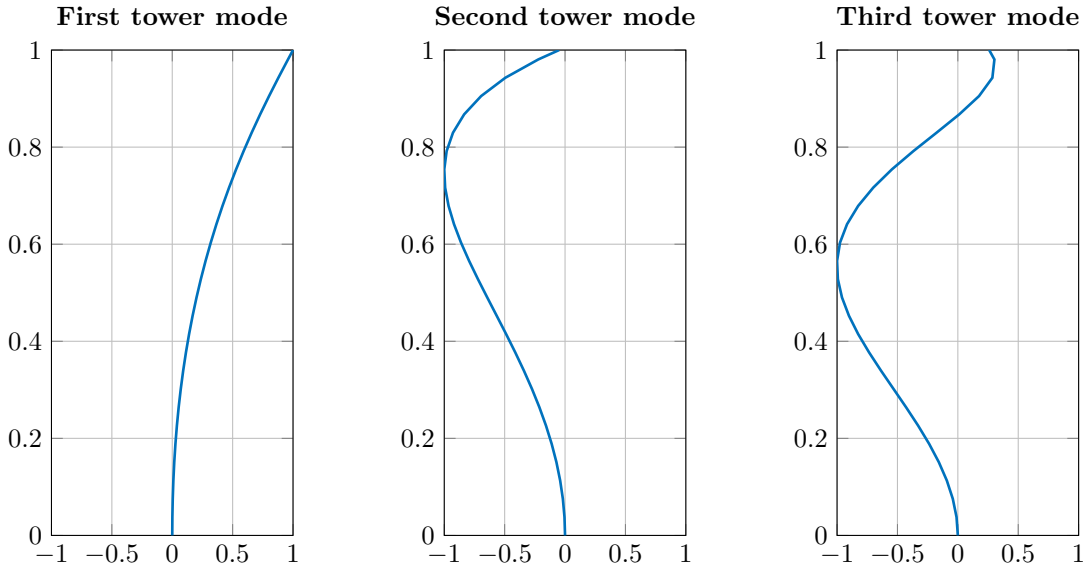

Figure 6.17. Clamped fore-aft tower mode shapes obtained from the simplified beam model. The mode shapes are calculated including RNA mass and RNA pitch moment of inertia.

Table 6.6: Comparison of tower fore-aft frequencies.

Mode	**Plane beam model** [Hz]	**LIFES50+ reference** [Hz]
First	0.5753	0.5529
Second	2.4204	2.4372
Third	5.5305	N.A.

6.5 Mooring tension during seaquake

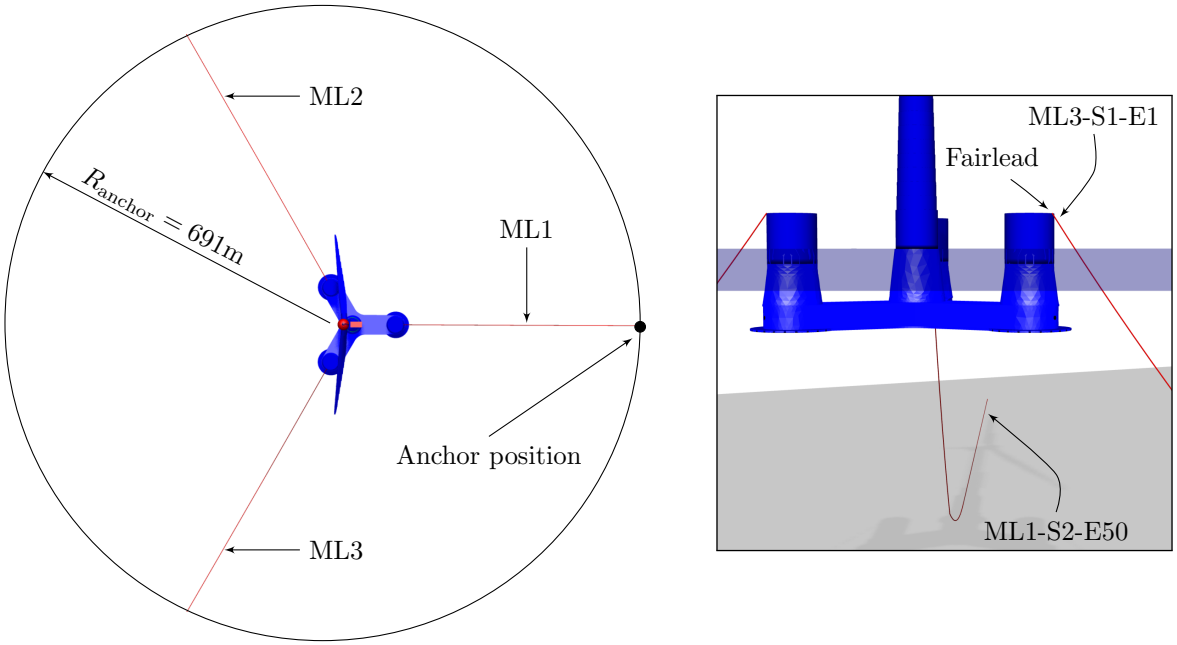

Figure 6.18. Configuration of the mooring system, with nomenclature for different parts, including mooring line (ML) element numbering.

In this section, the response of the mooring lines during seaquake excitation of the platform is studied. The mooring line elements are modelled as RIFLEX bar elements, only transferring loading between the platform and the anchor as tensile forces. As in previous sections, the response is studied in a calm environment without any wind or current acting on the FWT. The tension-time histories presented are gathered from the RIFLEX modelled mooring lines in SIMA. The numbering of the mooring line elements originates from the discretization in RIFLEX, where the line is divided into two segments. The first segment (S1) comprises the upper 160m of the lines, and is divided into 20 bar elements (E). The second segment (S2) comprises the remaining length of the line down to the anchor, and is divided into 50 elements. The force acting on the anchor is assumed to be equal to the tension in the mooring line element at the lower end of the mooring line. In reality, the force acting on the anchor would be reduced as the anchor line passes through a depth of soil before reaching the anchor. This reduction is referred to as soil-line interaction. The system is, as previously, given 200s of transient response before the seaquake loading is applied. When the seaquake loading is applied, the tensile forces in the mooring lines are approximately 1665kN and 971kN at the top and the bottom of the line, respectively. The initial tension can be seen in fig. 6.19, along with the tension in the six selected mooring line elements during seaquake pressure from the 2D acoustic model. Three of the elements are connected to the platform, one element for each anchor line. These elements experience the highest tension, with practically identical time histories. The higher tension in these elements is due to the large weight of the chain mooring lines. The tensile forces in the three remaining elements, which are all connected to the anchors, are also coinciding for all practical purposes.
As in section 6.2.4, different PVA's of the seabed are considered according to the scaling factors in table 6.2. The mooring tension for six PVA's are presented in fig. 6.20. The peak mooring tension for the same PVA's is presented in table 6.7. The MPM tension calculated from the environmental analyses in section 5.2 was based on tension in the mooring line element connected to the anchor. A comparison between the peak tensions in the mooring lines and the MPM is given in table 6.7. It is observed that even a seaquake resulting from a seabed PVA as large as 0.3g does not yield a peak mooring tension larger than the previously estimated MPM. The mooring tension during seaquake scaled to different seabed PVA's, presented in fig. 6.20, shows that for seabed PVA's of 0.15g and above, the tension falls to zero for a short time interval. The absence of tension in the mooring line may cause snap-tension once the line gets loaded.

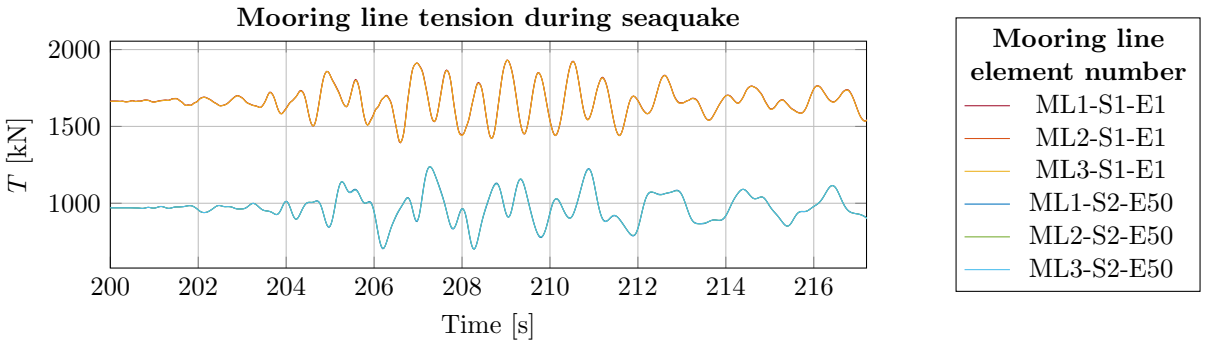

Figure 6.19. Mooring line tension, in selected ML elements, due to the platform response during the unscaled seaquake pressure from the 2D acoustic model. The element numbers are explained in fig. 6.18.

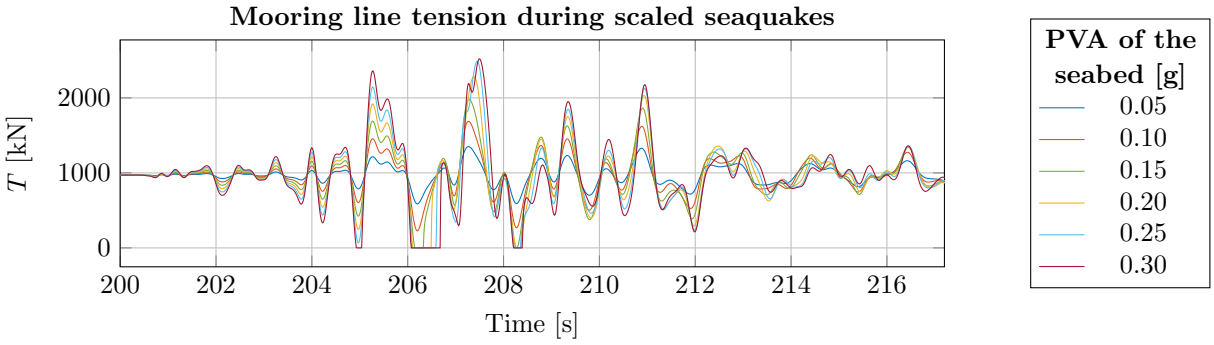

Figure 6.20. Tension in one of the mooring line elements connected to seabed during seaquake pressures scaled to correspond to different PVA's of the seabed. The tension is only due to the response of the platform.

Table 6.7: Peak mooring line tensile forces during seaquakes scaled to correspond to different seabed PVA's.

PVA of the seabed		**Peak mooring tension**		**Compared**
		At anchor	**At fairlead**	**to MPM**
[g]	$\left[\frac{\text{m}}{\text{s}^2}\right]$	[kN]	[kN]	[%]
0.0345	0.3381	1238	1932	18.4
0.0500	0.4905	1351	2043	20.0
0.1000	0.9810	1688	2368	25.0
0.1500	1.4715	1982	2666	29.4
0.2000	1.9620	2282	3040	33.8
0.2500	2.4525	2489	3161	36.9
0.3000	2.9430	2522	3302	37.4

6.6 Seaquake response during production

Previously, the seaquake response of the FWT was studied in a calm environment without any wind, current or wind waves acting on it. In this section, the seaquake response of the FWT while in production of electricity is studied. The wind and current are oriented along a direction parallel to one of the mooring lines, with the hub facing the wind. This situation is chosen because it yields a large mean tension in the windward mooring line. This is expected to be the worst situation for an FWT subjected to a seaquake, because the platform response will produce tension in the mooring line in addition to the large mean tension because of the wind- and current loading. Even though higher wind speeds were acting on the FWT during the extreme conditions in section 5.2, the mean mooring line tension was lower because the wind speed was above the cut-out limit. Hence, the rotor was set to the parked configuration. Since the heave response of the platform is expected to be similar to the ones for previous seaquake analyses, without wind and current, the response of the tower and the nacelle will not be considered in this section.

6.6.1 Initial transient response to wind and current

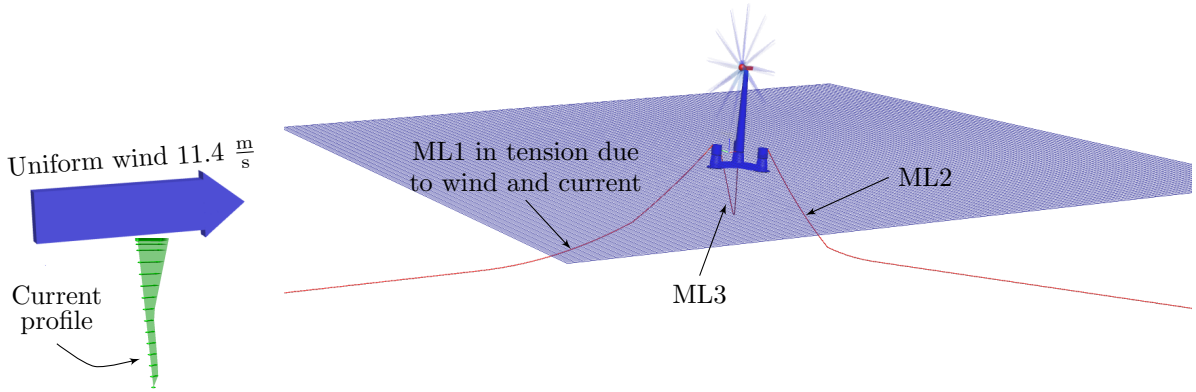

Figure 6.21. Configuration of the SIMA model during seaquake analyses while simultaneously generating electrical power from wind blowing parallel to one of the anchor lines.

The wind is set to be uniform in SIMA with a wind speed corresponding to the rated wind speed of the DTU 10 MW Reference Wind Turbine of 11.4m/s (Bak et al., 2013). No wind waves are acting on the platform during these analyses, which is a contradiction w.r.t. the wind conditions. However, adding wind waves in addition would make it hard to determine effects of a seaquake alone on a mooring line in tension. Current is introduced using the same profile shapes as in section 5.2, applying eq. (5.11) and eq. (5.12) with 1-year reference values of the wind- and tide induced current speed at the surface of 0.59m/s and 0.23m/s, respectively, gathered from the LIFES50+ D1.1 report (Gómez et al., 2018). The resulting profile is shown in fig. 6.22. Damping of the initial transient response is implemented in a similar way as in section 6.1, with damping coefficients somewhat adjusted to allow for the surge motion. The transient response of the platform due to wind and current, and the effect of the added damping, is shown in fig. 6.23. For the damped model, the platform stabilizes at a surge of about 19m and a pitch of around 4°, when subjected to wind and current.

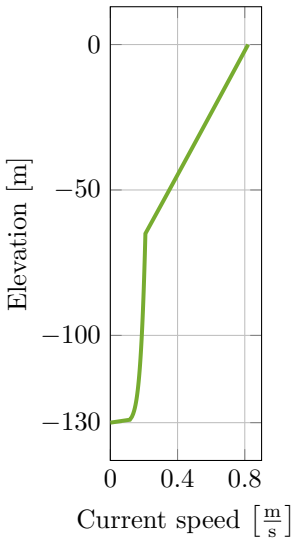

Figure 6.22. Current profile.

The surge motion of the platform tightens the windward mooring line, while the mooring lines on the leeward side experience reduced tension. The tension in the mooring lines during the transient response of the damped model, with wind and current applied to the FWT, is shown in fig. 6.24. The mooring line element connected to the seabed on the windward side of the FWT, referred to as ML1-S2-E50, stabilizes at a tension of about 2120kN compared to 971kN in 6.5. In the opposite end of the mooring line, in the bar element referred to as ML1-S1-E1, the tension stabilizes at approximately 2788kN compared to

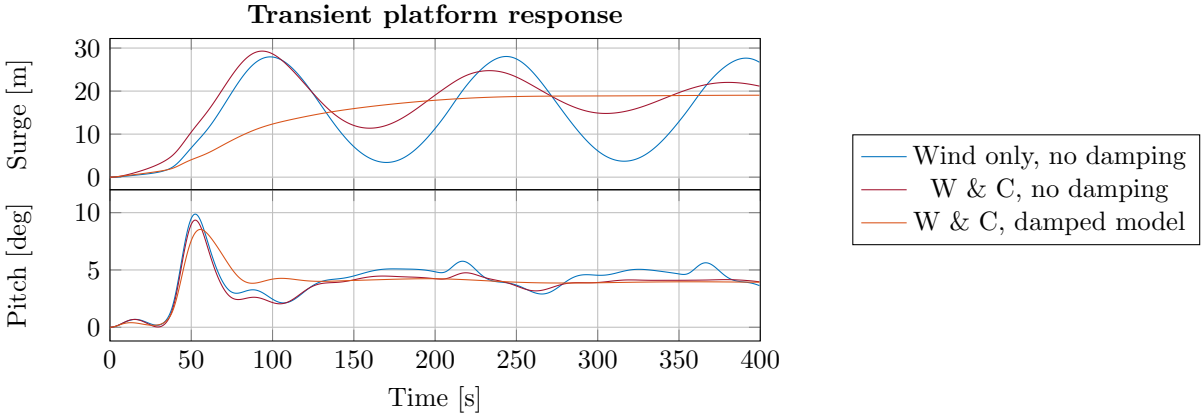

Figure 6.23. Transient surge- and pitch response of the platform due to uniform wind only, and to uniform wind (W) combined with current (C), with- and without added damping.

1665kN without any wind or current.

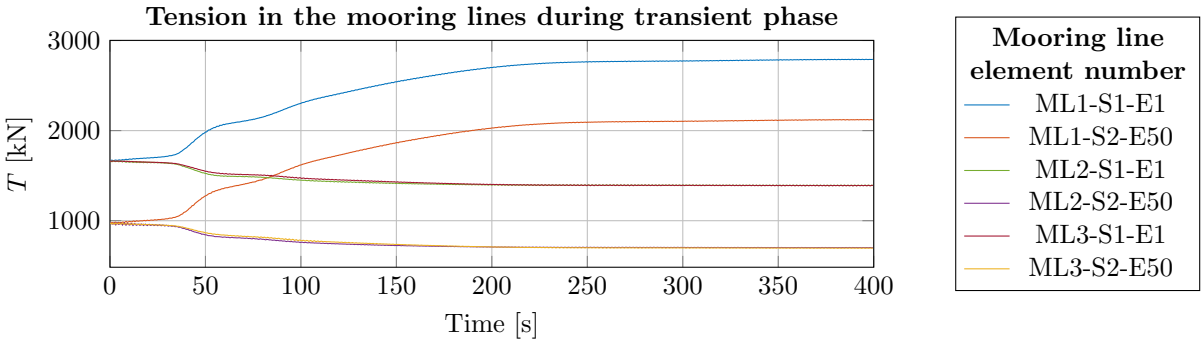

Figure 6.24. Mooring line tension, for the model with added damping, subjected to uniform wind and current.

6.6.2 Applying seaquake loading during wind and current

The seaquake loading is applied to the model with initial added damping after 400s of transient response, to give the FWT time to settle at the new position due to the uniform wind and current, with the windward mooring line in high tension. The seaquake pressure applied to the FWT is the one obtained from the 2D Abaqus acoustic model, as shown in fig. 6.7. The resulting tension in the windward mooring line when the FWT is subjected to wind, current and seaquake is presented in fig. 6.25. To study the effect of a more severe seaquake on the mooring line tension, the resulting seaquake pressure from the 2D Abaqus acoustic analysis is scaled to correspond to different PVA's of the seabed, as done in section 6.2.5. The individual scaled pressures are then applied to the platform in separate SIMA analyses in addition to wind and current. The peak mooring line tensions registered in the windward mooring line during the different scaled seaquakes are listed in table 6.8.

The MPM mooring tension from 5.2 was calculated based on the extreme value probability distribution of mooring tension at the anchor during environmental loads. Table 6.8 shows how the peak tension at the anchor during wind, current and seaquake compares to the environmental MPM tension. Scaling the seaquake to correspond to a seabed PVA of 0.3g yields a peak tension at 64.2% of the MPM, compared to 37.4% for the analysis without wind or current in section 6.5. A different effect of the combined seaquake-, current- and wind loading is the low tension levels obtained on the leeward side of the FWT. As shown in fig. 6.24, the tensile forces in the two mooring lines on the leeward side of the FWT stabilize at approximately 1400kN and 700kN, for the bar element at the top- and the bottom of the line, respectively, during the transient phase after applying wind and current. The seaquake response of the leeward lines is shown in fig. 6.26. Observing the tension in the mooring line during seaquake

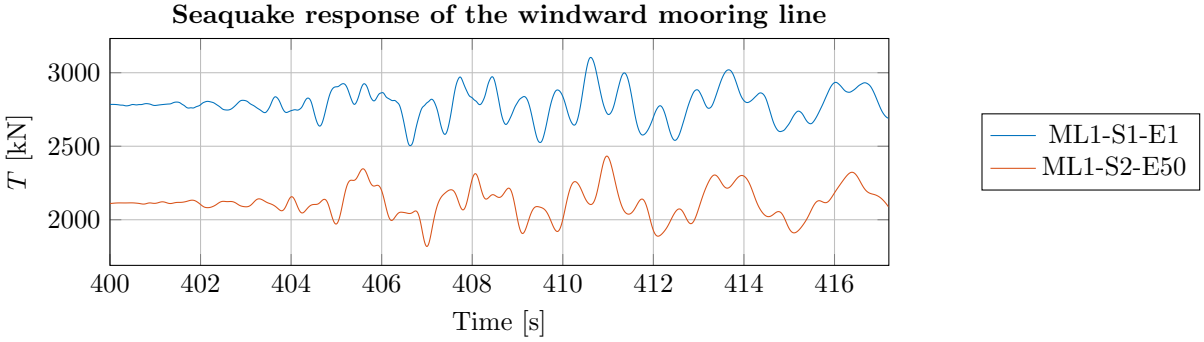

Figure 6.25. Tension at each end of the windward mooring line during combined uniform wind, current and seaquake loading from the unscaled 2D Abaqus acoustic pressure.

Table 6.8: Windward mooring line peak tension due to platform response, in addition to wind and current, following seaquake pressures scaled to correspond to different PGA's of the seabed. The peak tensions are compared with the MPM mooring tension of 6744kN, calculated in 5.2.

PVA [g]	**Peak mooring line tension** [kN]		**Compared to**
of the seabed	**At anchor**	**At fairlead**	**MPM**
Unscaled (0.0345)	2433	3104	36.1%
0.1	2974	3654	44.1%
0.2	3683	4370	54.6%
0.3	4328	5023	64.2%

pressures scaled to seabed PVA's of 0.2g and 0.3g, it is clearly shown that the leeward mooring lines experience slack (zero tension).

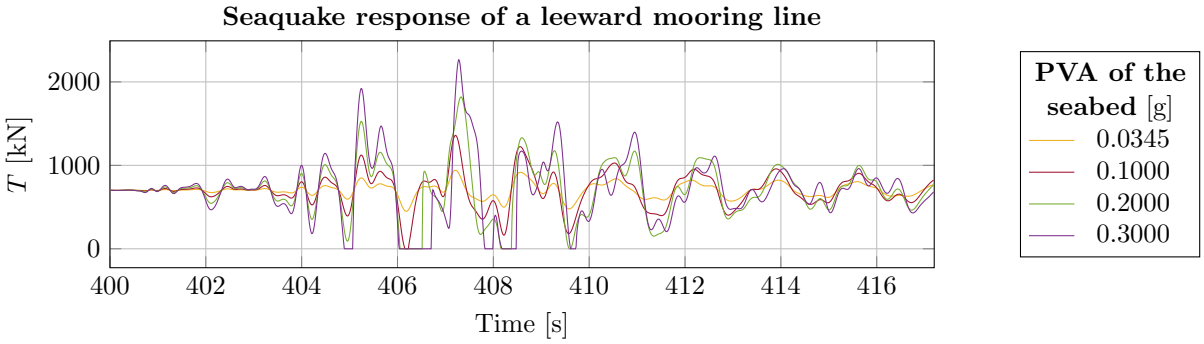

Figure 6.26. Tension in one of the two leeward mooring lines during seaquake, in addition to wind and current loading. The tension is sampled from the element connected to the anchor.

Chapter 7

Numerical model of soil and anchor

In this chapter, available modelling options for the soil and anchor, which will be implemented in the SSI analysis of an anchor design developed by OO, are studied. The natural frequencies and modes shapes for a homogeneous soil profile are determined for several types of solid elements. These results are then compared with theoretical natural frequencies in order to validate the different element types and numerical integration methods. Three options for the modelling of the anchor are considered. A model of a simply supported plate, with a uniformly distributed load, is assessed to verify the mid-span displacement against a theoretical solution derived from plate theory.

7.1 Soil model

The numerical model of the soil must be able to describe and predict the soil amplification related to propagation of shear waves through the different soil layers. Appropriate boundary conditions must be introduced and a sufficiently fine mesh must be employed. In this section, the chosen boundary conditions and FE meshes are validated against the theoretical transfer function, mode shapes and natural frequencies presented in 2.2.4.

7.1.1 Description of a basic soil model

A soil profile in free-field conditions (without the presence of a structure) excited by a horizontal ground motion at the bottom, causing shear waves propagating upwards through the layer, will behave like a shear-beam. All of the soil particles in the same plane will move horizontally together. This means that the distance between two nodes in the same horizontal plane will not change during the motion. An appropriate boundary condition able to reproduce the behaviour of a shear-beam must be chosen. A homogeneous soil profile is evaluated.

Geometry and material properties

The soil model has a width of L_x= 100m in the x-direction, a thickness of L_y= 1m in the y-direction and a depth of H= 60m in the z-direction, and is shown in fig. 7.1. The chosen material properties for the model are shown in table 7.1. These do not correspond to the properties given in 3.2. The relation between the shear wave velocity v_s, shear modulus G and Young's modulus E is given by

$$G = \frac{E}{2(1+\nu)} \qquad \text{and} \qquad v_{\mathrm{s}} = \sqrt{\frac{G}{\rho}} \tag{7.1}$$

Rayleigh damping is used to include damping, where the first and fifth theoretical natural frequencies are used to determine the Rayleigh coefficients α and β. The theoretical natural frequencies are shown in table 7.2. A damping coefficient of $\xi = 5\%$, which is a typical damping value used for soil, is assigned to the first and fifth modes. The resulting Rayleigh coefficients are $\alpha = 0.7069$ and $\beta = 0.0013$

Table 7.1: Material properties of the basic soil model.

E [MPa]	ν [ ]	G [MPa]	ρ [kg/m^3]	v_{s} [m/s]
457.47	0.495	153	1700	300

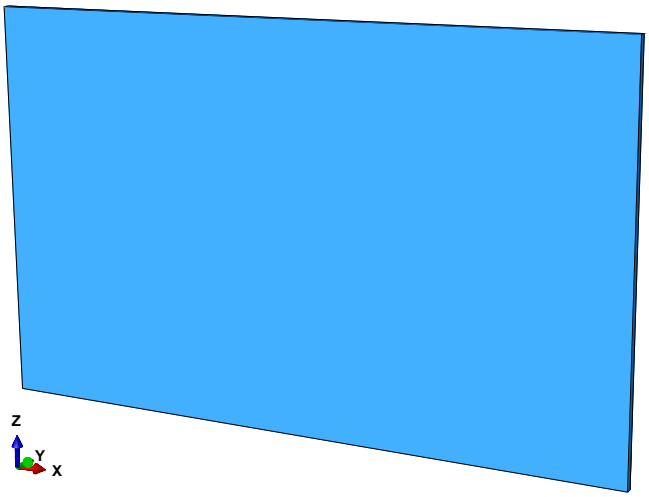

Figure 7.1. The soil profile considered for the validation of the modelling options, along with its coordinate system.

Table 7.2: The first five theoretical natural frequencies of the considered homogeneous soil profile.

Mode number	**Theoretical natural frequency** [Hz]
1	1.25
2	3.75
3	6.25
4	8.75
5	11.25

Boundary conditions and constraints

The model is excited in the x-direction at the bottom of the soil profile. Pinned supports are introduced at the bottom and along the vertical surfaces parallel to the x-direction, to prevent any displacement in the y- or z-direction such that the soil model will deform similarly to a shear-beam. The two vertical surfaces parallel with the y-direction at the two ends of the model, along the x-direction, are constrained using a tie-constraint. This type of constraint ensures that the translational DOFs of two constrained nodes are equal at all times during the simulation (Dassault Systèmes Simulia Corp., 2014). The nodes located in the same horizontal plane will then have the same translation which corresponds with the way a shear-beam deforms. An illustration of the applied tie-constraint is shown in fig. 7.2.

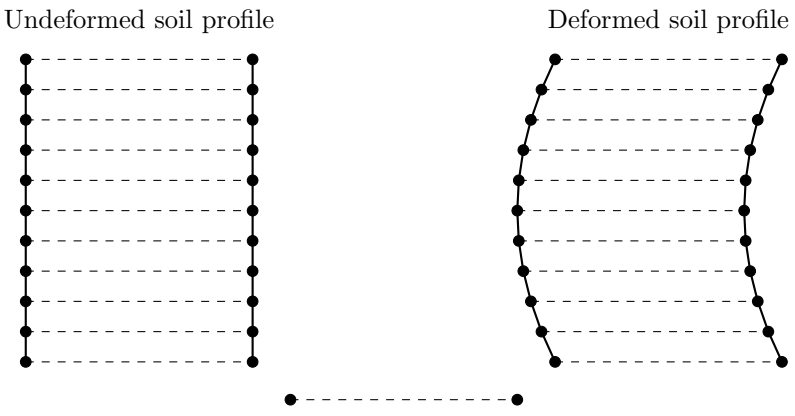

Figure 7.2. An illustration of the applied tie constraints.

Element type and mesh size

The response of the FE model is affected by the mesh discretization. High-frequency modes have shorter wavelengths than lower order modes, and the mesh must be fine enough to not filter out these modes. Therefore, the maximum dimension of any element in the soil model should be limited to 1/8 of the shortest wavelength considered (Kramer, 1996, p.283). An upper limit of 1/10 of the shortest wavelength is chosen for the basic model.

$$\lambda_{\min} = \frac{v_s}{f_{\max}} \qquad \Longrightarrow \qquad L_{e,\max} = \frac{\lambda_{\min}}{10} \tag{7.2}$$

where $f_{\max}$ is the highest frequency from the acceleration input, and L_e is the characteristic element length, i.e. the shortest distance between two nodes within an element. The maximum frequency in the considered horizontal acceleration input is roughly $f_{\max} = 6\text{Hz}$ (see 3.3). The shear wave velocity determines the smallest wavelength and the corresponding maximum characteristic element length.

$$\lambda_{\min} = \frac{300\text{m/s}}{6\text{Hz}} = 50\text{m} \qquad \text{and} \qquad L_{e,\max} = \frac{30\text{m}}{10} = 5\text{m} \tag{7.3}$$

Four meshes with solid elements are considered for the homogeneous soil model. More specifically, two meshes consisting of brick elements of linear and quadratic order, and two meshes consisting of tetrahedrons of linear and quadratic order, are investigated. The mesh size for the quadratic elements can be increased since L_e will correspond to half of the length of an element side. For a second-order element, the minimum distance between an end- and a middle-node, which is half of the side length, will be the characteristic element length.

Table 7.3: Element size for the different considered meshes.

Element type	**Element size** [m]
Linear brick (C3D8R)	1
Quadratic brick (C3D20R)	4
Linear tetrahedron (C3D4)	1
Quadratic tetrahedron (C3D10)	4

7.1.2 Natural frequencies and mode shapes

The first five mode shapes of the soil layer are shown in fig. 7.3. The natural frequencies obtained from the four meshes are compared with the theoretical frequencies in table 7.4 and table 7.5.

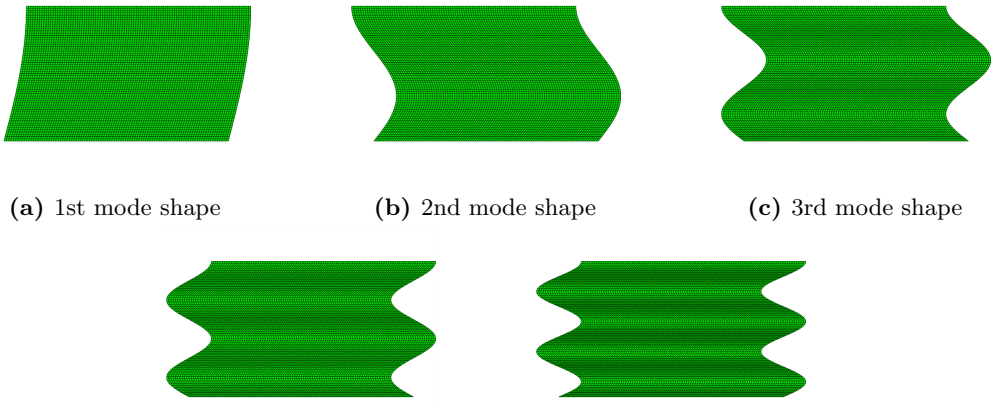

(a) 1st mode shape **(b)** 2nd mode shape **(c)** 3rd mode shape

(d) 4th mode shape **(e)** 5th mode shape

Figure 7.3. The five first mode shapes of the homogeneous soil layer.

Table 7.4: Theoretical and numerical natural frequencies of soil layer using linear (C3D8R) and quadratic (C3D20R) brick elements.

Mode	**Theoretical** [Hz]	**Numerical (brick)**[Hz]		**Error**[%]	
		Linear	Quadratic	Linear	Quadratic
1	1.25	1.25	1.2492	0.0	0.064
2	3.75	3.749	3.7476	0.027	0.064
3	6.25	6.2455	6.2463	0.072	0.059
4	8.75	8.7378	8.7461	0.139	0.045
5	11.25	11.224	11.249	0.231	0.89

Table 7.5: Theoretical and numerical natural frequencies of soil layer using linear (C3D4) and quadratic (C3D10) tetrahedron elements.

Mode	**Theoretical** [Hz]	**Numerical (tetrahedron)**[Hz]		**Error**[%]	
		Linear	Quadratic	Linear	Quadratic
1	1.25	1.2501	1.2490	0.008	0.08
2	3.75	3.7519	3.7471	0.051	0.077
3	6.25	6.2589	6.2454	0.142	0.074
4	8.75	8.7746	8.7453	0.28	0.054
5	11.25	11.304	11.248	0.48	0.018

Generally, it is expected that the solution from an FE analysis will be stiffer than the theoretical/exact solution. As the mesh size is made smaller and smaller, the FE solution should converge. Convergence can also be achieved by using elements with a higher order of interpolation. One drawback of using linear brick and tetrahedron elements is that they cannot represent bending exactly. When subjected to bending, these elements will be too stiff. To overcome this for brick elements, reduced integration can be used. This will soften the behaviour of the element, which results in a lower stiffness of the FE mesh.

By considering the natural frequencies obtained with the two quadratic elements, it seems that the FE results are less stiff than the theoretical solution. A lower stiffness results in lower natural frequencies. This goes against the previously described behaviour of an FE analysis. A possible explanation could be the material parameters specified in Abaqus. More specifically, the Poisson's ratio exceeds 0.48, which could cause potential issues for convergence (Dassault Systèmes Simulia Corp., 2014). The linear elements yield larger frequencies than the quadratic ones for most of the modes. This is due to the effects of shear locking causing a stiffer behaviour for the linear tetrahedrons. When considering the uncertainties due to the chosen Poisson's ratio, this result is as expected. For the linear bricks, the frequencies for some of the modes are lower than the corresponding frequencies for the second order elements. This is most likely due to the softening effect of reduced integration.

The effect of reduced integration for linear brick elements can be considered more closely. The first natural frequency of the soil layer is determined for different element sizes. The results are shown in table 7.6.

Table 7.6: Natural frequency for the 1st mode for different mesh sizes using linear brick elements with reduced integration (C3D8R).

Element size [m]	**Frequency** [Hz]
4	1.2494
2	1.2499
1	1.2500
0.5	1.2469

The convergence of the C3D8R elements does not seem consistent with the theoretical convergence of FE analyses. There could be two possible reasons for this. The first reason is the softening from reduced integration being larger for larger elements than for smaller elements. When the mesh becomes fine enough, the frequency seems to convergence towards a similar value as for the quadratic elements. The second cause could be the previously explained convergence issues which can occur when using a Poisson's ratio larger than 0.48 without employing hybrid elements.

Even though the numerical model does not seem to exactly replicate the lower order theoretical natural frequencies, the results are still good enough and sufficiently accurate for the purpose of analyzing SSI in this thesis. If linear elements are used, a sufficiently small element size must be chosen to obtain results with sufficient accuracy. Larger quadratic elements can also be used to produce results with similar accuracy.

7.1.3 Numerical soil amplification

The numerical soil amplification for six frequency values are considered. The soil amplification refers to the amplification of displacements at the bottom of the domain when shear waves propagate vertically through the soil. The numerical amplification is the soil amplification given by the numerical FE model. A sinusoidal displacement with a unit amplitude (=1m), with six different frequencies, is introduced at the bottom of the soil profile, along the x-direction. The following frequencies are considered: 1.25Hz, 2.5Hz, 3.75Hz, 5Hz, 6.25Hz and 7.5Hz. Linear and quadratic solid elements are used to calculate the soil amplifications from the FE model. These are compared with the theoretical amplifications in 2.2.4. The damping of the theoretical results is modified to correspond with the Rayleigh damping properties, which have been described previously. The theoretical and numerical soil amplifications are shown in fig. 7.4. Small linear and larger quadratic elements seem to yield results with similar accuracy, which corresponds with the results from table 7.4. For larger frequencies, the numerical amplifications deviate more from the theoretical values than for lower frequencies. This is expected since the natural frequencies for higher order modes are more difficult to predict accurately than for lower order modes. The amplification,

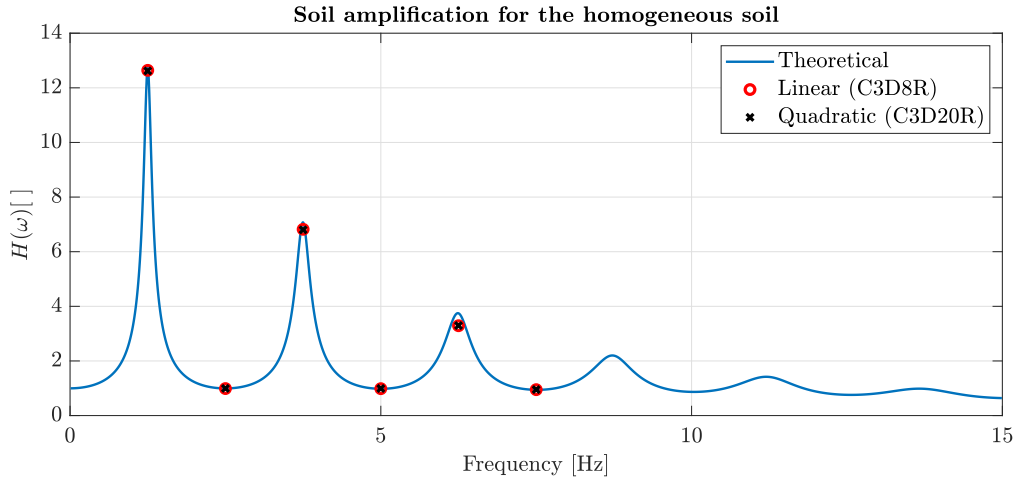

Figure 7.4. Theoretical and numerical soil amplifications for the homogeneous soil model. The numerical results are obtained from implicit time domain analysis using linear (C3D8R) and quadratic (C3D20R) brick elements.

using linear elements, for two frequencies (1.25 Hz and 2.5 Hz) is shown in fig. 7.5. As a sinusoidal unit-displacement is introduced at the bottom, the soil amplification will correspond to the displacement at the top of the soil profile.
In order to verify if the correct damping is included in the model, the damping ratio can be estimated by considering the two amplification plots in fig. 7.5. The logarithmic decrement can then be used to estimate the damping ratio. The two ratio estimates are shown in table 7.7. There are uncertainties related to the employed method for damping estimation, but the magnitude of the estimates seems to indicate that the damping is correctly represented in the basic numerical model.
The numerical results are close to the theoretical ones. As in 7.1.2, the results are sufficiently accurate for the intended purpose in this thesis. Both linear and quadratic elements can be used to produce adequate

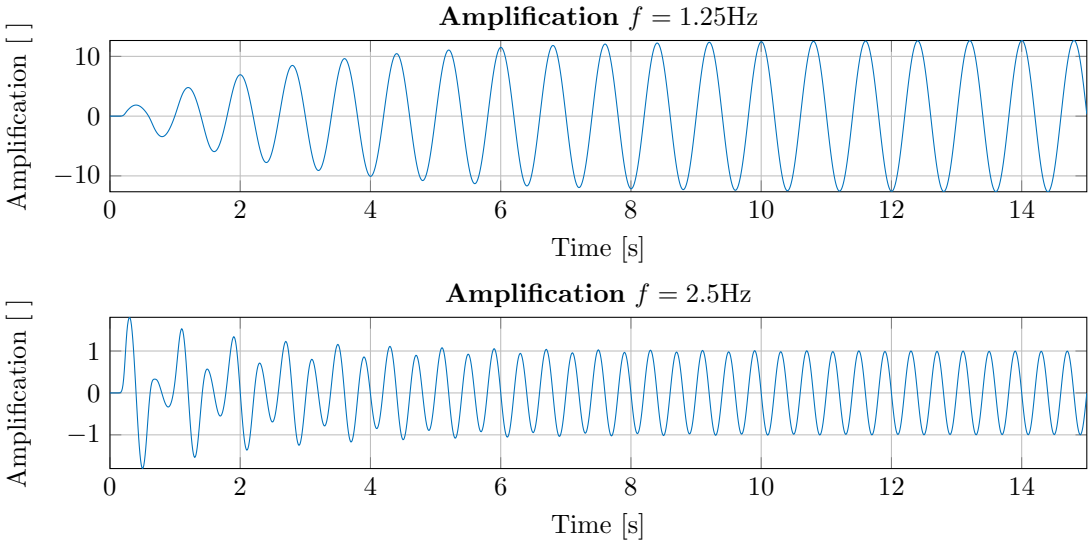

Figure 7.5. Soil amplifications with linear elements (C3D8R) from a time domain analysis using an implicit method. The applied frequencies are 1.25 Hz (1st natural frequency, top) and 2.5 Hz (bottom).

Table 7.7: Damping ratios from Rayleigh damping and logarithmic decrement estimates.

Frequency [Hz]	**Ratio from Rayleigh damping**	**Estimated ratio**
1.25	0.05	0.051
2.5	0.033	0.031

results. For an explicit integration method, the critical time step could lead to large computational efforts. For the considered material properties and an element size of for instance 1m, the critical time step from Abaqus is in the order of 10^{-6}s. As element sizes for the SSI model could be smaller than for the homogeneous soil model, especially the soil elements around the anchor, the critical time step will be too small and a very large number of time steps will be necessary. The acceleration input which will be considered in this thesis has a duration of around 17s. With a critical time of step of 10^{-6}s, the required number of steps would be equal to 17 million. This would result in an immense computational effort. Therefore, an implicit method is chosen as the basis for the simulations in the more complex SSI model. This allows for a larger time step and subsequently a smaller computational effort.

7.2 Anchor model

There are several options for the modelling of the anchor in the soil for the SSI analysis. The anchor can be modelled using solid or shell elements with contact interactions introduced between the solid soil elements and the anchor elements. Alternatively, the anchor can be modelled using skins. Skin elements are shell elements which use the same nodes as the surface these are attached to (Dassault Systèmes Simulia Corp., 2014). If skins are used, the potential issues w.r.t. modelling of contact between the soil and the anchor can be avoided. The three element types are studied and the corresponding solutions for the deflection at the middle of a simply supported plate are compared with the theoretical solution from plate theory.

7.2.1 Description of a basic plate model

In order to investigate the available modelling options for the anchor plates, the mid-span displacement for a quadratic simply supported plate with an evenly distributed load is studied using an FE model in Abaqus. The results of the simulations can be compared with a theoretical solution for the displacement obtained from plate theory (see A.3). An illustration of the plate, material and geometrical properties, the loading and boundary conditions is shown in fig. 7.6.

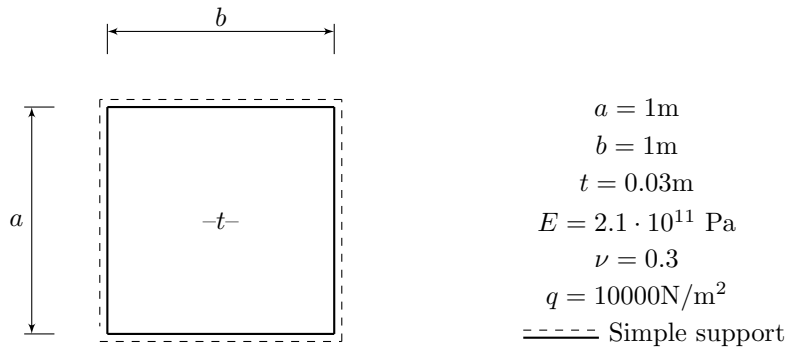

Figure 7.6. Material properties, geometry, boundary- and loading conditions of the considered simple plate.

The soil regions around the anchor in the SSI model will most likely need to be modelled using tetrahedron elements, since the anchor has sharp corners which make it difficult to use a structured mesh with brick elements. Therefore, the considered meshes for this simple plate model will use solid tetrahedrons or triangular shell elements. Both linear and second order elements are considered for this sensitivity analysis.

Bending cannot be represented correctly when using linear solid elements. It is necessary to have multiple linear elements over the thickness of the plate, in order to get acceptable results. Three elements over the plate are used for the linear solid elements. Elements with equal length for all sides should be used to limit the effect of shear locking. For second order solid elements, bending can be represented exactly. It is therefore not necessary to have many elements over the thickness for second order tetrahedrons. One element is therefore used over the plate thickness.

Shear locking does not occur for shell elements as transverse shear is included in their element formulation. Only one shell element can be used over the plate thickness. Membrane locking can be a potential issue for shell elements, especially for very thin shells . This can cause the model to become too stiff.

A model consisting of only a skin is not possible to establish as a skin must be attached to a part or surface in Abaqus. Therefore, a model consisting of a planar shell with $t = 0.01\text{m}$ using triangular shell elements, and a skin with $t = 0.02\text{m}$ using corresponding triangular shell elements, is established to verify the behaviour of skins. The chosen element types and sizes are shown in table 7.8.

Table 7.8: Element type and size for the simple plate model.

Designation	**Element type**	**Size** [m]	**Additional info.**
Solid, linear	C3D4	0.01	3 elements over thickness
Solid, quadratic	C3D10	0.03	1 element over thickness
Shell, linear	S3R	0.03	1 element over thickness
Shell, quadratic	STRI65	0.05	1 element over thickness
Skin, linear	S3R	0.03	1 element over each thickness
Skin, quadratic	STRI65	0.05	1 element over each thickness

7.2.2 Results

The results of the FE simulations are shown in table 7.9. These are compared with a theoretical solution. The theoretical value for the displacement in the middle of the plate is approximately $7.82 \cdot 10^{-5}$m.

Table 7.9: Results for the simple plate model compared with a theoretical displacement.

Designation	**Displacement** [m]
Theoretical	$7.82 \cdot 10^{-5}$
Solid, linear	$2 \cdot 10^{-5}$
Solid, quadratic	$2.47 \cdot 10^{-5}$
Shell, linear	$7.95 \cdot 10^{-5}$
Shell, quadratic	$8.01 \cdot 10^{-5}$
Skin, linear	$9.41 \cdot 10^{-5}$
Skin, quadratic	$9.52 \cdot 10^{-5}$

The shell elements yield good results w.r.t. the theoretical value. The solid elements give a very small displacement. This is due to shear and volume locking. Bending strains become too small due to these effects. The behaviour of the skin models is a little softer than the ones of the equivalent shell models. The cause of this is uncertain but the accuracy of the results is still good w.r.t. the theoretical displacement. Both linear and quadratic shell elements can be used in the SSI model to produce results with sufficient accuracy.

One additional benefit of using skins is that shell elements have less DOFs than solid elements, which reduces the required computational time of an analysis. Imposing constraints, to model the contact between the anchor and the surrounding soil, is expected to lead to a larger computational time than using skins would. Generally, contact can be challenging to represent correctly in an FE model. Therefore, skins will be employed in the SSI model. One possible drawback of this method is that the skin (anchor) will be attached to the soil, which could result in the total stiffness being too large. More specifically, it would not allow for sliding or the occurrence of gaps between the anchor and the soil.

Chapter 8

SSI analysis of the anchor

This chapter presents the soil model used for the SSI analysis and the fully integrated SSI model itself. Appropriate thicknesses for the components of the anchor are determined. The results from the SSI analyses, using both elastic and plastic material properties, are presented.

8.1 Soil model

8.1.1 Geometrical and material properties

The material properties of the soil profile are shown in table 8.1. The soil profile consists of clay with a linearly varying undrained shear strength s_u with the depth H. The values indicated in the table are the limits at the top and bottom of the profile, respectively. The shear modulus G, of the soil, can be determined by the following formula, where G and s_u have the same unit (Andersen, 2015).

$$G = 1000 \cdot s_{\mathrm{u}} \tag{8.1}$$

Table 8.1: Material properties of the soil profile for the SSI-analysis.

ρ [kg/m^3]	H [m]	ν [ ]	s_{u} [kPa]	G [kPa]
1700	55	0.495	2-84.5	2000-84500

The Young's modulus can be determined using the following expression:

$$E = 2(1 + \nu) \cdot G \tag{8.2}$$

As a material with a varying Young's modulus cannot be introduced in Abaqus, the soil profile must be discretized into several layers with different constant shear and Young's moduli. Two discretizations will be considered for the soil profile. More specifically, one fine and one coarse discretization will be studied. It is desirable that the soil stiffness around the anchor is represented accurately. Therefore, smaller soil layers should be considered here than for the remaining soil under the structure. The two soil discretizations are shown in fig. 8.1.
For each soil layer in both models, the average between the Young's modulus at the top and bottom of the given layer is used. The same applies for the shear modulus. The average shear wave velocity of each layer is determined from the average G.

$$v_{\mathrm{s}} = \sqrt{\frac{G}{\rho}} \tag{8.3}$$

The minimum wavelength of the shear waves depends on the shear wave velocity and the maximum frequency of the earthquake acceleration. The maximum frequency, $f_{\max}$, from 3.3 is equal to 6Hz. For the homogeneous soil model in 7.1, the limit of the maximum element size was set to 1/10 of the smallest considered wavelength. In order to avoid very small elements, resulting in a considerable computational effort, a larger upper limit for the element size is used for the SSI model. The characteristic size of the elements for the FE analysis should not exceed 1/5 of the smallest wavelength (Kramer, 1996, Ch.7.3).

$$\lambda_{\min} = \frac{v_{\mathrm{s}}}{f_{\max}} \quad \text{and} \quad L_{\mathrm{e,max}} = \frac{\lambda_{\min}}{5} \tag{8.4}$$

The material properties for the layers in both discretizations are shown in C.3. The error due to locking is reduced when elements with equal side lengths are used. Therefore, for the fine soil discretization a

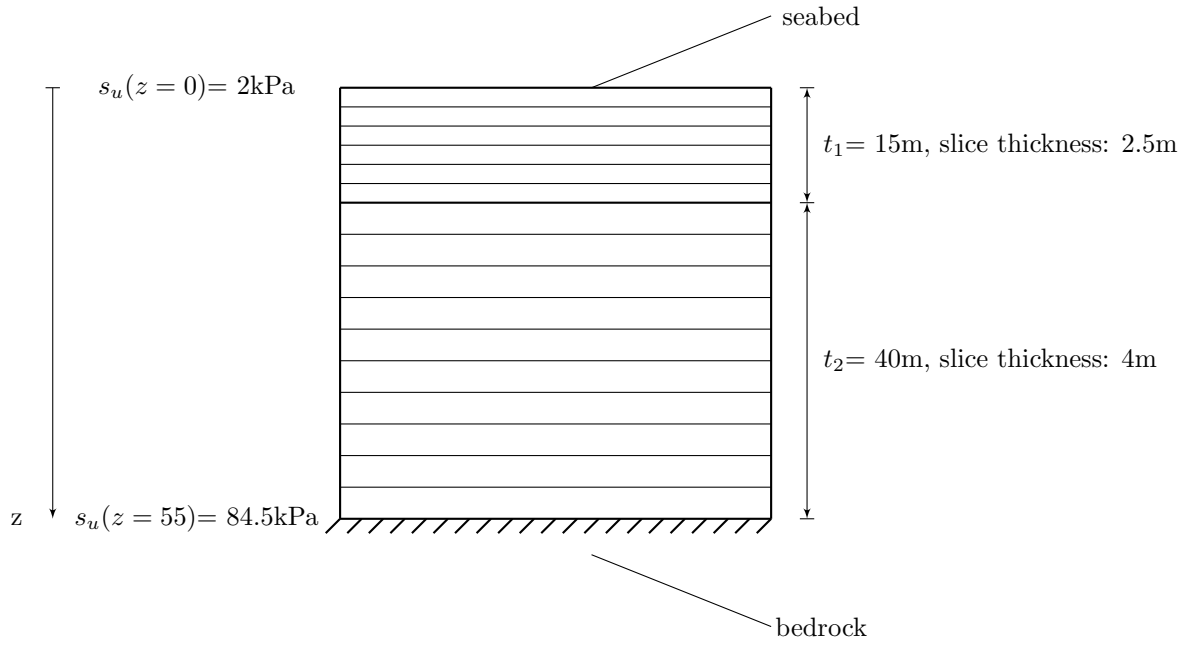

(a) Coarse soil discretization

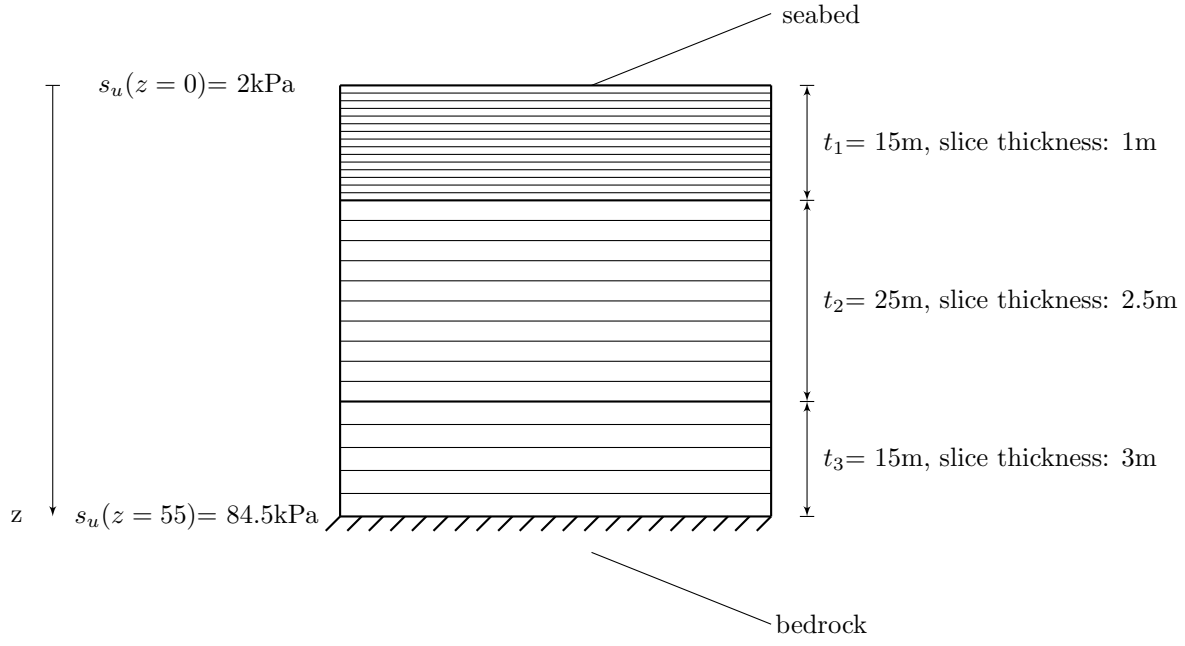

(b) Fine soil discretization

Figure 8.1. Coarse and fine discretization with the corresponding slice thicknesses.

width of 30m is used, and for the coarse one a width of 40m is used. These widths are chosen based on the element sizes in tables 8.2 and 8.3. The width should not affect the natural frequencies. Only the height of the model is important. The thickness of each model is 1m.

8.1.2 Element and mesh properties

Fine soil discretization

A summary of the element- and mesh properties for the fine soil discretization is shown in table 8.2.

Table 8.2: Mesh properties for the fine soil discretization.

Depth [m]	**Element type**	**Element size** [m]
0-15	C3D10	1
15-40	C3D10	1.25
40-55	C3D10	1.5

Coarse soil discretization

A summary of the element and mesh properties for the coarse soil discretization is shown in table 8.3. Two meshes are considered.

Table 8.3: Mesh properties for the coarse soil discretization.

Depth [m]	**Element type**	**Size (coarse mesh)** [m]	**Size (fine mesh)** [m]
0-15	C3D10	2.5	1.25
15-55	C3D10	4	2

8.1.3 Mode shapes and natural frequencies

Fine soil discretization

The first six mode shapes of the soil profile are shown in fig. 8.2. The corresponding natural frequencies are presented in table 8.4.

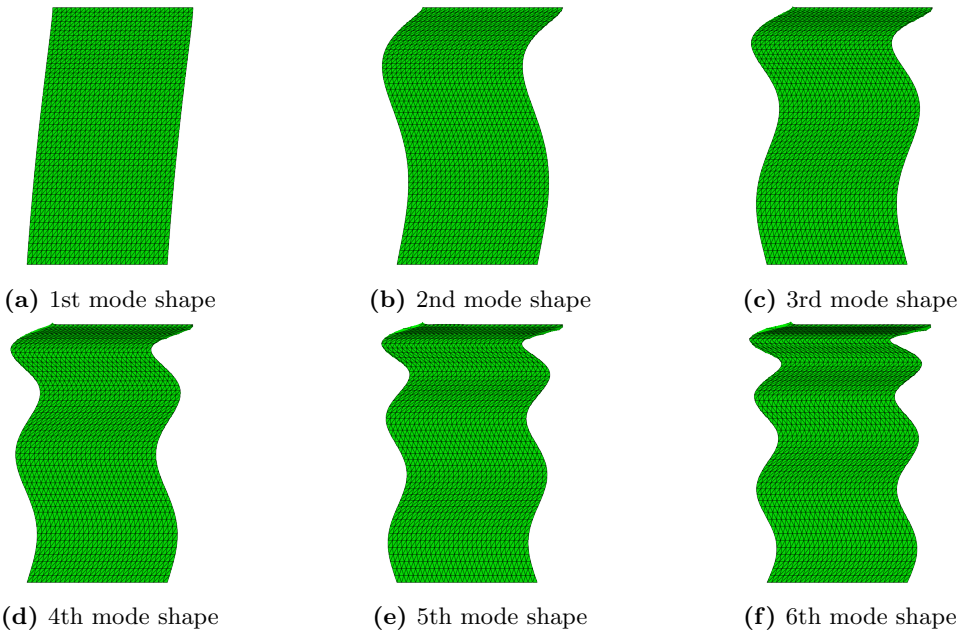

(a) 1st mode shape **(b)** 2nd mode shape **(c)** 3rd mode shape

(d) 4th mode shape **(e)** 5th mode shape **(f)** 6th mode shape

Figure 8.2. Mode shapes for the considered soil profile.

Coarse soil discretization

The natural frequencies for the fine and coarse meshes using the coarse soil discretization are shown in table 8.5.
There is not much difference between the natural frequencies in tables 8.4 and 8.5. This confirms the independence of the natural frequencies w.r.t. the width of the soil profile. It also suggest that the coarse soil discretization can be used for the SSI model without affecting the accuracy of the natural

Table 8.4: Natural frequencies of the soil profile using the fine soil discretization.

Mode number	**Frequency** [Hz]
1	0.78
2	2.99
3	4.13
4	5.28
5	6.44
6	7.59

Table 8.5: Natural frequencies of the soil profile using the coarse soil discretization.

Mode number	**Frequency (coarse mesh)** [Hz]	**Frequency (fine mesh)** [Hz]
1	0.78	0.78
2	2.97	2.97
3	4.10	4.09
4	5.26	5.25
5	6.41	6.39
6	7.56	7.52

frequencies too much. The maximum element size in Abaqus will be limited by the thickness of each soil layer. Using the coarse soil discretization will allow for larger elements for the layers beneath the anchor, where larger elements should be used to limit the total number of elements. The computational effort for solid elements is in general large, due to the large number of DOFs. Therefore, the number of elements should be limited as much as possible. By assessing the results in table 8.5, it is observed that using a fine mesh does not yield more accurate results w.r.t. convergence than a coarse mesh does. A coarse mesh can then be used for the SSI model to reduce the number of elements and the required computational time.

8.1.4 Damping properties

Rayleigh damping is used to include damping in the SSI model. By considering the frequency content from the Fourier amplitudes in 3.3, the majority of the frequency content of the earthquake accelerations is between 0 and 5Hz. Furthermore, strong motion accelerations with a shortened duration are considered, which could lead to a narrower range for the frequency content (i.e a smaller upper limit). Therefore, a damping ratio of 5% is assigned to the first and third mode. Assigning 5 % damping to the first mode will provide sufficient damping for the two first modes. 5 % damping for the third mode will result in a damping larger than 5 % for the fourth and higher order modes. By assigning the damping to the first and third mode, for the majority of the frequency content of the signal, the intended damping value will be used. In order to determine the correct coefficients for the Abaqus simulations, the frequencies must be in rad/s. The resulting Rayleigh damping coefficients, using the natural frequencies for the coarse soil discretization with a coarse mesh, are equal to:

$$\alpha = \xi \frac{2\omega_1\omega_3}{\omega_1 + \omega_3} = 0.05 \cdot \frac{2 \cdot 0.78 \cdot 4.10 \cdot (2\pi)^2}{(0.78 + 4.10) \cdot 2\pi} = 0.4118 \tag{8.5}$$

$$\beta = \xi \frac{2}{\omega_1 + \omega_3} = 0.05 \cdot \frac{2}{(0.78 + 4.10) \cdot 2\pi} = 0.0033 \tag{8.6}$$

These coefficients are included for each soil layer in the SSI model.

8.2 Anchor design

8.2.1 Design philosophy

The geometry of the OO-Anchor has not yet been determined by OO. Some of the geometry of the structure must therefore be determined in order to conduct the SSI analysis presented in this chapter. As the intention of this thesis is to assess the general effect of an earthquake on the floater and the anchor, the work related to the design of the anchor will be limited to the required geometrical properties such as plate thicknesses and some of the geometry of the connection between the anchor and the mooring line. An illustration of the anchor is shown in fig. 8.3. A mooring line is attached to the anchor at the padeye through the use of a shackle. Some initial general measurements, such as the heights and widths of the different plates, are chosen as a basis for the calculations. These are indicated in fig. 8.4 and will not be modified throughout the analyses. Further work should be carried out to evaluate different geometrical configurations for the anchor, and to assess the remaining structural components of the structure in detail. Structural details such as welds or stiffeners will not be considered in this thesis, but it is important to consider these for design purposes. Including stiffeners inside the anchor would be beneficial and could reduce the required thickness of the hollow triangular part. Fatigue will not be considered either, but such mechanisms could be very important as the load from the anchor could have a great variation over time. Buckling will not be checked either, but this type of failure mechanism should be considered for the final design of the anchor. The anchor could be susceptible to buckling due to the thin plates w.r.t. the side lengths of the hollow triangular cross section. However, the soil within the hollow triangular part could contribute with soil pressures which prevent buckling.

As the OO-Star Wind Floater and the OO-Anchor are offshore structures, the Eurocodes do not directly apply for these structures. Codes which are specifically created for the design of offshore structures must be employed. DNV GL has developed appropriate design codes which can be applied for the structures of interest. Some of these codes use clauses specified in the Eurocodes. Hence, some parts of the Eurocodes must be considered. One of the differences between the Eurocodes and the DNV GL standards is the inclusion of the important effect of corrosion for offshore structures. Three of the design codes from DNV GL and one of the Eurocodes are needed for the simple design checks related to the anchor.

- DNVGL-OS-C101 *Design of offshore structures* (DNV GL, 2018a)
- DNVGL-ST-0119 *Floating wind turbines* (DNV GL, 2018b)
- DNVGL-OS-B101 *Metallic materials* (DNV GL, 2015)
- EC3-1-8 *Design of joints* (Standard Norge, 2009)

There are many available steel types/grades. The chosen characteristic yield strength for the steel for the anchor components is 355MPa. There are 4 available steel grades with the chosen yield limit. These are VL A36, VL D36, VL E36 and VL F36 (DNV GL, 2015, p.21), and are classified as high-strength steel grades. Steel structures usually have thin components. A steel component with a large thickness will have a large probability of containing material imperfections which reduce the yield limit of the steel. Therefore, for larger thicknesses the design codes specify a reduced yield limit as a function of the thickness of the components. Residual stresses can occur during a welding process. It is likely that the anchor will be composed of large plates welded together instead of one hollow triangle cast in one piece. In order to account for the residual stresses from welding, the design codes tend to reduce the yield limit of the material. Steel grades with increased weldability are available. These grades, with a yield limit of 355MPa, are VL AW36, VL DW36 and VL EW36. The variation of the yield limit for these three steel grades, with increased weldability, as a function of component thickness, is shown in table 8.6. These will be used in the analyses of the anchor.
Elastic analyses will be carried out in order to determine the anchor thickness. The von Mises yield criterion can be used to check yielding. In order to avoid having to consider a a reduced cross sectional area, the cross section of the anchor must be in Class 3 or above. For cross sections in Class 4, local buckling can occur and the capacity will be reduced. The material factor for plated structures, γ_M, is equal to 1.15 (DNV GL, 2018a, p.47). The material factor is also set to 1.10 in other sections of relevant design codes, but the more conservative value will be used. This will account for some of the simplifications w.r.t. the considered load cases for the design of the anchor. The design yield stresses, based on the characteristic limits given in table 8.6 and the chosen material factor, are shown in table 8.7.

Table 8.6: Characteristic yield limits as a function of thickness for VL AW36, VL DW36 and VL EW36 (DNV GL, 2015, p.20).

Thickness [mm]	**Characteristic yield limit** [MPa]
$t \leq 25$	355
$25 < t \leq 50$	335
$50 < t \leq 75$	320
$75 < t$	310

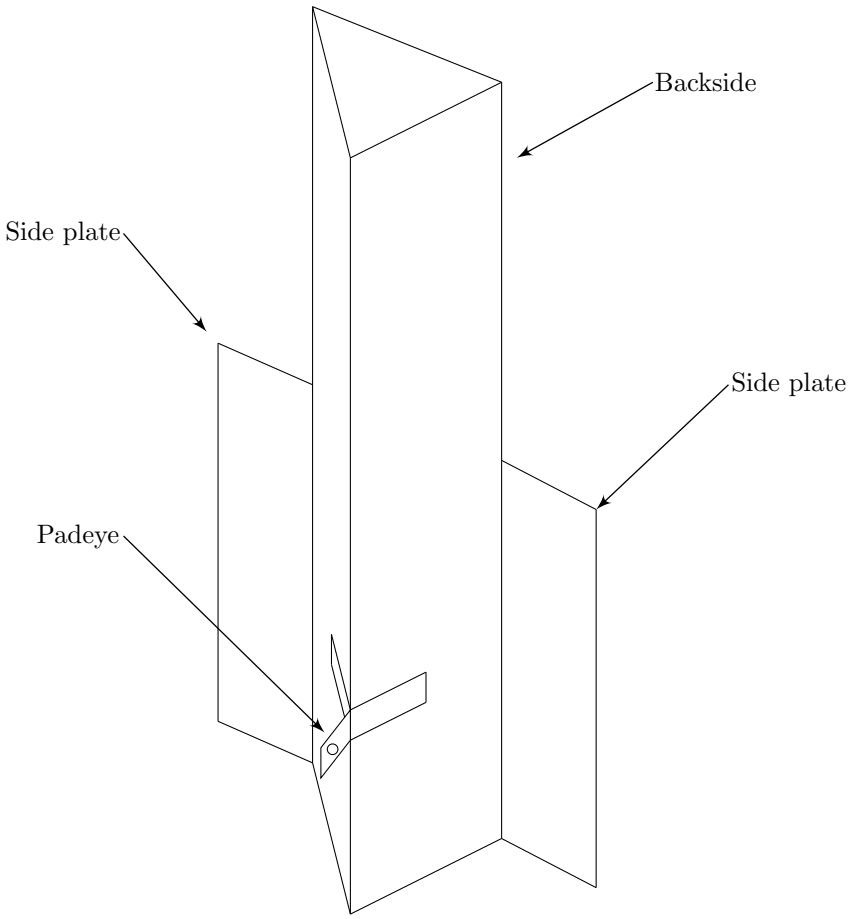

Figure 8.3. A 3D illustration of the intended geometry of the OO-Anchor. The figure is not to scale. Thicknesses are not shown.

Table 8.7: Design yield limits as a function of thickness for VL AW36, VL DW36 and VL EW36 (DNV GL, 2015, p.20).

Thickness [mm]	**Design yield limit** [MPa]
$t \leq 25$	308
$25 < t \leq 50$	291
$50 < t \leq 75$	278
$75 < t$	269

8.2.2 Important load cases

The two most important loads which must be considered, in order to determine the required steel thickness, are the geostatic stresses from the surrounding soil and the concentrated load from the mooring line acting on the structure through the padeye. In order to determine the geostatic stress from the

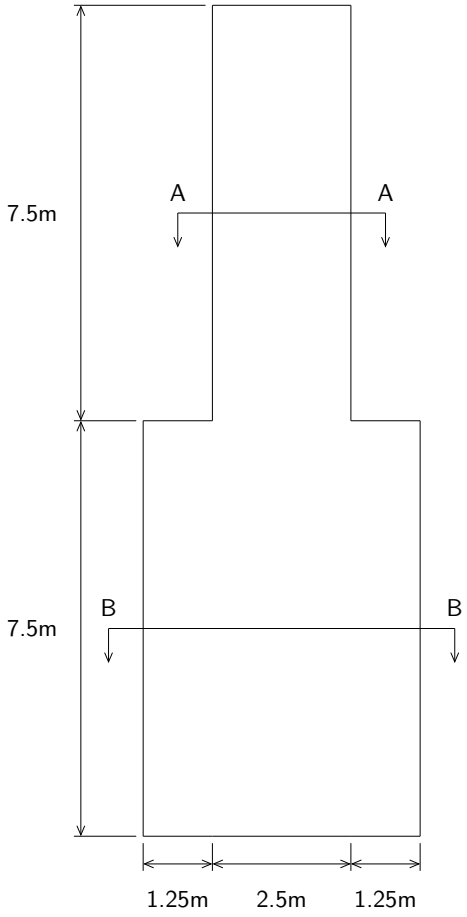

(a) Geometry of the back of the anchor.

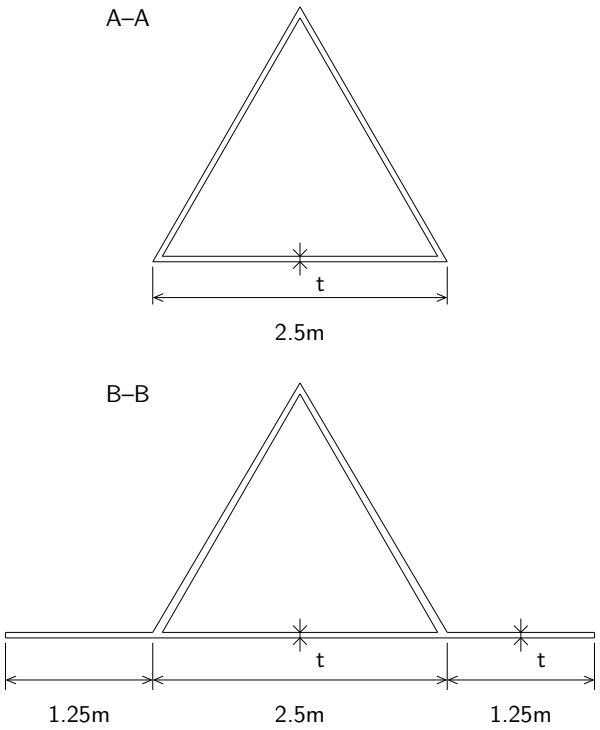

(b) Cross section consisting of a hollow triangle with equal side lengths (A-A). The cross section for the lower part is also shown (B-B). The required thickness is not yet determined.

Figure 8.4. Geometry of the backside and the cross sections of the anchor.

soil acting on the outside and inside of the anchor, an appropriate soil model must be established. As the focus of this thesis is related to structural dynamics, and due to the lack of required geotechnical knowledge from the authors of this thesis, the required soil stresses are provided by C. F. Davidsen, within the department of geotechnics at NTNU, who is conducting a parallel study on the OO-Anchor for his thesis (Davidsen, 2020).

The soil model in C. F. Davidsen's thesis is established using the FE software Plaxis (Bentley systems, 2019). The properties of this soil model, such as density and shear strength, correspond to the ones which are used for the SSI analyses described in this chapter. Effective normal and shear stresses, acting on the anchor from the soil, can be obtained from this model. These can then be applied to an FE model of the anchor using shell elements in Abaqus. The most important load combination to consider will be geostatic stresses from the surrounding soil, along with a concentrated force from the mooring line acting on the padeye (through a shackle). A concentrated force is applied in the Plaxis model at a point corresponding to the location of the padeye. The location of the padeye along with the inclination of the concentrated force will determine the rotation of the anchor in the soil. From a geotechnical perspective, it is desired that when being loaded by the force the structure is only displaced horizontally without any rotation. The normal and shear stresses obtained from the Plaxis model are given in the ultimate limit state (ULS).

According to OO, an approximate value for the design tension in the mooring line is 10000kN, for the mooring system used in the SIMA model. The design mooring tension determined in 5.2.2 is equal to 10926kN. The mooring tensile forces determined in 6.5 and 6.6 do not exceed the design mooring tension. Therefore, a seaquake is not critical for the mooring line force acting on the the anchor. Based on these results, the assumption of a force of 10000kN seems reasonable. However, the force which acts on the anchor is expected to be reduced due to soil-line interaction. For a catenary mooring system, a

large portion of the mooring line will lie on the seabed and in the soil. Interactions between the soil and the line will occur due to friction (Larsen & G.Svanø, 1999). This will reduce the load along the line. Therefore, an anchor force of 8000kN (in ULS) with an inclination of 16.5° w.r.t. the horizontal plane is chosen, based on recommendations from OO and C. F. Davidsen. This corresponds to a padeye located 10m beneath the top of the of the anchor. More details are shown in B.3.

8.2.3 Padeye design

The padeye will be designed using the relevant DNV GL code sections and EC3-1-8. The calculations associated with the simple design checks performed for the padeye are shown in B.3. The chosen dimensions are shown in fig. 8.5.

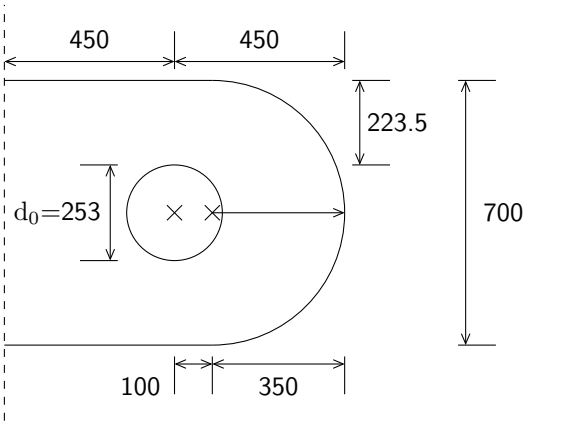

(a) Chosen dimensions for the "cantilever" part of the padeye. The measurements are in mm.

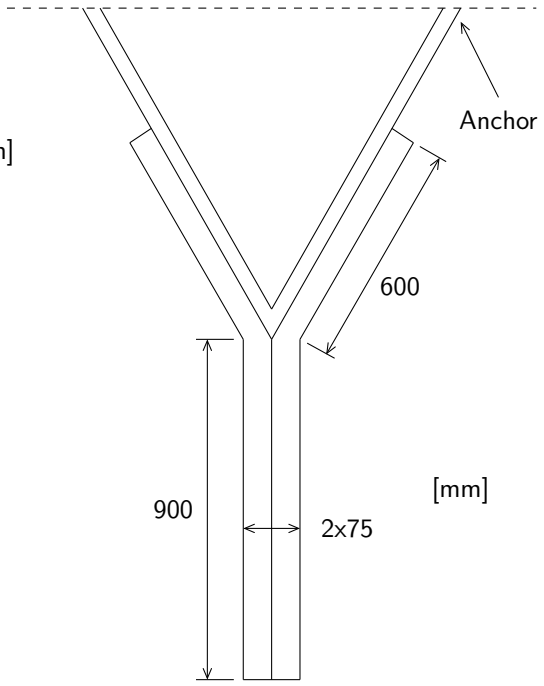

(b) Chosen dimensions for the remaining parts of the padeye, seen from above. The measurements are in mm.

Figure 8.5. The chosen dimensions for the padeye geometry. The measurements are in mm.

8.2.4 Anchor thickness

Model description

The anchor thickness will be determined using a separate FE model in Abaqus, with no soil included. The anchor load will be applied to the structure along with the soil pressures and shear stresses from the Plaxis model. An elastic analysis will be conducted and the thickness will be determined based on the equivalent von Mises stresses in the structure. In order to avoid unrealistically large stress concentrations, the anchor force should be modelled as a distributed load, instead of assigning the force to one single node. The surface, over which the horizontal and vertical components of the anchor load will be assigned, corresponds to the geometry of the part of the padeye welded to the sides of the anchor, as shown in fig. 8.5. The distribution surface has a height of 700mm and a width of 600mm.

Half of the anchor structure will be modelled and "symmetry" boundary conditions will be introduced at the appropriate locations in the model. The symmetric model is shown in fig. 8.6. The geometry of the FE model corresponds to the geometry presented in fig. 8.4. Different thicknesses for the hollow triangular part and the side plates will be considered. As only half of the structure is included in the FE model, only half of the anchor force is used in the Abaqus and Plaxis models in order to ensure the correct magnitude for the stresses. A horizontal force of 4429kN and a vertical force of 1136kN are

applied to the previously described distribution surface (see B.3). These components are included using surface tractions. Soil pressures and shear stresses, produced by the Plaxis model, are introduced on the surfaces of the anchor components as pressures and surface tractions, respectively.

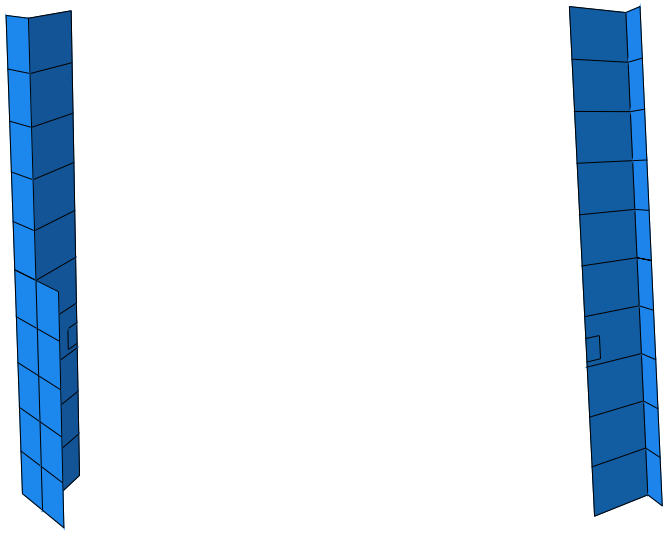

Figure 8.6. Symmetric FE model of the anchor.

It is important to take into account that equilibrium will be not be obtained in the Abaqus model when using the soil stresses from Plaxis. The Plaxis model contains features such as springs which ensure equilibrium for the anchor without imposing any boundary conditions directly on the structure. Equilibrium should theoretically be obtained in the Abaqus model when the external anchor force and the corresponding soil stresses are applied. This will most likely not be the case and boundary conditions have to be introduced to compensate for the difference between the anchor force and the soil stresses. It is desirable to avoid rotations of the structure in order to have enough similarity between the Abaqus and Plaxis models. The model is pinned at three nodes at the top and bottom of the hollow triangular part. The distribution of stresses will be different for the Abaqus model compared with the actual distribution where there is equilibrium between the concentrated force and the soil stresses. It is therefore important to not consider stress concentrations at the top and bottom of the model close to the pinned nodes, since the chosen boundary conditions will lead to larger forces in these areas of the model.

The thickness is determined by comparing the stresses from the model with the design yield stresses given in table 8.7. The properties related to material definition and the mesh of the model are shown in table 8.8. Shell elements are chosen for the model since these generally are better at representing bending than the corresponding solid elements. One other argument for the choice of shell elements is that skins, which use shell elements, are used to represent the anchor in the SSI model. This will allow for an easier comparison between the stresses obtained from the SSI model and the symmetric design model considered in this section.

Table 8.8: Material and mesh properties for the symmetric anchor FE model.

E [GPa]	ν [ ]	**Element size** [m]	**Element type**
210	0.3	0.05	STRI65 (second order triangular shell element)

Results

A typical or expected thickness for the anchor is around 1% of a representative dimension, such as the side length of the hollow triangle section. The corresponding value for the expected thickness is then 25mm. Thicknesses smaller than this value should then not be considered. The hollow triangular part of the anchor is expected to require a smaller thickness than the plates on the sides. A closed hollow

section will give a large capacity even with a small thickness. The two plates act as cantilevers fixed to the anchor. Large bending stresses are expected to occur near their fixed ends.

The maximum equivalent von Mises stress for the triangle part and for the side plate is considered as an adequate design criterion for both parts of the structure. The results for three thickness configurations are shown in table 8.9.

Table 8.9: Maximum von Mises stresses for thickness configurations compared with design yield limits. "tri" denotes the hollow triangular part, "pl" denotes the plates on the sides.

t_{tri} [mm]	$f_{\text{yd,tri}}$ [MPa]	t_{pl} [mm]	$f_{\text{yd,pl}}$ [MPa]	$\sigma_{\text{max,tri}}$ [MPa]	$\sigma_{\text{max,pl}}$ [MPa]	OK/Not OK
30	291	30	291	495	720	Not OK
40	291	60	278	219	109	OK
40	291	50	278	219	156	OK

The results for the second configuration, with a thickness of 40mm for the triangle part and 60mm for the plates, indicate that the thickness of the plates can be reduced. Since many design checks which usually are required are not performed, the thickness of the plates are reduced to 50mm to be on the safe side. Membrane locking in shell elements can also affect the results by giving non-conservative stresses. Decreasing it to 40mm could lead to a low reserve capacity. As the thickness of the sides of the triangular section is small compared with their length, it is possible that this section could be a Class 4 section. This would lead to an effective cross sectional area smaller than the total area of the cross section, and would result in a lower capacity. For a thickness of 40mm, there is an adequate reserve capacity. Additionally, stiffeners can be used to increase the capacity of the hollow part if local buckling becomes an issue. Therefore, a thickness of 40mm is assumed to be sufficient for the hollow triangular section. The chosen thickness configuration is 40mm for the three plates of the hollow triangular part, and 50mm for the plates on the sides.

8.3 SSI model

In this section, the full SSI model consisting of the anchor and the soil with varying material properties is presented. The load from the mooring line will be applied along with earthquake excitation in the form of acceleration-time series at the bottom of the model. A linear elastic- and a plastic SSI model will be considered.

8.3.1 Model description

The full SSI model consists of the soil profile discretized into layers with different material properties, and the anchor represented by a skin. The approach of using skins was chosen instead of an approach using contact because of the simplicity and lack of uncertainties related to skins compared to the second approach. An appropriate extrusion is performed on the soil domain in order to obtain the surface, on which the skin representing the anchor is attached. The skin is highlighted in fig. 8.7. The soil domain is discretized using the coarse discretization presented in fig. 8.1a. The full model along with the discretization of the soil domain is shown in fig. 8.8.

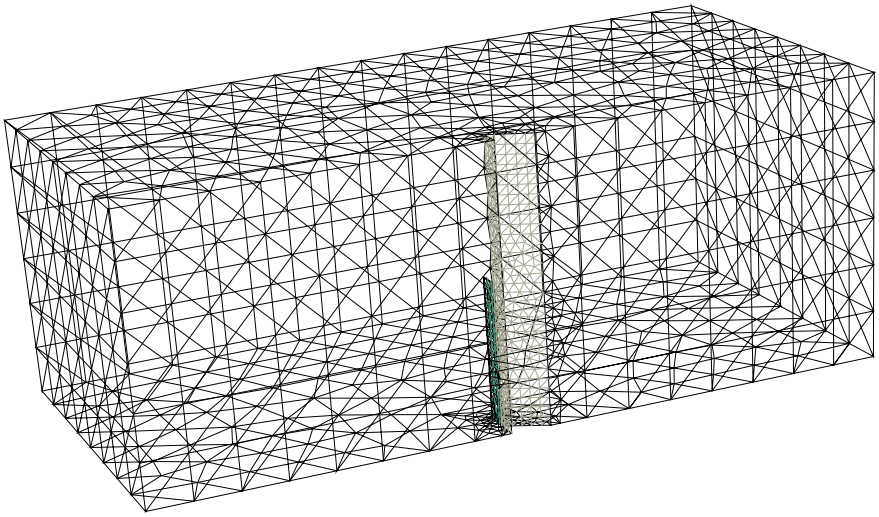

Figure 8.7. A visualisation of the skin elements in the upper part of the soil domain. The skin elements are highlighted with a green (side plate) and a light gray (hollow triangular part) color.

8.3.2 External loading

Both the load from the mooring line and the accelerations due to earthquake will be considered in the model. Both horizontal and vertical acceleration will be considered. Shear waves cannot propagate through water during a seaquake. Hence, the mooring lines and the floater will not be affected by the surrounding water, when only horizontal acceleration is considered. However, for vertical acceleration, the motion of the platform due to seaquake pressure will result in tensile forces in the mooring lines. The forces acting on the anchor due to seaquake response of the platform, shown in 6.5 and 6.6, are smaller than the recommended mooring tension of 10000kN. As no specific site is considered, this value will be used instead of the design mooring tension ($T_d = 10926$kN). In order to account for the reduction of the load along the mooring line due to soil-line interaction, a load of 8000kN is used (as in 8.2.2). The area over which the load is distributed corresponds to the previously determined padeye dimensions in 8.2.3. The distribution surface has a width of 600mm and a height of 700mm, and is located at a depth of 10m (i.e 5m above the bottom of the anchor and 10m under the top of the soil volume). A symmetric soil model is considered which means that only half of the anchor load is used. The horizontal component of the load is equal to 4429kN and the vertical component is 1136kN. The loads are applied as surface tractions and are shown in fig. 8.9.

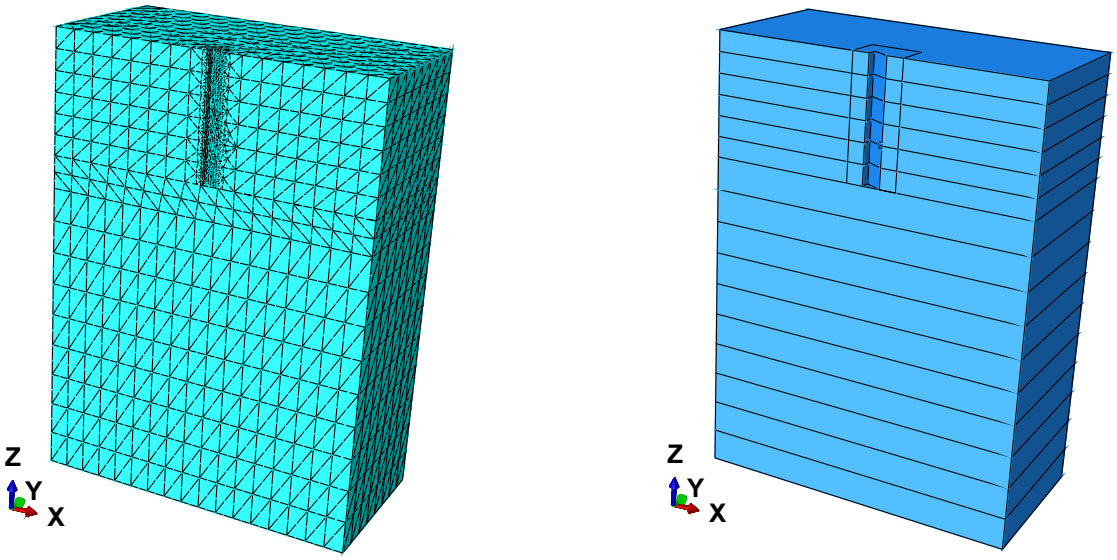

(a) A visualisation of the full FE model of the soil profile and the anchor.

(b) A visualisation of the soil layers represented by partitions in Abaqus.

Figure 8.8. A visualisation of the full FE model of the soil profile and the anchor and the discretization of the soil into layers using partitions.

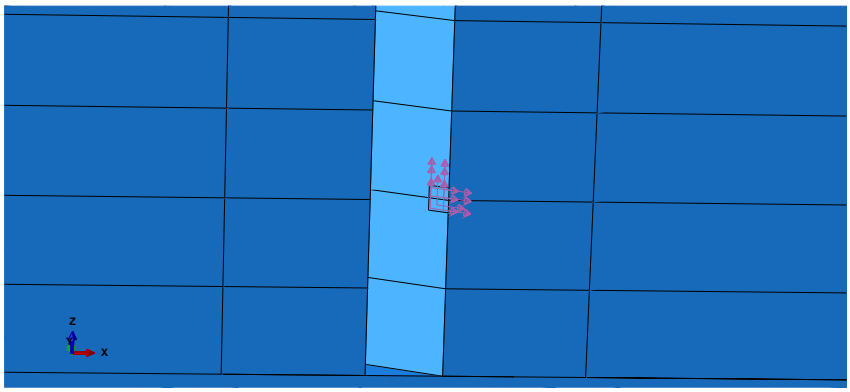

Figure 8.9. An illustration of the applied surface tractions which represent the static load from the mooring line. The horizontal component is equal to 4429kN and the vertical component is 1136kN. The tractions are applied over a surface of 700x600 mm^2.

8.3.3 Geometrical and material properties

The geometry of the anchor, which is shown in fig. 8.4, along with its material properties are given in table 8.10. The material properties of the steel in the anchor are assumed to be homogeneous and linearly elastic.

The soil volume has the dimensions $L_x = 40$m, $L_y = 20$m and $L_z = 55$m. These dimensions and the corresponding material properties correspond to the ones considered in 8.1. The coarse soil discretization, shown in fig. 8.1a, is used to divide the soil volume into layers with different materials properties. The material properties from table 8.1 are used for the SSI model. The geometry and material properties of the soil volume are presented in table 8.11. The material properties for each layer of the chosen soil discretization are presented in C.3.

For the plastic SSI model, the Mohr-Coulomb failure criterion is used (see 2.2.6) to introduce plastic material properties. The intention is to use an elastic-perfectly plastic material model. The friction and dilation angles for each layer are equal to zero. For a pure clay, the friction angle is equal to 0°. Clays are characterized by a low amount of dilation. In order to have no hardening, the cohesion yield

stress is set as the average undrained shear strength in each layer (see table C.3) and the corresponding absolute plastic strain is set equal to zero.

Table 8.10: Geometry and material properties of the anchor.

Geometry	
Side length of triangle	2.5 m
Height of triangle part	15 m
Thickness of hollow triangle	0.04 m
Length of side plate	1.25 m
Height of side plate	7.5 m
Thickness of side plate	0.05 m
Depth of location of padeye	10 m
Padeye load surface	600x700 mm^2
Material properties	
Density of steel	7750 kg/m^3
Young's modulus of steel	210 GPa
Poisson's ratio for steel	0.3

Table 8.11: Geometry and material properties for the soil volume.

Geometry	
L_x	40 m
L_y	20 m
L_z	55 m
Soil layer thickness, 0-15m	2.5m
Soil layer thickness, 15-55m	4m
Material properties	
Density of clay	1700 kg/m^3
Poisson's ratio for clay	0.495
Shear strength, top	2.0 kPa
Shear strength, bottom	84.5 kPa
Young's modulus, top	5.98 MPa
Young's modulus, bottom	252.66 MPa
Rayleigh coefficient α	0.4118
Rayleigh coefficient β	0.0033
Friction angle	0°
Dilation angle	0°
Absolute plastic strain	0

8.3.4 Boundary conditions and constraints

As a symmetric model is considered, a symmetry boundary condition is introduced on the surface of the model which corresponds to the symmetry plane. More specifically, a "YSYMM" boundary condition is used. In order to ensure the correct shear-beam behavior along the excitation direction, the two end surfaces perpendicular to the excitation direction (x-direction) are constrained using the tie-constraint defined in 7.1. The vertical boundary surface, with an outward surface normal parallel to the positive y-direction, is pinned in the y-direction and free to move in the other two directions. This is done to ensure the correct shear-beam behaviour along the direction of excitation (x-direction).

The bottom of the soil domain is pinned in the y- and z-direction and is free to move in the x-direction.

The earthquake excitation is introduced as an acceleration boundary condition in the x-direction at the bottom of the model. The most dominant of the two horizontal components of the Loma Prieta earthquake accelerations, presented in 3.3, will be used in the analyses. The strong motion acceleration is used (see fig. 3.8). The PGA of the horizontal acceleration is 0.7215m/s^2. For the plastic SSI model, analyses will be performed with horizontal and vertical excitation simultaneously. The strong motion part of the vertical component of the Loma Prieta earthquake will be used for the vertical excitation (see fig. 3.8). For these analyses, the bottom of the soil domain is only pinned in the y-direction.

The seismic excitation causes shear waves which propagate vertically through the soil from the bottom of the soil volume. These will be reflected by the soil boundary surfaces. A large enough soil volume should be used in order to reduce this wave reflection since the reflection of energy will be reduced due to the material damping introduced in the soil materials. A length of 40m in the x-direction and 20m in the y-direction is expected to be sufficient as the side length of the hollow triangular part of the anchor is 2.5m. A possible remedy to the wave reflection problem would be to introduce dampers or dashpots at the boundaries of the soil volume. It could then be possible to reduce the volume of the soil domain and consequently the number of elements for the FE simulations.

8.3.5 Element and mesh properties

The mesh properties of the model are shown in table 8.12. The size of the elements for the surfaces, where the anchor skin is applied, will either be 0.5 or 0.25m, depending on the analysis. When the stresses in the anchor are of interest, then finer elements should possibly be used in order to obtain accurate results. Otherwise, when the effects on the soil is of interest 0.5m will be used.

For the upper 15m of the soil profile, the element size is 2.5m. For the remaining 40m under the anchor the element size is 4m. The size of the solid soil elements around the anchor decreases from 2.5m to 0.5m or 0.25m over the surfaces shown in fig. 8.10. These two partitions will be denoted as Partition 1 and Partition 2, respectively. When only considering the elastic soil material properties, Partition 1 is used. A finer mesh is used for the anchor to get more accurate stresses. A coarser mesh is used for the anchor in the plastic SSI model. Elastic material properties are expected to not accurately describe the soil behaviour. Therefore, a fine mesh is expected to not yield more accurate results. Plastic material properties will describe the soil behaviour more accurately. Hence, a finer mesh is used for the soil for the plastic model by using Partition 2.

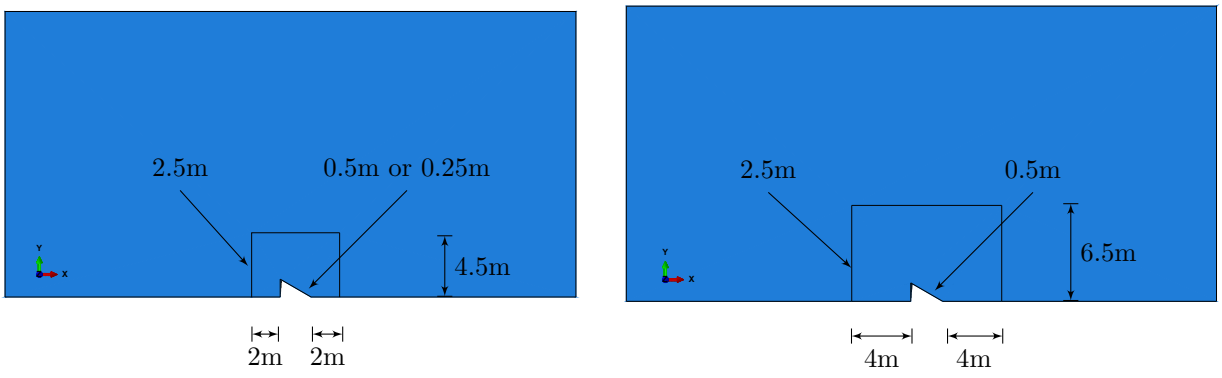

(a) Partition 1

(b) Partition 2

Figure 8.10. The two partitions to be used in the SSI model. The surface at the top of the soil volume is shown. The annotations indicate the element size along the surfaces.

8.3.6 Model simplifications

A summary of the most important simplifications introduced in the SSI model is presented below.

- Representing the anchor through the use of a skin does not allow for gaps to occur or sliding between the soil and anchor surfaces, which is often present for this type of structure.

Table 8.12: Mesh properties for the SSI model.

Part	**Element type**	**Element size** [m]
Soil, 0-15m	C3D10	2.5
Soil 15-55m	C3D10	4
Anchor	STRI65	0.5 or 0.25

- A coarse discretization of the soil is chosen to limit the total number of elements. The material properties of the soil in the model do not increase linearly with the depth, but these do in reality. In the model, the variation of the properties is represented by a series of layers with constant material properties.
- For the elastic SSI model, the material properties are limited to the linear elastic range. Yielding of the soil around the anchor is not accounted for.
- For the plastic SSI model, an elastic-perfectly plastic material model is assumed. No hardening is accounted for.

8.4 Results–elastic SSI model

A static analysis, where only the design mooring tension is considered, is performed. Then, dynamic analyses which include both the design mooring tension and earthquake excitation are conducted.

8.4.1 Static analysis

In order to determine how fine the anchor skin elements should be, static analyses are performed for the SSI model with only the anchor load as external loading. The resulting stresses can then be compared with the design model in 8.2.4. As the two models have different boundary conditions, the comparison of the results from the two models will not be entirely valid. However, the stresses around the padeye should be similar for the two models. Both models use second order triangular shell elements. The model used for the design of the anchor has an element size of 0.05m. It is assumed that this element size gives a converged FE solution. The stresses from the static analyses from the elastic SSI model, compared with the stress used for the design of the thicknesses, are presented in table 8.13.

Table 8.13: Comparison of the maximal stresses in the design model and the elastic SSI model. The element size is indicated in brackets.

Model	**Max. stress padeye** [MPa]	**Max. stress side plate** [MPa]
Design (0.05m)	219	156
SSI (0.5m)	183	73
SSI (0.25m)	187	74

Using finer elements should yield more accurate results for the SSI simulations. The Plaxis model does not have the same boundary conditions as the SSI model. The material properties are a series of discrete values in Abaqus, while they are continuous for the Plaxis model (Davidsen, 2020). Furthermore, the Plaxis model uses plastic material properties while the elastic SSI model does not. Nevertheless, based on these results, an element size of 0.25m should be used for the anchor for the elastic SSI model.

8.4.2 Dynamic analysis

Anchor stresses

The full model with elastic material properties is analyzed using an implicit integration method. A time step of 0.0025s is employed.

The stresses are expected to be large mainly in two areas of the model. The first one is the padeye, over which the anchor force components are distributed. The second area is the fixed end of the side plate. Areas on the back side of the anchor near the side plate can also have important concentrations of stress. The von Mises equivalent stress is extracted at selected nodes in the previously mentioned areas. The specific points/nodes are shown in fig. 8.11. The points on the padeye surface are denoted with the symbol "p". Points near the fixed end of the side plate are denoted with "sp". Finally, the points on the back of the triangular part are denoted with the symbol "b".
The force from the mooring line is applied during the same step as the earthquake excitation. One available option for the load application is an instantaneous application. One disadvantage with this alternative is that undesired effects for the results will occur in the beginning of the time histories. Applying a load instantaneously is equivalent to a short impulse. The response will have a transient term which increases the initial response of the structure. After a certain time, the transient part will be reduced to zero and the response will be composed of only the steady-state part. In order to avoid an instantaneous load, one additional second is added at the start of the acceleration-time histories. During this initial second, the load increases linearly towards its correct amplitude while the acceleration is maintained at zero. For the remaining part of the time histories, the components of the anchor force are kept constant and the excitation is applied. The duration of the response will consequently be 18.2s instead of 17.2s.

The stresses are shown in fig. 8.12. The initial second is not shown. During this time, the stress-curve is linear due to way in which the mooring line force is applied. After the first second, the stress

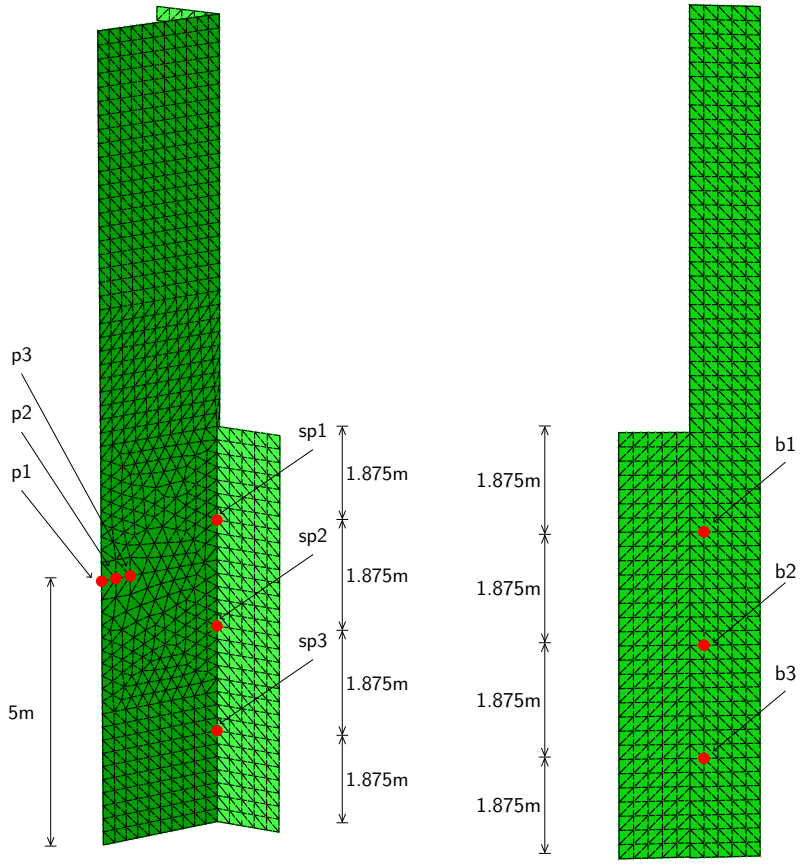

(a) Front of anchor

(b) Back of anchor

Figure 8.11. The chosen points for measurements of the equivalent von Mises stress from the elastic SSI simulations.

due to the anchor force is obtained. The design yield limits are given in table 8.7. The limit for the triangular part is 291MPa. The limit for the side plate is 278MPa. The capacity is sufficient for the points on the side plate and the backside. The capacity is also sufficient for the points on the padeye surface. The padeye nodes exhibit the largest stresses.

Point p1 shows the largest stresses amongst all of the chosen points. The average stress during the earthquake excitation is approximately 187MPa, and this is assumed to correspond to the static stress due to the concentrated anchor force. The maximum stress during the time of excitation is around 201MPa. This indicates that the SSI effects increase the stress by 14MPa. However, the reserve capacity is 90MPa, which is a sufficient amount.

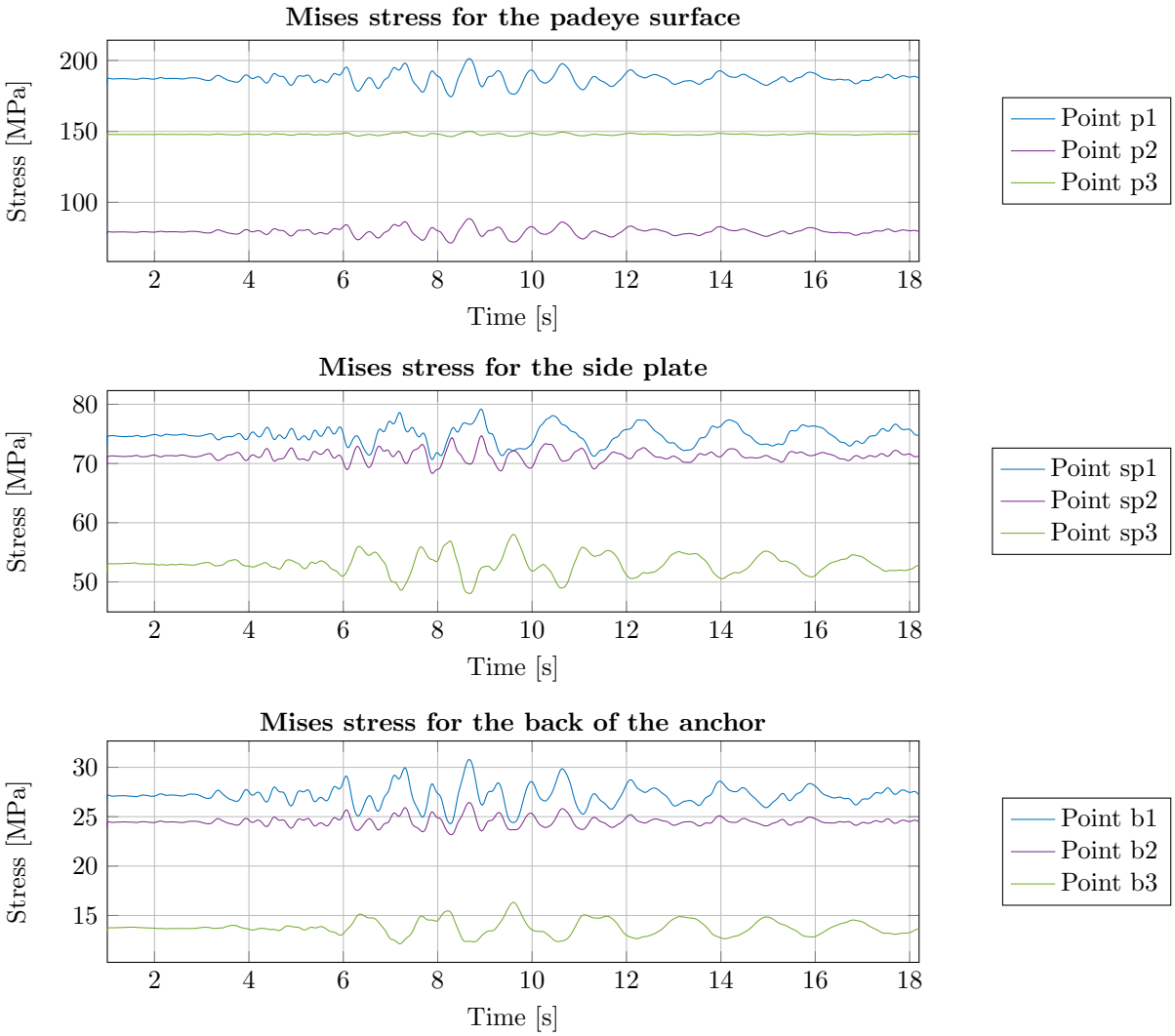

Figure 8.12. Stresses for the considered points near the padeye, on the side plate, and on the backside of the anchor. During the first second, the mooring line force is ramped up linearly without any earthquake excitation.

Soil response

In order to assess if an elastic material model is reasonable for the soil, the displacements and the stresses in the soil should be studied. The displacements due to the static anchor load (i.e after 1s) and the displacements after application of the entire horizontal excitation (i.e after 18.2s) are shown in fig. 8.13. The magnitude of the displacements is 10^{-2}m or 1cm, which is very small when the dimensions of the model are considered.

The soil pressure is examined at three different points around the anchor. The first point is located in the middle of the first soil layer (0-2.5m). The second point is located in the middle of the second layer (2.5-5m). The third point is located near the padeye at a depth of 10m. All three points are located on the front surface of the anchor, which is the surface where the padeye is attached. The pressure-time series for the three points are presented in fig. 8.14. The pressure for the three points has a magnitude of 10^6Pa or more. In the Mohr-Coulomb failure criterion considered for the plastic soil material properties, the undrained shear strength is used as the yield limit for the soil layers. For layer 1 and 2, the average shear strength is 3.875kPa and 7.625kPa, respectively. The shear strength at the depth of the padeye is 17kPa. Therefore, yielding will occur for the soil around the anchor. This justifies the use of a plastic material model. As the displacements in fig. 8.13b are considered to be small, effects of non-linear geometry are assumed to not be large enough to be taken into account. However, plastic material properties will affect the stiffness of the model and could result in larger displacement, which could warrant the inclusion of non-linear geometry. Not including geometric non-linearity will reduce the computational time of the simulations for the plastic SSI model because the stiffness matrix doesn't have to be computed for each increment.

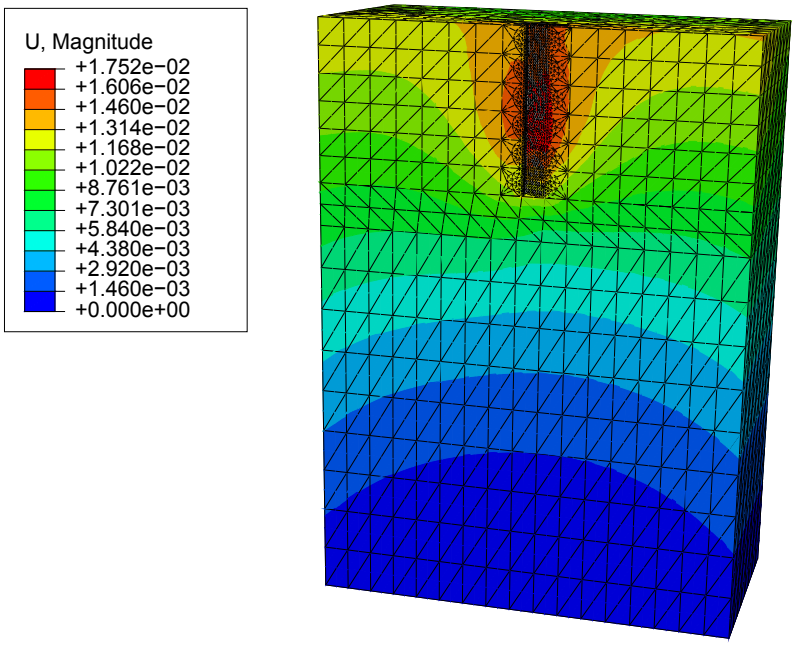

(a) The displacement due to the static anchor load (after 1s).

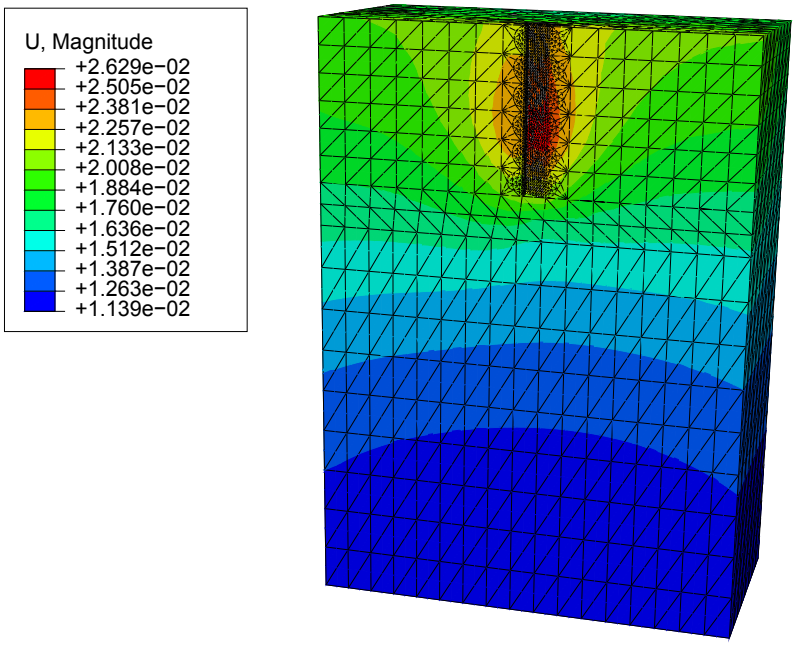

(b) The displacement after 18.2s due to the static anchor force and the earthquake accelerations.

Figure 8.13. Contour plots of the displacements from the elastic SSI model. The displacements are given in m.

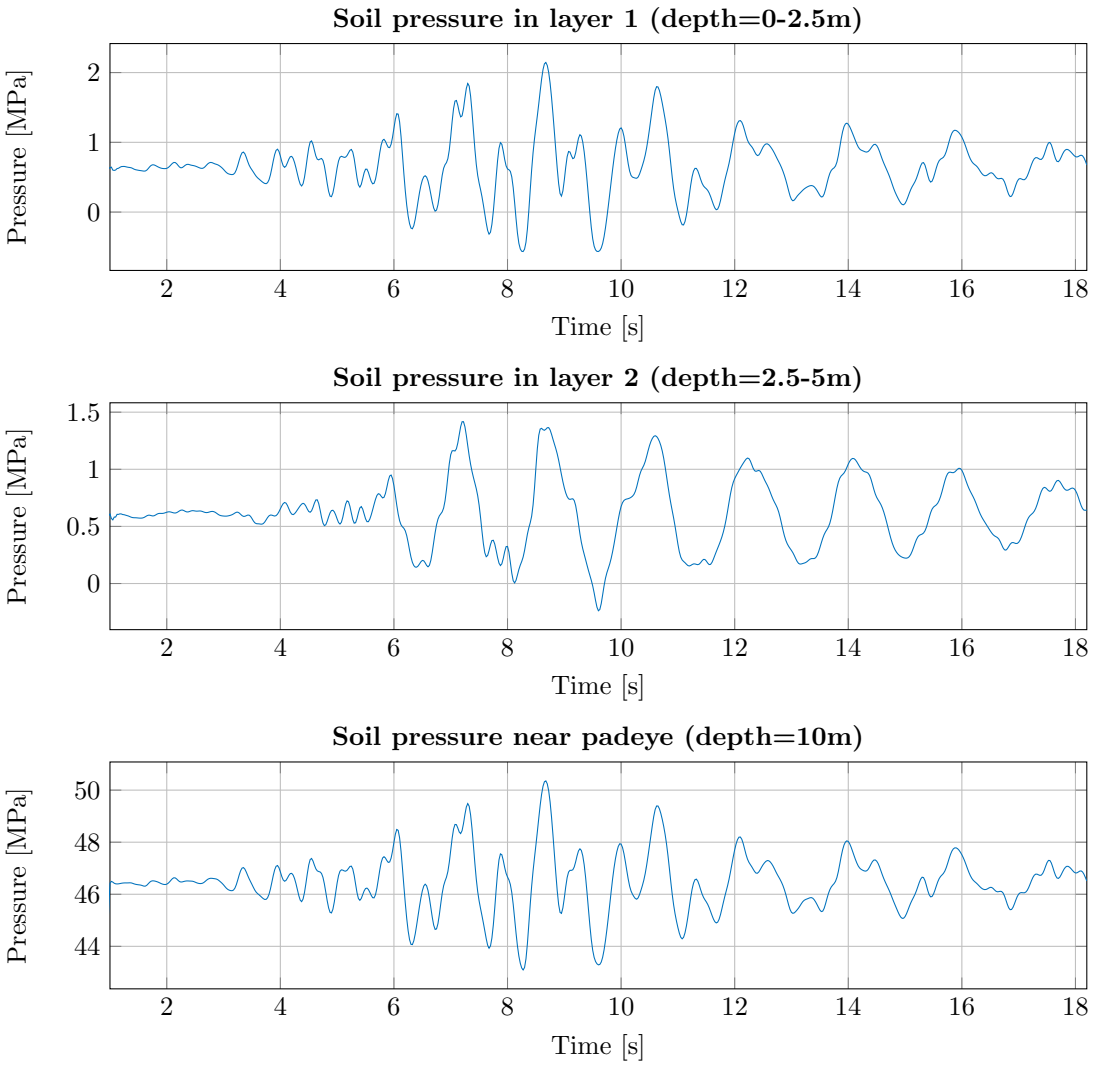

Figure 8.14. Pressure for the three considered points of the soil around the anchor.

8.5 Results–plastic SSI model

As in 8.4, an initial static analysis with only the design mooring tension is carried out, followed by dynamic analyses including earthquake excitation.

8.5.1 Static analysis

As in 8.4.1, a static analysis is performed for the plastic SSI model. The maximum stress in the padeye and in the side plate is compared with the results from the design model. The results for the elastic and plastic SSI models are also compared. Partition 2 is used, which means that the mesh for the soil is finer than for the elastic SSI model. The results of the static analysis are shown in table 8.14.

Table 8.14: Comparison of the maximal stresses in the design model and the plastic SSI model.

Model	**Max. stress padeye** [MPa]	**Max. stress side plate** [MPa]
Design	219	156
Elastic SSI	187	74
Plastic SSI	192	118

The plastic SSI model yields a lower stress for the padeye and the side plate compared to the design model. The stresses for the padeye region are similar for both of the SSI models, but the plastic SSI model yields larger stresses for the side plate. As plastic material properties are included, the stiffness of the soil around the soil is different for the two SSI models. The reduced stiffness, due to material yielding, seems to result in larger forces for the side plate. This is most likely related to larger displacements for the plastic SSI model. It should still be noted that the boundary conditions for the design model are not identical to the ones of the SSI model. Therefore, a comparison between the models will be not be entirely valid.

8.5.2 Dynamic analysis

Several dynamic analyses are performed for the SSI model with an elastic-perfectly plastic material model. The first analysis will consider only a horizontal excitation. The following analyses will consider scaled horizontal excitation. More specifically, the horizontal acceleration will be scaled such that its PGA is equal to 0.1g, 0.2g and 0.3g. The PGA of the original unscaled horizontal excitation is 0.7215 m/s^2. Analyses with simultaneous horizontal and vertical excitation will also be performed. One initial analysis is performed with unscaled acceleration in both directions at the bottom of the model. The PGA of the horizontal acceleration is then scaled such that it is equal to 0.1g, 0.2g and 0.3g. The vertical excitation is scaled using the same factors. The time step for the implicit dynamic analyses is set to 0.0025s. As for the dynamic analyses with the elastic SSI model, the static load is increased linearly during the first second of the analysis without any earthquake excitation, in order to avoid transient response effects.

The main interests of the analyses are the stress in the components of the anchor and the displacements of the soil. The total displacement of the soil after the entire duration of the excitation can be used as an indication if the anchor will be pulled out of the soil or not. The strains in the soil will also be considered for this evaluation. Some critical points w.r.t. stress concentrations are chosen in the components of the anchor. These are indicated in fig. 8.15. One point is chosen from the surface representing the padeye, two from the fixed end of the side plate and two points from the backside of the structure. The node on the padeye surface is denoted with "P", the nodes from the side plate with "SP" and the nodes from the backside with "B".

Horizontal excitation

The equivalent von Mises stress for the chosen nodes is presented in fig. 8.16. The maximum stresses for the five points are shown in table 8.15. The results indicate that yielding occurs for the side plate. The displacement of the soil volume after the entire horizontal excitation is shown in fig. 8.17.

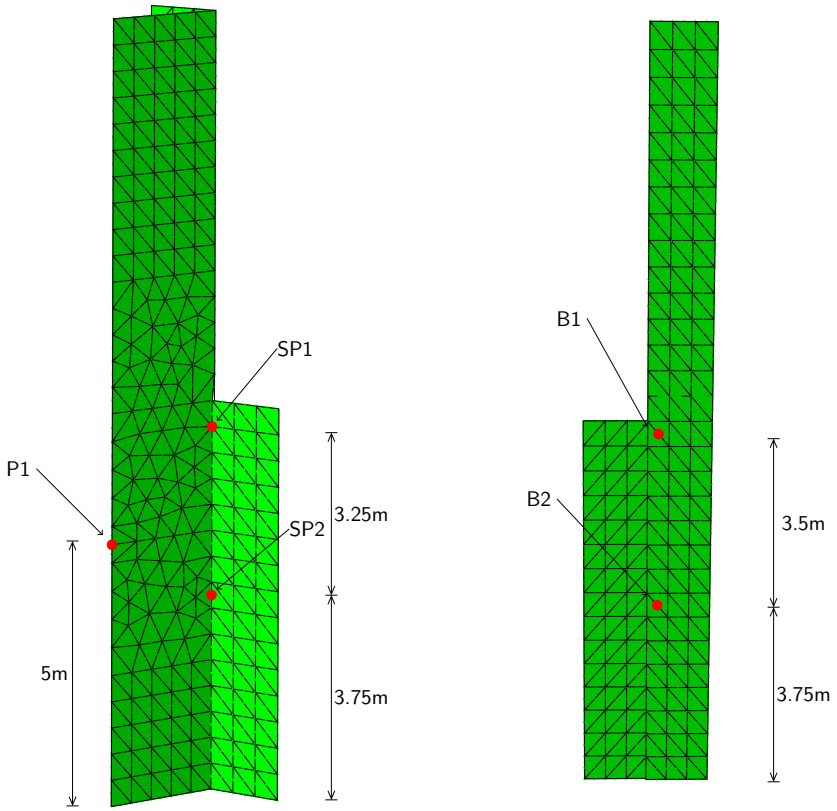

(a) Front of anchor **(b)** Back of anchor

Figure 8.15. The chosen points for measurements of the equivalent von Mises stress from the plastic SSI simulations.

The results suggest that the effects of horizontal excitation is more critical for the side plate than for the padeye region. This could be reasonable as the side plate is free at one end and prevents horizontal displacements of the anchor, which leads to large concentrations of stresses.

Table 8.15: Maximum stress for the five points from the plastic SSI analyses with unscaled horizontal excitation.

Point/Node	**Max. stress** [MPa]	**Design yield limit** [MPa]
P1	267.9	291
SP1	302.7	278
SP2	258.6	278
B1	140.1	291
B2	129.1	291

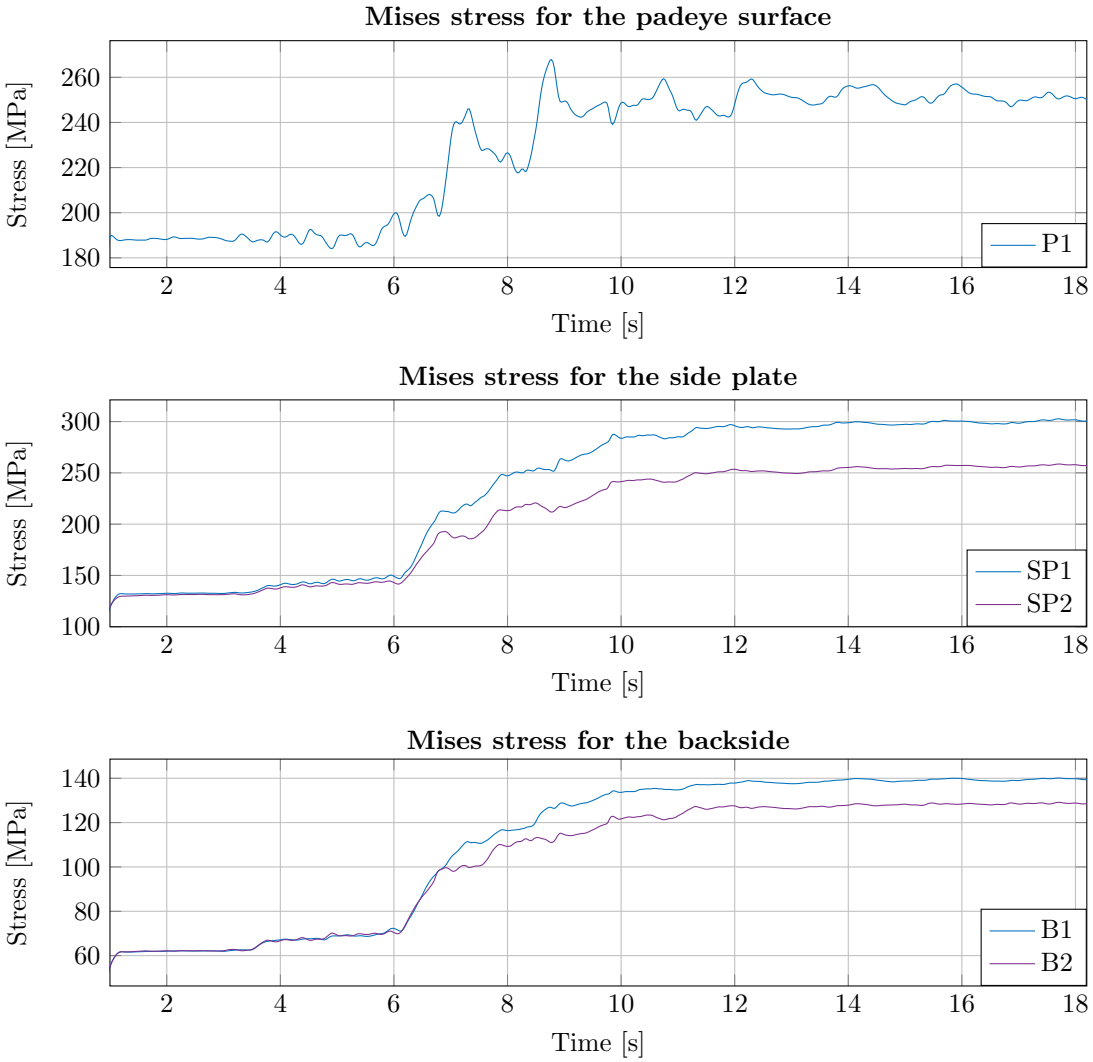

Figure 8.16. Stresses for the considered points using the unscaled horizontal excitation.

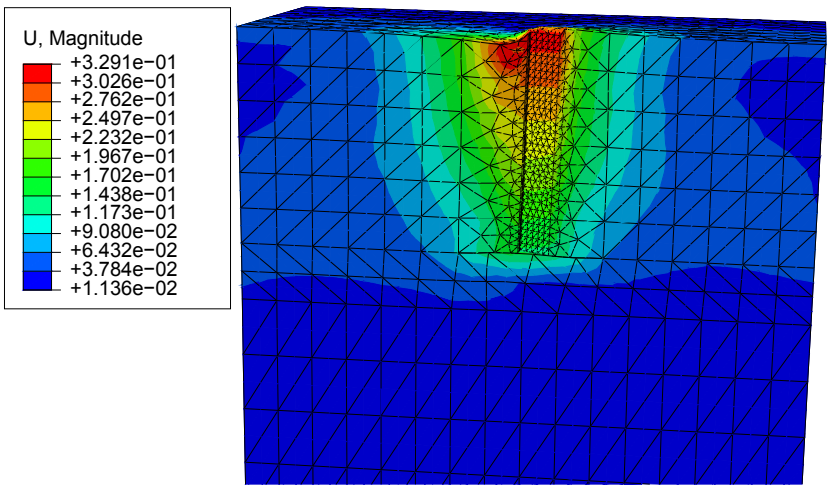

Figure 8.17. Soil displacements after applying the entire unscaled horizontal earthquake acceleration. The values are given in m.

Scaled horizontal excitation

The maximum stresses for the five nodes from the simulations with scaled horizontal excitations are presented in table 8.16. The results for the unscaled horizontal excitation are also included. The displacements after the entire excitation are shown in fig. 8.19. The maximum soil displacements for all of the considered horizontal accelerations are summarized in table 8.17. The displacement-time histories for a point at the top of soil domain in front of the anchor, shown in fig. 8.18, are presented in fig. 8.20.

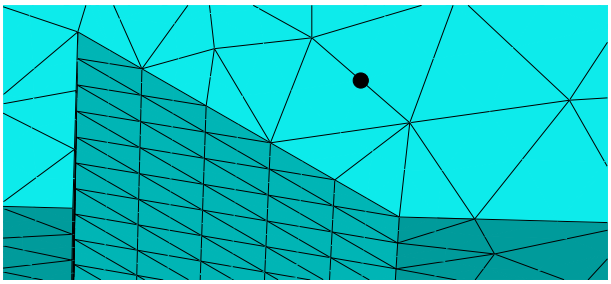

Figure 8.18. The node, at which the displacement-time histories are extracted, is indicated with a black dot. The point is located in front of the anchor at the top of soil domain.

Yielding occurs for the padeye for a PGA between 0.1 and 0.2g. The capacity of the side plate is exceeded for all of the considered horizontal excitations. The capacity of the backside of the anchor is not exceeded for any of the considered levels of PGA. It is not expected that this side of the structure is critical w.r.t. the overall capacity. Using plastic material properties results in larger displacements than using elastic properties. As an elastic-perfectly plastic model is considered, the stiffness of the soil around the anchor will be reduced due to material yielding. This results in larger displacements.

Table 8.16: Maximum stress for the five points from the plastic SSI analysis with unscaled and scaled horizontal excitations.

Point	**Max. stress** [MPa]				**Design yield**
/Node	PGA=0.074g	PGA=0.1g	PGA=0.2g	PGA=0.3g	**limit** [MPa]
P1	267.9	285.2	306.2	322.3	291
SP1	302.7	328.0	362.3	377.0	278
SP2	258.6	281.9	312.8	325.0	278
B1	140.1	151.6	167.9	175.9	291
B2	129.1	140.0	154.5	160.6	291

Table 8.17: Maximum displacement for the four considered horizontal excitations.

	Max. displacement [m]		
PGA[g]	**Magnitude**	**Horizontal**	**Vertical**
0.074	0.33	0.315	0.17
0.1	0.48	0.47	0.23
0.2	0.86	0.85	0.36
0.3	1.05	1.04	0.42

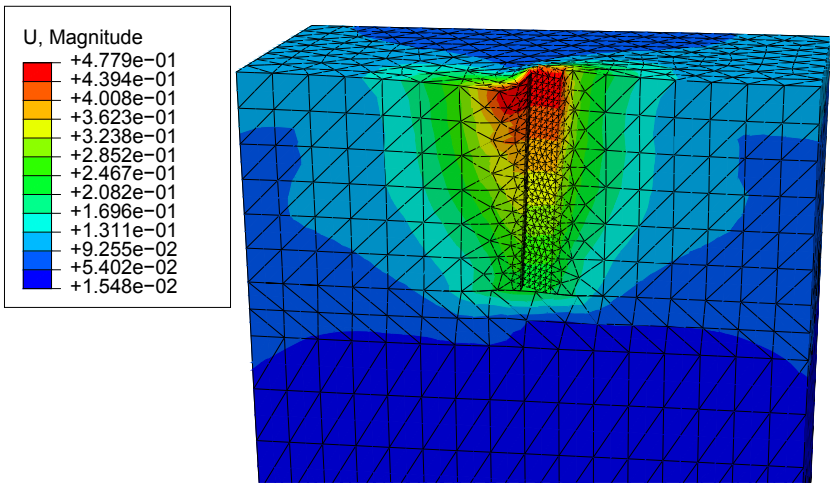

(a) PGA=0.1g

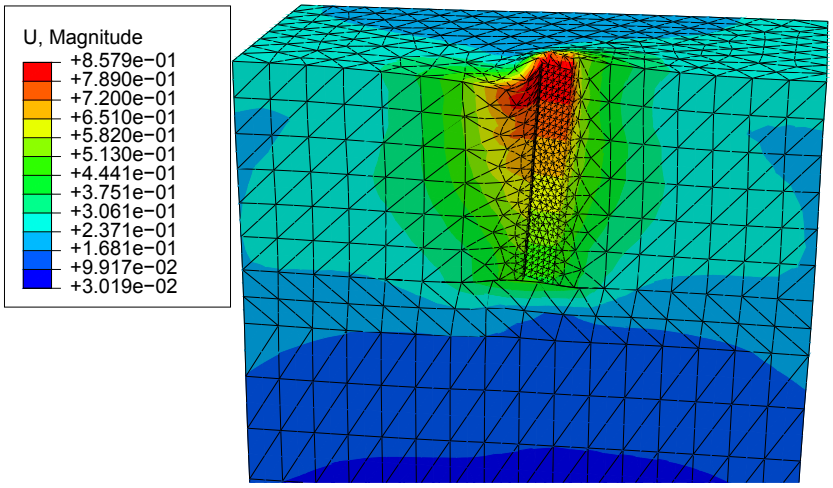

(b) PGA=0.2g

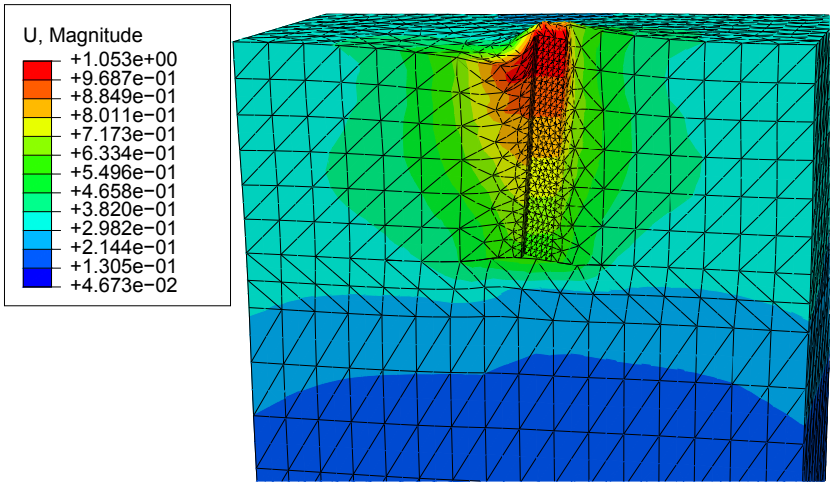

(c) PGA=0.3g

Figure 8.19. Soil displacements after applying scaled horizontal earthquake excitation. The values are given in m. A scaling factor equal to 3 has been used for the contour plots.

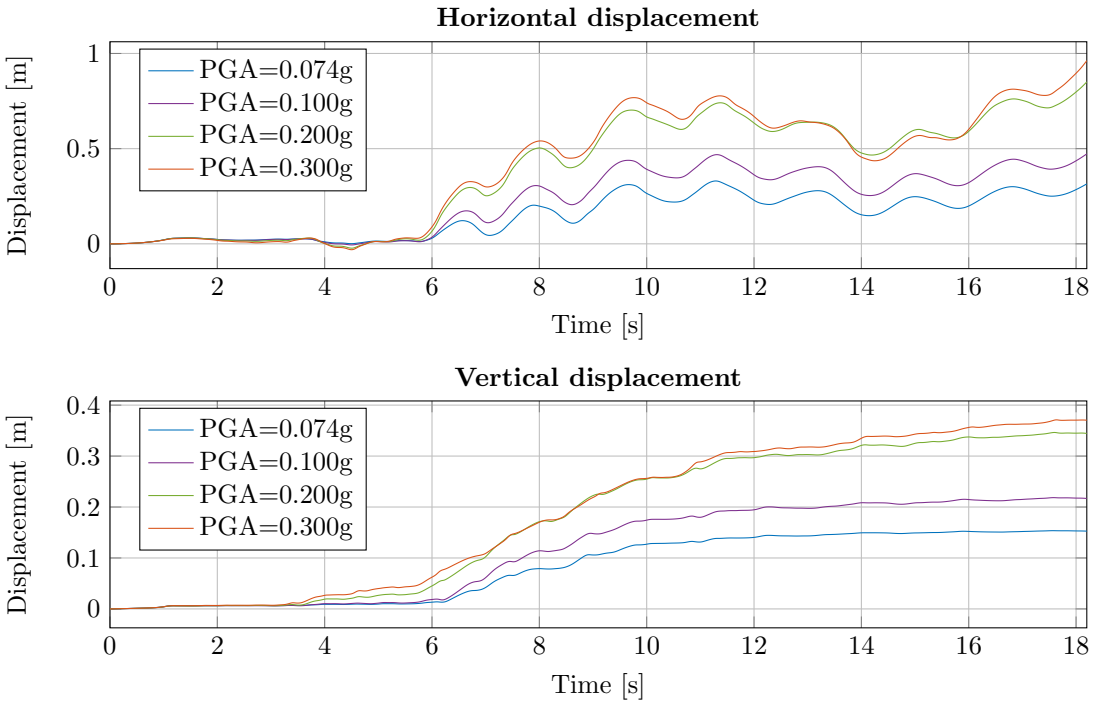

Figure 8.20. Horizontal and vertical displacement for the node in the soil in front of the anchor (see fig. 8.18). Only horizontal acceleration is applied at the bottom.

Horizontal and vertical excitation

The stresses from a simulation with simultaneous unscaled horizontal and vertical excitation are shown in fig. 8.21. The maximum stresses are summarized in table 8.18. The corresponding displacements of the soil volume are presented in fig. 8.22. The results indicate that the vertical excitation does not result in any large additional stresses for the structure. The horizontal excitation is scaled to the same PGA levels as previously with the vertical excitation scaled by the same factor. Since the vertical acceleration does not result in any large increases of the stress in the anchor, only the displacement is considered for the scaled excitations. These results are presented in table 8.19. The displacements for the node shown in fig. 8.18 are presented in fig. 8.23.

It can be observed, by comparing the results from table 8.17 and table 8.19, that the addition of vertical excitation results in an increase of the displacement magnitude (resultant). More specifically, the vertical displacement is increased, as expected. The horizontal displacements dominate the magnitude as the PGA of the horizontal acceleration is larger than the PGA of the vertical acceleration.

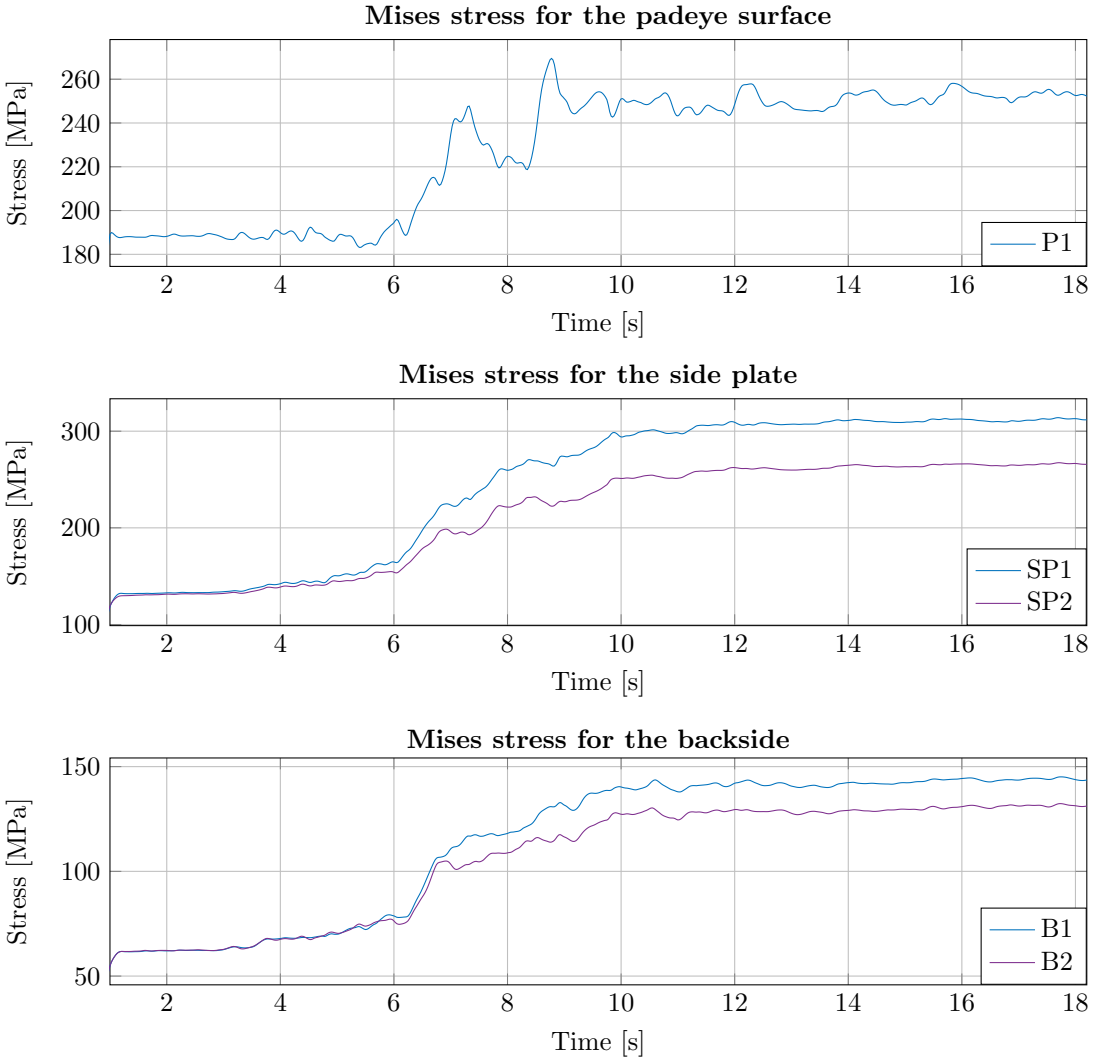

Figure 8.21. Stresses at the considered points of the anchor using unscaled horizontal and vertical excitations simultaneously.

Table 8.18: Maximum stress for the five points from the plastic SSI analyses with unscaled horizontal and vertical excitation.

Point/Node	**Max. stress** [MPa]	**Design yield limit** [MPa]
P1	269.5	291
SP1	314	278
SP2	267.4	278
B1	145.1	291
B2	132.3	291

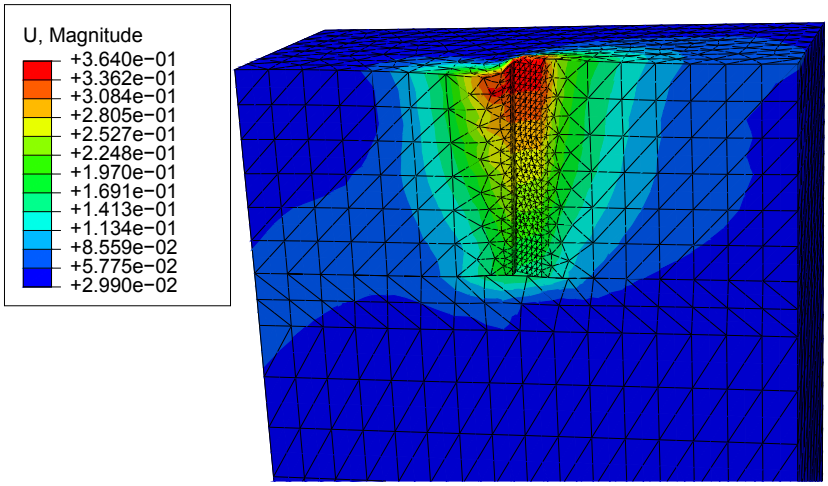

Figure 8.22. Soil displacements after applying the entire unscaled horizontal and vertical accelerations simultaneously. The values are given in m. A scaling factor equal to 3 has been used for the contour plots.

Table 8.19: Maximum displacement for the four considered cases with simultaneous horizontal and vertical bottom acceleration.

		Max. displacement [m]		
Horizontal PGA[g]	**Scaling factor** [-]	**Magnitude**	**Horizontal**	**Vertical**
0.074	1	0.36	0.355	0.22
0.1	1.36	0.52	0.51	0.28
0.2	2.72	0.96	0.93	0.46
0.3	4.08	1.22	1.19	0.56

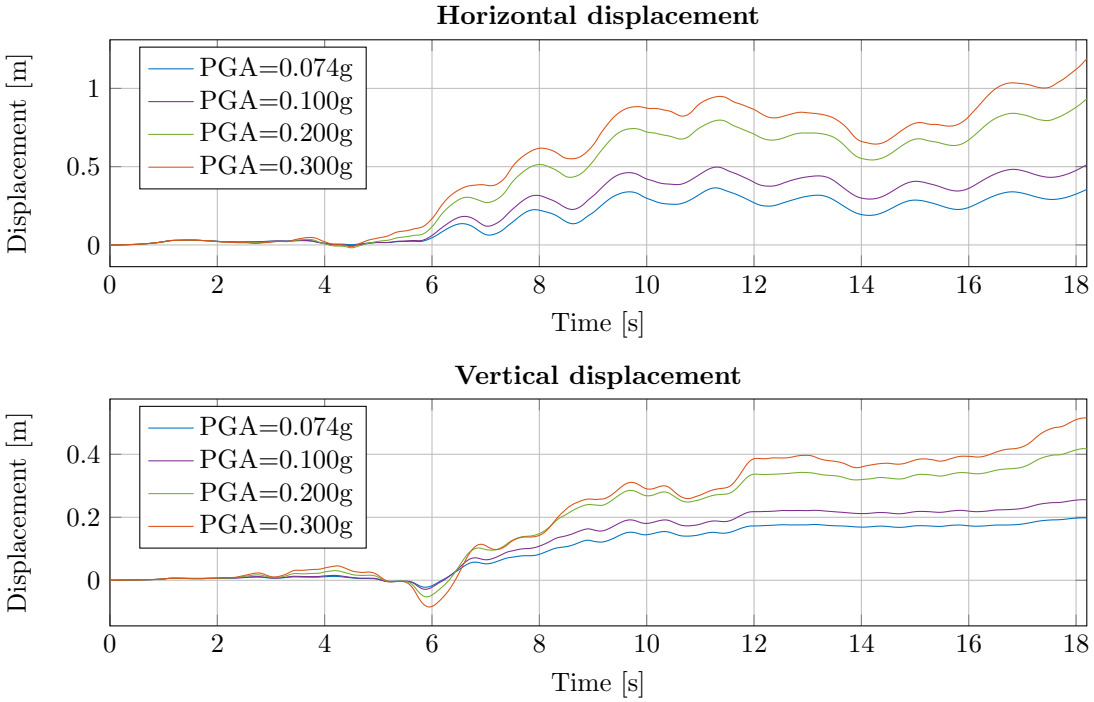

Figure 8.23. Horizontal and vertical displacement for the node in the soil in front of the anchor (see fig. 8.18). Horizontal and vertical acceleration is applied at the bottom. The PGA refers to the horizontal acceleration.

Soil strains

The results from table 8.17 and table 8.19 indicate that the displacements for the horizontal PGA's 0.2g and 0.3g could be large enough for the anchor to be pulled out of the seabed. The horizontal displacement is larger than 0.8m and the vertical displacement is larger than 0.3m for these PGA levels. The soil is considered to be ductile. Hence, it is possible that these displacements do not result in the anchor being pulled out of the seabed. In order to verify this, the total strains in the soil after the earthquake accelerations should be studied. The strains for four simulations with a horizontal PGA of 0.2 and 0.3g are considered. For the first ones, acceleration is only applied in the horizontal direction. For the second analyses, accelerations are applied horizontally and vertically. A third partition denoted Partition 3 is used. This is illustrated in fig. 8.24. A finer mesh is obtained with this partition compared to Partition 2. The strains for the points in fig. 8.25 are studied. The results are shown in fig. 8.26.

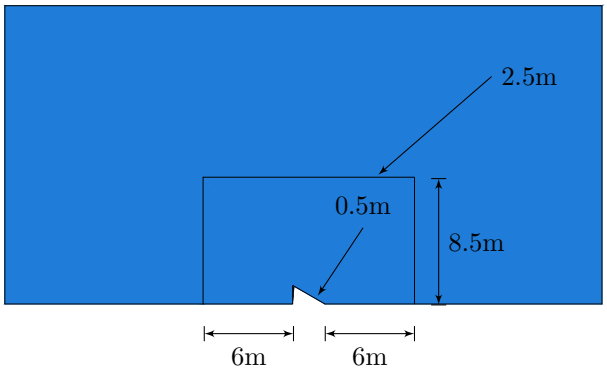

Figure 8.24. Partition 3, which is used for the analyses where the soil strains are of interest. The annotations refer to the element size at the surfaces.

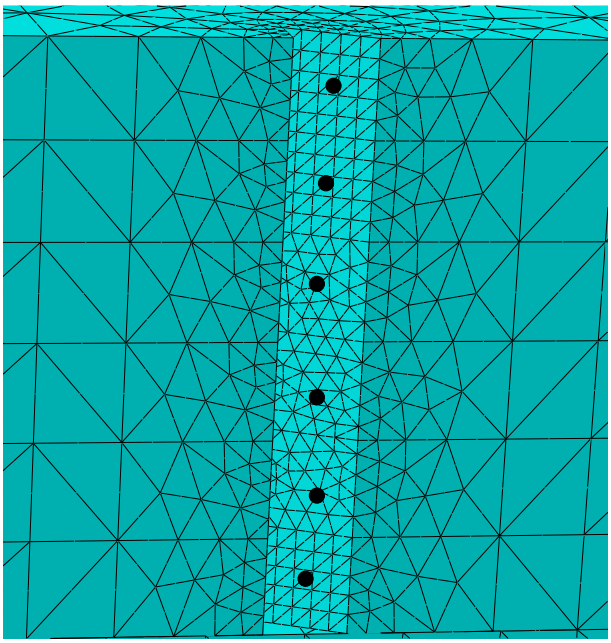

Figure 8.25. The points, at which the principal strain is studied, are indicated with black dots. These are located at the front anchor and in the middle of the upper six soil layers.

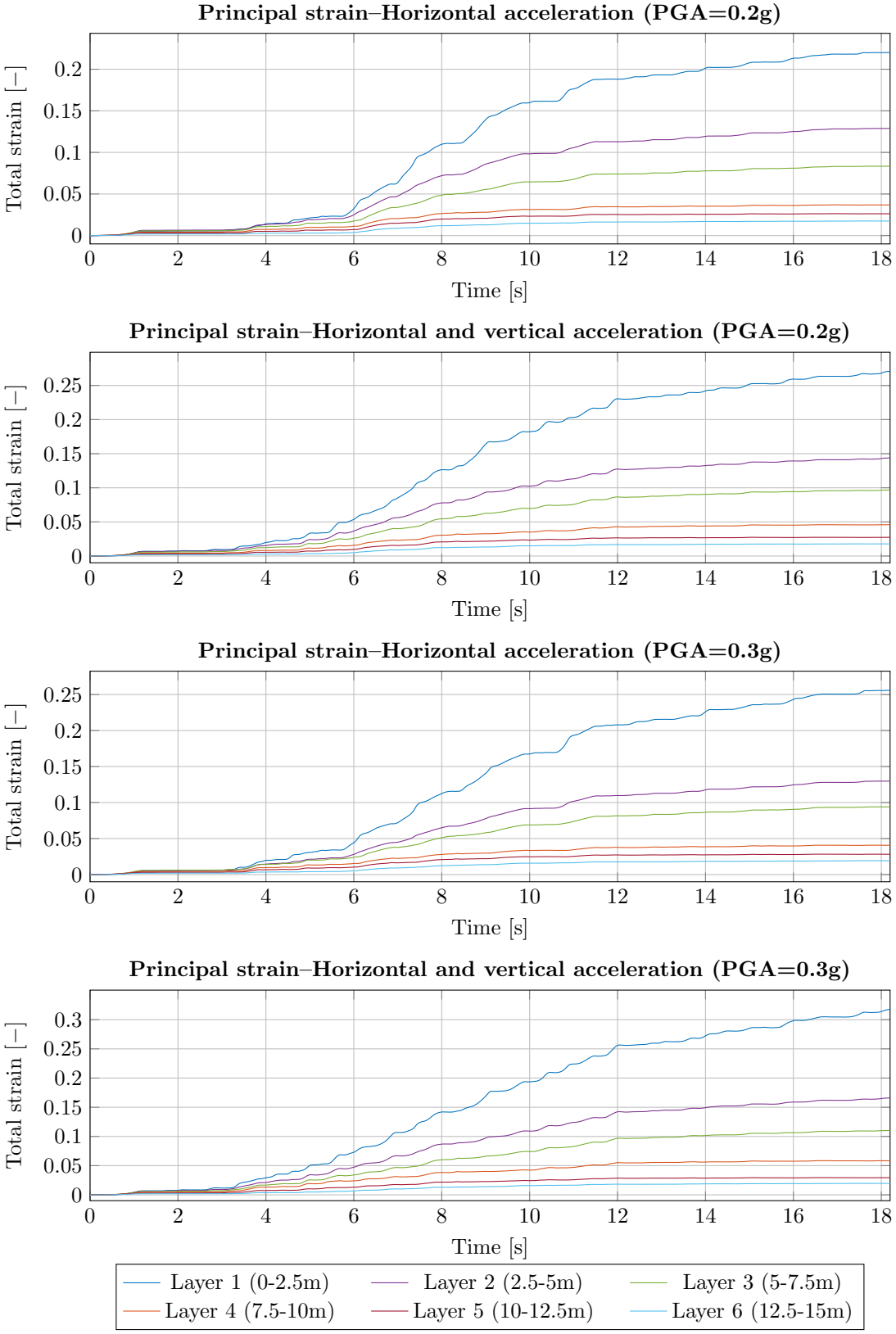

Figure 8.26. Principal strain for the points in the middle of the six soil layers around the anchor (see fig. 8.25). Horizontal PGA's of 0.2 and 0.3g are considered. The vertical accelerations are scaled accordingly.

The strains are larger in the upper soil layers as the yield limit and stiffness are smaller than for the lower layers. A strain limit of 5% is considered (Andersen, 2015). The total strains from the four analyses indicate that the chosen strain limit is exceeded for the three upper layers. When considering simultaneous horizontal and vertical acceleration with a horizontal PGA of 0.3g, it is observed that the strain in layer 4 also exceeds the limit of 5%. The results from fig. 8.26 indicate that it is possible that the anchor is pulled out of the seabed after an earthquake with a PGA equal to or larger than 0.2g.

Chapter 9

Discussion

9.1 Acoustic models

9.1.1 Numerical behaviour

It is important that the numerical behaviour of the acoustic FE models is sufficiently accurate and that these function as intended. The results from the models depend on the boundary conditions introduced in the model and the acoustic material properties of the seawater and seabed mediums. These factors will affect the reflection and decay of energy within the model during the seaquake.

During an actual seaquake, the variation of energy/pressure between the seabed and the water surface is expected to vary based on a number of different factors. Points along the seabed will radiate spherical pressure waves. This will result in a three-dimensional propagation of pressure with a complex variation. The three-dimensional pressure variation will depend on the topography of the seabed, i.e if it is flat or inclined. For all of the acoustic models studied in chapter 4, the incident seaquake wave is applied as a planar wave at the seabed. For the one-dimensional acoustic models, the pressure propagates as a planar wave. One of the reasons for this is the lack of boundary conditions on the vertical faces of the model. No energy is absorbed by the these surfaces. For the two-dimensional model, non-reflective acoustic impendances are introduced on the vertical surfaces at the two ends of the model. This resulted in a non-planar pressure wave propagating from the seabed during the excitation. This is shown in fig. 9.1, where the pressure in the model 0.075s after the excitation is applied is presented. A likely explanation to this is the vertical non-reflecting acoustic impedances. These seem to absorb some of the pressure propagating vertically from the seabed. The radiation of pressure from the seabed, for the 2D model, resembles the expected spherical radiation for an actual seaquake. Three-dimensional effects can not be represented by this model however, as it is only two-dimensional.

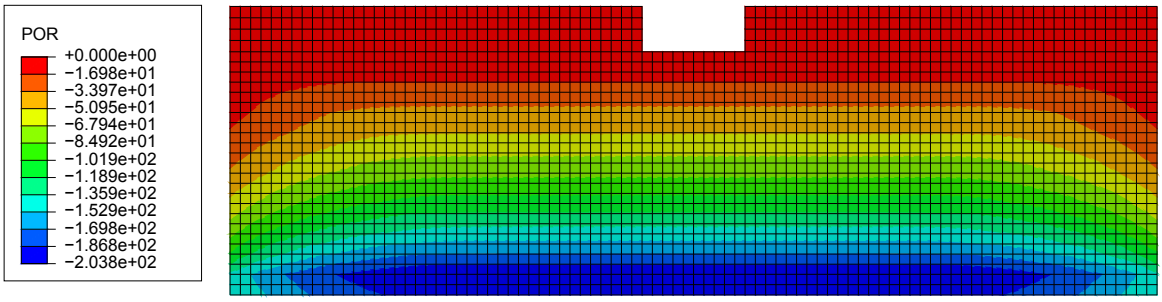

Figure 9.1. Contour plot of the acoustic pressure ([Pa]) in the 2D model at 0.075s. A non-planar pressure wave propagating from the bottom is shown.

In the chosen 2D acoustic model, the bedrock is modelled as an acoustic medium located under the medium which represents the seawater. At the bottom of the bedrock medium, a non-reflective acoustic impedance is introduced. When pressure waves are reflected by the water surface, and propagate downwards towards the seabed, a part of the wave will be reflected by the seabed while the rest is transferred into the bedrock. The non-reflective impedance ensures that the energy transmitted into the bedrock does not return to the model. By considering the studies related to the initial basic 1D model in chapter 4, it can be concluded that the use of a non-reflective acoustic impedance at the bottom of the model yields the desired numerical behaviour. The reflection of pressure at the boundary between the seawater and bedrock depends on the acoustic properties of the two mediums. More specifically, it depends on the density and speed of sound in the two mediums. The density and speed of sound in the bedrock will generally always be larger than for the seawater. This will of course depend on the chosen rock type to represent the bedrock. The large discrepancy between the acoustic material properties of the bedrock

and the seawater results in a large reflection coefficient. The boundary between the two mediums will have a behaviour similar to the one of a rigid reflector surface, and most of the pressure will be reflected back into the seawater medium. From the results in 4.2, it can be concluded that the boundary between the two acoustic mediums in the model behaves as intended w.r.t. the theoretical reflection coefficient.

9.1.2 Uncertainties related to the seaquake modelling

The chosen boundary conditions of the 2D acoustic model yield a sufficiently good numerical behaviour, when comparing with theoretical solutions and the expected pressure variation of an actual seaquake. Other uncertainties, which could affect the results for the pressure due to seaquake, are mainly the chosen representation of the seabed, the applied seaquake acceleration, at the surface between the bedrock and the seawater acoustic mediums, due to the vertical earthquake excitations and the possibility of having interaction between the seawater and the motion of the floating structure.

Seabed

The seabed is modelled as an acoustic medium consisting of a homogeneous bedrock layer, without any layers of sediments above it. When considering a real seabed, it is likely that there will be some layers of sediments such as clay above the bedrock. This is the case for the considered soil profile for the SSI analyses in this thesis. The presence of clay layers would affect the reflection of pressure at the seabed, as clay will have different acoustic material properties than rock materials. The type of rock which the bedrock consists of will also be uncertain and will be specific to the geographical site of interest. With the assumed bedrock properties, equivalent to the ones of granite, the reflection coefficient at the seabed is approximately 81%. As the density and speed of sound in soil materials such as clay are generally lower than the ones for rock materials, including layers of clay in the acoustic model could result in a lower pressure reflection in the model. Less pressure would be reflected by the surface between the sediments and the seawater, since the density of sediments is generally closer to the density of water than for rock materials. This can be seen by assessing the expression for the theoretical reflection coefficient in eq. (2.97). Hence, a larger part of the total pressure in the model would be absorbed by the mediums representing the seabed, and disappear from the model through the non-reflective impedance at the bottom. Subsequently, the magnitude of the pressure over time during the seaquake would be lower and less conservative forces could be obtained under the floating structure.

Including sediment layers in the acoustic models could also introduce an amplification of the accelerations at the bottom of the bedrock through the soil up to the seabed. Similarly to the soil amplification associated with vertically propagating shear waves in soil (described in 2.2.4), soil amplification also occurs for vertically propagating pressure waves. When the frequency content of the earthquake excitation corresponds with the natural frequencies associated with the vertical compression motion, the acceleration is amplified through the sediment layers. The resulting pressure at the seabed would therefore be larger than the ones at the bedrock. This would yield larger pressures under the floater and subsequently a larger response for the structure.

Seaquake acceleration

The acceleration, specified at the top of the bedrock layer representing the seabed (seaquake acceleration), in the 2D acoustic model is a planar incident wave applied over a plane horizontal seabed surface. The width of the model is 450m and it is highly unlikely that over the such a distance the seabed remains perfectly horizontal and plane. The assumption of a plane seabed neglects all the effects of the seabed topography on the pressure variation in the model. An inclination of the seabed will give an inclined pressure propagation, as the pressure waves propagate perpendicularly w.r.t. the seabed surface. This would affect the amplification of pressure within the model. If a valley-shaped seabed is considered, the amplification of pressure could be greater than for a plane horizontal seabed. A possible improvement for the 2D model would then be to include the topography of a seabed specific to a geographical site of interest.

The effects of incoming ocean waves on the seaquake pressure is not considered in the acoustic model. It is uncertain whether or not this simplification is conservative or not when considering the pressure acting under the floating platform. The combined effect of the pressure due to seaquake and ocean waves on the platform is expected to be highly complicated. It would be challenging to determine which part

of the response is caused by the seaquake. It is expected to be highly unlikely that a seaquake would occur during an unfavorable sea state like the one described in 5.2. An analysis considering waves, with a mean wave amplitude, specific to a geographical site, could have been conducted.

One last uncertainty regarding the seaquake loading is that the seabed has a uniform vertical displacement in the acoustic models. This occurs due to the use of a planar incident wave and the use of plane seabed. In reality, the displacement is expected to be different at different points along the surface of the seabed, especially if a surface with a width of 450m is considered. This would affect the distribution of pressure. When considering a seabed with an arbitrary topography, it is uncertain whether or not the simplification of a seabed with a uniform vertical displacement is conservative or not. A uniform vertical displacement of the seabed, as in the 2D acoustic model, is expected to be conservative w.r.t. the pressure under the floater for a plane horizontal seabed.

Fluid-structure interaction

The seaquake force used in the SIMA model is determined from the pressure obtained in the 2D acoustic model. In the Abaqus model, the bottom of the platform is modelled as a rigid surface with full reflection and no displacement. No interaction between the water and the platform is included in the model. In reality, the platform would experience some displacement during the seaquake pressure. This will lead to additional pressure waves radiating through the water from the floating structure. Hence, the pressure acting on the platform would be influenced by the motion of the platform itself, and not only by the pressure generated from acceleration at the seabed. In order to include the effects of this additional pressure, a coupled analysis including the structure and the seawater must be performed. The representation of the bottom of the floater as a rigid surface is assumed to be reasonable, based on the large natural period associated with the heave motion of the platform. The natural frequency for the heave motion is small compared to the frequency content of the excitation, which is between 0 and 6Hz. Since the response is dominated by inertia forces (mass controlled), it is assumed to be small.

The assumption of a rigid surface for the bottom of the platform affects the pressures which are introduced at the bottom of the wind turbine in the SIMA model. This model includes effects, related to interactions between the fluid and the structure, such as hydrodynamic damping and added mass. Therefore, it is assumed that the only source of error is related to the pressure obtained from the Abaqus model.

9.1.3 Sensitivity analysis

The water depth considered for the 2D acoustic model is 130m. The results obtained from the model using different water depths should also be investigated. Depths of 70m, 200m and 300m are also considered. None of the properties for the 2D acoustic model are modified except for the water depth. The bottom of the floater is still considered to be located 22m beneath the ocean surface. The resulting pressure-time histories, using the unscaled strong motion vertical acceleration, for the new depths are shown and compared with the pressure obtained with a depth of 130m in fig. 9.2. The pressure under the middle of the platform is assessed.
Pressure peaks occur at different times for the four depths. This is related to the speed of sound in water. As the pressure wave velocity is constant for the four depths, the pressure will be amplified at different time instants since it takes more time for a wave to propagate upwards and downwards to meet another wave when the depth increases. By observing the magnitude of the pressure for the four depths, it can be seen that the pressure seems to diminish when the depth increases. The one exception is the peak which occurs for a depth of 130m between 6 and 7s. One possible reason for this exception could be that for a depth of 130m the frequency content of the vertical seabed acceleration is close to one of the natural frequencies of the seawater medium, related to propagation of pressure waves. Another reason could be an unfavourable constructive interference between two waves, where one wave propagates upwards and the other propagates downwards after being reflected by the rigid reflector surface. No damping is introduced in the 2D acoustic model. Therefore, a likely explanation to the trend where a larger depth results in lower pressure amplitudes, could be the non-reflecting acoustic impedances used at the vertical surfaces, at each end of the model. A larger depth means that the impedance acts over a larger surface, which could lead to larger reduction of the total energy in the model. It is expected that some damping will be present in the water. More specifically, damping related to the viscosity of the water could slightly decrease the pressure in the seawater domain. A larger depth would then result in more

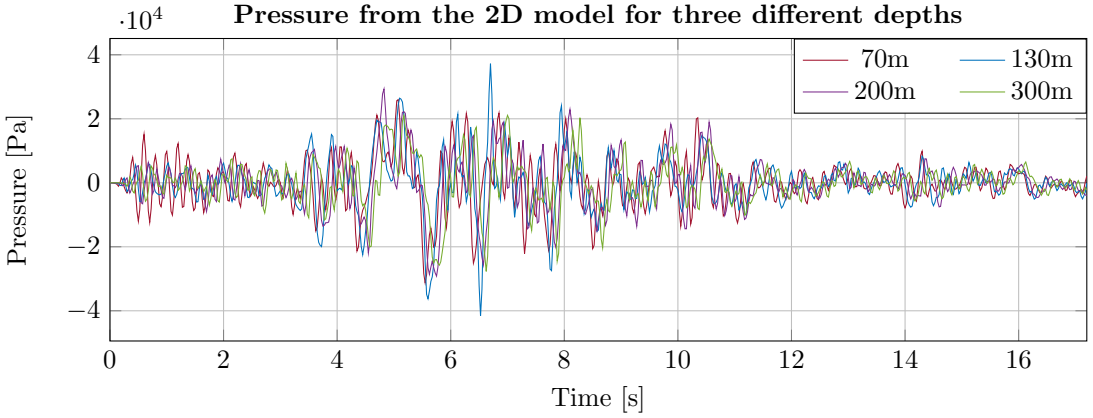

Figure 9.2. Pressure-time series from the 2D acoustic with four different depths (70m, 130m, 200m and 300m). The unscaled strong motion vertical acceleration series has been considered.

dissipation of energy due to viscous effects. This corresponds with the previous observation of decreasing pressure amplitudes for increasing water depths in the 2D acoustic models.

9.1.4 Alternative models

Instead of using acoustic FE models in Abaqus, alternative softwares could possibly have been considered to model the pressure under the floater during a seaquake. HydroD is a software for hydrodynamic analysis and stability analysis, which allows for analysis in the frequency and time domain (DNV-GL, 2016). The analyses are based on one common model which is fully integrated with finite elements. HydroD is often used for ballasting, hydrostatic and hydrodynamic analysis of large fixed and floating structures. Typical examples of structures analyzed with the software are gravity-based platforms, ships, semi-submersibles and tension leg platforms. HydroD is the user interface for the hydrodynamics solvers WADAM and WASIM (DNV-GL, 2016). WADAM is a hydrodynamic analysis program which can calculate wave-structure interaction for fixed and floating structures of arbitrary shape. It is possible to perform so-called multi-body analyses with HydroD. Analyses can be run in the frequency domain for several different bodies, where full hydrodynamic interaction between the bodies is included. Such an analysis could be a viable alternative to the acoustic models considered in this thesis. More specifically, the floating platform could possibly be represented by one body and the seabed by an other. WADAM allows for floating and fixed bodies in multi-body analyses. The hydrodynamic interaction between the bodies is computed from potential theory as for a single structure, but the number of DOFs is increased (DNV-GL, 2017, p.17-18).

S. H. Karlsen used HydroD to assess the forces on ships during barge transportation of heavy objects (Karlsen, 2010). For a stationary vessel, HydroD uses WADAM to determine the hydrodynamic forces acting on a floating body. In WADAM, potential Airy wave theory and a sink-source technique is employed to describe the motion and pressure. Based on this, the resulting forces on a floating body of arbitrary shape can be determined. Panel models of the hull geometry and the structural model were created in GeniE, which is a tool for high level geometry modelling of offshore structures developed by DNV GL. WADAM determines the response for single linear waves in a specified frequency interval. More specifically, the software calculates the frequency dependent transfer functions. S. Rusnes used WADAM to consider how the interaction between floating cylinders is affected by wave loading (Rusnes, 2010). Finally, S. M. Hermstad used Wadam to calculate hydrodynamic wave loading, mass, damping and stiffness for the Bergsøysund Bridge, which is a floating pontoon bridge (Hermstad, 2013). The floating pontoons were modelled using software for hydrodynamic analysis such that the resulting hydrodynamic properties could be implemented in a time domain analysis in Abaqus. More specifically, panel models of the pontoons were created in GeniE and the hydrodynamic properties/parameters were extracted from WADAM.

9.2 Seaquake response

9.2.1 Results

Platform and nacelle response

Applying the seaquake loading obtained from the acoustic models yields small vertical displacements of the platform, compared to displacements during environmental loading using the sea state described in 5.2. The exception is the heave response due to the conservative pressure from the 1D rigid model in 6.2.1. This was however deemed unrealistic, and is not considered to represent the real pressure acting on the platform due to a seaquake. The platform heave during one simulation of environmental loading is shown in fig. 9.3. Here, heave amplitudes close to 10m are obtained. It is uncertain whether the considered sea state yields a representative large heave displacement and -acceleration of the platform or not. However, the sea state was deemed to result in a sufficiently large structural response to serve as the basis for a comparison with the seaquake response.

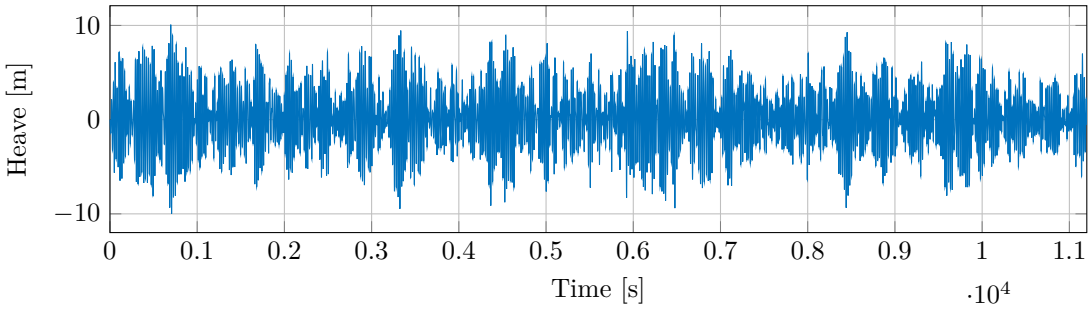

Figure 9.3. Platform heave during one three-hour simulation of environmental loading.

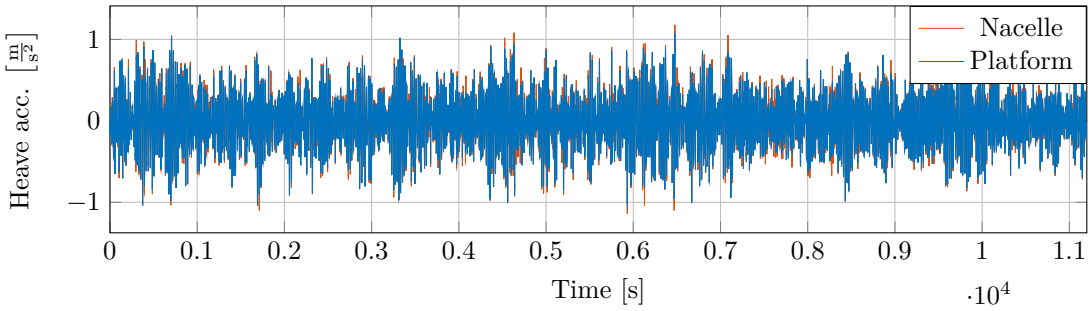

Figure 9.4. Platform- and nacelle heave accelerations during one three-hour simulation of environmental loading.

The peak vertical accelerations obtained, due to unscaled acoustic pressures, are however larger than accelerations obtained during the environmental loading. Heave acceleration of the platform and the nacelle during one three-hour environmental loading simulation is presented in fig. 9.4. Amplitudes of around $1^{m}/_{s^2}$ are obtained during the environmental simulation. The peak accelerations are similar for the platform and the nacelle, unlike what is experienced during seaquake loading, where the platform accelerations are amplified through the tower. This is expected to to be the result of the higher frequency content of the seaquake loading approaching one of the natural frequencies of the tower. The peak vertical accelerations of the platform and the nacelle due to the considered seaquake are $1.6484^{m}/_{s^2}$ and $2.5997^{m}/_{s^2}$, respectively. These are the result of applying the unscaled 2D acoustic pressure described in 6.2.4. The scaling of the seaquake pressure, as shown in table 6.3, increases the response accordingly. It is uncertain whether the larger PVA values of the seabed are realistic or not. A representative PVA would have to be determined for a specific site of interest for design purposes. The higher accelerations, especially at the elevation of the nacelle, could potentially lead to harmful stresses in connections between the nacelle and the tower. Advanced equipment contained within the nacelle could potentially get damaged as well.

Tower response

The tower in the provided SIMA model of an FWT is divided into 27 sections, with one beam element per section as illustrated in fig. 9.5. As the computational effort involved with calculating the response of the FWT to several three-hour environmental simulations was quite large, a finer discretization of the tower has not been considered as it would increase the computational effort even further. However, a finer discretization could lead to a more accurate representation of the tower and nacelle response during seaquake, because it would lead to a better representation of the natural frequencies of the real tower. How accurately damping in the tower is handled in the provided model is uncertain. As damping present in a steel structure of this type is expected to be quite low, the obtained response is likely not too exaggerated.

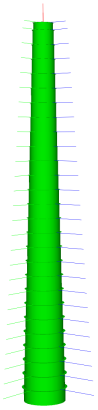

Figure 9.5. Discretization of the wind turbine tower in the SIMA model.

9.2.2 Modelling limitations

The analyses of the seaquake response of an FWT were carried out using a SIMA model developed by SINTEF Ocean. Due to the limited knowledge of the authors on the subjects of hydrodynamics and floating structures, a lot of effort was put into trying to comprehend the underlying theory behind the model. The limited experience regarding modelling of floating structures meant that the behaviour of the provided model was trusted to be representative for the real structure, and the ability to verify the results was limited.

Representation of the semi-submersible platform

The loading on the FWT model due to seaquake was introduced as concentrated forces, acting vertically on the bottom of the semi-submersible platform. The platform is shown in fig. 9.6. As the platform in the provided model was modelled as a rigid body, without any flexibility, this was thought to represent the loading in a sufficient way. Effects such as internal forces in the platform itself, during the seaquake loading, can however not be captured this way. To accurately model the internal load effects on the platform during a seaquake, a 3D FE model, including the material properties of the concrete and the post-tensioned reinforcement would have to to be developed. The seaquake pressure could then be distributed over the surfaces of the platform to represent the loading more accurately, and internal load effects could be considered. The large pressures acting on the platform due to seaquake could possibly lead to large bending moments and shear forces at the section between the pontoon and the central column, which is not considered in this thesis.

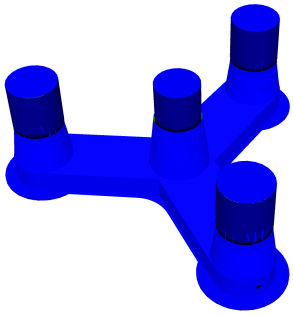

Figure 9.6. Wind turbine platform modelled as a rigid body in SIMA.

Seaquake loading on the mooring system

The way the loading is introduced in SIMA means that the only part of the model which experiences the seaquake at first hand is the rigid platform. In reality the seaquake pressure, resulting from the vertical motion of the seabed, would also influence the response of the mooring system directly. The influence of pressure on the mooring system is not captured in this thesis. As the mooring lines are slender and flexible, the influence of pressure is not expected to present much of an issue. The mooring system could however comprise other equipment sensitive to the large pressures like flotation devices. In this thesis, seaquake loading on the mooring system is only indirectly introduced through the platform response.

Anchor excitation

A comprehensive study of the anchor response due to earthquake excitation, with simultaneous loading from a mooring line, was conducted. However, no excitation of the anchors is performed during the seaquake analyses of the FWT in SIMA. For a catenary moored FWT, like the one studied in this thesis, excitation of the anchors alone would likely not lead to any issues for neither the mooring system nor the

turbine itself. This is due to the relatively small ground displacements during an earthquake compared to the horizontal displacements of an FWT during loading from the environment. The mooring system has to be flexible enough to allow for first order wave motion without any problems, which makes the system able to handle the ground motion imposed by an earthquake, without large tensile forces developing in the mooring lines. The combined effect of platform excitation from a seaquake and anchor excitation by an earthquake could however lead to higher tension values in the mooring lines than what is obtained in this thesis, by platform excitation alone. To be able to perform a simulation of simultaneous excitation of the anchors and the platform, a comprehensive model would have to be developed to handle this complicated situation. In order to be able to accurately model the response of the entire system, the model would likely have to include the anchors, embedded in a soil layer, as well as the mooring lines, the water and a structure representing the FWT on top. Such a model could possibly be handled by a general purpose FE program e.g. Abaqus.

9.2.3 Uncertainties regarding modelling in SIMA

Damping and added mass during seaquake

Hydrodynamic damping of the platform, as well as added mass, during motion due to seaquake excitation is handled by the hydrodynamic properties defined in the SIMA model. Damping due to the generation of waves radiating outwards from the platform in motion, is frequency dependent. The added mass is also frequency dependent and these have both likely been determined by a hydrodynamic solver like WADAM. As the frequency content of the seaquake excitation on the platform is high compared to the regular excitation from wind-waves, it is uncertain how accurately the damping and added mass is represented for these high frequencies.

Reported SIMO accelerations

Close to the project deadline, OO reported possible errors w.r.t. the accelerations provided by SIMO. This can represent a possible source of error for the accelerations presented in the thesis. In order to verify the obtained accelerations, these are estimated using numerical differentiation on the corresponding displacement data. More specifically, the nacelle accelerations during seaquake excitation of the platform, using the unscaled 2D acoustic pressure, are considered. The obtained acceleration from SIMO along with the estimate based on numerical differentiation are shown in fig. 9.7. Basing the differentiation on the entire position signal gave large amounts of numerical noise. This is further described in B.5. The results indicate that the correct acceleration is provided by SIMO, but some uncertainty is still present.

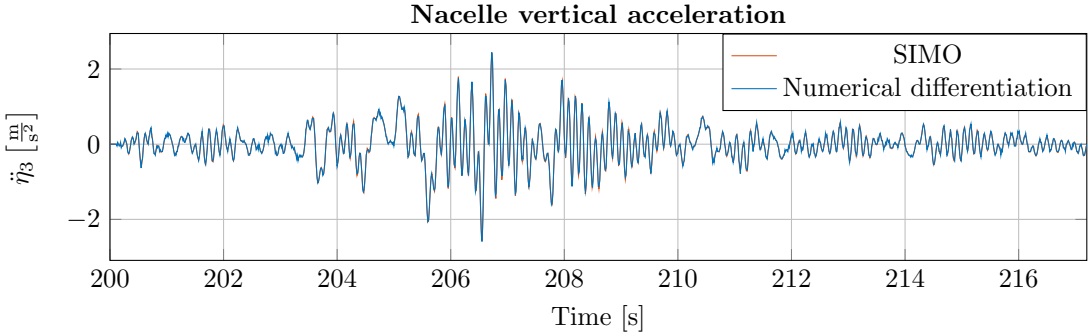

Figure 9.7. Comparison between vertical acceleration in the nacelle reported by SIMO, and acceleration based on numerical differentiation of every 10th value of the corresponding position signal.

Snap-tension due to mooring line slack

During seaquake excitation on the FWT during calm environmental conditions, parts of the mooring lines experience slack (no tension), (see fig. 6.20). The slack occurs for the scaled seaquake pressures which correspond to a seabed PVA of 0.15g or higher. This is likely due to the relatively high frequency motion of the platform, which the mooring lines can't keep up with due to their large inertia. The slack is even more pronounced for the leeward mooring lines during the simultaneous environmental loading and seaquake in 6.6. During design of the mooring system of an FWT, the pre-tensioning and the

configuration of the mooring lines are adjusted to avoid zero tension to a large extent. This is verified during the environmental loading analyses, described in 5.2, where the tension in the leeward mooring lines rarely approaches zero. Tension in the leeward mooring lines, at the anchor, during one of the simulations with environmental loads is shown in fig. 9.8. How accurately the tensile forces in a mooring line are represented as the line is stretched, following zero tension, in the SIMA analyses is uncertain. The phenomenon referred to as "snap-tension" is when an unloaded structural component, like a mooring line, abruptly goes into tension. To be able to accurately represent this phenomenon in the model, a detailed model of the mooring line including individual chain links would likely have to be developed, using an explicit solver with a very small time step to capture the response.

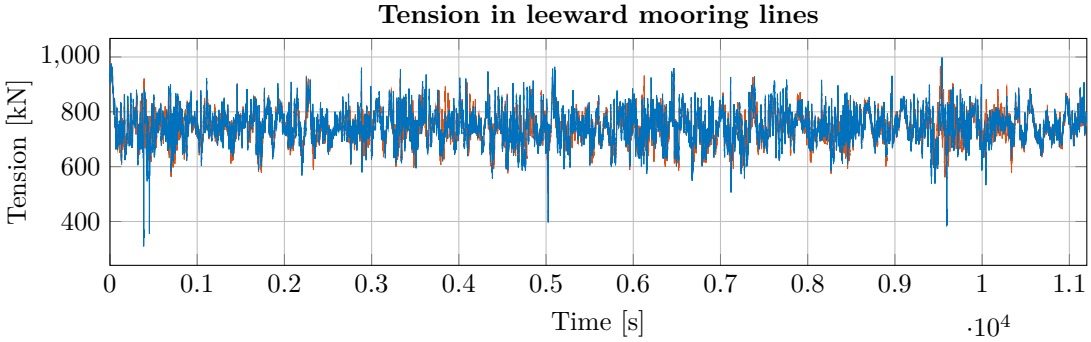

Figure 9.8. Tension in the two leeward mooring lines, at the anchor, during one of the three-hour simulations of environmental loads.

9.2.4 Different mooring systems

The considered model of an FWT comprises a catenary mooring system. This system has been used in anchoring of offshore structures for decades. Catenary mooring lines provide station keeping of the floating structure by the suspended weight occurring as the lines are tightened. To provide the necessary station keeping for the floating structure, the lines have to be quite heavy. For large depths, other mooring system alternatives may have to be considered as the suspended weight of the catenary lines becomes too large. Also, for shallow water depths, a catenary mooring system has to be pre-tensioned to a level which limits horizontal motion. This is done to spare the cables connected to the seabed, which transfer the electric power produced by the turbine.

Taut mooring

For taut mooring systems, the station keeping is provided by the axial stiffness of pre-tensioned mooring lines. The lines can be made of lightweight materials like polyester. Compared to catenary mooring lines, taut mooring lines follow a more or less straight line from the anchor connection to the connection on the floating structure, as shown in fig. 9.9b. Hence, a vertical force component will be acting on the anchor due to the platform response, and the anchor must be designed accordingly. This system, as for the catenary system, has to be flexible enough to handle first order wave motion without any issues. Horizontal excitation of the anchors due to earthquake is therefore not expected to yield problematic straining of the lines. However, the inclination of the lines at the anchor may lead to vertical forces on the anchor during seaquake excitation on the platform. The effect of a seaquake on a taut mooring system is not considered in this thesis and should be investigated further.

TLP

A TLP system is likely more prone to vertical ground accelerations produced by an earthquake compared to the previously mentioned mooring systems. This is due to the large pretension and stiffness of the tension legs, which could potentially transfer large stresses from a vertical seaquake excitation of the anchor up to the connection at the platform.

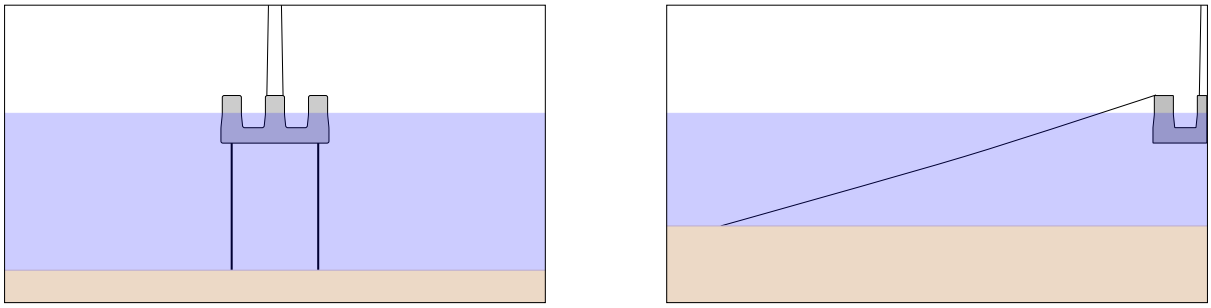

(a) TLP **(b)** Taut

Figure 9.9. Two different mooring systems for floating platforms.

9.3 SSI model

9.3.1 Elastic and plastic soil material properties

The results in 8.4 and 8.5 show that the material properties have an important effect on the response of the anchor and the soil. The maximum displacement of the soil volume, for the elastic SSI model using the unscaled horizontal excitation, is approximately 3cm. For the plastic SSI model, with the same excitation, it is approximately 30cm. The Mises stress in the anchor is larger for the plastic model than for the elastic model. This is especially the case for the side plate, where the stress is smaller than 100 MPa for the elastic model and it is larger than 300 MPa for the plastic model. When the yield limit (shear strength) is reached for a soil layer, the stiffness of the layer is reduced since an elastic-perfectly plastic model is used. A reduced stiffness results in larger displacements for the soil around the anchor and consequently larger stresses for the anchor. As the side plate prevents horizontal displacement, it seems reasonable that the stress in this component is increased when plastic material properties are utilized.

The magnitude of the maximum displacements of the soil domain from 8.5 creates doubts regarding the neglecting of effects due to non-linear geometry. For instance, when a PGA of 0.3g is considered for the horizontal excitation, the maximum displacement is over 1m. This cannot be considered as a small displacement when it is compared with the dimensions of the anchor like the height which is 15m. Non-linear geometry should have been included in the FE models. This was not done due to the large additional computational time that would be required. The FE models contain approximately 30000 second-order solid elements. The large number of unknowns would result in a large computational time as the stiffness matrix must be computed for each increment when non-linear geometry is considered. As an implicit integration method is used for the dynamic analyses, the effective stiffness matrix, which is non-diagonal, is inverted to determine the response in the next time increment (see A.2), which increases the computation time. Computing the stiffness matrix for each increment when considering a non-linear geometry would increase the computational effort even further.

9.3.2 Numerical behaviour of skins

The use of skins to represent the anchor structure could give rise to sources of error. The skin is bounded or attached to the surface on which it is assigned. Hence, it is expected that the response of the part, on which the skin is assigned, will affect the response of the skin. When comparing the results for the elastic and the plastic SSI models, the numerical behaviour of skins could be a reason for the large difference between the responses for the models. When the stresses in the soil around the anchor exceed the yield limit within one of the layers, the overall stress state in the soil is modified. The stress in the remaining soil layers is expected to increase due to the lack of hardening in the soil layer which has yielded. This increase of soil stresses could possibly result in an increase for the stress in the skin. The stresses in the anchor are expected to increase when the soil yields due to the reduced stiffness. However, it is possible that, for a model which implements contact between the soil and the anchor, where the anchor is not attached to the soil, the increase in stress will not be as large as the previously observed differences between the two SSI models.

The possible undesired effects of skins on the anchor stresses could mean that the stresses from the plastic SSI model are unrealistically large. The capacity of the side plate is already exceeded for a horizontal excitation with a PGA of 0.074g, which is not a particularly large PGA. Large stresses can be expected for this component as its purpose is to prevent horizontal displacement of the structure. It is uncertain whether or not stresses over 300 MPa are reasonable. The results should nevertheless not be ignored. An alternative model using a different approach for the modelling of the anchor should be considered. More specifically, a model where the anchor is represented by one part and not a skin, and contact imposed between the soil and the anchor should be considered. Such a model could allow for sliding between the structure and the surrounding soil, which is present for actual structures. It is uncertain if allowing for sliding between the anchor and the soil is conservative w.r.t. the stresses and displacements of the structure. Modelling contact between parts in an FE model can be challenging and time consuming and was not done in this thesis.

As it seems the behaviour of skins affects the stresses in the anchor, it could be possible that it also

affects the stiffness of the overall model. More specifically, the displacements of soil are affected by the stiffness of the anchor and vice versa. If the stresses in the structure are too large it could also be expected that the displacements are too large. The scaled horizontal excitation with a PGA of 0.3g yields a maximum displacement of approximately 1m. This PGA level is considered to be quite large and such a displacement magnitude could be reasonable. However, it could also be too conservative due to the previously explained sources of error.

9.3.3 Damping

The damping in the SSI model is based on the natural frequencies of the soil profile without the presence of any structure. As mentioned in 2.2.5, SSI can reduce the natural frequencies of the system (anchor+soil) compared to the ones for a corresponding free-field soil profile. An unfavourable consequence of reduced natural frequencies could be that a larger number of natural frequencies are within the range of the frequency content of the earthquake accelerations. Hence, larger displacements and accelerations could occur around the anchor, which result in larger stresses in the anchor and larger displacements for the surrounding soil. Alternatively, the mode shapes and natural frequencies of the SSI model, including the soil and the anchor, could have been determined, to be used as the basis for the Rayleigh damping coefficients in the model. An estimate for the overall damping ratio related to the combined energy dissipation in the soil and the anchor would be difficult to obtain. A typical damping value for clay is around 5%, while for steel, typical damping values are in the range of 0 to 0.5% (Chandrasekaran, 2018, p.258). Hence, most of the energy dissipation in the SSI model is due to the material damping associated with the soil. Therefore, it is reasonable to mainly consider the damping from the soil. A possible improvement for the SSI model could be to base the Rayleigh damping coefficients on the natural frequencies of the SSI model, which includes both the soil and the structure.

Vertical accelerations were applied simultaneously with horizontal accelerations at the bottom of the SSI model. The damping within the model is based on the mode shapes and natural frequencies associated with propagation of shear waves. No specific damping, based on the mode shapes associated with the propagation of pressure waves, is introduced. Hence, the correct damping for the vertical accelerations, which produce pressure waves, is not included. Only one set of Rayleigh damping coefficients can be defined per material in Abaqus. As the horizontal accelerations have larger amplitudes than the vertical components, it is more important to include sufficiently accurate damping mechanisms for the shear waves than for the pressure waves. However, it should be noted that resonance related to vertical modes could result in large displacements at the top of the soil profile, if too little damping is included in the model.

9.3.4 Reflection of waves

As no dampers are introduced at the boundaries of the soil volume, it is important to consider a soil domain which is large enough for the material damping to reduce the amplitude of waves reflected at the boundaries. The displacement of the soil domain is assessed to verify this. It is expected that most of the displacement will be concentrated around the anchor. An overview of the displacements at the top surface of the soil volume are shown in fig. 9.10. The results are obtained with the plastic SSI model and the unscaled horizontal bottom acceleration. The plot shows that displacement in areas near the edges of the soil domain is small compared to the displacement around the anchor. As verified in chapter 7, the damping is modelled correctly and as intended in the SSI models. Therefore, it can assumed that a large enough soil volume has been considered to sufficiently damp out the undesired effects of waves reflected at the edges of the model.

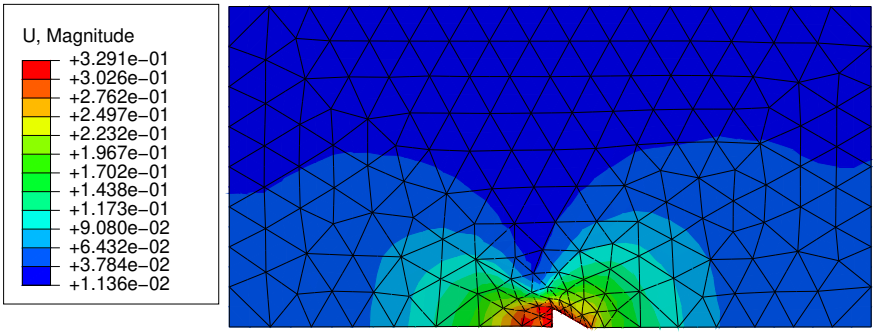

Figure 9.10. An overview of the displacement for the soil domain obtained from the plastic SSI model after applying the entire unscaled horizontal bottom excitation. The values are given in m.

9.3.5 Sensitivity analysis

In order to limit the computation time of the analyses, the number of elements must be limited. The number of elements depends on the size of the transition surface where the element decreases from 2.5m to 0.5m around the anchor. Using more elements is expected to yield more accurate results. More specifically, the displacements will increase when a larger number of elements is used as the FE solution is said to converge from below. Using too few elements will also not allow for an accurate description of the displacement variation around the anchor. Partition 2 is employed for all the analyses for the plastic SSI model, except the analyses for the soil strains where Partition 3 is used. It should be verified if a finer mesh should have been used for the SSI analyses where the anchor stresses and soil displacements were of interest. The unscaled horizontal excitation is considered. The results for the displacement for Partition 2 and Partition 3 are compared in fig. 9.11.
For both meshes, the largest displacement is concentrated around the top of the anchor. The two distributions are quite similar. The maximum displacement for Partition 2 is around 33cm, while the largest displacement from Partition 3 is approximately 36cm. Using a finer mesh leads to an increase of 9% for the maximum displacement. As the intent of this thesis is to study the overall effects of earthquakes on the anchor, and not specifically design the anchor, such an increase is deemed to not be significant enough to warrant the use of a a finer mesh than the one obtained with Partition 2.

9.3.6 Effects of an earthquake

The response of the anchor and the soil during an earthquake will depend on the properties of the soil volume. Some important parameters are the depth, the shear strength and the shear modulus. The natural frequencies of the soil profile, related to vertical propagation of shear waves, are inversely proportional with the depth of the layer of sediments. These are proportional with the shear modulus through the shear wave velocity (see 2.2.4). If a larger depth is considered, a larger number of natural frequencies would be within the frequency range of the earthquake excitation, which would lead to larger soil amplifications. Sediment layers with a larger shear modulus would experience smaller soil amplification as the natural frequencies are increased. A larger shear strength would result in smaller displacements for the soil as more energy is absorbed before yielding occurs. These parameters depend on the considered geographical site.

The main effects of interest are the overall stresses in the anchor and the displacement of the soil and the structure when subjected to earthquake excitation. The results in 8.5 indicate that the horizontal excitation can cause problems for the overall capacity of the anchor. As explained earlier, the use of skins presents a potential source of error which could amplify the stresses in the anchor. The capacity of the side plate is exceeded. Even though the stresses could be too conservative, these should not be overlooked. For a design process, the considered PGA in a seismic analysis will depend on the location of interest. Possible improvements could be to change the geometry of the structure or use a steel type with a larger design yield limit. The stresses in the structure due to the combination of a static anchor force and horizontal excitation should be considered more closely for the design of the anchor.

In order to evaluate the stability of the anchor in the soil, the displacements from section 8.5 must be considered. In this case, stability refers to if the anchor is pulled out of the seabed during an earth-

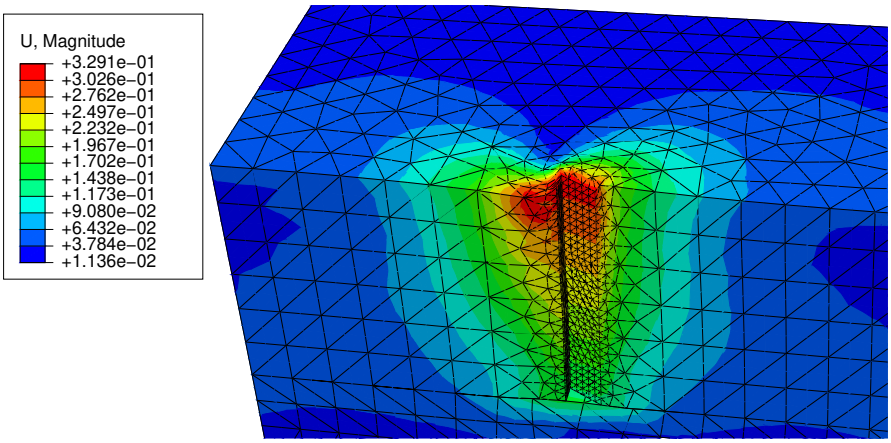

(a) Partition 2

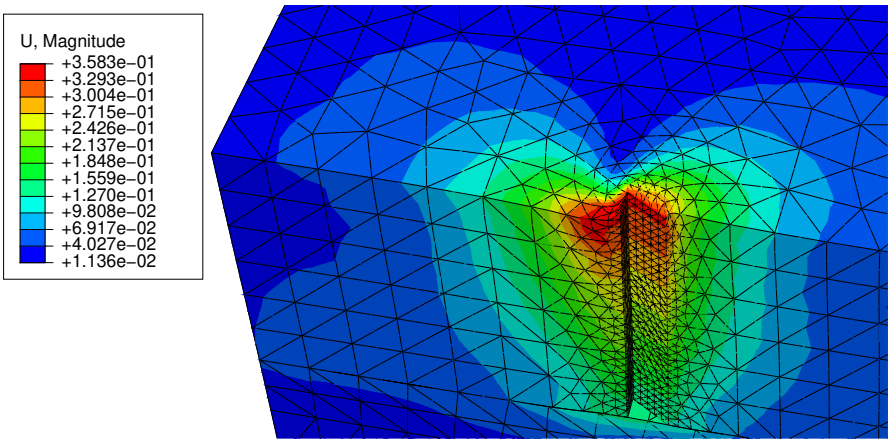

(b) Partition 3

Figure 9.11. Comparison of the soil displacement, after applying the entire unscaled horizontal excitation, for Partition 2 and Partition 3. The values are given in m.

quake or not. As skins are used to represent the anchor in the models, which causes the anchor to be attached to the soil at all times, the analyses cannot directly show if the structure is pulled out of the soil or not. The size of the displacements must therefore be the basis for this assessment. The horizontal excitation is dominant w.r.t. the magnitude of the maximum displacement. When only horizontal acceleration is considered, the displacement magnitude is 0.33m, 0.48m, 0.86m and 1.05m for the PGA levels 0.074g, 0.1, 0.2g and 0.3g, respectively. For simultaneous horizontal and vertical excitation, the displacement magnitude is 0.36m, 0.52m, 0.96m and 1.22m for the same PGA levels. Only the displacements corresponding to a horizontal PGA of 0.2 and 0.3g are considered to potentially cause issues for the stability of the anchor.

The total strains in the three upper layers of the soil in front of the anchor exceed the chosen limit value of 5%. This is the case for both of the considered horizontal PGA's. This could indicate that the anchor can be pulled out of the seabed due to an earthquake with a PGA of 0.2g or larger. Horizontal acceleration (without vertical acceleration) with a PGA equal to or larger than 0.2g results in the strain limit being exceeded. The addition of the vertical acceleration does not increase the strains substantially. However, the vertical excitation increases the vertical displacements, which could make it easier for the structure to be pulled out of the seabed. There is no common practice when it comes to assessing if an anchor is pulled out of a soil volume during an earthquake. Using a strain limit of 5% for the soil is considered to be a practical solution (Andersen, 2015). The total deformation of the soil after the earthquake can also be used as a criterion. For instance, a limit of 20-30% of a representative dimension of the structure can be used as an upper limit for the deformation. However, this could be a bit random and not be sufficient for a criterion for the stability assessment. It should also be noted that different types of clay will behave differently. Therefore, one criterion cannot be applied for all sediment

types. Other studies and assessments should be performed in order to get a better understanding of the consequences of earthquakes for the position of the anchor in the seabed.

Chapter 10

Conclusions and further work

10.1 Conclusions

In this thesis, the effects of seaquakes on an FWT, moored to a depth of 130m by a catenary system, were studied. The seaquake pressures acting on the platform of the FWT, due to earthquake accelerations in the seabed, were determined using acoustic FE models in Abaqus. The platform of the OO-Star Wind Floater was represented by a fixed rigid body. In order to study the effects on selected components of the wind turbine, the pressures obtained from the acoustic models were applied as concentrated forces at the bottom of the floating platform in a provided SIMA model of the FWT. The main responses of interest were the acceleration of the platform, the stress in the turbine tower, the acceleration in the nacelle and the tensile force in the mooring lines. In addition to the seaquake response, the response due to environmental loading was studied. The environmental loading comprised wind waves, current and wind based on information about the oceanographic and meteorological conditions at the Gulf of Maine on the east coast of the United States. The selected environmental parameters were chosen to represent harsh conditions, resulting in large peak mooring tension, to serve as a reference for the seaquake response. An anchor design developed by OO, called the "OO-Anchor", was also studied. More specifically, the effects of earthquakes w.r.t. soil-structure interaction were of interest. An FE model, including a soil domain and the anchor, was established using Abaqus, where earthquake accelerations were applied at the bottom of the model. The anchor and soil response were studied conducting analyses in the time domain. Mainly, the stresses within the structure, along with the soil displacements due to earthquake excitations were of interest. Several conclusions were drawn based on the results of the analyses.

1. Based on the platform response due to seaquake pressure, the 1D free-field and rigid reflector acoustic models do not result in desirable representations of the pressure under the FWT during a seaquake. The 1D free-field model yields pressures which are assumed to not be conservative enough. The 1D rigid reflector model yields a response of the platform which is deemed to be too conservative and not realistic. A 2D acoustic model was developed based on the two 1D limit cases. The 2D model, where the platform is represented by a rigid body with free-field water domains on each side, yields the pressure which is expected to be the closest to reality, based on the underlying assumptions.

2. Based on the obtained SIMA response of the FWT during seaquake, it can be concluded that seaquake excitation imposes vertical platform oscillations with a higher frequency content than what is usually present for such a structure. The higher frequency content could possibly lead to amplification of platform accelerations along the tower, resulting in higher accelerations in the nacelle. The PVA of the considered earthquake was 0.0345g. In the platform, the resulting PVA was found to be 0.168g. The corresponding value for the nacelle was 0.265g. The peak vertical accelerations during harsh environmental conditions were found to be approximately 0.1g. This could indicate that the effect of seaquake should be considered during design, depending on the seismic hazard at the given site. Amplification of the seabed PVA was found to be approximately 4.88 and 7.69 for the platform and the nacelle, respectively. Larger seabed PVA's were also considered by scaling the seaquake pressure accordingly. The amplifications were found to be irrespective of seabed PVA.

3. The upper part of the tower experiences the highest stress levels during seaquake excitation of the platform. This is most likely due to the combination of a lower cross sectional area, the large RNA inertia, and amplification of platform accelerations through the tower. However, the stress in the upper part of the tower, during the considered earthquake, only reaches about 24% of the stress due to self-weight. The capacity of the tower seems to be sufficient during seaquake.

4. Obtained peak mooring tensile forces during seaquake only reach a fraction of the design tension based on results from environmental loads. Therefore, the design mooring line tension to be used for the design of the anchor is not determined by tensile forces due to motion of the platform during

seaquake. However, it should be noted that parts of the mooring lines experience zero tension at some points during the seaquake excitation of the platform. This is only the case for seaquake pressures scaled to correspond to seabed PVA's of around 0.1g or above. Abrupt tension loading of a chain catenary mooring line could possibly lead to large local stresses in individual chain links, and should be avoided. Hence, larger pre-tensioning of the mooring line should possibly be used at locations prone to seismic activity.

5. The largest concentrations of stress for the anchor occur in the side plate. Based on a static analysis, the chosen thickness of 50mm provides sufficient capacity. However, when earthquake accelerations are considered, the capacity is exceeded for the considered horizontal PGA levels (0.074g, 0.1g, 0.2g and 0.3g). The capacity of the hollow triangular part, in the areas around the padeye, is almost exceeded when considering a PGA of 0.1g. Therefore, it is important to consider earthquakes for the design of the anchor.

6. The use of a skin to represent the anchor in the SSI model does not allow for sliding between the soil and the structure or gaps to occur. This affects the overall stiffness of the model. The stresses and displacements of the anchor are affected by the stress state in the surrounding soil. As the stiffness of the soil is much smaller than the one of the anchor, this could cause the results to be too conservative.

7. Horizontal accelerations, propagating vertically as shear waves through the soil profile, are more important to consider than vertical accelerations, when it comes to the stresses in the anchor. The most important effect of vertical earthquake accelerations is the increase of the vertical displacements of the anchor, which could cause the structure to be pulled out of the seabed.

8. Based on the total principal strains in the soil layers around the anchor, when considering horizontal PGA levels of 0.2g and above, it is possible that the anchor could be pulled out of the seabed during an earthquake. The observation is based on a chosen strain limit of 5%. The considered strain or displacement limit will depend on the type of sediments around the anchor.

10.2 Recommendations for further work

The models presented in this thesis included many underlying assumptions and simplifications. Modelling the pressure during seaquake using acoustic FE models in Abaqus was considered to be a viable option, instead of using potential theory implemented in other programs such as WADAM. The considered SIMA model of the wind turbine was provided by SINTEF Ocean, and was only slightly altered. It was assumed that the provided SIMA model could simulate the seaquake response of the FWT with sufficient accuracy. Finally, the anchor was represented by a skin attached to the soil domain in the Abaqus model, used to study SSI for the structure. Alternative models could have been considered in order to verify the results of the models employed in this thesis. Some suggestions for further work are proposed.

1. A coupling between the motion of the FWT and the surrounding water should be introduced in the Abaqus acoustic model, to obtain more accurate results for the pressure under the platform. Alternatively, instead of considering an acoustic model in Abaqus, a multi-body analysis could have been performed using a software for hydrodynamic analysis, such as HydroD. The seabed and the FWT could be represented by two separate bodies with a medium representing the seawater between the two.

2. In the 2D acoustic model, a plane and horizontal seabed with a uniform vertical displacement was considered. Generally, the seabed is neither plane nor horizontal, and it will not experience a uniform displacement. A specific seabed, situated at a location suitable of offshore wind development, should be considered to evaluate the effects of an arbitrary topography of the seabed on the seaquake pressure under the platform.

3. A coupled model comprising anchors in a soil domain, the water above, in addition to the anchor lines and the FWT, could be developed. Such a complex model would have to be carefully validated, imposing constraints between different parts of the model, using a general purpose FE-analyzer e.g. Abaqus. The earthquake excitation could then possibly be introduced at the bottom of the soil domain, to study the global response of the entire system.

4. The response of an FWT anchored by a taut-/TLP mooring system, subjected to seaquake, should be studied. A TLP is expected to be more sensitive to vertical accelerations at the seabed due to the high stiffness related to vertical motion. An FWT located in shallow water anchored by taut mooring lines could be subjected to higher pressures leading to larger vertical motion.

5. A more detailed model of the wind turbine tower, including internal stiffeners and connections to the platform and the nacelle, should be studied. The response of the wind turbine tower, due to vertical accelerations imposed by seaquake loading, could then be assessed w.r.t. the buckling capacity of the tower.

6. An FE model of a chain mooring line subjected to abrupt application of tension should be established. A detailed model, possibly containing individual chain links, enforcing contact conditions, would have to be developed to capture the potentially large local stresses. An explicit solution algorithm would have to be employed using a fine time step to capture the peak stresses as the links suddenly come into contact.

7. The effects of nonlinear geometry were not considered for the plastic SSI model in this thesis, in order to reduce the required computational effort. As indicated by the displacements from the model, the assumption of small displacements was not valid. Therefore, in order to get more accurate displacements, non-linear geometry should be included in the analyses.

8. In order to allow for gaps and sliding to occur between the anchor and the surrounding soil, an FE model which imposes contact between the soil and the anchor should be developed. This could serve as a basis for validation of the results from the SSI model considered in this thesis, which uses skins to represent the anchor. A more accurate representation of the total stiffness of the system could then possibly be obtained.

9. The soil strains given by the SSI model indicate that the anchor could be pulled out of the seabed during an earthquake with a horizontal PGA equal to or larger than 0.2g. Other analyses need to be conducted in order to verify this result, as there is no common way of assessing this issue. The conclusion w.r.t. the anchor stability depends on many factors such as the considered type of sediment, which will vary according to the considered site.

Bibliography

ABAQUS Inc. and Dassault Systèmes. (2017). *ABAQUS 2017*. https://www.3ds.com/products-services/simulia/products/abaqus/ (accessed: 21.05.2020)

Ambraseys, N. (1985). *A damaging seaquake*.

Andersen, K. (2015). Cyclic Soil Parameters for Offshore Foundation Design. the 3rd McClelland Lecture.

Bak, C., Zahle, F., Bitsche, R., Kim, T., Yde, A., Henriksen, L. C., Hansen, M. H., Blasques, J. P. A. A., Gaunaa, M., & Natarajan, A. (2013). *The DTU 10-MW Reference Wind Turbine*.

Bentley systems. (2019). *Plaxis*. https://www.plaxis.com/ (accessed: 23.05.2020)

Bridon-Bekaert The Ropes Group. (2020). *Moorline Polyester*. https://www.bridon-bekaert.com/en-us/steel-and-synthetic-ropes/offshore-construction/mooring/anchoring-lines/moorline-polyester (accessed: 19.05.2020)

Castro-Santos, L., & Diaz-Casas, V. (2016). *Floating Offshore Wind Farms*. Springer.

Chandrasekaran, S. (2018). *Dynamic Analysis and Design of Offshore Structures: Second Edition*. Springer.

Chopra, A. K. (2012). *Dynamics of structures* (Fourth edition). Pearson.

Cook, R. D., Malkus, D. S., Plesha, M. E., & Witt, R. J. (2001). *Concepts and applications of finite element analysis* (Fourth edition). John Wiley; Sons.

Crowe, C. T., Elger, D. F., Williams, B. C., & Roberson, J. A. (2010). *Engineering Fluid Mechanics* (9th Edition). John Wiley; Sons (Asia) Pte Ltd.

Dassault Systèmes Simulia Corp. (2014). *ABAQUS/CAE 6.14-Documentation*. Dassault Systèmes Simulia Corp., Providence, RI, USA.

Davidsen, C. F. (2020). *A Framework in Python for Parametric studies of OO-anchor in clay with Plaxis 3D*. NTNU.

D.Cook, R., & C.Young, W. (2015). *Selected chapters from Advanced Mechanics of Materials* (NTNU edition). Pearson.

DNV GL. (2010). *DNV-RP-C205 Environmenltal conditions and environmental loads*. DNV GL AS.

DNV GL. (2015). *DNV GL-OS-B101 Metallic materials*. DNV GL AS.

DNV GL. (2018a). *DNV GL-OS-C101 Design of offshore structures*. DNV GL AS.

DNV GL. (2018b). *DNV GL-ST-0119 Floating wind turbines*. DNV GL AS.

DNV GL. (2018c). *DNV-OS-E301 Position mooring*. DNV GL AS.

DNV-GL. (2016). *Hydrodynamic analysis and stability analysis software-HydroD*. https://www.dnvgl.com/services/hydrodynamic-analysis-and-stability-analysis-software-hydrod-14492 (accessed: 19.05.2020)

DNV-GL. (2017). *Wadam User manual*.

Dowling, D. R. (2012). *Fluid Mechanics* (Fifth edition). Elsevier.

Dr. techn. Olav Olsen. (2020a). *Fornybar energi*. https://www.olavolsen.no/no/forretningsomrader/fornybar-energi (accessed: 26.05.2020)

Dr. techn. Olav Olsen. (2020b). *Gjennombrudd for OO-Star Wind Floater*. https://www.olavolsen.no/no/aktuelt/post-SdQPQ-gjennombrudd-for-oo-star-wind-floater (accessed: 21.05.2020)

Emdal, A., Eiksund, G., Grande, L., Grimstad, G., & Nordal, S. (2016). *Geoteknikk beregningsmetoder*. NTNU Geoteknikk.

Equinor. (2017a). *How Hywind works*. https://www.equinor.com/en/what-we-do/floating-wind/how-hywind-works.html (accessed: 21.05.2020)

Equinor. (2017b). *Produksjonsstart ved verdens første flytende vindpark*. https://www.equinor.com/no/news/worlds-first-floating-wind-farm-started-production.html (accessed: 21.05.2020)

Fukioka, K., Nihei, Y., & Iijima, K. (2016). *Seaquake Loads Acting on Offshore Wind Turbine*.

Gómez, P., Sánchez, G., Llana, A., & Gonzalez, G. (2018). *Deliverable D1.1 Oceanographic and meteorological conditions for the design*.

Henrik Veder Group. (2020). *9094-01-HVG-Catalogus TAB 9-Mooring and towing*. https://www.hendrikvedergroup.com/products-services/products (accessed: 02.06.2020)

Hermstad, S. M. (2013). *Dynamic Analysis of the Bergsøysund Bridge in the Time Domain*. NTNU.

K. Mochizuki, K. T., H. Kihara, & Naito, S. (1997). *Effects of Seaquake on Offshore Floating Structure*. The International Society of Offshore; Polar Engineers.

Karimirad, M. (2014). *Offshore Energy Structures*. Springer.

Karlsen, S. H. (2010). *Barge transportation of heavy objects*. NTNU.

Kjølhaug, R. A., & Kaynia, A. M. (2015). Vertical earthquake response of megawatt-sized wind turbine with soil-structure interaction effects. *Earthquake Engineering Structural Dynamics*, 2356.

Kramer, S. L. (1996). *Geotechnical Earthquake Engineering*. University of Washington, Prentice-Hall, Inc.

Larsen, K., & G.Svanø. (1999). *Analytical Models for Mooring Chain-Soil Interaction*.

Martinelli, L., Domaneschi, M., & Shi, C. (2016). Submerged Floating Tunnels under Seismic Motion: Vibration Mitigation and Seaquake effects. *Procedia Engineering 166*, 229–246.

Mathisen, K. M. (2019). *Lecture 7-Solution of the Dynamic Equilibrium Equations by Explicit Direct Integration, TKT4197 Nonlinear Finite Element Analysis*, NTNU.

MathWorks. (2019). *MATLAB R2019a*. https://www.mathworks.com/products/matlab.html (accessed: 21.05.2020)

Næss, A. (2013). Stochastic dynamics of marine structures. *Cambridge England*, Cambridge University Press.

Nejad, A. R., Bachynski, E. E., & Moan, T. (2017). On tower top axial acceleration and drivetrain responses in a spar-type floating wind turbine, 1.

Nerland, L. A., & Røsvik, M. (2017). *Vertical earthquake response of a Submerged Floating Tunnel including Seaquake loading*. NTNU.

Newman, J. N. (2017). *Marine Hydrodynamics* (40th Anniversary Edition). The MIT Press.

Pettersen, B. (2020). *Marin Teknikk 3: Hydrodynamikk*. Akademika.

Power technology. (2017). *Full circle: Decommissioning the first ever offshore wind farm*. https://www.power-technology.com/features/full-circle-decommissioning-first-ever-offshore-windfarm/ (accessed: 21.05.2020)

Rusnes, S. (2010). *Hydrodynamic interaction between floating bodies*. NTNU.

Science Learning Hub Pokapu Akoranga Putaiao. (2007). *Seismic waves*. Retrieved April 13, 2020, from https://www.sciencelearn.org.nz/resources/340-seismic-waves

SINTEF Ocean. (2019a). *RIFLEX 4.16.1 Theory Manual*. SINTEF.

SINTEF Ocean. (2019b). *SIMA-SINTEF*. https://www.sintef.no/en/software/sima/ (accessed: 21.05.2020)

SINTEF Ocean. (2019c). *SIMO 4.16.1 Theory Manual*. SINTEF.

SINTEF Ocean. (2019d). *SIMO 4.16.1 User Guide*. SINTEF.

Standard Norge. (2009). *Eurocode 3: Design of steel structures Part 1-8: Design of joints*. Standard Norge.

Uenishi, K., & Sakurai, S. (2014). *The Generation of Seaquakes and Its Impact on Floating Bodies*.

Vorländer, M. (2008). *Auralization: Fundamentals of Acoustics, Modelling, Simulation, Algorithms and Acoustic Virtual Reality* (First edition). Springer.

Wolf, J. P. (1985). *Dynamic Soil-Structure Interaction*. Prentice-Hall, Inc.

Yu, W., Müller, K., & Lemmer, F. (2018). *Deliverable D4.2 Public Definition of the Two LIFES50+ 10MW Floater Concepts*.

Appendix A

Additional theory

A.1 Central difference method

Central difference method expressions for velocity and acceleration at t_i:

$$\dot{u}_i = \frac{u_{i+1} - u_{i-1}}{2\Delta t} \qquad \ddot{u}_i = \frac{u_{i+1} - 2u_i + u_{i-1}}{(\Delta t)^2} \tag{A.1}$$

Substituting these expressions into the equation of motion at t_i yields

$$m\left(\frac{u_{i+1} - 2u_i + u_{i-1}}{(\Delta t)^2}\right) + c\left(\frac{u_{i+1} - u_{i-1}}{2\Delta t}\right) + ku_i = p_i \tag{A.2}$$

Re-organizing terms to obtain known quntities at the right side:

$$\underbrace{\left[\frac{m}{(\Delta t)^2} + \frac{c}{2\Delta t}\right]}_{\hat{k}} u_{i+1} = \underbrace{p_i - \left[\frac{m}{(\Delta t)^2} - \frac{c}{2\Delta t}\right] u_{i-1} - \left[k - \frac{2m}{(\Delta t)^2}\right] u_i}_{\hat{p}_i} \tag{A.3}$$

$$\implies u_{i+1} = \frac{\hat{p}_i}{\hat{k}} \tag{A.4}$$

To solve eq. (A.4) for u_1, $\hat{p}_i$ has to be obtained for $t = 0$. This requires the value of u_{-1} which can be obtained as follows

$$u_{-1} = u_0 - \Delta t(\dot{u}_0) + \frac{(\Delta t)^2}{2}\ddot{u}_0 \tag{A.5}$$

A.2 Newmark's Method

The following approximations is the basis of a family of time-stepping methods developed by N.M Newmark.

$$\dot{u}_{i+1} = \dot{u}_i + \Delta t\left[\gamma\ddot{u}_{i+1} + (1-\gamma)\ddot{u}_i\right] \tag{A.6}$$

$$u_{i+1} = u_i + \Delta t\dot{u}_i + \frac{\Delta t^2}{2}\left[2\beta\ddot{u}_{i+1} + (1-2\beta)\ddot{u}_i\right] \tag{A.7}$$

Where β and γ are parameters which define how the acceleration varies over a time step, the accuracy characteristics, and the stability of the method (Chopra, 2012).

$\gamma = \frac{1}{2}$ and $\beta = \frac{1}{4}$ $\implies$ Constant average acceleration method, also known as the *trapezoidal rule.*

$\gamma = \frac{1}{2}$ and $\beta = \frac{1}{6}$ $\implies$ Linear acceleration method.

Following the approximations in eqs. (A.6) and (A.7), expressions for acceleration and velocity can be obtained

$$\ddot{u}_{i+1} = \frac{1}{\beta\Delta t^2}(u_{i+1} - u_i - \Delta t\dot{u}_i) - \left(\frac{1}{2\beta} - 1\right)\ddot{u}_i \tag{A.8}$$

$$\dot{u}_{i+1} = \frac{\gamma}{\beta\Delta t}(u_{i+1} - u_i) - \left(\frac{\gamma}{\beta} - 1\right)\dot{u}_i - \Delta t\left(\frac{\gamma}{2\beta} - 1\right)\ddot{u}_i \tag{A.9}$$

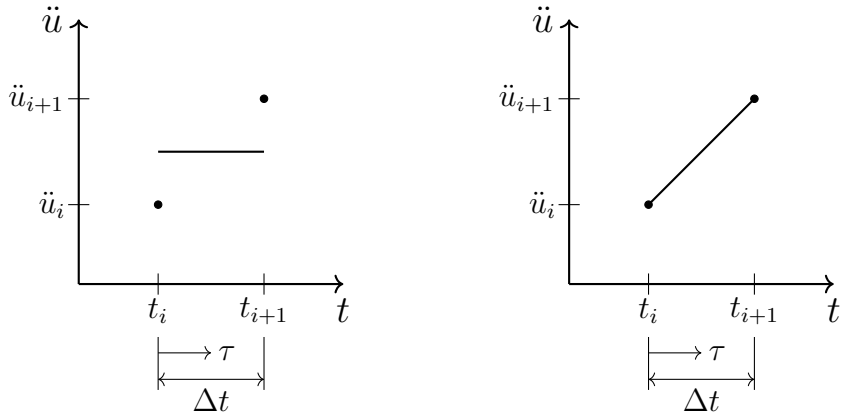

(a) Constant average acceleration **(b)** Linear acceleration

Figure A.1. Special cases of the Newmark method.

Substituting the approximations for velocity and acceleration into the equation of motion at t_{i+1} yields

$$\overbrace{\left[\frac{m}{\beta\Delta t^2}+\frac{\gamma c}{\beta\Delta t}+k\right]}^{\hat{k}} u_{i+1} = p_{i+1} + m\left[\frac{1}{\beta\Delta t^2}u_i + \frac{1}{\beta\Delta t}\dot{u}_i + \left(\frac{1}{2\beta}-1\right)\ddot{u}_i\right] + \underbrace{c\left[\frac{\gamma}{\beta\Delta t}u_i + \left(\frac{\gamma}{\beta}-1\right)\dot{u}_i + \Delta t\left(\frac{\gamma}{2\beta}-1\right)\ddot{u}_i\right]}_{\hat{p}_{i+1}} \tag{A.10}$$

$$\implies u_{i+1} = \frac{\hat{p}_{i+1}}{\hat{k}} \tag{A.11}$$

A.3 Theoretical displacement, simply supported plate

The differential equation for a plate is given by (D.Cook & C.Young, 2015):

$$\frac{\partial^4 w}{\partial x^4} + 2\frac{\partial^4 w}{\partial x^2 \partial y^2} + \frac{\partial^4 w}{\partial y^4} = \frac{q(x,y)}{D} \tag{A.12}$$

where: w = displacement
$q(x,y)$ = distributed load
D = flexural rigidity

The flexural rigidity of the plate is given by:

$$D = \frac{Et^3}{12(1-\nu^2)} \tag{A.13}$$

where: E = Young's modulus
ν = Poisson's ratio
t = plate thickness

The exact solution of the partial differential equation of a simply supported plate with evenly distributed load can be determined using Fourier series. The load is expanded using a Fourier series.

$$q(x,y) = \sum_{m=1}^{\infty}\sum_{n=1}^{\infty} q_{mn}\sin\left(\frac{m\pi x}{a}\right)\sin\left(\frac{n\pi y}{b}\right) \tag{A.14}$$

where: m, n = integers
q_{mn} = amplitude
a, b = plate dimensions

The amplitude q_{mn} is given by:

$$q_{mn} = \frac{4}{ab} \int_0^b \int_0^a q \cdot \sin\Big(\frac{m\pi x}{a}\Big) \sin\Big(\frac{n\pi y}{b}\Big) \tag{A.15}$$

For a constant load q, q_{mn} becomes:

$$q_{mn} = \frac{4}{mn\pi^2}(1 - \cos(m\pi))(1 - \cos(n\pi)) \tag{A.16}$$

The deflection is given by:

$$w(x, y) = \sum_{m=1}^{\infty} \sum_{n=1}^{\infty} \frac{q_{mn}}{\pi^4 D[(m/a)^2 + (n/b)^2]^2} \sin\Big(\frac{m\pi x}{a}\Big) \sin\Big(\frac{n\pi y}{b}\Big) \tag{A.17}$$

Including ten terms in each summation ($m = n = 10$) is expected to give an accurate representation of the loading.

Appendix B

Additional results

B.1 Free decay

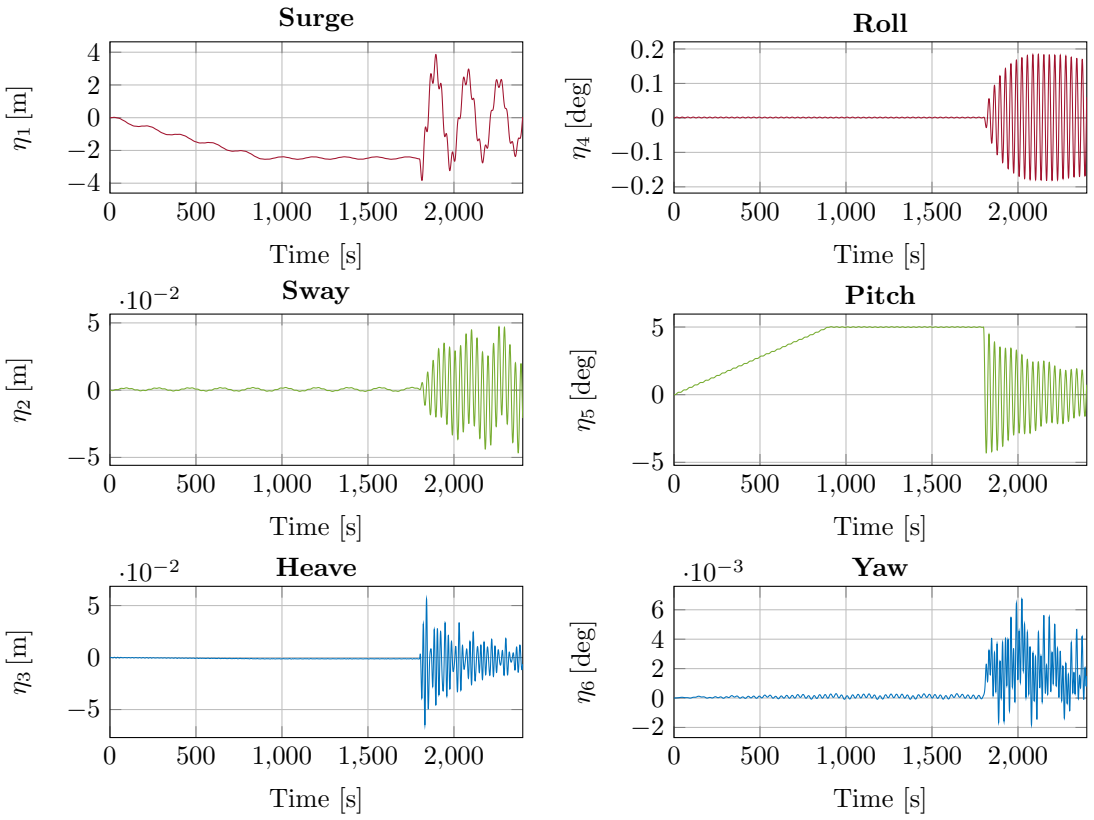

Figure B.1. Platform motion in remaining degrees of freedom during free decay in pitch, showing the entire simulation length. As the turbine is rotated to the initial pitch of 5 degrees, the platform also experiences surge, which is likely due to the mooring lines. After the turbine is released at 1800s, there is a certain amount of response in sway, heave, roll and yaw as well.

B.2 Environmental loading results

Table B.1: Peak- and mean values of tension in the loaded mooring line during three-hour environmental loading simulations using 30 different wave seeds.

Wave	**Line tension** [kN]	
seed	$\bar{T}_i$	$T_{\max,i}$
1001	1930	7525
1002	1937	7051
1003	1951	7291
1004	1941	11433
1005	1943	10337
1006	1955	6397
1007	1941	6186
1008	1963	7806
1009	1936	6728
1010	1927	6429
1011	1946	9189
1012	1937	6896
1013	1965	8753
1014	1942	6524
1015	1952	7051
1016	1957	6286
1017	1939	7171
1018	1954	7399
1019	1942	6615
1020	1957	5990
1021	1959	7314
1022	1956	6266
1023	1940	6609
1024	1936	6668
1025	1933	7036
1026	1946	6113
1027	1951	6105
1028	1967	7569
1029	1948	7295
1030	1952	6578

B.3 Required dimensions for the padeye

The design force from the anchor line is considered to be equal to 8000kN. The inclination w.r.t. the horizontal plane is 16.5°. The concentrated force is shown in fig. B.2b. The required diameter for the pin is taken from a manual containing diameters for shackle pins. The anchor load in terms of tons must be determined. Then the appropriate diameter is chosen. The chosen shackle type is a GN forged rope shackle denoted H14. The required pin diameter is $d = 250$mm (Henrik Veder Group, 2020, p.6). The corresponding pin hole diameter is given by, assuming a standard bolt hole (DNV GL, 2018a, Table 4, p.100):

$$d_0 = d + 3\text{mm} = 253\text{mm} \tag{B.1}$$

Using the geometrical requirements from fig. B.2a the plate height and edge distances can be deter-

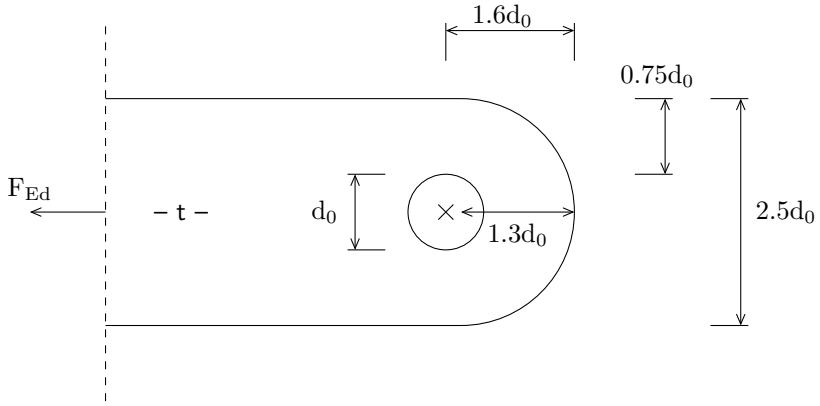

(a) Required dimensions for a pin ended members (Standard Norge, 2009, table 3.9).

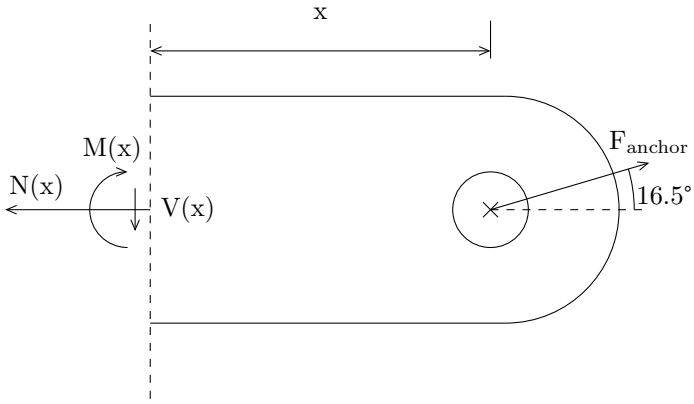

(b) The concentrated force from the anchor line/cable acting on the padeye. General section forces are shown.

Figure B.2. Required dimensions and forces acting on the padeye.

mined. These dimensions also satisfy the general requirements for the minimum edge distances for bolts (Standard Norge, 2009, Table 3.3). The material factor is $\gamma_M = 1.15$. The yield limit as a function of thickness, for steel grades with improved weldability, is given in table B.2. The required thickness based

Table B.2: Characteristic yield limits as a function of thickness for VL AW36, VL DW36 and VL EW36 (DNV GL, 2015, p.20)

Thickness [mm]	**Characteristic yield limit** [MPa]
$t \leq 25$	355
$25 < t \leq 50$	335
$50 < t \leq 75$	320
$75 < t$	310

on the hole diameter d_0 is given by:

$$t \geq 0.7\sqrt{\frac{F_{\text{anchor}}\gamma_{\text{M}}}{f_y}} \tag{B.2}$$

Using two plates with a thickness of 75mm each will give a characteristic yield limit of 320MPa, and will satisfy the minimum thickness requirement. This results in a total thickness of 150mm for the padeye.

The chosen dimensions for the "cantilever" part of the padeye are indicated in fig. B.3. The welds

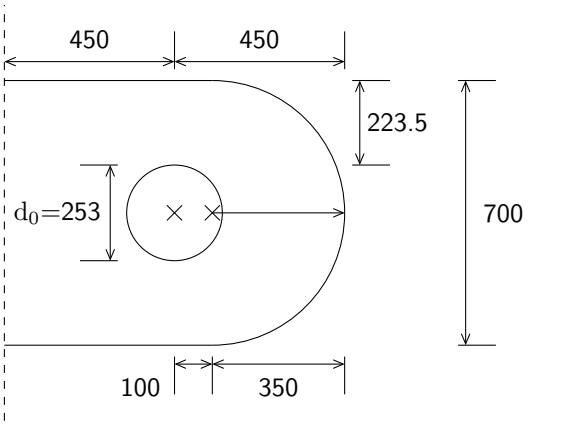

(a) Chosen dimensions for the "cantilever" part of the padeye. The measurements are in mm.

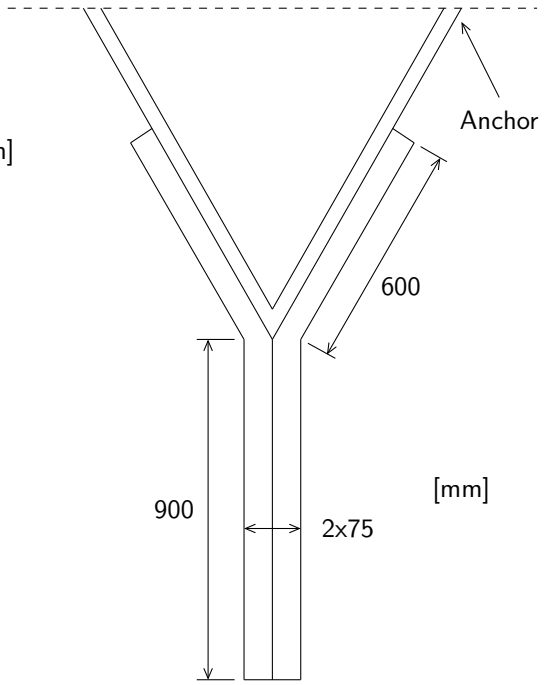

(b) Chosen dimensions for the remaining parts of the padeye, seen from above. The measurements are in mm.

Figure B.3. The chosen dimensions for the padeye geometry. The measurements are in mm.

which attach the padeye to the anchor plates will not be designed. For the check of the capacity, it is assumed that the welds have a sufficient throat thickness. These should be considered more closely for a more extensive design check.

Check of the capacity at the end of the "cantilever" part

A section at a distance of 450mm from the centre of the pin hole is considered. The following sectional forces must be considered for this section:

- $N_{\text{Ed}} = N(x = 0.45\text{m}) = 8000\text{kN} \cdot \cos(16.5°) \approxeq 7671\text{kN}$ (tension)
- $V_{\text{Ed}} = V(x = 0.45\text{m}) = 8000\text{kN} \cdot \sin(16.5°) \approxeq 2272\text{kN}$
- $M_{\text{Ed}} = M(x = 0.45\text{m}) = 8000\text{kN} \cdot \sin(16.5°) \cdot 0.45\text{m} \approxeq 1022.5\text{kNm}$ (tension at the bottom of the cross section)

The cross section of the padeye along with the two locations which are to be checked are shown in fig. B.4. In order to be able to use an elastic analysis, the cross section must be classified in at least Class 3. The classification is performed the DNV GL codes (DNV GL, 2018a, Appendix A, Table 3). The relative strain coefficient is:

$$\varepsilon = \sqrt{\frac{235}{f_y}} = \sqrt{\frac{235}{320}} = 0.857 \tag{B.3}$$

For pure compression:

$$\frac{d}{t_w \varepsilon} = \frac{700}{150 \cdot 0.857} = 5.45 < 42 \quad \Rightarrow \quad \text{Class 1} \tag{B.4}$$

For bending:

$$\frac{d}{t_w \varepsilon} = \frac{700}{150 \cdot 0.857} = 5.45 < 124 \quad \Rightarrow \quad \text{Class 1} \tag{B.5}$$

With a cross section height of 700mm and a total width of 150mm, the following cross section parameters

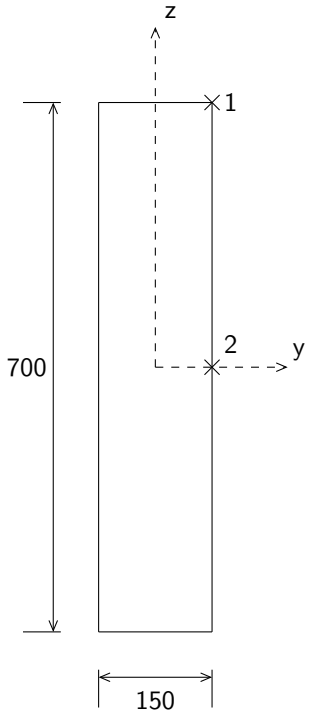

Figure B.4. Padeye cross section. The measurements are in mm. The capacity is checked at the two indicated points.

are obtained:

$$S_y = 9.1875 \cdot 10^6 \text{mm}^3 (\text{at the neutral axis}) \tag{B.6}$$

$$I_y = 4.2875 \cdot 10^9 \text{mm}^4 \tag{B.7}$$

The stress at the two points indicated in fig. B.4 must not exceed the design yield stress. Elastic analysis is used for the capacity check.

$$\sigma_1 = \frac{N_{\text{Ed}}}{A} + \frac{M_{\text{Ed}}}{I_y} \cdot h/2 = \frac{7671 \cdot 10^3 \text{N}}{150 \cdot 700 \text{mm}^2} + \frac{1022.5 \cdot 10^6 \text{Nmm} \cdot 350 \text{mm}}{4.2875 \cdot 10^9 \text{mm}^4} = 156.6 \text{MPa} \tag{B.8}$$

$$\sigma_2 = \sqrt{\sigma_{\text{N},2}^2 + 3 \cdot \tau_2^2} \quad (\text{von Mises' yield criterion}) \tag{B.9}$$

$$\sigma_2 = \sqrt{(\frac{N_{\text{Ed}}}{A})^2 + 3 \cdot (\frac{V_{\text{Ed}} \cdot S_y}{I_y \cdot b})^2} = \sqrt{(\frac{7671 \cdot 10^3 \text{N}}{150 \cdot 700 \text{mm}^2})^2 + 3 \cdot (\frac{2272 \cdot 10^3 \text{N} \cdot 9.1875 \cdot 10^6 \text{mm}^3}{4.2875 \cdot 10^9 \text{mm}^4 \cdot 150 \text{mm}})^2} = 92.2 \text{MPa} \tag{B.10}$$

The design yield stress is:

$$f_{\text{yd}} = \frac{f_y}{\gamma_{\text{M}}} = \frac{320}{1.15} = 278.3 \text{MPa} \quad \Rightarrow \quad \sigma_1 < f_{\text{yd}} \quad \text{and} \quad \sigma_2 < f_{\text{yd}} \tag{B.11}$$

The "cantilever" part of the padeye is then assumed to a have sufficient load bearing capacity.

Check of the capacity for the remaining parts of the padeye

The parts of the padeye welded to the sides of the anchor each have a thickness of 75mm. The design forces and moments for the ends of these, furthest away from the pin hole, are assumed as follows:

- $N_{\mathrm{Ed}} = \frac{7671\mathrm{kN}}{2 \cdot \cos(30°)} \approxeq 4429\mathrm{kN}$ (tension)
- $V_{\mathrm{Ed}} = \frac{2272\mathrm{kN}}{2} = 1136\mathrm{kN}$
- $M_{\mathrm{Ed}} = \frac{1022.5\mathrm{kNm}}{2} + 1136\mathrm{kN} \cdot 0.6\mathrm{m} = 1192.85\mathrm{kNm}$ (tension at the bottom of the cross section)

As these sectional forces and moments are either similar to or smaller than the previous ones, it can be seen that the capacity is expected to be adequate for the remaining parts welded to the sides of the anchor.

B.4 Results–plastic SSI model

The stress-time series from the plastic SSI model for the chosen nodes, for some of the performed simulations, are presented.

B.4.1 Scaled horizontal excitation–PGA=0.1g

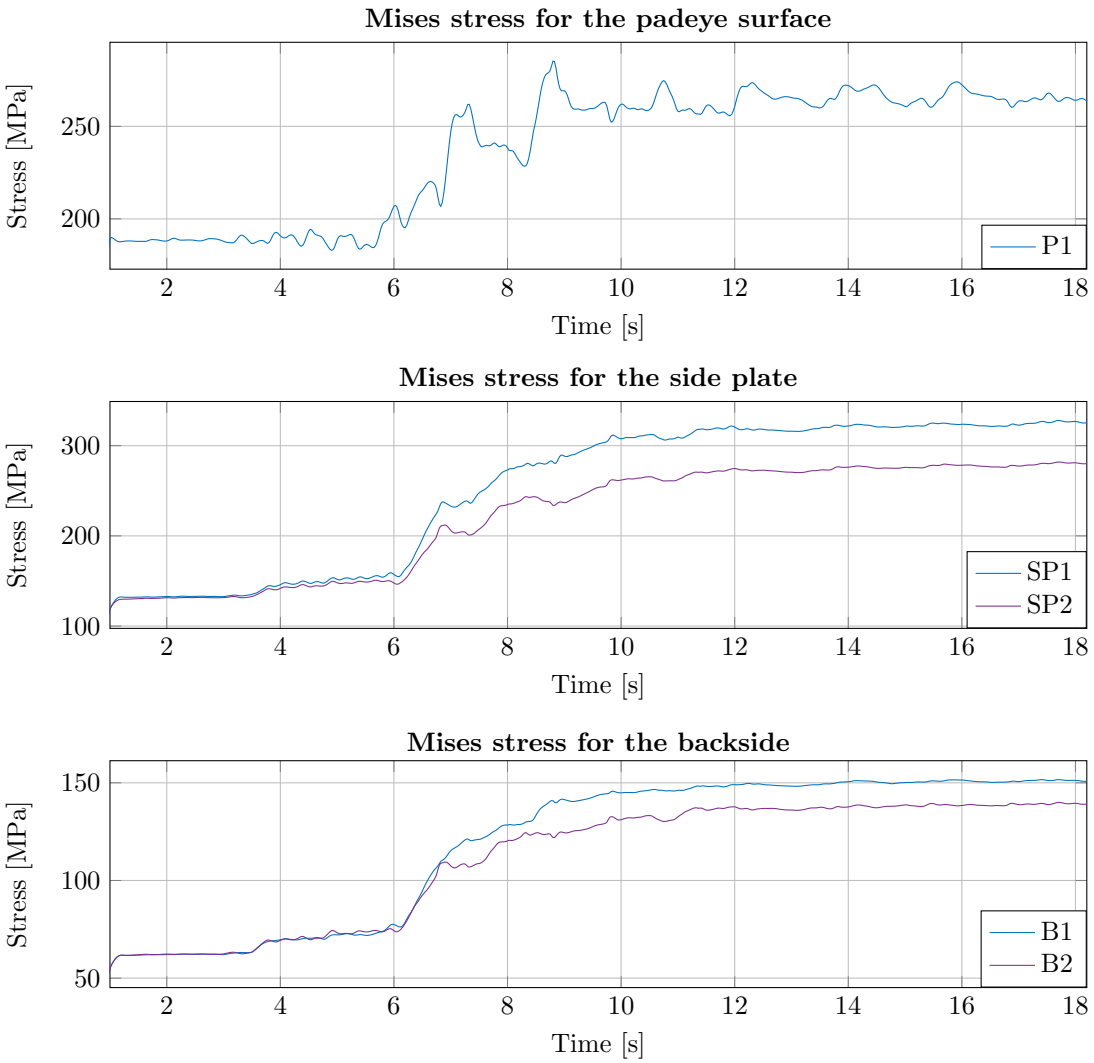

Figure B.5. Stresses for the considered points using a scaled horizontal excitation. The PGA is scaled to 0.1g.

B.4.2 Scaled horizontal excitation–PGA=0.2g

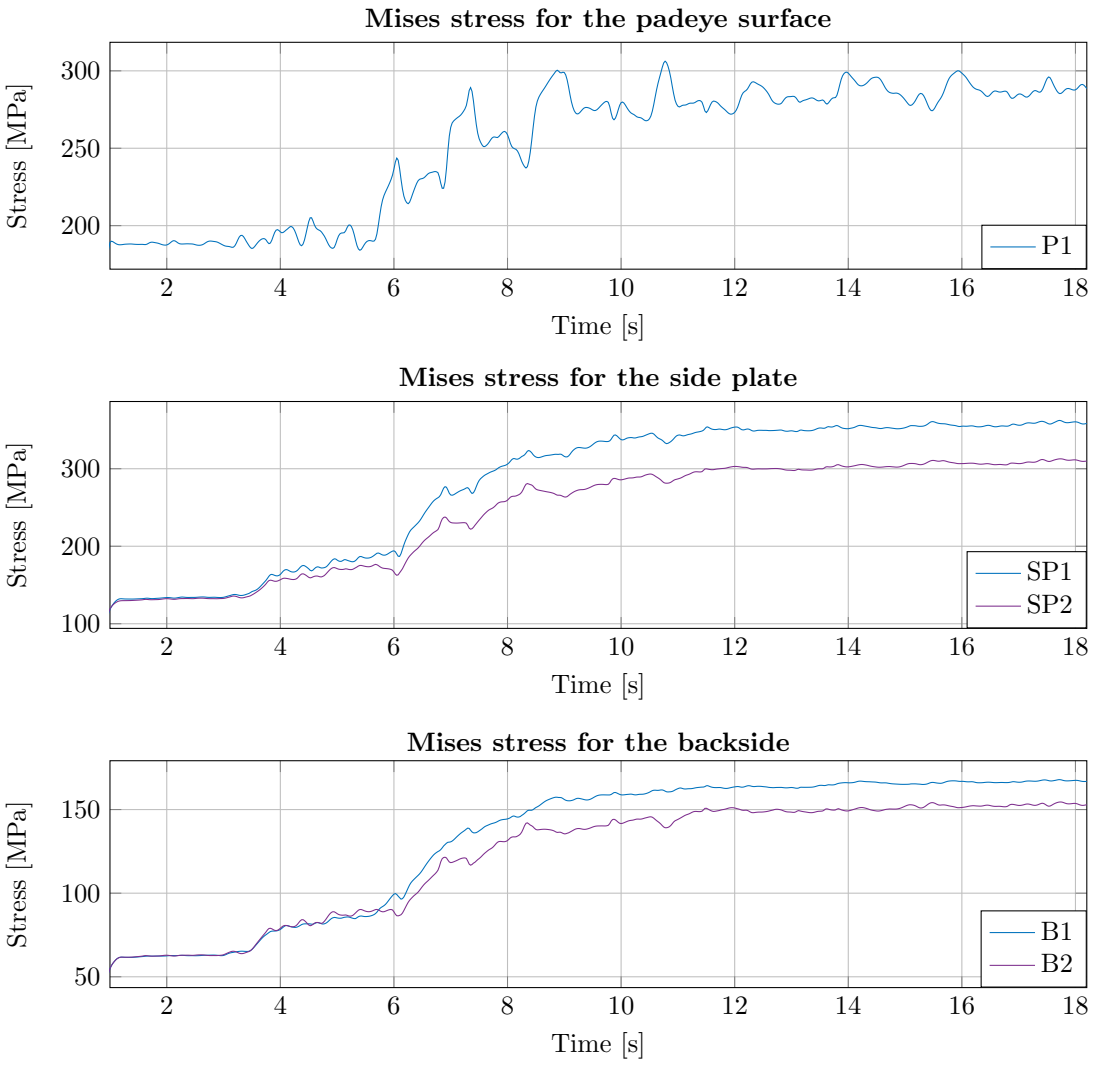

Figure B.6. Stresses for the considered points using a scaled horizontal excitation. The PGA is scaled to 0.2g.

B.4.3 Scaled horizontal excitation–PGA=0.3g

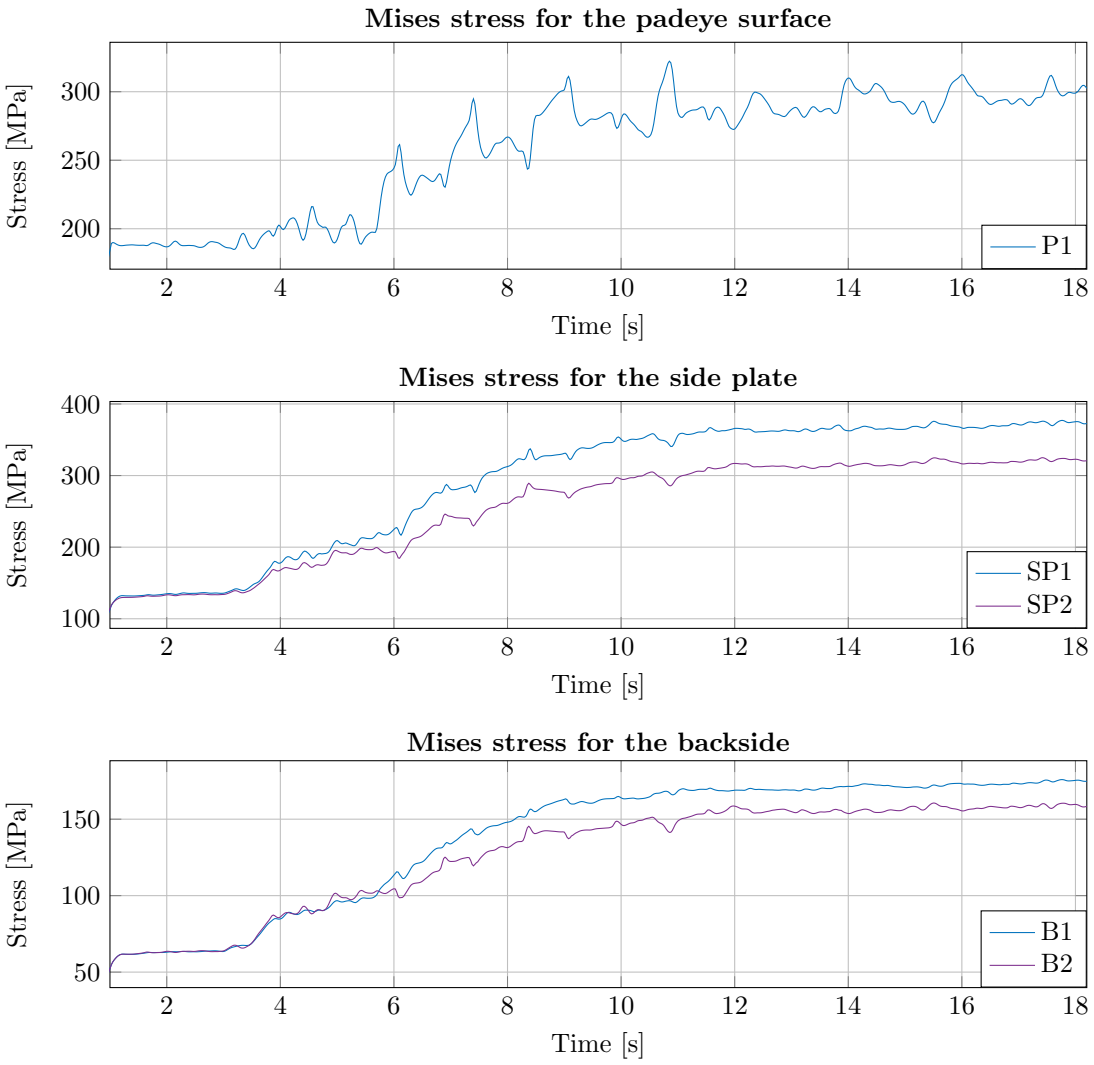

Figure B.7. Stresses for the considered points using a scaled horizontal excitation. The PGA is scaled to 0.3g.

B.4.4 Horizontal and vertical excitation

The displacements for the scaled simultaneous horizontal and vertical accelerations are shown in fig. B.8.

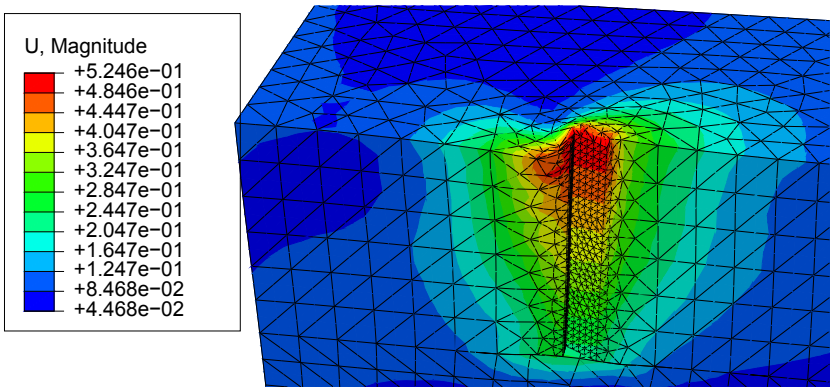

(a) Horizontal PGA=0.1g

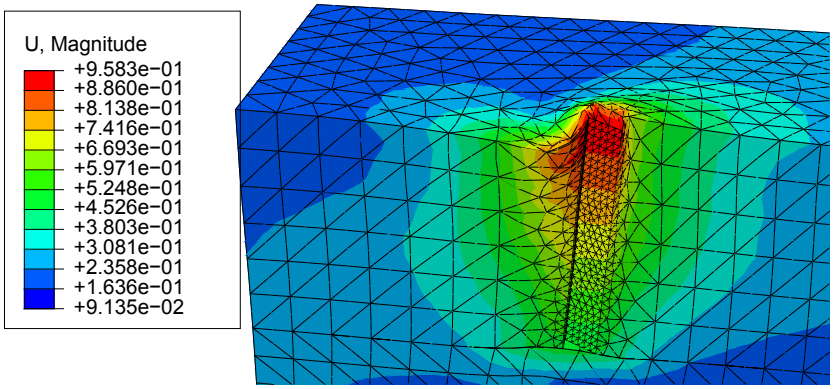

(b) Horizontal PGA=0.2g

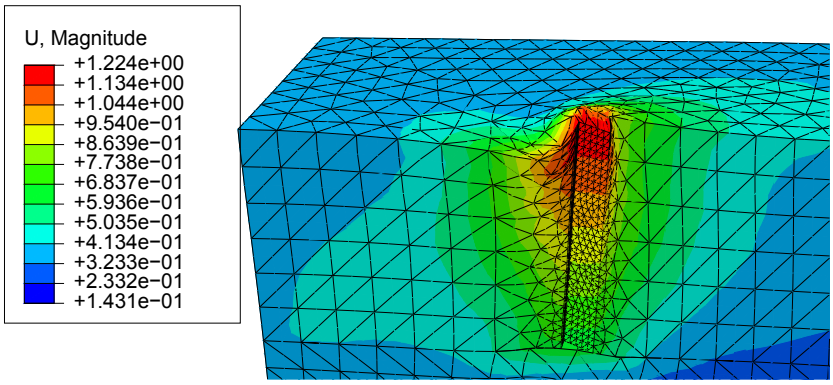

(c) Horizontal PGA=0.3g

Figure B.8. Soil displacements after applying the entire scaled horizontal and vertical accelerations simultaneously. The values are given in m. A scaling factor equal to 3 has been used for the contour plots.

B.5 Acceleration by numerical differentiation

To verify the obtained accelerations of the SIMO bodies, numerical differentiation of the corresponding position is performed. The numerical differentiation is employed by a second-order central difference method:

$$\ddot{\eta}_3(t_i) \approx \frac{\eta_3(t_{i+1}) - 2\eta_3(t_i) + \eta_3(t_{i-1})}{\Delta t^2} \tag{B.12}$$

Obtained acceleration based on numerical differentiation of the complete position array ($n = 1$) gave a large amount of numerical noise. This is likely due to the combination of the small time step employed in the SIMO calculations ($\Delta t_{\text{SIMO}} = 0.00125$s) in addition to a moderate precision on the stored position values, resulting in round-off error. Basing the acceleration on differentiation of an altered position array, including every n-th value of the original signal, yielded acceleration signals as shown in fig. B.9. By only including every n-th value, the corresponding time step used in eq. (B.12) becomes $n \cdot \Delta t_{\text{SIMO}}$. The calculation is shown in D.6.

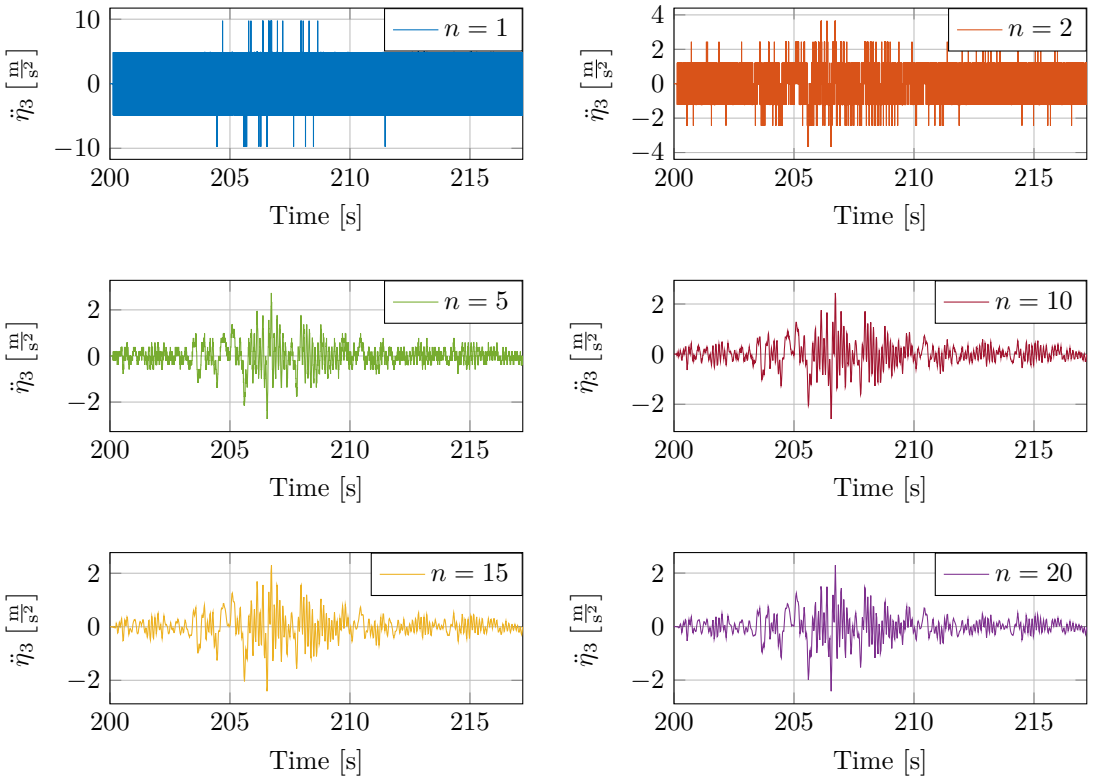

Figure B.9. Vertical nacelle acceleration during the unscaled Abaqus 2D seaquake excitation of the platform, obtained by numerical differentiation of the corresponding position array, containing every n-th value of the original signal.

Appendix C

Additional information

C.1 Generic soil profile

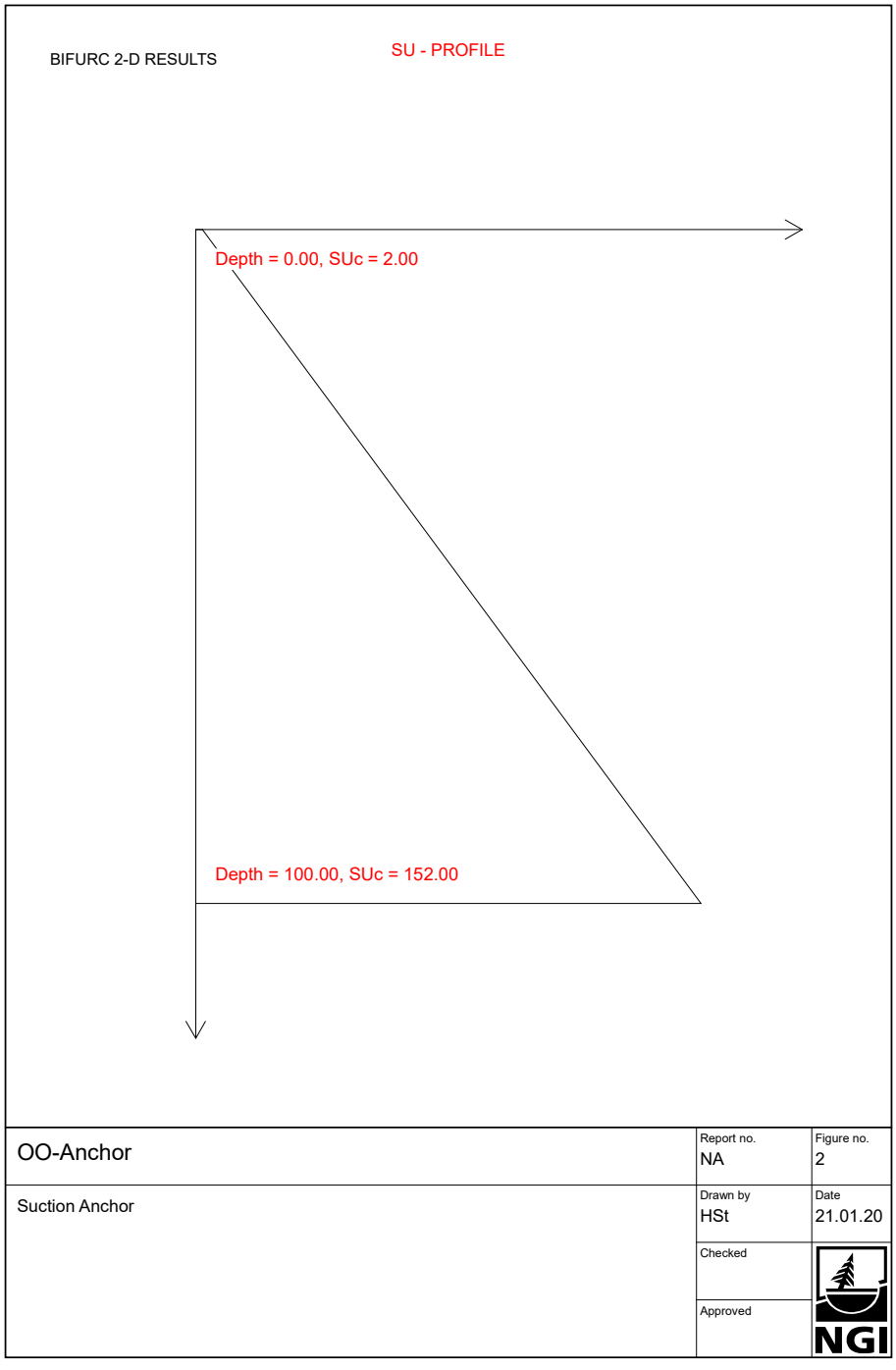

C.2 LIFES50+ OO-Star Wind Floater 10MW additional data

Table C.1: Discretization of the wind turbine tower collected from the LIFES50+ D4.2 report (Yu et al., 2018). Properties are sampled at the midpoint of each segment as shown in fig. C.1.

Section	**Elevation lower [m]**	**Elevation upper [m]**	**Diameter outer [m]**	**Thickness of wall [m]**	**Cross sectional area [m^2]**	**Mass of section [kg]**
1	0.000	3.946	11.385	0.075	2.665	8.667E+04
2	3.946	7.892	11.154	0.074	2.576	8.378E+04
3	7.892	11.838	10.923	0.072	2.454	7.983E+04
4	11.838	15.785	10.692	0.070	2.336	7.598E+04
5	15.785	19.731	10.462	0.068	2.220	7.222E+04
6	19.731	23.677	10.231	0.066	2.108	6.855E+04
7	23.677	27.623	10.000	0.065	2.029	6.599E+04
8	27.623	31.569	9.769	0.063	1.921	6.248E+04
9	31.569	35.515	9.538	0.061	1.816	5.908E+04
10	35.515	39.462	9.308	0.059	1.714	5.576E+04
11	39.462	43.408	9.077	0.057	1.615	5.254E+04
12	43.408	47.354	8.846	0.056	1.546	5.030E+04
13	47.354	51.300	8.615	0.054	1.452	4.724E+04
14	51.300	55.246	8.385	0.052	1.361	4.428E+04
15	55.246	59.192	8.154	0.050	1.273	4.140E+04
16	59.192	63.138	7.923	0.048	1.188	3.863E+04
17	63.138	67.085	7.692	0.047	1.129	3.672E+04
18	67.085	71.031	7.462	0.045	1.048	3.410E+04
19	71.031	74.977	7.231	0.043	0.971	3.158E+04
20	74.977	78.923	7.000	0.041	0.896	2.916E+04
21	78.923	82.869	6.769	0.039	0.825	2.682E+04
22	82.869	86.815	6.538	0.038	0.776	2.524E+04
23	86.815	90.762	6.308	0.036	0.709	2.307E+04
24	90.762	94.708	6.077	0.034	0.645	2.099E+04
25	94.708	98.654	5.846	0.032	0.585	1.901E+04
26	98.654	102.600	5.615	0.030	0.526	1.712E+04
27	102.600	104.630	5.441	0.029	0.484	8.104E+03

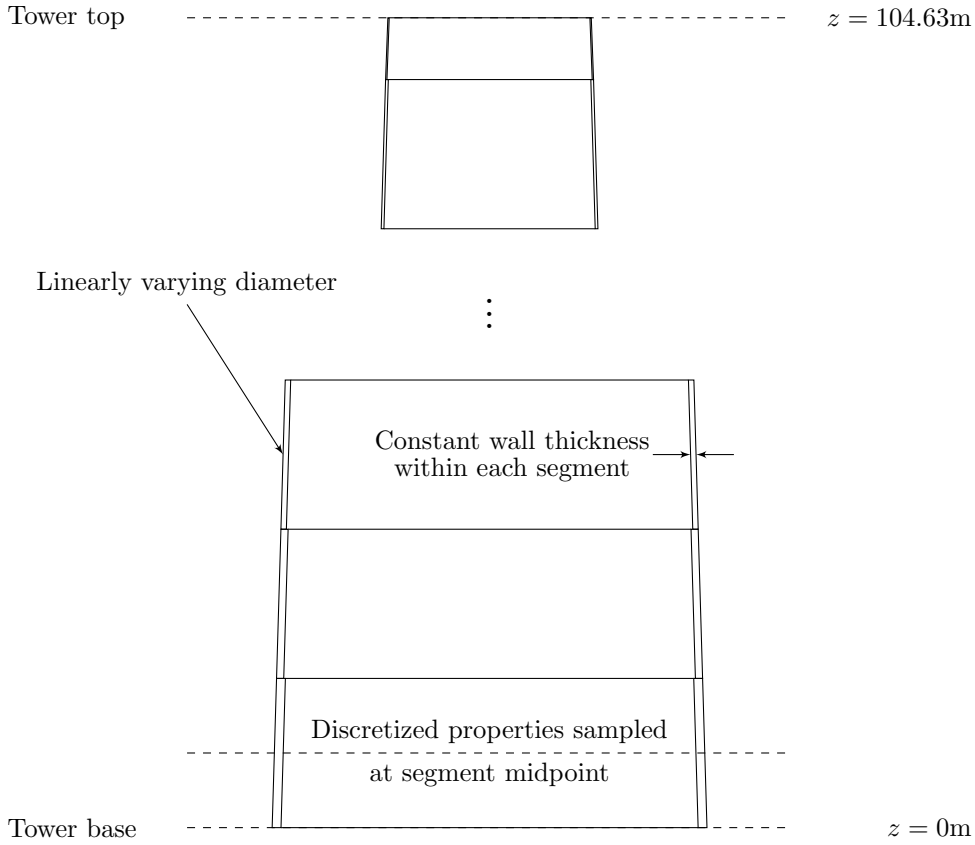

Figure C.1. Definition of the wind turbine tower (Yu et al., 2018).

C.3 Discretizations of soil profile for SSI analyses

Table C.2: Material properties for the fine discretization of the soil profile.

Layer number	**Depth** [m]	**Avg.** G [MPa]	**Avg.** E [MPa]	$L_{e,max}$ [m]
1	0-1	2.75	8.2225	1.3407
2	1-2	4.25	12.7075	1.667
3	2-3	5.75	17.1925	1.9386
4	3-4	7.25	21.6775	2.1768
5	4-5	8.75	26.1625	2.3914
6	5-6	10.25	30.6475	2.5883
7	6-7	11.75	35.1325	2.7712
8	7-8	13.25	39.6175	2.9428
9	8-9	14.75	44.1025	3.1049
10	9-10	16.25	48.5875	3.2590
11	10-11	17.75	53.0725	3.4061
12	11-12	19.25	57.5575	3.5471
13	12-13	20.75	62.0425	3.6827
14	13-14	22.25	66.5275	3.8135
15	14-15	23.75	71.0125	3.9399
16	15-17.5	26.375	78.8613	4.1519
17	17.5-20	30.125	90.0738	4.4373
18	20-22.5	33.875	101.2863	4.7054
19	22.5-25	37.625	112.4988	4.9590
20	25-27.5	41.375	123.7113	5.2002
21	27.5-30	45.125	134.9238	5.4308
22	30-32.5	48.875	146.1363	5.6519
23	32.5-35	52.625	157.3488	5.8648
24	35-37.5	56.375	168.5613	6.0701
25	37.5-40	60.125	179.7738	6.2688
26	40-43	64.250	192.1075	6.4802
27	43-46	68.750	205.5625	6.7033
28	46-49	73.250	219.0175	6.9192
29	49-52	77.750	232.4725	7.1286
30	52-55	82.250	245.9275	7.3320

Table C.3: Material properties for the coarse discretization of the soil profile.

Layer number	**Depth** [m]	**Avg.** G [MPa]	**Avg.** E [MPa]	$L_{\mathrm{e,max}}$ [m]	**Avg.** s_u [kPa]
1	0-2.5	3.875	11.5863	1.5914	3.875
2	2.5-5	7.625	22.7988	2.2324	7.625
3	5-7.5	11.375	34.0113	2.7267	11.375
4	7.5-10	15.125	45.2238	3.1441	15.125
5	10-12.5	18.875	56.4363	3.5123	18.875
6	12.5-15	22.625	67.6488	3.8455	22.625
7	15-19	27.500	82.2250	4.2396	27.500
8	19-23	33.500	100.1650	4.6793	33.500
9	23-27	39.500	118.1050	5.0810	39.500
10	27-31	45.500	136.0450	5.4533	45.500
11	31-35	51.500	153.9850	5.8017	51.500
12	35-39	57.500	171.9250	6.1304	57.500
13	39-43	63.500	189.8650	6.4423	63.500
14	43-47	69.500	207.8050	6.7398	69.500
15	47-51	75.500	225.7450	7.0247	75.500
16	51-55	81.500	243.6850	7.2985	81.500

Appendix D

Matlab scripts

D.1 Fourier amplitudes for earthquake time histories

```
%DESCRIPTION: THIS SCRIPT DETERMINES THE FOURIER AMPLITUDES OF THE
%COMPONENTS OF THE LOMA PRIETA ACCELERATION SERIES

%SYMBOLS:
%acc_vector= acceleration series for the different components [m/s^2]
%dt= time step [s]
%t= time vector [s]
%N= number of points []
%f= frequencies [Hz]
%F= Fourier transform
%f1= frequencies for one sided Fourier transform [Hz]
%A= one-sided Fourier transform
%a= real component of the one-sided Fourier transform
%b= imaginary component of the one-sided Fourier transform
%c= Fourier amplitude

clear
close all
clc

%Importing the three series
filename1= 'RSN789_LOMAP_PTB207.txt';
fileID= fopen(filename1,'r');  %Opening the file, it returns a file identifier
data1= textscan(fileID,['%f' '%f' '%f' '%f' '%f'], 'Headerlines',4);
%['%f''%f''%f'] means that the .txt file has three columns with data
% Headliners is the number of rows that are not data at top of file.
fclose(fileID);
filename2= 'RSN789_LOMAP_PTB297.txt';
fileID= fopen(filename2,'r');
data2= textscan(fileID,['%f' '%f' '%f' '%f' '%f'], 'Headerlines',4);
fclose(fileID);
filename3= 'RSN789_LOMAP_PTB-UP.txt';
fileID= fopen(filename3,'r');
data3= textscan(fileID,['%f' '%f' '%f' '%f' '%f'], 'Headerlines',4);
fclose(fileID);
acc_matrix1= cell2mat(data1);  %from cell to matrix
acc_matrix2= cell2mat(data2);
acc_matrix3= cell2mat(data3);
[nrow,ncol]= size(acc_matrix1); %number of rows and columns in the matrix
acc_vector1= zeros(1,nrow*ncol-3);
acc_vector2= zeros(1,nrow*ncol-3);
acc_vector3= zeros(1,nrow*ncol-3);
counter= 1; %counter for element in acc_vector
for i=1:nrow
   for j=1:ncol
      if i==nrow  %Checking last row where there are only three numbers
       if j<4
        acc_vector1(counter)= acc_matrix1(i,j);
```

```
        acc_vector2(counter)= acc_matrix2(i,j);
        acc_vector3(counter)= acc_matrix3(i,j);
        counter= counter+1; %updating the counter
       end
      else
       acc_vector1(counter)= acc_matrix1(i,j);
       acc_vector2(counter)= acc_matrix2(i,j);
       acc_vector3(counter)= acc_matrix3(i,j);
       counter= counter+1; %updating the counter
      end
   end
end
%Converting from g to m/s^2
acc_vector1= acc_vector1*9.81;  %horizontal x-direction
acc_vector2= acc_vector2*9.81;  %horizontal y-direction
acc_vector3= acc_vector3*9.81;  %vertical direction

%Time vector
dt= 0.005;    %time step between values
t= 0:dt:dt*(length(acc_vector1)-1);

%Fourier amplitudes
N= length(t);
f= 1/(2*dt)*linspace(-1,1,N); %Frequencies for two sided Fourier transform
F1= fftshift(fft(acc_vector1,N))/N; %Two sided Fourier transform
F2= fftshift(fft(acc_vector2,N))/N;
F3= fftshift(fft(acc_vector3,N))/N;
f1= f(N/2+1:end); %Frequencies for one sided Fourier transform
A1= 2*F1(N/2+1:end); %One sided Fourier transform
A2= 2*F2(N/2+1:end);
A3= 2*F3(N/2+1:end);

%Fourier amplitude spectrum
a1= real(A1(1,:));    %Real components of FFT
b1= imag(A1(1,:));    %Imaginary components of FFT
c1= sqrt(a1.^2+b1.^2); %Amplitude at each frequency value
a2= real(A2(1,:));
b2= imag(A2(1,:));
c2= sqrt(a2.^2+b2.^2);
a3= real(A3(1,:));
b3= imag(A3(1,:));
c3= sqrt(a3.^2+b3.^2);

Freq1= f1(1:801); C1= c1(1:801); %Extracting a part of the values
Freq2= f1(1:801); C2= c2(1:801);
Freq3= f1(1:801); C3= c3(1:801);
```

D.2 Analytical solution for propagation of pressure due to seaquake

```
%DESCRIPTION: ESTIMATION OF THE ANALYTICAL PRESSURE FOR TWO CASES: ONE WITH
%ZERO TOP PRESSURE AND ONE WITH ZERO TOP DISPLACEMENT

%SYMBOLS:
%vertical_acc= full length vertical acceleration series [m/s^2]
%vertical_vel= full length vertical velocity series [m/s]
%vertical_disp= full length vertical displacement series [m]
%t= full length time [s]
%dt= time step [s]
%L= number of points in acceleration series []
%U= Fourier transform of displacement at the seabed in terms of frequencies
%   in Hz or rad/s
%fs= frequency [Hz]
%f= Nyquist frequency [Hz]
%w= angular frequency [rad/s]
%H= Transfer function
%P= Fourier transform of pressure at point of interest
%vp= pressure wave velocity [m/s]
%k= wave number series [rad/m]
%D= height of column for the two cases (index 1 for the case with zero top
%   pressure, 2 for the case with zero top displacement)
%z= depth for bottom of the floater for the case with a free field at the
%   top
%Ks= Bulk modulus of water [N/m^2]
%xi= damping ratio
%pressure= pressure series at the points of interest [Pa]

close all
clear
clc

%Loading the acceleration and time series
vertical_acc= load('Vertical_series_unscaled.mat','acc_vector3');
%Entire time series
t= load('Time_series.mat','t');
vertical_acc= vertical_acc.acc_vector3;
t= t.t;
dt= t(2)-t(1);

%Compution the displacement series using numerical integration
vertical_vel= cumtrapz(t,vertical_acc);
vertical_disp= cumtrapz(t,vertical_vel);
L= length(vertical_disp);

%One sided Fourier transform of the vertical displacement using an FFT
%algorithm
Uf= fftshift(fft(vertical_disp,L));
Uf0= 2*Uf(L/2+1:end);
fs= 1/dt;
f= fs/2*linspace(0,1,L/2);
w= f*2*pi;
Uw0= Uf0/(2*pi);

%Transfer functions for the two considered cases
D1= 130; z= D1-22; D2= 108; vp= 1500; Ks= 2.34*10^9; xi= 0.05;
k= w/vp;
```

```
H1= Ks*k.*(1+1i*xi).*(-sin(k.*(1-1i*xi)*z)+tan(k.*(1-1i*xi)*D1).*cos(k*(1-1i*xi)*z));
H2= Ks*k.*(1+1i*xi)./sin(k*(1-1i*xi)*D2);

%One-sided Fourier transform of the two pressure series
Pw1= H1.*Uw0; Pw2= H2.*Uw0;
Pf1= 2*pi*Pw1; Pf2= 2*pi*Pw2;
%Two-sided transforms of the two pressure series
P1= zeros(1,L); P2= zeros(1,L);
P1(1:L/2)= fliplr(0.5*Pf1); P1(L/2+1:end)= 0.5*Pf1;
P2(1:L/2)= fliplr(0.5*Pf2); P2(L/2+1:end)= 0.5*Pf2;
P1= ifftshift(P1); P2= ifftshift(P2);
P2(1)= 0; P2(end)= 0; %Avoiding NaN-values

%Pressure time series for the two cases
pressure1= ifft(P1,'symmetric'); pressure2= ifft(P2,'symmetric');
```

D.3 Extreme value distribution for design mooring tension

```
% DESCRIPTION: THIS SCRIPT FITS A GUMBEL DISTRIBUTION TO MAXIMAL MOORING LINE
% TENSIONS OBTAINED FROM SEVERAL SIMULATIONS OF ENVIRONMELTAL LOADING

% SYMBOLS:
% N: number of individual SIMA simulations of mooring line tension
% T_bar: Contains the mean mooring line tension during the last three hours
% of each SIMA simulation
% T_max: Contains the maximum mooring tension during the last three hours
% of each SIMA simulation
% MPM: The most probable maximum mooring line tension
% T_cm: characteristic mean tension
% T_cd: characteristic dynamic tension
% gam_m: mean tension load factor
% gam_d: dynamic tension load factor
% Td: design tension

clc
clear all
close all

%% MOORING TENSION DATA
%=========================================================================
% SIMA Parameters: Hs=10.9m, Tp=14.8s, gam=1.813
% Wave seed numbers: [1001:1:1030]

T_bar = [1930 1937 1951 1941  1943  1955 1941 1963 1936 1927 ...
    1946 1937 1965 1942 1952 1957 1939 1954 1942 1957 ...
    1959 1956 1940 1936 1933 1946 1951 1967 1948 1952]';
T_max  = [7525 7051 7291 11433 10337 6397 6186 7806 6728 6429 ...
    9189 6896 8753 6524 7051 6286 7171 7399 6615 5990 ...
    7314 6266 6609 6668 7036 6113 6105 7569 7295 6578]';

%% FIT PROBABILITY DISTRIBUTION
%=========================================================================
paramEstsMaxima = evfit(-T_max);
y = linspace(4000,12000,8001);

p_pdf = evpdf(-y,paramEstsMaxima(1),paramEstsMaxima(2));
p_cdf = cumtrapz(y,p_pdf);

figure
plot(y,p_pdf)
title('Probability density function')
xlabel('Peak tension [kN]')
grid on

figure
plot(y,p_cdf)
title('Cumulative distribution function')
xlabel('Peak tension [kN]')
grid on
hold on


x_values = sort(T_max);
N = length(T_max);
```

```
for i = 1:N
    plot(x_values(i),i/(N+1),'ro')
end
%% FIND THE MOST PROBABLE MAX
%=========================================================================
idx = find(abs(p_cdf-0.37) < 0.0003);
MPM = y(idx);
line([MPM MPM],[0,.37],'Color','red','LineStyle','--')
line([4000 MPM],[.37,.37],'Color','red','LineStyle','--')
%% CALCULATE DESIGN MOORING TENSION
%=========================================================================
% Td = gam_mean * T_c,mean + gam_dyn * T_c,dyn (DNVGL-ST-0119 8.2.2.1)

gam_m = 1.3;  % (DNVGL-ST-0119 TABLE 8-1, ULS,CC1)
gam_d = 1.75; % (DNVGL-ST-0119 TABLE 8-1, ULS,CC1)

T_cm = mean(T_bar);
T_cd = MPM - T_cm;

Td = gam_m*T_cm + gam_d*T_cd; % Design tension
```

D.4 Beam model of wind turbine tower

```
%%DESCRIPTION: THIS SCRIPT ESTABLISHES THE SYSTEM MATRICES FOR A BEAM
%%ELEMENT MODEL OF THE WIND TURBINE TOWER. THE NATURAL FREQUENCIES AND
%%CORRESPONDING MODE SHAPES ARE DETERMINED.

%%SYMBOLS:
%tower_data= structural properties of the tower given in an external file
%lowerElevations= elevation of the bottom end of the tower elements [m]
%upperElevations= elevation of the top end of the tower elements [m]
%outerDiameters= outer diameter of the tower elements [m]
%wallThicknesses= wall thickness of the tower elements [m]
%sectionMasses= total mass of the tower elements [m]
%Z= vertical nodal coordinates [m]
%E= modulus of elasticity [N/m^2]
%n_elem= number of sections/elements []
%n_node= number of global nodes []
%n_dof= number of global degrees of freedom []
%m_nac= mass of nacelle [kg]
%m_rot= mass of rotor blades [kg]
%m_RNA= mass of rotor-nacelle assembly [kg]
%I_RNA= RNA pitch moment of inertia
%m_plt= mass of platform [kg]
%K= stiffness matrix
%M= mass matrix
%w= natural frequencies [rad/s]
%phi= mode shape []
%f= natural frequencies [Hz]

%=========================================================================
clc
clear all
close all

%1.0 Define general properties and read tower data from file
%=========================================================================
tower_data = readmatrix('tower_distr_properties');

lowerElevations = tower_data(:,2);
upperElevations = tower_data(:,3);
outerDiameters = tower_data(:,4);
wallThicknesses = tower_data(:,5);
sectionMasses = tower_data(:,7);

Z = [lowerElevations;upperElevations(end)];

E = 2.1e+11; %[N/m^2]

n_elem = 27;
n_node = n_elem + 1;
n_dof = 3*n_node;

%1.1 RNA and Platform properties
%=========================================================================
m_nac = 446006;
m_rot = 230717;
m_RNA = m_nac + m_rot;
I_RNA = 1.062E+08;
```

```
m_plt = 2.1709e+07;
%2.0 Assemble global stiffness and mass matrices
%=========================================================================
K = zeros(n_dof);
M = zeros (n_dof);
for i = 1:n_elem
    L(i) = Z(i+1)-Z(i);             % Element i length
    t(i) = wallThicknesses(i);      % Element i wall thickness
    r1(i) = outerDiameters(i)/2;    % Element i outer radius
    r2(i) = r1(i) - t(i);           % Element i inner radius
    A(i) = pi*(r1(i)^2-r2(i)^2);    % Element i cross-sectional area
    I(i) = pi/4*(r1(i)^4-r2(i)^4);  % Element i second moment of area

    interval = [3*(i-1)+1:3*(i+1)]; % Interval of element i contribution

    K(interval,interval) = K(interval,interval) + ...
        plane_beam_stiffness(E,I(i),A(i),L(i));
    M(interval,interval) = M(interval,interval) + ...
        beam_mass_matrix(sectionMasses(i),L(i));
end
%2.1 Add mass and stiffness from platform
%=========================================================================
M(1,1) = M(1,1) + m_platform;

K_hydrostatic = [5.4189e+06 0 49136;
                 0 0 0;
                 49136 0 2.7988e+9];

K_surge = [0 0 0;
           0 1e+06 0;
           0 0 0];

K([1:3],[1:3]) = K([1:3],[1:3]) + K_hydrostatic + K_surge;
%2.2 Introduce fixed boundary condition at the bottom and RNA mass
%=========================================================================

% Deleting rows and corresponding colums of K and M, and setting K(1,1) =
% M(1,1) = K(2,2) = M(2,2) = K(3,3) = M(3,3) = 0 to impose fixed boundary

K([1:3],:) = zeros(3,n_dof);
K(:,[1:3]) = zeros(n_dof,3);
K([1:3],[1:3]) = eye(3);

M([1:3],:) = zeros(3,n_dof);
M(:,[1:3]) = zeros(n_dof,3);
M([1:3],[1:3]) = eye(3);

M(end-1,end-1) = M(end-1,end-1) + m_RNA; % including RNA mass
M(end,end) = M(end,end) + I_RNA; % RNA pitch inertia
%2.3 Solve eigenvalue problem and get mode shapes + frequencies
%=========================================================================
[PHI,B] = eig(K,M); % Eigenvalue problem
w = sqrt(diag(B));

phi_1 = PHI(2:3:end,4);
phi_1_norm = phi_1./max(abs(phi_1));
phi_2 = PHI(2:3:end,5);
phi_2_norm = phi_2./max(abs(phi_2));
```

```
phi_3 = PHI(2:3:end,6);
phi_3_norm = phi_3./max(abs(phi_3));
w1 = w(4);
w2 = w(5);
w3 = w(6);

f1 = w1/(2*pi);
f2 = w2/(2*pi);
f3 = w3/(2*pi);
```

D.5 Theoretical displacement of simply supported plate

```
%DESCRIPTION: THIS SCRIPT CALCULATES THE SOLUTION OF THE DIFFERENTIAL
%EQUATION RELATED TO BENDING OF PLATES. THE LOAD IS EXPANDED USING A
%FOURIER SERIES

%SYMBOLS:
%E= Young's modulus [Pa]
%t= plate thickness [m]
%v= Poisson's ratio
%D= bending stiffness of plate
%a & b= length of the plate sides [m]
%q= evenly distributed load [N/m]
%m & n= indexes im Fourier series
%w_mn= amplitude of displacement component in Fourier series [m]
%q_mn= amplitude of load component in Fourier series [N/m]
%w_mid= displacement at the middle of the plate [m]

%INPUT:
%[E,t,a,q,m,n]

%OUTPUT:
%w_mid

clear
close all
clc

%Input values
E= 2.1*10^11;
t= 0.03;
v= 0.3;
a= 1;
b= 1;
q= 10000;

%Bending stiffness
D= E*t^3/(12*(1-v^2));

%Number of terms in Fourier series
m= 10; n= 10;

%Displacement in the middle of the plate
w_mid= 0;
x= a/2; y= b/2;
for i=1:m
    for j=1:n
        q_mn= 4*q/(a*b)*a/(i*pi)*(1-cos(i*pi))*b/(j*pi)*(1-cos(j*pi));
        w_mn= q_mn/(pi^4*D*((i/a)^2+(j/b)^2)^2);
        w_mid= w_mid+w_mn*sin(i*pi*x/a)*sin(j*pi*y/b);
    end
end
```

D.6 Acceleration obtained by numerical differentiation

```
% DESCRIPTION: THIS SCRIPT CALCULATES ACCELERATION OF SIMO BODIES BASED ON
% NUMERICAL DIFFERENTIATION OF THE CORRESPONDING POSITION, BY A CENTRAL SECOND-ORDER
% FINITE DIFFERENCE METHOD

% SYMBOLS:
% hullBody:          SIMO body number
% nchan:             Number of channels in the SIMO results file
% nts:               Number of time steps
% dt_SIMO:           Time step employed in the SIMO calculations
% chanNames:         Names of the channels in the SIMO results file
% SIMO_bin:          Matrix containing SIMO response quantities
% size_SIMO_bin:     Size of the SIMO binary file
% chanMotions:       SIMO results channels containing the body motions
% chanAccelerations: SIMO results channels containing body accelerations
% chanFz:            SIMO results channel containing external vertical force
% chanWave:          SIMO results channel containing wave elevation
% time_SIMO:         time vector from SIMO
% BodyMotion:        array containing body motions in all 6DOF's
% BodyAccel:         array containing body accelerations in all 6DOF's
% n:                 every "n" entry of position signal used in differentiation
% start_idx:         index corresponding to time of application of seaquake
% stop_idx:          index corresponding to seaquake end time
% heave:             every "n" entry of the SIMO heave motion during seaquake
% t:                 every "n" entry of the SIMO time array during seaquake
% dt:                time step used in differentiation
% N:                 number of entries in the reduced motion- and time signals
% heave_acc:         SIMO body heave acceleration obtained by numerical differentiation

close all
clear all
clc

%% READ SIMO RESULTS
%========================================================================
hullBody = 2; %SIMO body number
% Read the SIMO results text file to get the channel names and number
% of steps
[nchan, nts, dt_SIMO, chanNames] = ...
    readSIMO_resultstext('results.txt');
% Read the binary file
SIMO_bin = read_simoresults('results.tda',nts);
size_SIMO_bin = size(SIMO_bin);
if (size_SIMO_bin(1)<nts || nts<1); ...
    disp('Unable to read SIMO results'); return; end
% Determine which channels to read for the platform motions, wave
% elevation
[chanMotions, chanAccelerations, chanFz, chanWave] = ...
    getchannelNumbers(chanNames,hullBody);
if (chanMotions(1)<1 || chanWave<1 || chanAccelerations(1)<1); ...
        disp('Unable to read SIMO results'); return; end
time_SIMO = SIMO_bin(:,2);
% summarize data in matrix
BodyMotion = SIMO_bin(:,chanMotions);
BodyAccel = SIMO_bin(:,chanAccelerations);

%% NUMERICAL DIFFERENTIATION BY A SECOND ORDER CENTRAL DIFFERENCE METHOD
```

```
%==========================================================================
n = 10;
start_idx = round(200/dt_SIMO);
stop_idx = round(217.2/dt_SIMO);

heave = BodyMotion(start_idx:n:stop_idx,3);
t = time_SIMO(start_idx:n:stop_idx,1);
dt = n*dt_SIMO;

N = length(heave);

heave_acc = zeros(N,1);

for i = 2:N-1
   heave_acc(i,1) = (heave(i+1)-2*heave(i)+heave(i-1))/(dt^2);
end
```

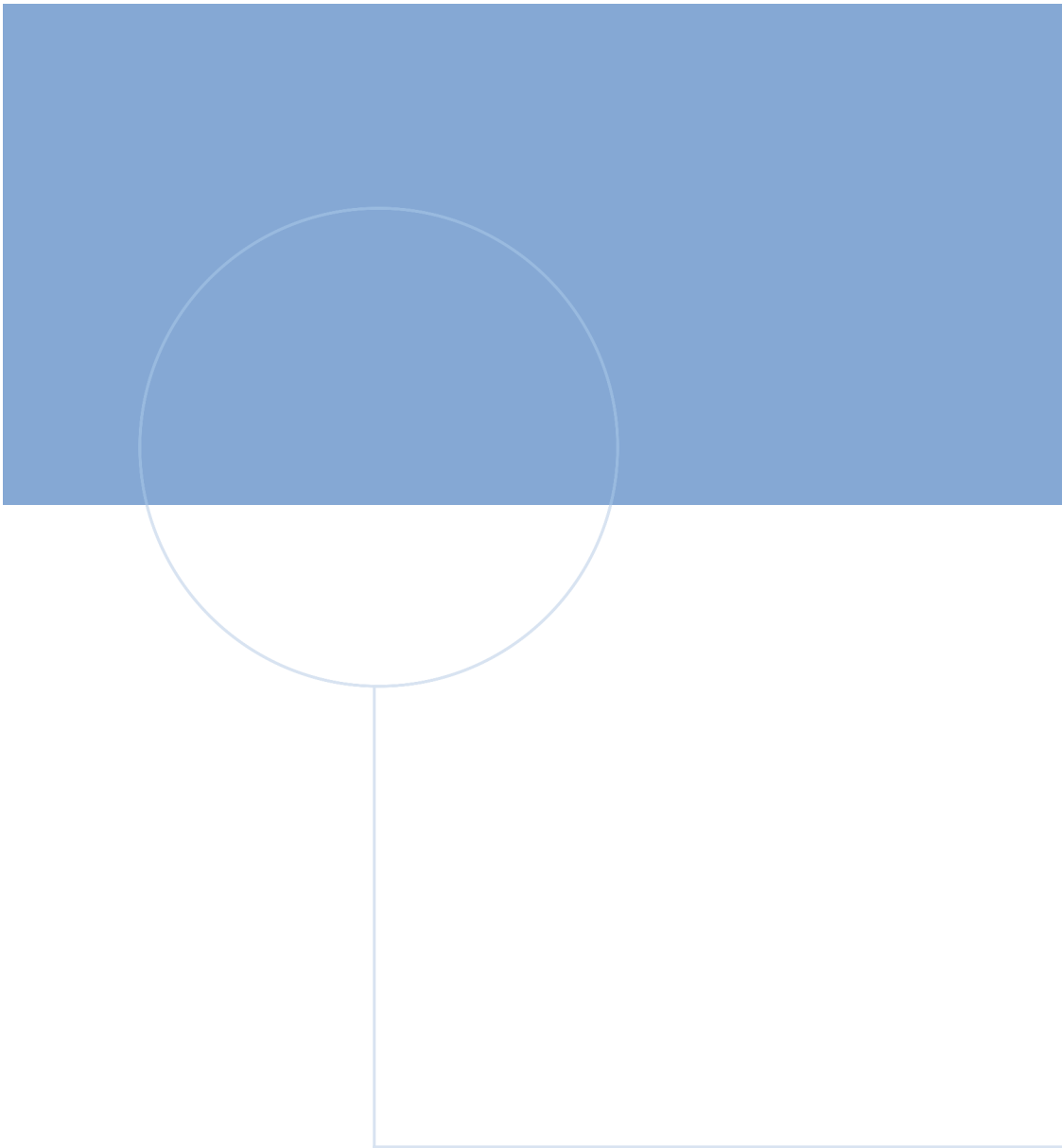

NTNU

Norwegian University of
Science and Technology